3D Hierarchically-Structured Twinned Alumina Nanosheets for Filtration and Catalysis

Katrina Roebuck

Thesis submitted in partial fulfillment
of the requirements for the degree of
Doctor of Philosophy in Chemical Engineering

In

Department of Chemical and Biological Engineering
Faculty of Engineering
University of Ottawa

Abstract

Currently, complex nanostructures can be synthesized in two distinct forms: non-porous aggregates that maintain their structure when subject to external pressure but have poor flow characteristics, and highly porous particles or particle aggregates that are permeable to flow but collapse and stack under external pressure. The development of support materials for filtration and catalysis that maintain high throughput, resist fouling, and maintain high internal pore accessibility are therefore of great interest.

In this work, our primary objective was to synthesize a nanostructure by self-assembling nanoplatelets in a hierarchical structure. We sought to develop a material that in filtration would be highly permeable to flow, and maintain its structure when subject to external pressure. As a catalyst, we desired a material that provided easy access of reactants to its internal structure, and release of products to the bulk media in order to improve the catalyst specificity. We successfully synthesized this material and determined that the concentrations of ethanol and surfactant in the synthesis mixture controlled the morphology of the nanoparticles in the hierarchically-structured material (HSM).

We compared the performance of our HSM to commonly-used filtration aids during the filtration of a colloidal solution. Our HSM rapidly reduced the turbidity of the colloidal solution to $\leq$0.10 NTU at a flux that was up to 28 times higher than the fluxes obtained by the commonly-used filtration aids. Subsequently, we developed a protocol to immobilize lipase from crude porcine pancreas (cPPL), *Candida rugosa* (CRL), and *Candida antarctica* (CALB) onto the support material. We assessed the specific hydrolytic activities of immobilized crude porcine pancreas and *Candida rugosa* to determine the optimum synthesis conditions to produce the most effective HSM support. We determined that

synthesizing our HSM in 50 vol% ethanol-water followed by a 24 h epoxysilane treatment process produced particles with the highest lipase immobilized and retained (16.7 $\pm$ 0.2 mg cPPL / g support and 39.7 $\pm$ 0.9 mg CRL / g support). Extended silylation of the supports beyond 24 h was found to not significantly increase enzyme immobilization. Finally, we assessed the performance of immobilized CALB on our support material in a batch reactor for the reduction of free fatty acids (FFA) in acidic oil. The immobilized enzyme produced in this work rapidly reduced the FFA content during the initial 2 to 4 h of each run and maintained the FFA content below 0.50 wt% for up to 56 h even after being reused 5 times. CALB immobilized on TAN showed high reusability with no observable reduction in immobilized catalyst activity.

Résumé

Les nanostructures complexes peuvent être synthétisées sous deux formes distinctes: des agrégats non poreux qui maintiennent leur structure lorsqu'elles sont soumises à une pression externe, et des particules fortement poreuses ou des agrégats de particules perméables à l'écoulement, mais qui s'effondrent et s'empilent sous une pression externe. Le développement de matériaux poreux pour la filtration et la catalyse qui maintiennent un débit élevé en filtration, résistent à l'encrassement et maintiennent une forte accessibilité aux pores internes présentent un grand intérêt.

Dans ce travail, notre objectif principal était de synthétiser une nanostructure en auto-assemblant des nano-plaquettes dans une structure hiérarchique. Nous avons cherché à développer un matériau qui, en filtration, serait hautement perméable et maintiendrait sa structure sous une pression externe. En tant que catalyseur, nous avons souhaité un matériau qui fournirait l'accès facile des réactifs à sa structure interne et permettrait la libération des produits afin d'améliorer sa spécificité. Nous avons synthétisé avec succès ce matériau et déterminé que les concentrations d'éthanol et d'agent tensioactif dans le mélange de synthèse contrôlaient la morphologie des nanoparticules dans le matériau structuré par hiérarchie (HSM).

Nous avons comparé les performances de notre HSM aux agents de filtration couramment utilisés lors de la filtration d'une solution colloïdale. Notre HSM a rapidement réduit la turbidité d'une solution colloïdale à $\leq$0,10 NTU avec un flux qui était jusqu'à 28 fois plus élevé que les flux obtenus par des aides filtres diatomées. Par la suite, nous avons mis au point un protocole visant à immobiliser les lipases suivantes : lipase pancréatique porcine crue (cPPL), *Candida rugosa* (CRL) et *Candida antarctica* (CALB) sur le matériau de

support. Nous avons évalué les activités hydrolytiques spécifiques de la cPPL et du CRL immobilisés pour déterminer les conditions de synthèse optimales pour produire le support HSM le plus efficace. Nous avons déterminé que la synthèse de notre HSM dans une solution aqueuse contenant 50% en volume d'éthanol, suivi d'un traitement de 24 h à l'époxysilane, produit des particules ayant la plus haute immobilisation et rétention de lipase (16,7 $\pm$ 0,2 mg de cPPL / g et 39,7 $\pm$ 0,9 mg de CRL / g de support). La silylation étendue des supports au-delà de 24 h n'a pas permis d'augmenter significativement l'immobilisation enzymatique. Enfin, nous avons évalué la performance du CALB immobilisé sur notre matériau de support dans une réaction en lot pour la réduction des acides gras libres (FFA) dans une huile de colza acidifiée. L'enzyme immobilisée produite dans ce travail a rapidement réduit le contenu en FFA de l'huile pendant les 2 à 4 h initial de chaque essai et a maintenu le contenu en FFA inférieur à 0,50% en poids jusqu'à 56 h même après avoir été réutilisé 5 fois. Le CALB immobilisé sur TAN présentait une réutilisabilité élevée sans réduction observable de l'activité du catalyseur immobilisé.

Statement of Contributions of Collaborators

I hereby declare that I am the sole author of this thesis. I performed all of the nanosheet syntheses, lipase immobilization experiments, batch experiments involving filtration and FFA reduction, samples analyses, and performed the subsequent data analysis, except as indicated below. I have written all of the chapters contained in this thesis.

Some twinned alumina nanosheets used in Chapters 6 and 7 were synthesized by Xun Xun Shi and Xuewei Meng, respectively. Jiarong Zhou collected the Karl Fischer titration results presented in Chapter 7.

Bulat Gabidullin prepared XRD data presented in Chapter 3. Glenn Poirier (Chapters 3 – 5) performed carbon coating of samples for SEM analysis.

My supervisor, Dr. André Y. Tremblay, provided guidance throughout my research. He provided editorial comments of the written work, and provided assisted in the writing of the first article (Chapter 3).

Acknowledgements

Thank you Dr. Tremblay. Without your patience and your very good supervision, this thesis would not have been possible. I cannot express how grateful I am for the years of work you have put into making me a better researcher, a better writer, and a better person. I hope I have made you proud.

To Peter, my husband. I love you. You know what you did.

To my students, thank you for letting me be myself.

Thank you to the National Science and Engineering Research Council for their financial support of this project through a Discovery Grant.

To Dr. Taylor, thank you for your mentorship. See you later, have fun.

To the technical support team, thank you for all of your help. You are an integral part of the chemical engineering department and we would be lost without you.

To the cool office, one more escape room?

To Jiarong, 我的猫猫.

To Xuewei, 绿色铝驴.

To my parents: it's been a long ride! Thank you for catching me when I fell down. Thank you for your unconditional love. I'm gonna be a doctor!

Table of Contents

List of Tables

List of Figures

Nomenclature

Abbreviations

Al-0/TAN-0	Twinned alumina nanosheets synthesized in pure water at CTAB CMC
Al-25/TAN-25	Twinned alumina nanosheets synthesized in 25 vol% ethanol in water at CTAB CMC
Al-50/TAN-50	Twinned alumina nanosheets synthesized in 50 vol% ethanol in water at CTAB CMC
Al-x-*t*-*lipase type*	Twinned alumina nanosheets synthesized in *x* vol% ethanol in water at CTAB CMC, silylated for *t* hours, with immobilized *lipase type*
AOCS	American Oil Chemists' Society
ATR	Attenuated total reflectance
BSA	Bovine serum albumin
CALB	Lipase from *Candida antarctica*
CF	Cake filtration
CMC	Critical micelle concentration
cPPL	Crude porcine pancreatic lipase
CRL	*Candida rugosa* lipase
CTAB	Cetyl trimethylammonium bromide
DE	Diatomaceous earth
DE-512	Diatomaceous earth (medium grade)
DE-577	Diatomaceous earth (fine grade)
DG	Diglyceride(s)
DI	Distilled deionized water
DLS	Dynamic light scattering
DM	Dynamic membrane
DPA	Dynamic particle analyzer/analysis
DVB	Divinylbenzene
EC	Enzyme Commission number
ED	Electrodialysis

EDS	Energy dispersive spectrometry
ETES	2-(3,4-epoxycyclohexyl)ethyltriethoxysilane
FAAE	Fatty acid alkyl ester(s)
FFA	Free fatty acid(s)
FTIR	Fourier transform infrared (spectroscopy)
GMA-MMA	Copolymers of glycidyl methacrylate and methyl methacrylate
GPS	γ-glycidoxypropyltrimethoxysilane
HSM	Hierarchically-structured material
IB	Intermediate blocking
IOC	International Olive Council
JCPDS	Joint Committee on Powder Diffraction Standards
JEOL	Japan Electron Optics Laboratory
LDLO	Lowest lethal dose
MAG	Monoacylglycerol
MBR	Membrane bioreactor
MG	Monoglyceride(s)
Na(AOT)	Sodium bis(2-ethylhexyl)sulfosuccinate
NF	Nanofiltration
No.	Number
PBR	Packed bed reactor
PBS	Phosphate buffer solution
PC	Pore constriction
PEO	Poly(ethylene oxide)
pH	Potential of hydrogen
POS-PVA	Composite of polysiloxane and polyvinyl alcohol
PPL	Porcine pancreatic lipase
RO	Reverse osmosis

SCA	Silane coupling agent
SDBS	Sodium dodecylbenzenesulfonate
SDS	Sodium dodecyl sulfate
SEM	Scanning electron microscope/microscopy
SERS	Surface-enhanced Raman spectroscopy
SS	Stainless steel
SSR	Sum of square residuals
TAN	Twinned alumina nanosheet(s)
TAN-HV	High-volume filtration run using twinned alumina nanosheets
TCLO	Lowest toxic concentration
TDLO	Lowest toxic dose
TG	Triglyceride
UK	United Kingdom
UV-Vis	Ultraviolet-visible spectroscopy/spectrophotometry
vol	Volume
VTES	Vinyltriethoxysilane
VWR	**V**an **W**aters / **R**ogers (surnames of the original founders)
wt	Weight
XRD	X-ray diffraction

Symbols – English Letters

A	Area of filter paper available for filtration
C	Permeate solids concentration during DM filtration
C_{acid}	Concentration of hydrochloric acid added during titration
C_{FFA}	Concentration of FFA in oil mixture
C_i	Concentration of an ion in solution
C_0	Influent solids concentration during DM filtration

D_1	Packing density of one set of mono-sized spheres
$D_{1,2}$	Packing density of two sets of mono-sized spheres
$D_{1,2,3}$	Packing density of three sets of mono-sized spheres
d_{50}	Median particle size of a particle size distribution
d_{av}	Mean particle size of a particle size distribution
D_c	Center part density
F	Faraday constant
J_0	Average flux across filter paper OR initial permeate flux through clean membrane
J_{total}	Average flux across DM and filter paper
J_v	Permeate flux
K_i	Proportionality constant in membrane filtration models
m	Mass of sample used to estimate bulk density of DM OR mass of titration sample measured using analytical balance
MW_{FFA}	Molecular weight of FFA (oleic acid = 282.46 g/mol)
n	Exponent value to fit normalized filtration models
R	Universal gas constant
r_i	Radius of spheres used in sphere packing models
S	Surface area of container used in sphere packing models
SF	Separation factor
T	Absolute temperature
t	Time
U	Enzyme activity
V	Volume of container used in sphere packing models
V_{acid}	Volume of hydrochloric acid added during titration
V_{sample}	Volume of saturated sample used during water evaporation method
W_{dried}	Mass of dried sample used during water evaporation method
W_{sat}	Mass of saturated sample used during water evaporation method
x	Thickness of DM

Z_i	Charge on an ion in solution

Symbols – Greek Letters

α	Degree of micelle ionization
ΔG^0_{mic}	Gibbs free energy of micelle formation
$(\Delta G^0_{mic})_{cosolvent/water}$	Gibbs free energy contributed by the cosolvent
$(\Delta G^0_{mic})_{water}$	Gibbs free energy contributed by pure water
ΔG^0_{trans}	Gibbs free energy of transfer
ΔP	Pressure difference across DM and filter paper
ε	Sample porosity OR boundary evacuation coefficient OR dielectric constant
ε_0	Relative permittivity of a vacuum
ε_R	Relative permittivity of a solution
Θ	Scattering angle
κ	Debye length OR hydraulic permeability
λ	Wavelength OR hydraulic resistance
μ	Fluid viscosity OR average of a log-normal distribution
ρ_b	Bulk density of sample used to estimate thickness of DM
ρ_{water}	Density of water
σ	Standard deviation of a log-normal distribution
χ_{CMC}	Critical micelle concentration expressed as a mole fraction

Units – Roman Letters

Å	Angstroms
C	Coulombs
cm	Centimeters
°	Degrees (angle)
°C	Degrees Celsius

g	Grams
h	Hours
K	Kelvin
kg	Kilograms
kJ	Kilojoules
kPa	Kilopascals
kV	Kilovolts
L	Liters
LMH	Liters per meters squared per hour
M	Molar (moles per liter)
m	Meters
m^2	Square meters
m^3	Cubic meters
mD	Millidarcy (unit of permeability)
mg	Milligrams
min	Minutes
mL	Milliliters
mM	Millimolar (millimoles per liter)
mol	Moles
MPa	Megapascals
N	Normal
nm	Nanometers
NTU	Nephelometric turbidity unit
Pa	Pascals
ppm	Parts per million
psig	Pounds per square inch gauge
rpm	Revolutions per minute

s	Seconds

Units – Greek Letters

µL	Microliters
µm	Micrometers
μm^3	Cubic micrometers
µmol	Micromoles

1 Introduction

1.1 Background and Motivation

Materials science is an ever-evolving discipline in science and engineering. Materials with complex superstructures are of growing interest. Many of these materials exhibit structure over more than one length scale. These "hierarchically-structured materials" (HSMs) possess desirable properties such as higher surface area, internal pore accessibility, strength, and storage capabilities relative to simple porous materials lacking such hierarchy [1].

Currently, complex nanostructures can be synthesized in two distinct forms: stiff non-porous aggregates that maintain their structure when subject to external pressure but have poor flow characteristics, and highly porous particle or particle aggregates that are permeable to flow but collapse and stack under external pressure (Table 1-1).

Table 1-1: Currently Available Complex Nanostructures

Material	Structure	Source
Alumina	Non-porous, cantaloupe-like superstructures (2.5 μm diameter)	[2]
	Non-porous flower-like superstructures (1 μm long)	[3]
	Non-porous aggregated flower-like nanoleaves (0.06 – 0.09 μm thick)	[4]
	Dense mats of microscale fibers (0.1 – 0.15 μm diameter, 1 – 15 mm long)	[5]
	Self-supporting dense film of aggregated alumina fibers (0.005 – 0.008 μm diameter, 2 – 3 μm long)	[6]
Boehmite	Dispersed hexagonal nanoparticles (0.005 μm diameter)	[7]
	Dispersed hexagonal crystallites (0.015 – 0.040 μm diameter)	[8]
Ceria	Non-porous aggregated coarsened spherical clusters (0.390 μm diameter)	[9]
Various polymers	Dense mats of multilayered nanotubes (0.4 – 0.5 μm diameter)	[10]
	Dense mats of composite core-shell nanofibers (0.446 – 2.762 μm diameter)	[11]
Titania	Dense mats of hollow nanofibers (0.2 μm diameter)	[12]

Certain separation and/or catalysis applications are inherently more difficult, including those involving viscous [13–15] or colloidal fluids [16–18]. Filtration of viscous or colloidal fluids is common in food & beverage [15,19,20], medical [21–23], petrochemical [24,25], and sludge & wastewater [26,27] applications. Heterogeneous catalysis involving viscous or colloidal fluids is used to produce biodiesel [28,29] and hydrogenated edible oils [30–32]. Therefore, the development of support materials that maintain high throughput, resist fouling, and maintain high internal pore accessibility are of great interest. In other words, the ideal material would blend the stiffness of the non-porous particles and the permeability of the highly porous complex nanostructures discussed above.

1.1 Overview of Project Objectives

In this work, we focus on the synthesis and applications of a newly-synthesized shape-controlled HSM. Our overall objectives are as follows:

1. Examine the effects of synthesis conditions (i.e. cosolvent and surfactant) on nanosheet morphology.
2. Develop a synthesis regime for the production of hierarchically-structured twinned alumina nanosheets (TAN).
3. Compare the performance of hierarchically-structured TAN synthesized under different conditions as filtration aids during filtration of a colloidal bentonite solution to determine the optimal synthesis conditions.
4. Compare the performance of the optimal hierarchically-structured TAN filter aid to diatomaceous earth during filtration of a colloidal bentonite solution.

5. Develop a strategy for the effective immobilization of various lipases onto hierarchically-structured TAN.
6. Assess the effects of TAN synthesis conditions and silylation time on the specific hydrolytic activities of immobilized crude porcine pancreatic lipase and immobilized *Candida rugosa* lipase. Use these results to determine the synthesis conditions that produced the most effective TAN immobilization support.
7. Assess the performance of immobilized *Candida antarctica* lipase on TAN in a batch reactor for the reduction of free fatty acids in acidic oil.

1.2 Thesis Structure

This thesis consists of 9 chapters. The current chapter is the Introduction. Chapter 2 presents a detailed review of the literature on HSMs, alumina nanoparticles, filtration of viscous and colloidal material, and enzyme immobilization on highly accessible supports. Chapters 3 to 7 each represent an independent article published in or submitted to a peer-reviewed scientific journal. Due to this structure, some repetition of ideas and elements (i.e. experimental methodology) was inevitable. Chapter 8 provides a general discussion, conclusions, and recommendations for future work that pertains to the entire thesis. Chapter 9 contains references for the entire document. These references are numbered contiguously throughout the document.

CHAPTER 3 – The Self-Assembly of Twinned Boehmite Nanosheets into Porous 3D Structures in Ethanol-Water Mixtures; published in Colloids and Surfaces A: Physicochemical and Engineering Aspects 495 (2016): 238-247.

A detailed study on the self-assembly of twinned boehmite nanosheets was carried out in this work. Through the careful selection of synthesis parameters (ethanol:water volume fractions of 0:1, 0.25:0.75, and 0.5:0.5; CTAB concentrations of 25% below to 25% above the CMC, in 5% increments), it was determined that the shape and thickness of the boehmite nanosheets could be controlled. Furthermore, the boehmite nanosheets self-assembled to form highly-porous hierarchical structures with internal accessibility. It was also determined that the integrity of the highly-porous network of the 3D hierarchical structures was maintained upon calcination into alumina, suspension in water, and deposition on filter paper.

CHAPTER 4 – Optimal Aggregate Size Distribution for the Formation of Highly Efficient Nanosheet Dynamic Membranes; published in Journal of Membrane Science 514 (2016): 143-154.

In this study, the TAN were used as dynamic membranes in the filtration of a fine colloidal solution (i.e. bentonite clay). Three sets of alumina nanosheets were prepared (ethanol:water volume fractions of 0.0:1.0, 0.25:0.75, and 0.5:0.5; CTAB concentrations all at CMC) and characterized by dynamic image analysis. Confined sphere packing models were developed to estimate the packing densities of the three sets of alumina hierarchical structures.

CHAPTER 5 – Highly Permeable Twinned Alumina Nanoparticles for the Precoat Filtration of Fine Colloids; published in Separation and Purification Technology 182 (2017): 197-206.

In this study, the performance of hierarchically-structured TAN synthesized in 50:50 ethanol:water solutions as a filtration aid was compared to a commercially-available filtration aid (i.e. diatomaceous earth). The performance of the filter aids was assessed by monitoring flux decline and turbidity reduction during the constant-pressure filtration of a fine colloidal solution (i.e. bentonite clay).

CHAPTER 6 –Lipase Immobilization on Twinned Alumina Nanosheets (To be submitted)

In this study, the specific hydrolytic activity of free lipase and lipase immobilized on hierarchically-structured and functionalized TAN were assessed. Two sources of lipase were used: crude porcine pancreatic lipase and lipase from *Candida rugosa*. The TAN were synthesized in pure water, 25 vol%, and 50 vol% ethanol in water solutions and functionalized with an epoxysilane to promote enzyme immobilization. The effects of ethanol concentration in the synthesis mixture and the length of silylation time (0, 4, 24, or 96 h) on lipase immobilization were also assessed.

CHAPTER 7 – FFA-Selective Catalyst for the Pretreatment of Acidic Oils (To be submitted)

A detailed study on the enzymatic treatment of acidic oil was presented. Firstly, a protocol for the immobilization of lipase from *Candida antarctica* onto hierarchically-structured and functionalized TAN synthesized in 50:50 vol:vol ethanol:water solutions was established. The ability of the newly-fabricated immobilized enzyme preparation to reduce FFAs and inhibit TG hydrolysis in a 2.5 wt% FFA-in-oil mixture was assessed in a series of batch experiments at catalyst loadings of 0.3 and 0.03 wt%. These results were compared to those of a commercially-available supported enzyme.

2 Theoretical Background

2.1 Hierarchically-Structured Materials

2.1.1 Introduction

Hierarchically-structured materials can be defined simply as "solids [that] contain structural elements which themselves have structure." [33] Many natural substances are HSMs (e.g. bone, wood, vegetation); the synthesis process of man-made materials can also be tailored to produce HSMs. HSMs are of increasing interest in the material science community for their distinct advantages over materials without such hierarchy. The main motivation in synthesizing HSMs lies in the ability to impart greater accessibility to internal structures and overcome diffusional limitations associated with conventional porous materials [34]. However, the introduction of additional levels of porosity to HSMs to achieve greater internal accessibility is often at the detriment of other material properties, such as strength or hydrothermal stability [34].

2.1.2 Comprehensive Database Search for Scientific Literature on HSMs

A comprehensive database search was conducted in Scopus to determine the increasing interest of HSMs in the scientific literature. A summary of the parameters used in the database query is shown below in Table 2-1. The results were sorted into lists of 2000 documents or less (the maximum document limit in a single list allowed in Scopus). The lists were then further sorted by year, and then by subject area to generate sublists of 100 articles or less. The sublists generated were manually scrutinized to eliminate irrelevant articles and keep relevant articles. The original search yielded 16056 articles and review papers. After the manual review, the yield was reduced by 38% to 9880 articles and review papers. The results of the comprehensive literature search are shown in Figure 2-1.

Table 2-1: Parameters Used in Initial Database Query for HSMs

Search Parameter	Value
Search Term	(hierarchic OR hierarchical OR hierarchically) AND (structure OR structured)
Search Field(s)	article title, abstract, keywords
Date Range	1945 – present
Subject Area	engineering, materials science, medicine, chemistry, biochemistry, genetics, molecular biology, chemical engineering
Type of Scientific Literature	journal article or review

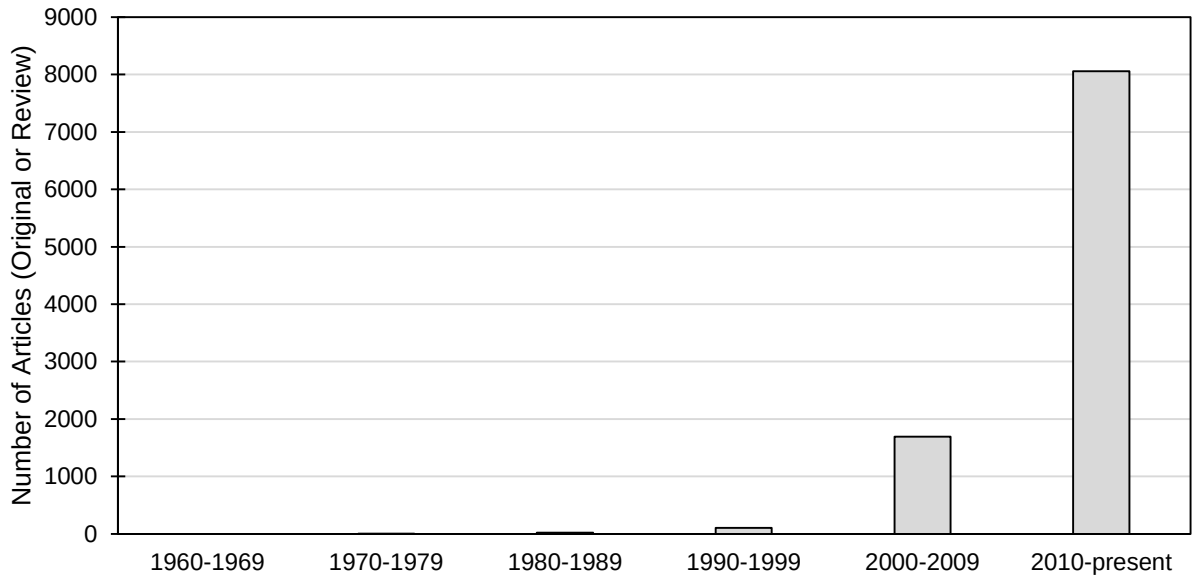

Figure 2-1: Results from Refined Literature Search for "Hierarchically Structured Material"

From the comprehensive literature search, it was determined that "hierarchical structure" and similar terms were discussed in the scientific literature as far back as the early 20th century. However, the terms were originally used by psychologists and psychiatrists to

describe sociological or psychological constructs. For example, Stern used the idea in his definition of character, as a means to describe the "hierarchical structure of goals and norms" [35]. In the context of engineering, structural hierarchy was introduced in the scientific literature in the 1970s and 1980s as an organization principle in data analysis [36–39] and process control systems [40–42]. For example, Diekmann-Moeller described a "hierarchically-structured automation system" used for the 2-level control of a continuous slab casting plant in 1987 [41].

In 1974, Holmes investigated "structural hierarchy" at the molecular level in biological structures (e.g. proteins, muscle tissue, viruses, organelles) [43]. He then drew parallels between the organization principles seen in the currently-emerging field of information technology to that seen at the microscopic level in natural systems. Research into the hierarchical structure of biological systems continued in the 1980s, with studies on protein folding [44–49], the mechanical and structural properties of cortical bone [50,51], and the structure and packing of human metaphase chromosomes [52–54]. The success of these characterization studies led to a better understanding of the complex hierarchical structure of biological systems. Studies on biomimicry of hierarchical structures [55], with a focus on the synthesis and applications of artificial grafts and tissue [56–60], began in the 1990s and continue to the present day. Interest in the hierarchical structure of non-biological systems was also evident in the 1980s, with studies conducted on the effects of the BeXor process, a patented hydrostatic extrusion process that produced biaxially-oriented polypropylene sheets [61–63], and the impact of thermal treatments on the development of hierarchically-structured polyimide films from polyamic acids [64].

2.1.3 Fabrication of Hierarchically-Structured Materials

Starting in the late 1990s and continuing to the present day, interest shifted to the synthesis of manmade HSMs from organic, inorganic, or composite materials. Many materials are used in the formation of these complex structures, including silica and silicalite [65–90], titania [65,72,85,91–97], zirconia [85,95,98,99], nickel oxide [100], iron oxide [101], alumina [65,85,102–105], zeolite [106–109], gold [110], hydroxyapatite [111,112], calcium carbonate [113], and composites [114,115].

Fabrication strategies for HSMs can be divided into two broad categories: self-assembly of aggregate superstructures from smaller constituents, or the deposition of the desired material on a sacrificial template. Some HSMs are fabricated using a combination of both strategies. Structure-directing agents, including sodium alkyl sulfates and sulfonates [81,112,116], quaternary ammonium surfactants [67,68,71,75,83,84,90,105,115,117–121], bolaamphiphiles [122], sarkosyl [123], polyethylene glycol cetyl ethers [93,97,104,108,121], and block copolymers [67,79,80,82,87–89,95,105,124–127], are used to direct the self-assembly of aggregate superstructures from simpler building blocks. Complex, hierarchically-structured porous networks can also be formed with the aid of sacrificial templating agents. The desired material self-assembles on or is directly deposited on the template; the template is subsequently removed via calcination or solvent extraction, leaving behind a porous shell [66]. Common templating agents include polymer beads [65,68,72,74,79,80,85,88,100,102,106,128], carbon black particles [109], starch gels [78], colloidal crystals [66,69,73,89], and living templates like multicellular filaments of *Bacillus subtilis* [70,107] or filamentous fungal spores of *Aspergillus niger* [110].

2.1.4 Modern Applications of Hierarchically-Structured Materials

In recent years, considerable research effort has been devoted to developing functional HSMs for use in a diverse array of applications. As previously mentioned, hierarchically-structured artificial tissues and grafts have been successfully synthesized. More recently, techniques to improve the biocompatibility, *in vitro* degradation rate, and resorbability of these materials have been developed [129]. Of particular importance is the use of multiple pore-forming agents to mimic the true multi-level hierarchical porosity of the native tissue. Biocompatible HSMs are also useful as drug delivery capsules for the delivery of chemotherapy drugs [130,131], analgesics [115,132], and peptides [133,134]. The hierarchical structure is particularly useful at controlling the rate of drug delivery [133]. HSMs can also be used in environmental applications. Photocatalysts break down organic compounds when exposed to light. These unique catalysts are useful in treating polluted air and water. Titanium oxide is the most widely-used photocatalyst due to its low cost, chemical stability, and high redox capabilities [97,135]. Hierarchically-structured titanium oxide is an even more efficient photocatalyst. In particular, the combination of mesopores and macropores increases overall surface area and the path length for photon penetration into the material, thereby improving its overall photoactivity [97].

2.1.5 Summary

Many natural and synthetic materials exhibit structural hierarchy. In recent years, research has focused on the synthesis and applications of these versatile materials. Manmade HSMs are fabricated from various organic, inorganic, and composite materials. Incorporation of structure-directing agents or sacrificial templating agents into the synthesis mixture is

imperative when fabricating HSMs. The unique structural properties of HSMs make them ideal for use as drug-delivery agents and photocatalysts.

2.2 Alumina Nanoparticles

2.2.1 Introduction

Aluminum(III) oxide, or alumina, is a naturally-occurring inorganic crystalline compound with the chemical formula Al_2O_3. Industrially, alumina is produced by the Bayer process, whereby bauxite ore, a mixture of hydrated aluminum and oxides of silicon, iron and is refined by selective extraction using hot sodium hydroxide [136]. The purity of the resulting smelter grade alumina is low [137] and must be further refined electrolytically by the Hall-Héroult process [138,139] to produce aluminum metal [140].

Crystalline alumina occurs in several well-defined and characterized polymorphic phases. For applications other than production of aluminum metal, alumina is produced synthetically via aluminum-rich precursors. This results in the formation of hydrated aluminum compounds such as bayerite ($AlOH_3$) or boehmite (γ-AlOOH). Subsequent dehydration and calcination of these compounds lead to the formation of the various alumina polymorphs. γ-Al_2O_3 (activated alumina) has a high surface area, making it an excellent adsorbent [141–143] and catalyst support [144–146]. α-Al_2O_3, which results from extended calcination, is an inert ceramic with high hardness and strength, making it useful as a catalyst support [147–150].

2.2.2 Synthesis Techniques

Careful control of the synthesis conditions during alumina production results in the fabrication of alumina nanoparticles. While bulk materials have constant physical properties, reduction in the size of particles to the nano-dimension yields materials with

interesting and useful properties [151]. Alumina nanoparticles exhibit these useful properties, such as high adsorptive capacity [152], biocompatibility [8], and tuneable surface properties [153]. Alumina nanoparticles are typically synthesized in a two-step process:

1. Nanoparticles of a precursor substance (e.g. boehmite) are fabricated.
2. The precursor nanoparticles are calcined to form #-alumina, where # represents the alumina phase.

2.2.2.1 Sol-Gel Synthesis

Perhaps the most well-known technique to synthesize an alumina precursor is discussed by Yoldas [154]. In his work, Yoldas hydrolyzed aluminum alkoxides in excess water to form a sol. Aluminum nitrates and chlorides are also used in sol-gel reactions to form alumina [153,155]. Cold water hydrolysis produces bayerite, $AlOH_3$, while hot water hydrolysis (especially under pressure) produces boehmite, γ-AlOOH [154]. The reaction is accelerated in the presence of an acid or base, which acts as both a catalyst and a peptizing agent [156–158]. Aging of the sol promotes gelation, whereby the sol particles polymerize and crosslink to form a dense, integrated network. The morphology of the aged gel is a strong function of pH (Figure 2-2). The gel may be used as is, or further processed via supercritical drying with an organic solvent to yield an aerogel [159,160]. Calcination of the gel yields the alumina polymorphs. A detailed reaction scheme is shown in Figure 2-3 for boehmite from aluminum isopropoxide in the presence of acid catalyst.

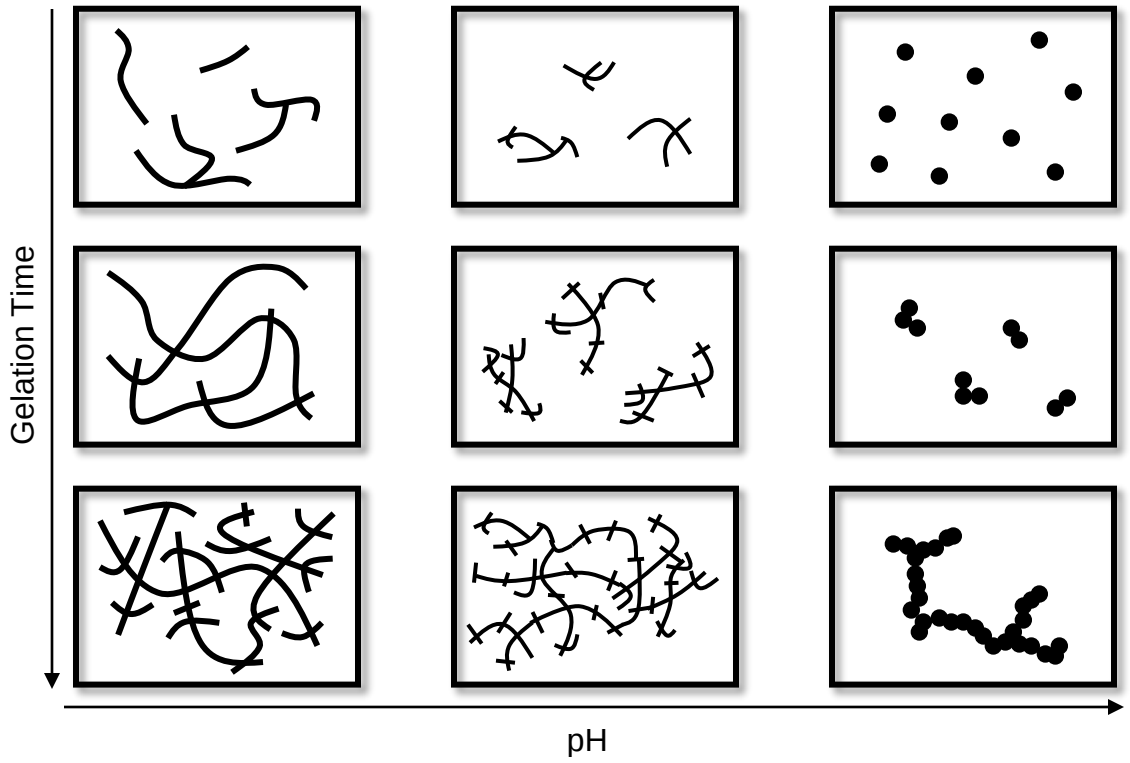

Figure 2-2: The Effect of pH on the Morphology of Aged Gels (Adapted from [161])

(1) Hydrolysis of the Precursor (Sol Formation)

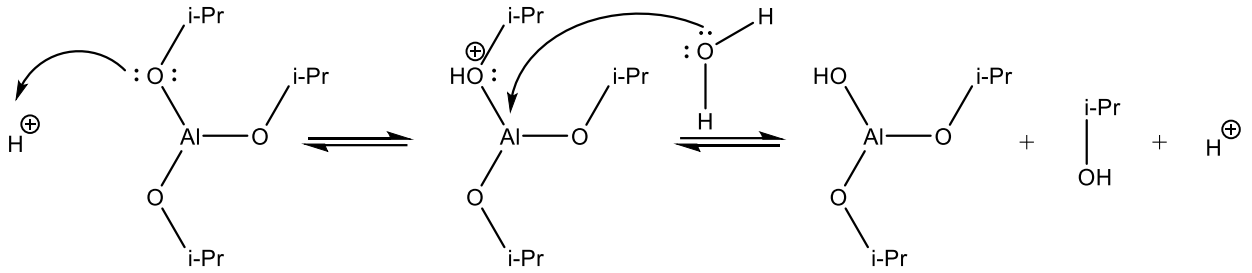

(2) Polycondensation of the Hydrolyzed Precursors (Gelation)

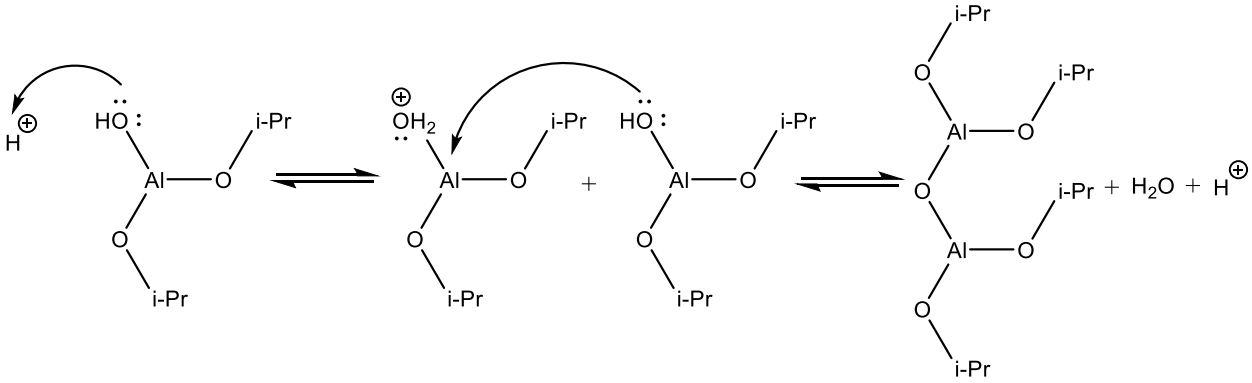

(3) Aging of the Gel

Repeated polycondensation reactions (2) increase the size of the gelation network.

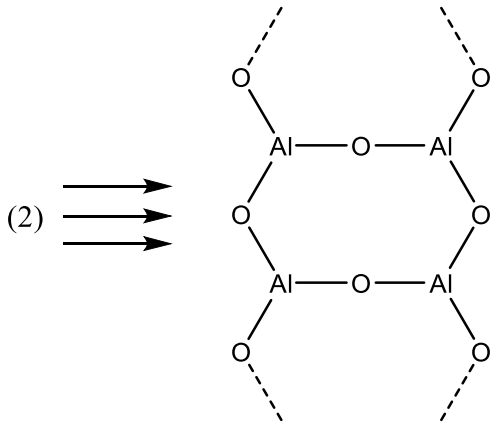

Figure 2-3: Sol-Gel Synthesis of Boehmite from Aluminum Isopropoxide with an Acid Catalyst (Adapted from [162])

The sol-gel method has been reported extensively in the literature for the synthesis of alumina nanoparticles and aerogels [154–156,159]. However, the method also presents several drawbacks, including the toxicity of the byproducts formed during sol synthesis (Table 2-2) [8] and cracking of the gel during the aging and drying processes [157,159,163]. Thus, sol-gel manufacturing of alumina is limited to small-scale applications like thin films [164,165], dip coating [165–167] or fibers [5,168].

Table 2-2: Toxic Effects of Byproducts Formed During Aqueous Sol Synthesis of Alumina Precursors[1]

Aluminum Precursors	Byproduct Formed During Aqueous Sol Synthesis	Test Type	Method of Delivery	Reported Dose	Effect(s)	Source
		LDLO		3570 mg/kg	Nausea, vomiting, respiratory depression, coma	[169]
Aluminum isopropoxide	Isopropanol	LDLO	Oral	5272 mg/kg	Chronic pulmonary edema, hypotension, coma	[170]
		TDLO		223 mg/kg	Hypotension, hallucinations	[171]
*Aluminum tri-*sec*-butoxide*	2-Butanol	TCLO	Inhalation	25 ppm	Lung and eye irritation, respiration changes	[172]
Aluminum nitrate nonahydrate	Nitric acid	LDLO	Oral	430 mg/kg	Severe tissue damage, respiratory depression, organ damage	[173]
Aluminum chloride hexahydrate	Hydrochloric acid	LDLO	Oral	2.857 mg/kg	Esophageal damage, hypotension, respiratory depression	[174]

1. All toxicity data given above are for human subjects.

2.2.2.2 Hydrothermal Synthesis

Alumina precursors can also be synthesized hydrothermally. In its most basic form, hydrothermal synthesis involves the dissolution and subsequent recrystallization of crystalline material from water at autogenous pressure. The reaction is carried out in a pressure vessel (autoclave) maintained at an elevated temperature (30 to 400°C) [175]. Subsequent calcination yields the various alumina polymorphs. The vessel is fitted with a hermetic seal designed to prevent leakage, but also fail safely should the reaction exceed the maximum allowable operating pressure. Autoclaves are commonly made of a stainless steel shell with a Teflon liner; they can also be fabricated from more resistant materials for reactions carried out with highly corrosive media (Figure 2-4).

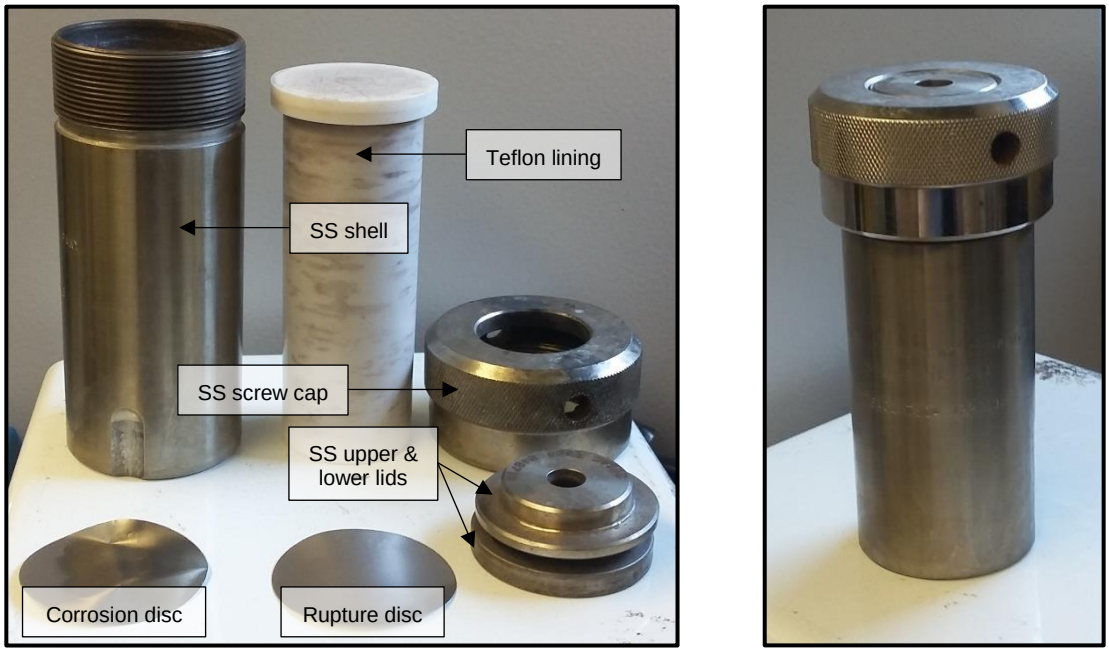

(a) (b)

Figure 2-4: Parr Instruments autoclave with stainless steel (SS) shell and Teflon lining. Designed to fail-safe through the opening in the top at pressures in excess of 1800 psig. (a) Disassembled, showing all individual components. (b) Fully assembled.

Hydrothermal synthesis takes advantage of the changing solvent properties of water (e.g. dielectric constant) at subcritical and supercritical conditions. The dielectric constant (ε) is an index of the polarity of a substance. Under ambient conditions, ε = 78 for water. Precursor compounds are typically polar salts that will dissolve readily under these conditions. As the critical temperature and pressure (374°C, 22.1 MPa) are approached, the dielectric constant of water rapidly decreases to ε < 10 (Figure 2-5) [176]. As such, the recrystallization process is initiated, resulting in the generation of nucleation sites for particle formation and the rapid growth of inorganic nanoparticles [177].

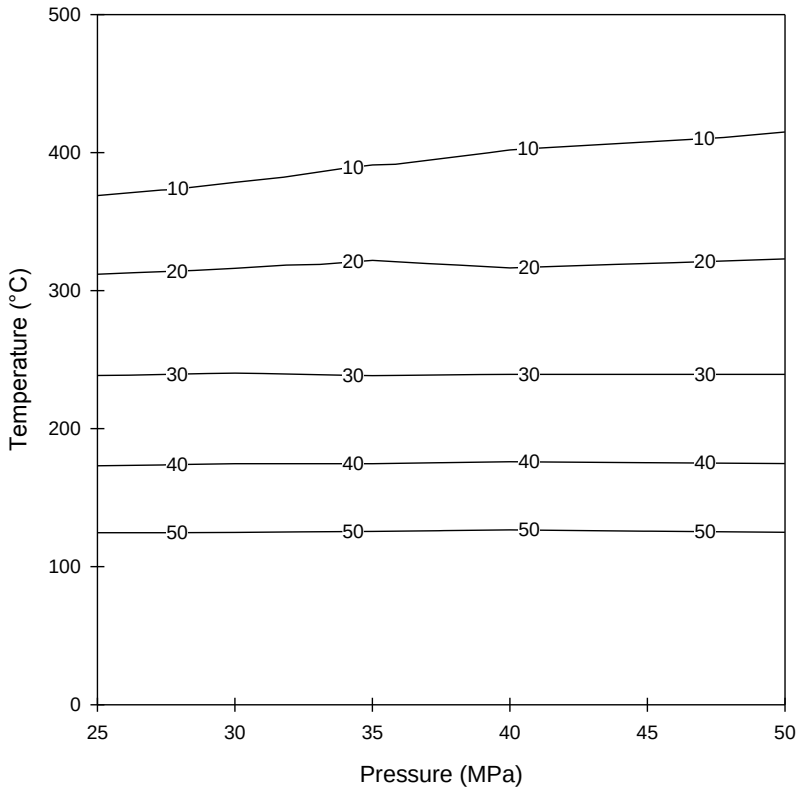

Figure 2-5: Dielectric constant of water as a function of pressure and temperature. Adapted from [176].

Control of the operating conditions will greatly affect the characteristics of the final product formed from hydrothermal synthesis. It has been shown that three primary physical parameters are of utmost importance: temperature, pressure, and time [176]. The operating temperature has a direct influence on the crystallographic phase of the final product [178]. Temperature fluctuations are avoided, as they disturb the dynamic equilibrium of the dissolution-recrystallization process. As discussed above, pressure can be used to manipulate the solubility of the material, directly affecting the recrystallization process. Reaction time is used to control the extent of recrystallization; it has direct effects on final particle size and morphology. Mathieu et al. tracked the evolution of boehmite morphology synthesized under hydrothermal conditions for reaction times between 17 and 168 h. The morphologies of the final products varied gradually from rounded nanoplatelets (d_{50} = 167 nm) to elongated nanofibers (1 to 3 μm long) as reaction time increased due to compounding particle aggregation [8]. Kim et al. also noted the formation of aluminum acetate hydroxide nanofibers from irregularly-shaped nanoparticles as reaction time was increased from 0.5 to 12 h [179].

2.2.3 Structure-Directing Agents

Control over the morphology of alumina nanoparticles is aided by the use of surfactants. Surfactants have been shown to control the crystallization rate by regulating the growth of particle agglomerates during sol-gel synthesis [180,181]. Furthermore, surfactants can interfere with the physisorption of water on the particle surface, inhibiting the polycondensation during sol-gel synthesis (Figure 2-3). The careful selection of surfactant type and concentration can be used to control the morphology of the final product [180]. Mirjalili et al. reported the formation of irregularly-shaped α-Al_2O_3 nanoparticles (d_{AV} =

250-300 nm) synthesized in the absence of surfactant by the sol-gel method; using sodium dodecylbenzenesulfonate (SDBS) or sodium bis(2-ethylhexyl)sulfosuccinate (Na(AOT)), the resulting α-Al_2O_3 nanoparticles were more spherical in shape and finely-dispersed (d_{AV} = 20-30 nm and d_{AV} = 120-180 nm, respectively) [180]. Liu et al. reported on the preparation of methane-reduction catalysts via the synthesis of fine, rod-like boehmite nanoparticles with the aid of non-ionic surfactants [153]. Bleta et al. used Pluronic F217, an amphiphilic triblock copolymer, to control the pore volume and specific surface area of boehmite and alumina nanoparticles synthesized from aluminum tri-*sec*-butoxide [182].

In hydrothermal synthesis, surfactants can be used to inhibit interlayer stacking of boehmite crystallites by bonding to surface hydroxyl groups of the crystallites through hydrogen bonding [183]. This directs the growth of the crystallites in the perpendicular to the stacking direction, resulting in elongated nanoparticles. Xu et al. demonstrated the efficacy of CTAB at directing the growth of non-porous flower-like boehmite nanoparticles (average thickness of 50 nm) with an elongated crystalline structure through hydrothermal synthesis [3]. Zhao et al. showed that PEO micelles directed the formation of regularly-shaped boehmite nanotubes. Without PEO, the final product only contained 20% nanotubes [183]. Zhu et al. found that the critical molar ratio of PEO/Al to direct boehmite morphology during hydrothermal synthesis was PEO/Al = 0.47. For PEO/Al < 0.47, boehmite nanoplatelets were synthesized; for PEO/Al > 0.47, boehmite nanofibers were synthesized [184].

However, surfactants also alter the phase transition temperatures during calcination due to their capping effect. The degree to which the phase transition temperatures are altered is dependent on the modified surface chemistry that the adsorbed surfactant imparts and the

degree of surface saturation of the surfactant molecules [180,182]. Mirjalili et al. noted an increase of up to 200°C in the phase transition temperatures of alumina nanoparticles during their transition pathway from $AlOH_3$ → Al(OOH) → γ-Al_2O_3 → δ-Al_2O_3 → Θ-Al_2O_3 → α-Al_2O_3 when the particles were synthesized with surfactants SDBS and Na(AOT) [180]. Bleta et al. reported that the addition of Pluronic F217 lowered the phase transition temperature of Al(OOH) → γ-Al_2O_3 from 380 to 300-330°C during thermal treatment [182].

2.3 Summary

Alumina is a naturally-occurring inorganic crystalline compound. It is produced industrially by the Bayer process. Crystalline alumina occurs in several well-defined and characterized polymorphic phases. Shape-controlled nanoparticles of alumina and its precursors are produced at a smaller scale using sol-gel and hydrothermal synthesis methods. Surfactants can be used as structure-directing agents. Various alumina polymorphs have been used as catalyst supports and adsorbents. Currently, alumina nanostructures can be synthesized as aggregates that have poor flow characteristics or highly porous particles or particle aggregates that do not maintain their structure when subject to flow.

2.4 Filtration of Colloidal Fluids with Dynamic Membranes

2.4.1 Introduction

The separation of fluid mixtures is a fundamental process in chemical engineering. Membrane filtration is a low-cost, low-energy alternative or supplement to traditional separation methods such as distillation. A membrane is a semi-permeable material that is permselective when subject to a driving force [185]. During pressure-driven membrane separation, performance decline is inevitable due to fouling. Membrane fouling occurs via four main mechanisms [26] (Table 2-3).

Table 2-3: Membrane Fouling Mechanisms

Filtration Model		
Complete blocking	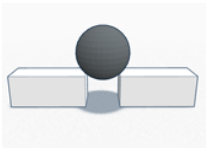	Every solute particle that reaches a pore blocks that pore. Solute particles do not aggregate.
Intermediate blocking	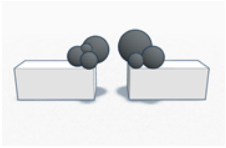	Not every solute particle that reaches a pore blocks that pore. Solute particles can aggregate to block a pore.
Pore constriction		Pore volume decreases proportionally with filtration volume. Solute particles deposit on pore walls.
Cake filtration	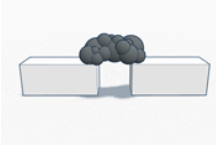	Flux decline is due to solute particle accumulation on membrane surface. Cake thickness is proportional to permeate volume.

Once membrane performance has declined substantially, the unit operation is taken offline for maintenance and cleaning. Membrane cleaning is accomplished via physical (e.g. air scouring, backflushing) and/or chemical means (e.g. acids, bases, bleaching agents) [186]. Chemical cleaning is used as a last resort on fouling that cannot be removed via physical removal techniques; however, these chemicals must be used carefully, as they can permanently damage the membrane, reducing overall membrane lifetime [186]. Some fouling cannot be removed with either physical or chemical treatment. Irreversible fouling results in permanent membrane performance loss. The extent of irreversible fouling is directly related to membrane properties (e.g. hydrophobicity, surface charge, surface roughness, pore size, morphology), operating conditions (e.g. operating pressure), and feed characteristics (e.g. turbidity) [187–189]. Once irreversible fouling has caused the membrane performance to decline substantially, the membrane filter is replaced. The cost of replacing entire filters represents a significant capital expenditure in industrial processes that use membrane filtration as a separation technique [190].

2.4.2 Development and Performance of Dynamic Membranes

An alternative approach is to trap the foulant material in a deposited layer on top of the membrane, referred to as a dynamic membrane (DM), secondary membrane, or formed-in-place membrane. Once the performance of the DM has declined significantly, the DM and the entrapped foulant can be physically removed by brushing, air scouring, cleaning with tap water, or acid cleaning [191,192]. DMs have two key benefits over conventional membrane filtration: (1) DMs can be formed and reformed *in situ*; (2) once the DM is severely fouled, it can be removed. As such, the costs of purchasing, maintaining and replacing membranes is drastically reduced or eliminated [193].

DMs were first reported in 1965 at Oak Ridge Laboratories by workers engaged in desalination research [194]. Marcinkowsky et al. reported the progressive formation of a semi-permeable layer on the cellulose acetate support by recirculating the feed solution of hydrous oxides. The researchers noted the salt retaining properties of these dynamically-formed hydrous oxide membranes [194].

DMs are formed by depositing a thin film of semi-permeable material on a support layer. Support layers are often cost-effective materials such as mesh [195–197] or filter cloth [198,199], which allow for higher operating flux at lower transmembrane pressures [191]. Deposition is carried out by recirculating the feed stream across a support layer to gradually build up the dynamic layer. To induce particle flocculation in the feed stream and enhance DM formation on the support layer, coagulants such as ferric chloride or aluminum sulfate are often added [200,201].

The use of DMs is currently well-established in wastewater treatment [193,197,199,202–205], where fouling of membrane filtration equipment is a common issue [199]. This phenomenon can be exploited by using the fouling species to form dynamic membrane layers, which can then entrap additional incoming foulants. Xu et al. determined the time necessary to form DM layers on a support mesh during the treatment of polluted river water by monitoring effluent turbidities. For influent turbidities of 18 – 162 NTU, DM formation time ranged from 1 – 50 min. These DMs reduced total carbon and total phosphorus content in the feed stream by 61 – 84% and 68 – 87% over 18 h of continuous use [201]. Sharp et al. measured the solids retention of dynamic membranes formed by coagulation of the feed with ferric chloride during pretreatment of raw feedwater. The DMs reduced the solids that penetrated to the support layer by 96 – 98%. The researchers

determined that the DMs formed a protective barrier, preventing foulants from reaching the support layer [200].

2.4.3 Dynamic Membrane Filtration of Colloidal Solutions

Separation of colloidal solutions is inherently problematic. Colloids are small particles dispersed in a homogeneous medium, with colloidal particles ranging in size from 1 nm to 1 μm [206]. Particles in this size range are difficult to separate via centrifugation or traditional filter media [206,207], but can be filtered via ultrafiltration (UF) or nanofiltration (NF) [207]. However, colloidal particles readily foul UF and NF membranes, resulting in the rapid decline of membrane performance parameters [206]. Alternatively, colloids can be removed from feed streams using DMs. As described earlier, DMs entrap the incoming foulant, minimize fouling of the support layer, and are removed once they are fouled.

2.4.4 Summary

Membrane filtration is a low-cost, low-energy alternative to traditional separation techniques. However, membrane performance declines over time due to fouling. An alternative technique is to fabricate a dynamic, permeable layer to entrap the foulant species. Dynamic membranes already find widespread use in wastewater treatment applications. Colloidal fluids, which are difficult to filter as they tend to form impermeable gel layers, may benefit from treatment using dynamic membranes.

3 The Self-Assembly of Twinned Boehmite Nanosheets into Porous 3D Structures in Ethanol-Water Mixtures

K. Roebuck and A. Y. Tremblay. Colloids and Surfaces A: Physicochemical and Engineering Aspects 495 (2016): 238-247.

Hypothesis

Surfactant molecules have high surface activity, and can therefore influence the self-assembly of nanomaterials. The self-assembly of twinned boehmite nanosheets into porous 3D superstructures will be greatly affected by the presence of surfactant monomer and micelles in various ethanol-water mixtures. It should be possible to influence the shape, thickness, and twinning of boehmite nanosheets by varying the concentration of the surfactant and ethanol in the synthesis mixture to obtain high porosity 3D superstructures.

Experiments

The critical micelle concentration (CMC) of cationic surfactant cetyl trimethylammonium bromide (CTAB) was determined in 0, 12.5, 25, 37.5, and 50 vol% ethanol-water mixtures. The effect of CTAB on boehmite particle morphology and superstructure formation during self-assembly was explored at the CMC, and at 20%, 15%, 10%, 5% below and above the CMC of CTAB in various ethanol-water mixtures.

Findings

Boehmite nanosheets with controllable shape and thickness were successfully formed in various ethanol-water mixtures. Prior to micelle formation, the average thickness of nanosheets formed in 0 vol%, 25 vol%, and 50 vol% ethanol-water were 200 nm, 110 nm and 100 nm, respectively.

Micelle formation reduced the availability of surfactant molecules for particle templating, broadening the nanosheet thickness distribution. Micelle formation was inhibited in 50 vol% ethanol-water due to the increase in Gibbs free energy needed to form micelles relative to the Gibbs free energy of micelles in 0 vol% or 25 vol% ethanol-water. The enthalpy-driven process gives greater control over the nanosheet thickness, producing particles with narrow thickness distributions. In general, the CMC represented the point at which control is lost over the thickness of the nanoplatelets; increasing the surfactant concentration above the CMC increased the thickness of the nanoplatelets.

Particle twinning during crystal growth produced an interconnected 3D network of boehmite particles with high porosity (79-88%) and hydraulic permeability (62.4-809 mD). The addition of ethanol during synthesis increased the porosity and reduced the bulk density of the 3D superstructures by 8-11% and 26-28%, respectively, and yielded a ten-fold increase in the hydraulic permeability. The integrity of the porous 3D network was maintained upon calcination, suspension in water and deposition by filtration onto cellulose filter paper.

3.1 Introduction

Particles with controlled morphology are of increasing interest in the field of materials science. Shape-controlled particles find use in catalysis [208–210], imaging [211–214], medical therapy [213–216], SERS [217–220], and photovoltaic devices [221,222].

The use of surfactants to control particle morphology has been previously explored [223–229]. At sufficiently high concentration, surfactant monomers self-assemble into well-defined shapes with high surface activity, giving them the ability to direct material synthesis. Boehmite (γ-AlOOH) is a naturally-occurring aluminum oxide hydroxide crystalline mineral that can be synthesized from organic or inorganic precursors [154,157]. Calcination

transforms boehmite into various alumina phases, increasing the material strength. Boehmite and dehydrated alumina powders possess a high surface area and a negative surface charge, making them ideal for applications as adsorbents [230–235] and catalyst supports [153,236–238]. Thickness and shape-controlled alumina platelets are used in the manufacturing of substrate-based special effects pigments. These pigments require alumina flakes with narrow thickness distributions and smooth finishes [239,240].

The effect of surfactants on boehmite and alumina particle morphology has been explored in the literature. Zhang et al. formed non-porous cantaloupe-like boehmite superstructures using mixtures of aluminum nitrate and high concentrations of aqueous CTAB [2]; Mathieu et al. formed aggregated platelets and long nanofibers by varying the synthesis time using a high concentration of aqueous sodium polyacrylate and aluminum chloride [8]; Liu et al. synthesized boehmite and alumina nanoleaves and non-porous 3D superstructures from aluminum chloride in 50% ethanol-water mixtures [4]; Kuang et al. formed aggregated boehmite and alumina nanotubes via a hydrothermal route in aqueous CTAB solutions using aluminum chloride [241]; Bleta et al. explored the effect of calcination temperature, precursor concentration, and the CMC of Pluronic F127 on the morphology of aggregated alumina nanofibers formed from aqueous aluminum tri-*sec*-butoxide solutions [182]. In all these studies, boehmite and alumina particles were synthesized as aggregated particles, fibers with high anisotropy or 3D structures that lacked internal porosity. In general, these building blocks form superstructures with anisotropic hydraulic permeability that consolidate or collapse when used as a filter [242,243]. Instead, it is desired to form homogeneous, uniformly-structured building blocks from boehmite that will link together to

form rigid, highly isotropic, porous 3D superstructures that do not collapse upon deposition on a substrate or during filtration.

In this work, the effect of ethanol content on the critical micelle concentration (CMC) of a cationic surfactant was assessed. Then, the effect of surfactant concentration and the effect of micelles on the shape, thickness, and twinning of boehmite particles during particle self-assembly was determined in 0, 25, and 50 vol% ethanol-water mixtures. The synthesis conditions at which porous 3D superstructures could be formed were determined. Particle characterization was performed via SEM, FTIR, and image analysis.

3.2 Experimental

3.2.1 Materials

Cetyl trimethylammonium bromide (CTAB), sodium hydroxide pellets and anhydrous ethanol were purchased from Sigma-Aldrich (Switzerland). Aluminum chloride hexahydrate (99%, nitrogen flushed) was purchased from Acros Organics. Cellulose filter paper (Whatman #1) was purchased from Fisher Scientific (Canada). All materials were used as purchased.

3.2.2 Methods

3.2.2.1 Conductometry Studies

The critical micelle concentrations of CTAB were determined in 0, 12.5, 25, 37.5, and 50 vol% ethanol-water mixtures via conductometric analysis at 298 K. A typical procedure was as follows: 250 mL of distilled, deionized water and known masses of CTAB were slowly added and stirred in a beaker. After each addition of CTAB, the conductivity of the solution was measured using a conductivity meter (VWR sympHony B40PCID, Pennsylvania). The measurements were performed in triplicate.

3.2.2.2 Particle Synthesis

Boehmite nanosheets were synthesized via metal salt hydrolysis. A typical procedure was as follows: 1.45 g of aluminum chloride hexahydrate was dissolved in distilled, deionized water under vigorous stirring. The pH of the solution was raised to 14 using sodium hydroxide pellets. CTAB was dissolved in anhydrous ethanol or distilled, deionized water. The surfactant solution was added to the precursor solution and was left to stir at room temperature for 24 h. After spinning, the mixture was poured into a Teflon-lined stainless steel autoclave (Parr Instrument Company, Illinois), sealed, and heated to 165°C for 12 h under autogenous pressure. The vessel was then left to cool at room temperature overnight. The precipitate formed during crystallization accumulated at the bottom of the autoclave in the form of a rigid disk. The disk of particles was placed in a fume hood to dry. It was then covered and stored for analysis.

3.2.2.3 Particle Characterization

Particles were mounted on aluminum stubs (Ted Pella, Redding, California). SEM imaging was performed using a JEOL 6610LV SEM at accelerating voltages of 10 and 20 kV (Japan Electron Optics Laboratory, Massachusetts) and a Phenom Pro Desktop SEM (Nanoscience Instruments, Virginia) at accelerating voltages of 5 and 10 kV. Particle thickness was determined by measuring the thickness of 20 nanosheets at each synthesis condition using ImageJ software. The data were then fitted to normal distribution curves using Microsoft Excel. FTIR analyses of the particles were conducted using a Cary 630 FTIR with ATR (Agilent Technologies, Canada). Powder X-ray diffraction (XRD) analysis was carried out at room temperature on a Rigaku Ultima IV powder diffractometer in Bregg-Brentano geometry

using CuKα radiation (λ = 1.5418 Å). The 2θ range of 3° to 100° was covered with 0.02° step width and 3°/min scan speed.

The bulk density of boehmite superstructures as a function of ethanol concentration was estimated by measuring the volume of known quantities of boehmite in water settled in a graduated cylinder. The porosity of the structures was estimated using the water evaporation method [244]:

$$\varepsilon = \frac{1}{V_{sample}}\left(\frac{W_{sat} - W_{dried}}{\rho_{water}}\right) \quad (3\text{-}1)$$

where ε is the porosity of the sample, V_{sample} is the volume of the saturated sample, W_{sat} is the mass of the saturated sample, W_{dried} is the mass of the dried sample, and ρ_{water} is the density of water.

To assess the integrity of the superstructures, boehmite particles were calcined at 600°C for 4 h, suspended in water, and deposited on cellulose filter paper. The hydraulic permeability of the superstructures were measured by passing 500 mL of distilled water through the filter cake at 7 kPa.

3.3 Results and Discussion

Water acts as both a solvent and reactant in the self-assembly of boehmite particles from aluminum chloride hexahydrate. The hydrolysis reaction occurs very rapidly in the presence of excess amounts of water, resulting in the formation of thicker nanosheets. A high proportion of ethanol is added to slow the hydrolysis reaction and aid in the formation of thinner nanosheets [4,245]. The formation of particles can also be affected by the addition of a cationic surfactant [246,247]. The templating effect of CTAB was explored in this work.

The effect of ethanol on the critical micelle concentration of CTAB was determined experimentally.

3.3.1 Conductometry Studies

Conductometry is a simple measurement tool that can be used to determine the CMC of an ionic surfactant. Briefly, the specific conductivity of the solution is measured for an increasing concentration of ionic surfactant. The results are plotted, and the graph can be split into two linear regions with different slopes. The breaking point in the graph is the CMC [248–250].

The CMC of CTAB and was determined in 0, 12.5, 25, 37.5, and 50 vol% ethanol-water mixtures by measuring specific conductivity versus surfactant concentration. The CMC of CTAB and the degree of micelle ionization (α), determined from the conductometric measurements [248–250], as a function of ethanol content is presented in Table 3-1. The critical micelle concentration and degree of micelle ionization were found to increase non-linearly as a function of ethanol content.

Table 3-1: Conductometric Data of CTAB as a Function of Ethanol Content

Ethanol Content by Volume	**Critical Micelle Concentration (mM)**	**Degree of Micelle Ionization (α)**
0%	0.90 ± 0.06	0.44 ± 0.03
12.5%	1.90 ± 0.03	0.49 ± 0.02
25%	3.90 ± 0.71	0.64 ± 0.07
37.5%	8.60 ± 0.43	0.67 ± 0.03
50%	19.20 ± 0.55	0.74 ± 0.01

Average ± Standard Deviation

3.3.1.1 The Effect of Ethanol on Critical Micelle Concentration

The addition of ethanol into the system raises the critical micelle concentration of CTAB. This is due to two main reasons:

1. *A reduction in relative permittivity (dielectric constant) of the solvent*.

   A reduction in relative permittivity causes an increase in the repulsion between the ionic heads of the surfactants molecules. This reduces their ability to aggregate and form micelles [251].

   This increase in repulsion can be quantitatively explained by the Debye length – the thickness of the ionic atmosphere around each ion in solution [250,252],

$$\frac{1}{\kappa} = \sqrt{\frac{\varepsilon_r \varepsilon_0 RT}{4\pi F^2 \sum C_i Z_i^2}} \qquad (3\text{-}2)$$

   where $1/\kappa$ is the Debye length, ε_R is the relative permittivity of the solution, ε_0 is the relative permittivity of a vacuum, R is the universal gas constant, T is the absolute temperature, F is the Faraday constant, C_i is the concentration of an ion in solution, and Z_i is the charge on the ion.

   Assuming all other variables remain constant, a ratio of the square roots of relative permittivities can be used to determine the effect of different solvents on Debye length [253]. In the case of an ethanol-water mixture, a reduction of 69.1% in the relative Debye length is expected at 50 vol% ethanol-water.

   In general, a reduction in Debye length will result in an increase in electrostatic repulsion of similarly-charged ions. It will also cause an increase in electrostatic attraction between oppositely-charged ions. Thus, the formation of micelles at higher

volume fractions of ethanol is inhibited based on a decrease in Debye length, leading to an increase in the critical micelle concentration [250].

2. *An increase in the solubility of the hydrophobic portion of the surfactant*.

   The increased solubility of the surfactant's hydrophobic moiety in ethanol increases the solubility of the surfactant monomer. Overall, this increases the concentration of surfactant required to induce micellar formation [251,254].

3.3.1.2 Thermodynamics of Micellization

The addition of a cosolvent to the solvent medium has a great impact on the surfactant's ability to form micelles. From Table 3-1, it can be seen that the addition of ethanol greatly reduces the ability of CTAB molecules to form micelles.

The Gibbs free energy of formation of micelles was determined using the phase separation model [255–257]:

$$\Delta G^0_{mic} = (2 - \alpha) RT ln \chi_{CMC} \tag{3-3}$$

where α is the degree of micelle ionization and χ_{CMC} is the critical micelle concentration expressed as a mole fraction.

The contribution of a cosolvent to the Gibbs free energy of transfer of micelle formation in water to the cosolvent/water mixture can then be determined by

$$\Delta G^0_{trans} = (\Delta G^0_{mic})_{cosolvent/water} - (\Delta G^0_{mic})_{water} \tag{3-4}$$

As seen in Figure 3-1, micelles are most favorably formed in pure water, and the amount of ethanol added to the solvent mixture is directly proportional to the reduction in spontaneity of micelle formation. These results coincide well with thermodynamic data from Akbaş and Kartal [255] and follow the same trend.

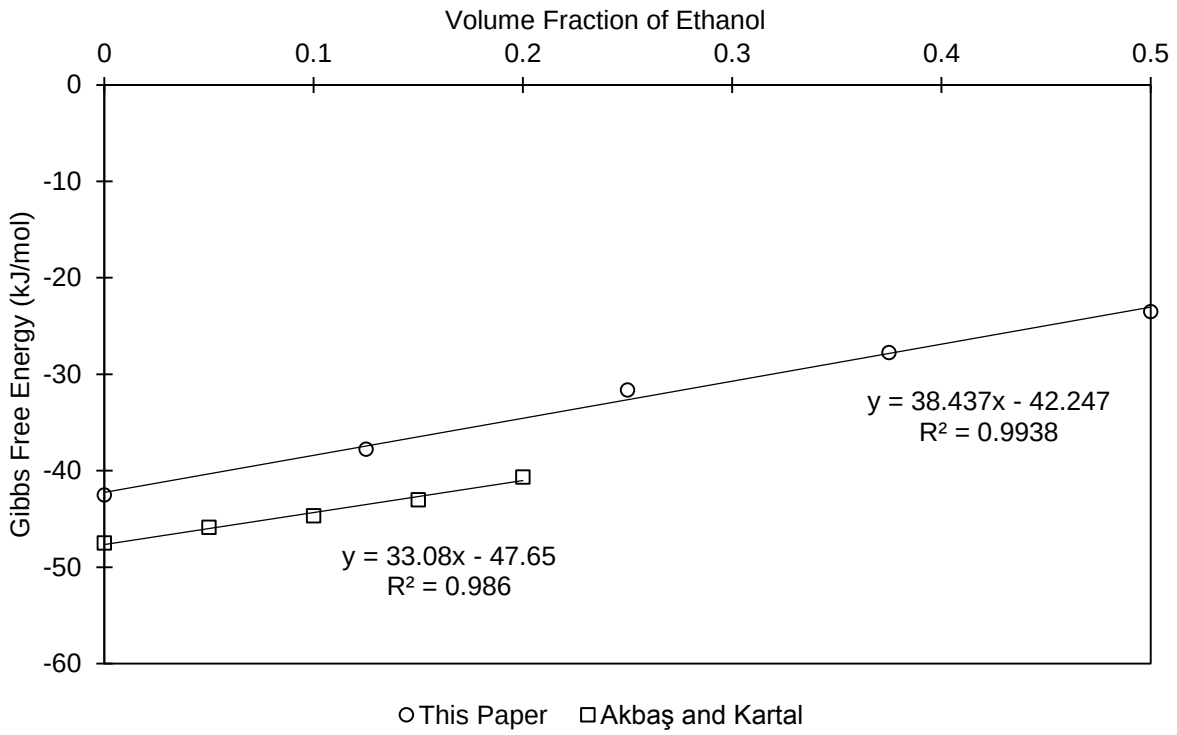

Figure 3-1: Gibbs Free Energy of Micellization of CTAB in Ethanol-Water Mixtures

From previous studies on surfactants in mixed solvent systems, it is known that micelle formation in pure water is entropy-driven, whereas micelle formation in mixed co-solvents/water is enthalpy-driven. In pure water, the self-assembly of CTAB monomers into micelles causes a breakdown in the structure of the local water network as a result of the hydrophobic effect. The hydrophobic effect is reduced when ethanol is added, as the hydrophobic moiety of CTAB is stabilized by the presence of the cosolvent. Thus, the micellization process will transition from an entropy- to enthalpy-driven process as ethanol is added [255–260].

3.3.1.3 Particle Synthesis

Boehmite particles were synthesized in 0, 25, and 50 vol% ethanol-water mixtures with surfactant concentrations from 20% below to 20% above the CMC, in 5% increments. The particle samples were analyzed by SEM, FTIR, XRD, and image analysis software to determine the effect of surfactant concentration on particle morphology at these conditions. Analysis of the FTIR spectrum in Figure 3-2 confirms that the as-prepared nanosheets are boehmite. The split peaks at 3080 – 3260 and medium peak at 1070 – 1150 cm^{-1} are characteristic of –OH stretching and bending, indicating the presence of bonded water molecules [157,261–266]. The strong peaks at 1066 and 740 cm^{-1} are indicative of Al—O stretching, confirming the existence of aluminum-oxygen bonds in the sample [157,263,264]. A peak at 755 cm^{-1} is characteristic of –H vibrations, which is further indication of bonded water molecules [157,264]. Weak peaks in the range of 1000 – 2000 cm^{-1} are hydrocarbon molecules, which are likely caused by the presence of surfactant or ethanol [263].

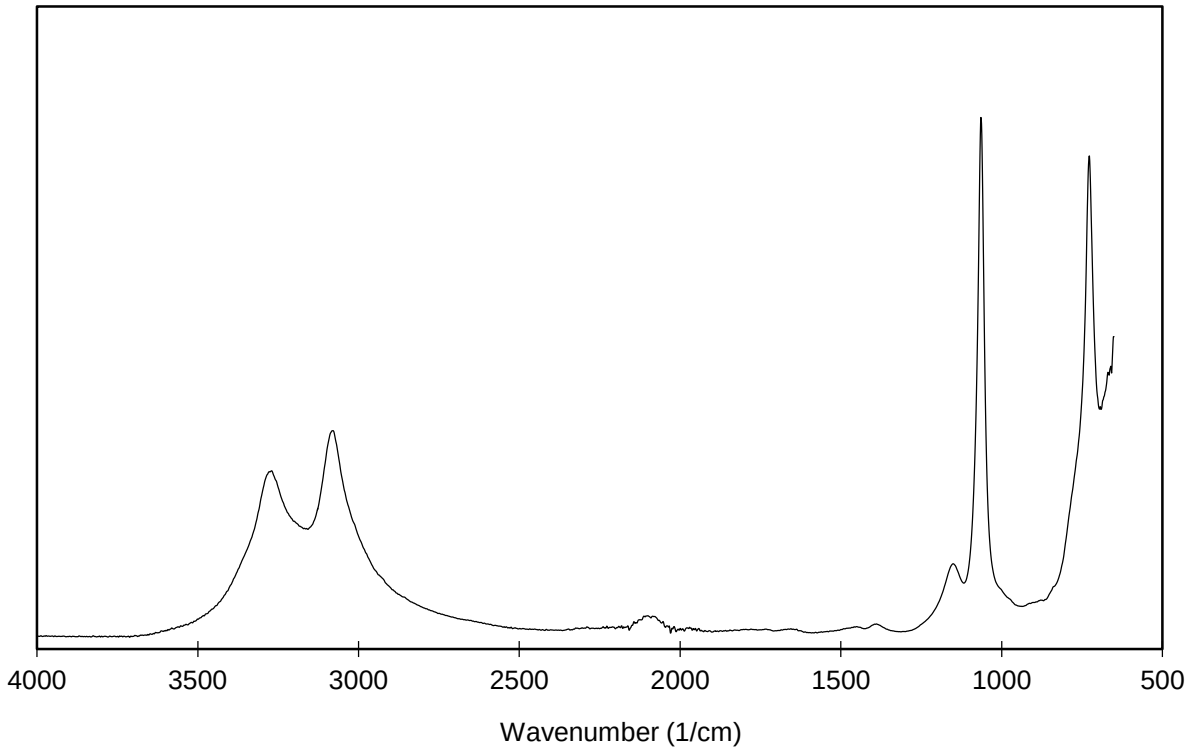

Figure 3-2: Characteristic absorbance FTIR of CTAB-templated boehmite particles

Analysis of the XRD data in Figure 3-3 indicates that the as-prepared nanosheets are boehmite. The main diffraction peaks can be indexed as boehmite (JCPDS card No. 21-1307) [267]. The intense (020) peak is characteristic of boehmite [157,268,269]. In addition to this, the spectra indicate that all boehmite samples produced were well-crystalized [269]. The decrease in peak intensity as a function of increasing ethanol/surfactant concentration is due to the capping effect of the surfactant, which in turn decreased the thickness of the particles [270,271].

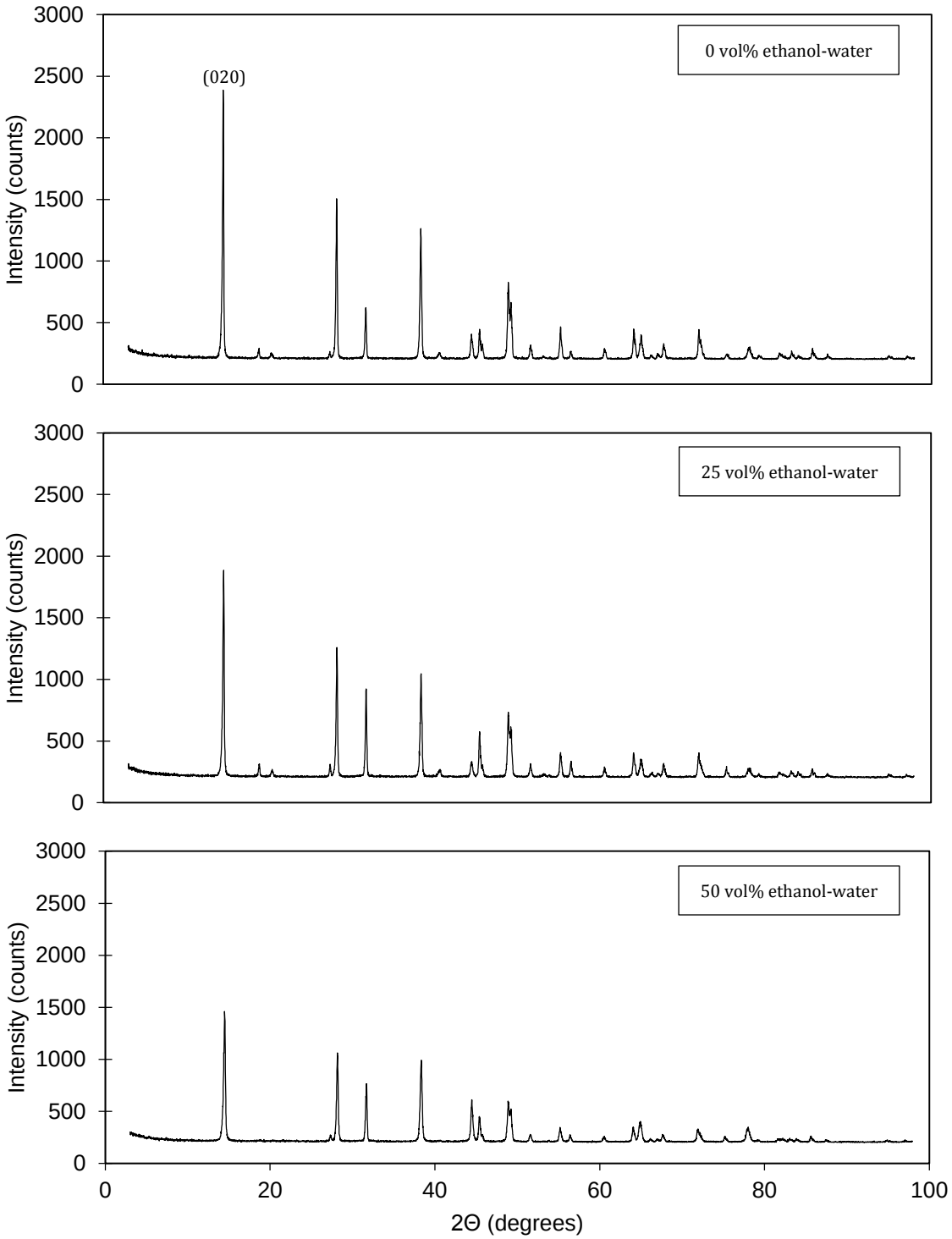

Figure 3-3: Powder XRD analysis of CTAB-templated boehmite particles

The boehmite nanosheet thickness distributions as a function of CTAB concentration and ethanol content are shown in Figure 3-4. The results show that nanosheet thickness in pure water and 25 vol% ethanol-water is constant prior to micelle formation, and increases as a function of CTAB concentration after the formation of micelles. In 50 vol% ethanol-water, the thickness of nanosheets is independent of CTAB concentration and micelle formation. The results also show that the addition of ethanol to the synthesis mixture reduces the thickness of nanosheets by half.

The results suggest that the formation of micelles in solution reduces the availability of free surfactant monomers for surface templating, thereby increasing nanosheet thickness. As the concentration of surfactant increases above the CMC, the thickness of the particles increases proportionally. This effect is less pronounced in 25 vol% ethanol-water due to the relative increase in the Gibbs free energy of micelles in 25 vol% ethanol-water versus pure water.

The results indicate that free monomers are always available to direct particle growth in 50 vol% ethanol-water. This is supported by the less favourable Gibbs free energy of micellization in ethanol solutions vs that of pure water, and the constant thickness of boehmite nanosheets formed in 50 vol% ethanol-water. Furthermore, the enthalpy-driven process gives greater control over the nanosheet thickness, producing particles with narrow thickness distributions.

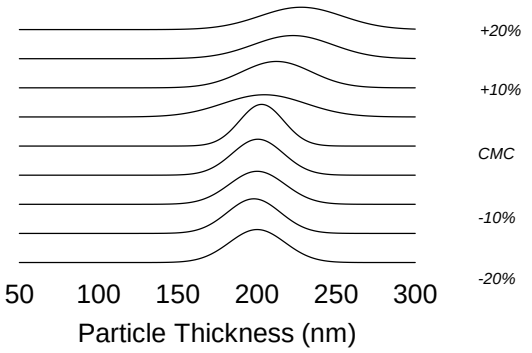

(a)

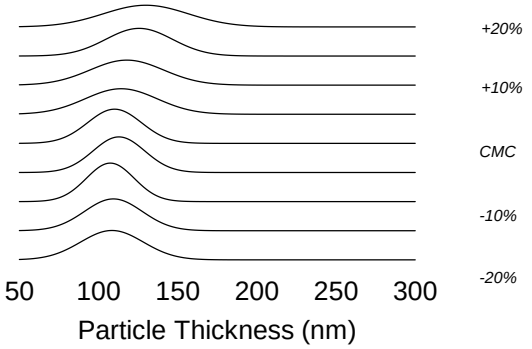

(b)

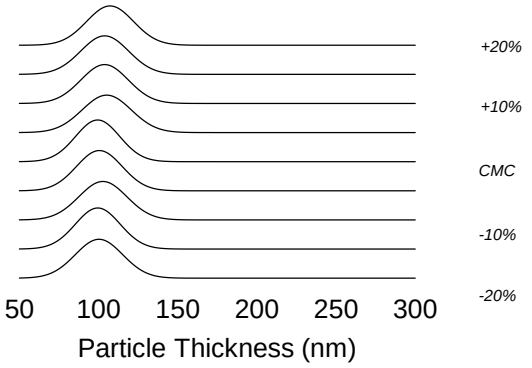

(c)

Figure 3-4: Particle thickness distributions for CTAB-templated boehmite nanosheets (a) 0 vol% ethanol-water; (b) 25 vol% ethanol-water; (c) 50 vol% ethanol-water

As shown in Figure 3-5, nanosheets synthesized in pure water are approximately 2x as thick as those synthesized in 25 or 50 vol% ethanol-water. Water is both a solvent and a reactant in the formation of boehmite from an aluminum precursor [4,272]. The results indicate that reducing the availability of water by the addition of a cosolvent like ethanol will moderate the self-assembly of boehmite platelets, resulting in thinner nanosheets.

The results also show that the formation of micelles increases the distribution of particle thicknesses in pure water and 25 vol% ethanol-water. Prior to micelle formation, the average and standard deviation at all synthesis conditions are approximately constant as seen in Figures 3-5 and 3-6. After micelle formation in pure water and 25 vol% ethanol-water, the average thickness and standard deviation increases as a function of the concentration of micelles. In 50 vol% ethanol-water, the average thickness and standard deviation remains constant, again indicating that micelle formation is greatly reduced.

The increase in standard deviation after micelle formation in pure water and 25 vol% ethanol-water is undesirable. Prior to micelle formation, the narrow thickness distributions are an indication of the strong templating ability of the surfactant monomers. The broadening of these distributions represents a decrease in the templating ability of the surfactant. In general, the CMC represents the point at which control is lost over the thickness of the nanoplatelets; increasing the surfactant concentration above the CMC will increase the thickness of the nanoplatelets.

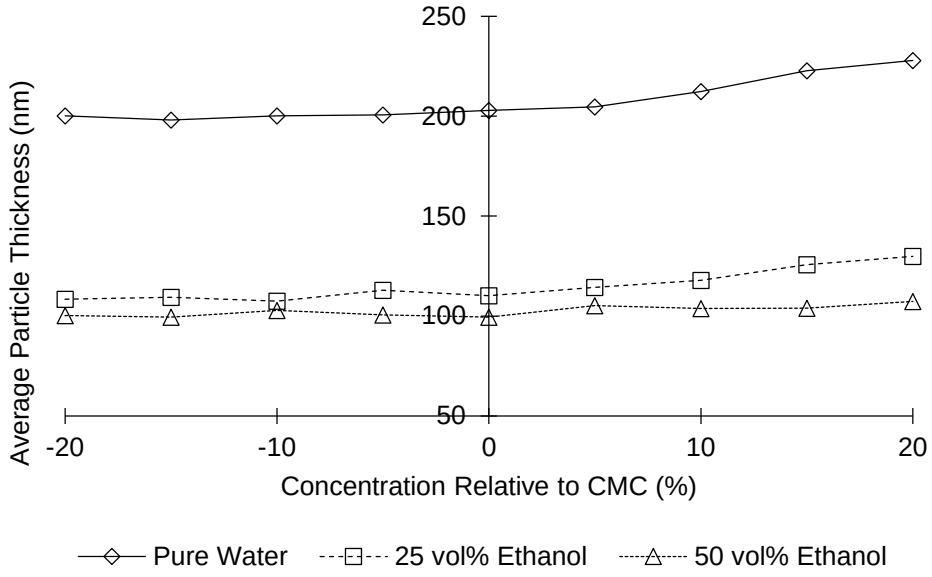

Figure 3-5: Average particle thickness versus concentration relative to CMC of CTAB-templated boehmite nanosheets

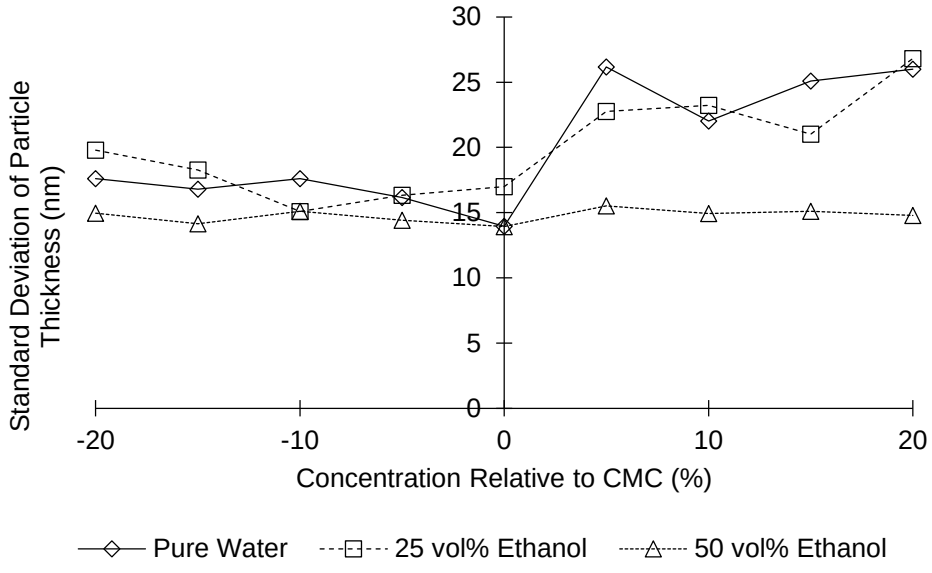

Figure 3-6: Standard deviation of particle thickness versus concentration relative to CMC of CTAB-templated boehmite nanosheets

The results show that nanosheet shape can be controlled by changing the ethanol concentration. In the absence of ethanol, boehmite nanosheets formed as thick rhombic platelets. In 25 vol% ethanol-water, two edges were added to the main faces, resulting in hexagonal platelets. In 50 vol% ethanol-water, the nanosheets elongated along the main faces while maintaining the hexagonal shape.

Boehmite naturally self-assembles in a rhombic structure, as seen in Figure 3-7a), with surface-active hydroxyl groups. The introduction of ethanol into the synthesis solution decreases the surface tension of the solvent mixture and facilitates the selective adsorption of surfactant molecules on the boehmite surface. This adsorption stabilizes the crystal faces, increasing growth in the lateral direction, as seen in Figure 3-7b) and c) [273,274].

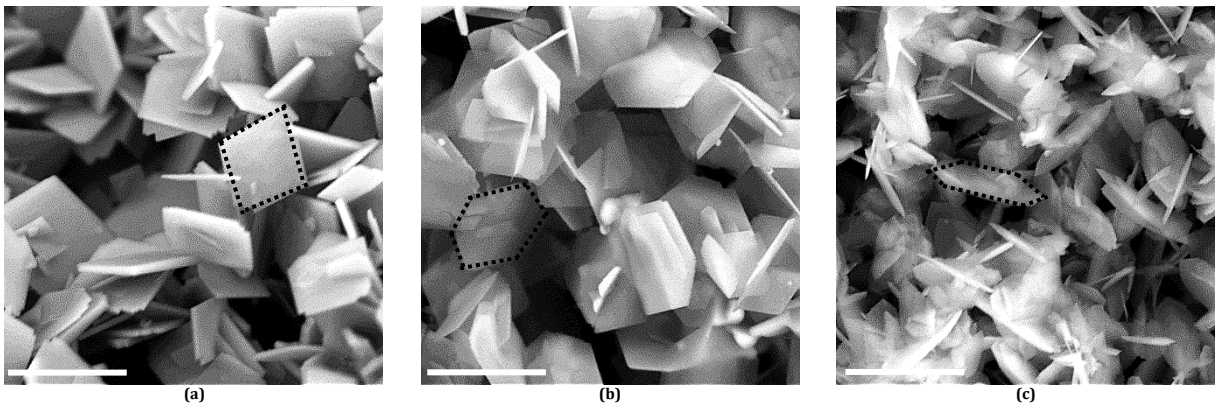

Figure 3-7: SEM images showing particle shape (dashed contour) of CTAB-templated boehmite nanosheets (scale: 5 μm)
(a) characteristic rhombic platelets in 0 vol% ethanol-water;
(b) characteristic hexagonal platelets in 25 vol% ethanol-water;
(c) characteristic elongated hexagonal platelets in 50 vol% ethanol-water.

3.3.2 Particle Superstructures

Evidence of particle twinning can be seen in Figure 3-7. The formation of growth twins during crystal formation [275–279] results in an interconnected three-dimensional network of boehmite nanosheets with high porosity.

When compared with boehmite or alumina particles and superstructures found in the literature, the platelets synthesized in this work form repeatable, uniform, homogeneous superstructures. In particular, twinning is a direct result of the concentration of surfactant used in the synthesis mixture. In this work, particles were synthesized at surfactant concentrations ranging from 25% below to 25% above the CMC of CTAB. As can be seen in Table 3-2, it is more common in the literature to use concentrations well above the CMC to synthesize nanoparticles. This leads to the formation of aggregated, non-porous particles and superstructures, which are unsuitable to form porous networks.

Table 3-2: Particle Morphology of Boehmite and Alumina Particles as a Function of CTAB Concentration

Precursor	Relative Concentration of Surfactant*	Concentration of Ethanol (vol %)	Structure	Source
Aluminum Nitrate Nonahydrate	3.47-41.67	0	non-porous, cantaloupe-like superstructures (2.5 μm diameter)	[2]
	30.49	0	non-porous, flower-like superstructures (1 μm long)	[3]
Aluminum Chloride Hexahydrate	0.75-1.25	0, 25, 50	twinned rhombic nanoplatelets with porous superstructure (0.1-0.225 μm thick)	This Work
	1.56	50	aggregated flower-like nanoleaves (0.06-0.09 μm thick): non-twinned and non-porous 3D superstructures	[4]
	10.39	0	aggregated boehmite and alumina nanotubes (0.03-0.07 μm long)	[241]

*Relative concentration of surfactant: ratio of the concentration of surfactant in the reference to the concentration of surfactant at the CMC as determined in this work.

Liu et al. studied the formation of boehmite nanoleaves using a hydrothermal synthesis protocol with 50% ethanol-water and CTAB at 30% above the CMC [4]. We did not observe the 3D flower-like superstructures obtained in their work. These structures are not hydraulically conductive, and are therefore undesirable in the formation of porous 3D superstructures.

The porosity, bulk density, and hydraulic permeability of boehmite superstructures at the CMC as a function of ethanol concentration is presented in Table 3-3. The addition of ethanol during synthesis increased the porosity and reduced the bulk density of the 3D superstructures by 8-11% and 26-28%, respectively, and yielded a ten-fold increase in the

hydraulic permeability. Those synthesized at 50 vol% ethanol-water also demonstrated a low variability in thickness across all surfactant concentrations. Superstructures formed from these nanoparticles have highly uniform size, and the highest porosity, lowest bulk density, and highest hydraulic permeability of the particles formed in this work. These characteristics suggest a future application in filtration.

Table 3-3: Characteristics of Boehmite Superstructures as a Function of Ethanol Content

Ethanol Content by Volume	**Porosity (%)**	**Bulk Density (kg/m^3)**	**Hydraulic Permeability (calcined) (mD)**
0%	79	123	62.4
25%	85	91	179
50%	88	89	809

The boehmite particles produced in pure water at the CMC were calcined at 600°C for 4 h. FTIR analysis confirmed the particles had transformed into alumina. One gram of particles were suspended in 2.5 L of water and passed through a cellulose filter at 7 kPa. A porous filter cake was formed, dried in air and analyzed by SEM.

In contrast to the particles formed by Liu et al. [4], these superstructures maintained an open porous network after calcination, suspension in water, and deposition, as seen in Figure 3-8. The top and side view show that compaction of the nanoplatelets does not occur indicating that the integrity of the superstructure was preserved after deposition on the filter as a cake. Unlike the nanosheets produced in this work, clay particles are nanosheets which exhibit little to no twinning. During formation, clay particles stack in highly-oriented parallel layers

[280]. This is undesirable in this work, as these structures collapse during filtration [281]. Thus, twinning is a necessary condition for the production of porous 3D networks.

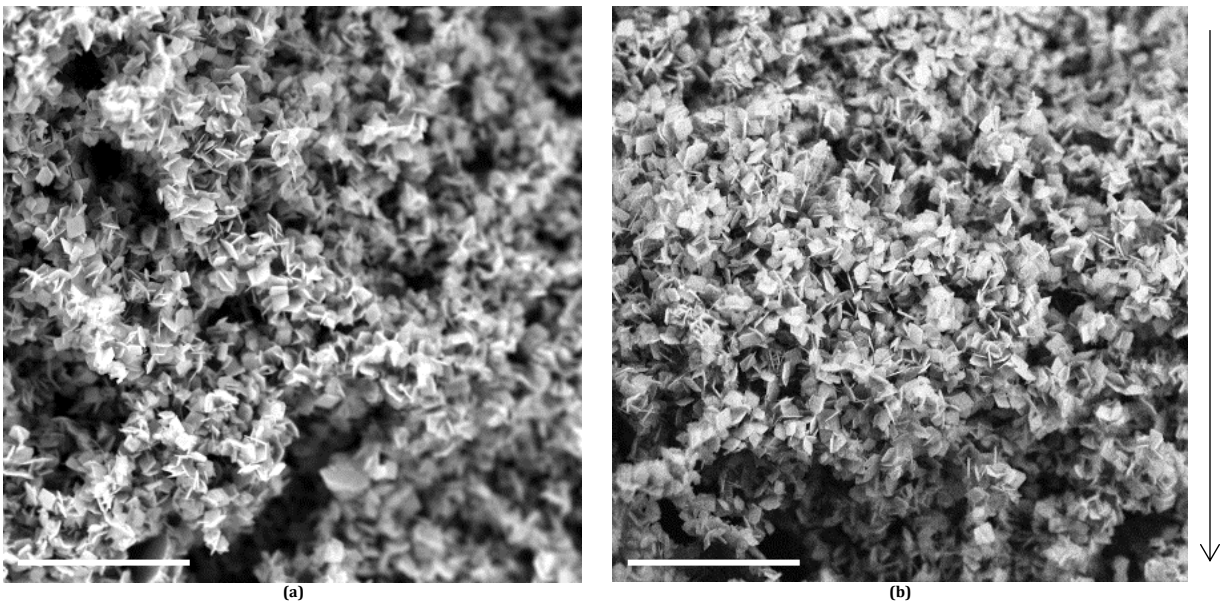

Figure 3-8: SEM images showing calcined boehmite particles (produced in pure water) deposited on cellulose filter paper
(a) top-view of filter cake (scale: 30 μm); (b) side-view of filter cake (scale: 30 μm), arrow indicates direction of flow during cake formation

3.4 Conclusions

Boehmite platelets were manufactured with specific control over shape and thickness. In particular, careful selection of the synthesis conditions (ethanol content, surfactant concentration) produced twinned nanosheets with controllable thickness and shape.

In pure water and in 25 vol% ethanol-water mixtures, prior to micelle formation, the thickness of boehmite particles remained constant. After micelle formation, the thickness of boehmite particles increased as a function of CTAB concentration, due to the increase in micelle concentration and a reduction in surfactant templating ability. This effect was more

pronounced in pure water. In general, thickness distributions were narrow below the CMC and broadened above the CMC.

In 50 vol% ethanol-water mixtures, the thickness of boehmite particles was independent of CTAB concentration and micelle formation. The higher ethanol concentration (enthalpy-driven process) controlled particle thickness producing narrow thickness distributions.

Particle shape was controlled by varying the ethanol concentration. In the absence of ethanol, boehmite particles assembled as thick rhombic platelets. In the presence of 25 vol% ethanol-water, boehmite particles assembled as thin hexagonal platelets. These hexagonal platelets were elongated in the presence of 50 vol% ethanol-water.

Particle twinning during crystal growth resulted in an interconnected network of boehmite particles with very high porosity and hydraulic permeability (79-88% and 62.4-809 mD, respectively). This porous structure was maintained upon calcination, suspension in water, and deposition on cellulose filter paper. In the absence of twinning, the particles would have stacked, as is the case with filter cakes formed from clay particles.

4 Optimal Aggregate Size Distribution for the Formation of Highly Efficient Nanosheet Dynamic Membranes

K. Roebuck and A. Y. Tremblay. Journal of Membrane Science 514 (2016): 143-154.

In this work, intrinsically-porous aggregates of nanosheets having mono-, di-, and tri-modal particle size distributions were synthesized to produce densely-packed dynamic membranes. Alumina nanosheets were synthesized in 0, 25, and 50 vol% ethanol-water mixtures (Al-0, Al-25, and Al-50, respectively). Using dynamic image analysis, it was determined that the alumina nanosheets twinned to form aggregate superstructures of distinct size distributions at each synthesis condition. The aggregates were intrinsically porous with three-dimensional pore connectivity. Dynamic membranes (DMs) were formed by the deposition of these aggregates on a substrate. The effect of ethanol content in the synthesis mixture on the performance of the DMs was investigated during the constant-pressure filtration of a bentonite solution. The results show that the Al-50 DM had the best performance based on flux and turbidity removal. The Al-50 DM reached the required turbidity level of <0.10 NTU at a flux that was 177% and 12% higher than the fluxes obtained by the Al-0 and Al-25 DMs, respectively. The superior performance of the Al-50 DM was explained by the presence of three aggregate size distributions providing optimal packing in the synthesized material. This reduced interstitial pores and resulted in a packing density of 74.7 –78.5% versus 54.0 – 54.2% for Al-0.

4.1 Introduction

Membrane separation is a low-energy alternative or supplement to traditional separation techniques [282–284]. However, membrane filtration has yet to become a fundamental treatment method due to the decline in membrane performance over time. Fouling and flux decline are an inevitable part of membrane operation. Thus, methods to reduce fouling have the potential to increase the operating lifetime of membranes [284,285], reduce maintenance time [286,287], reduce operating costs [285–287], and reduce energy consumption [284–287].

Numerous studies have been conducted on methods to counter the effects of membrane fouling through physical [288–291] and/or chemical means [289,290,292–295]. An alternative approach is to trap the foulant material in a deposited layer on top of the membrane, referred to as a dynamic membrane (DM), secondary membrane, or formed-in-place membrane. The DM and the entrapped foulant can then be physically removed by brushing, air scouring, cleaning with tap water, or acid cleaning [191,192].

DMs were first reported in 1965 at Oak Ridge Laboratories by workers engaged in desalination research [194]. The use of DMs is currently well-established in wastewater treatment, where DMs are formed using coagulants [200,201], adsorbents [193,202,296,297], and sludge or biofilm [197,199,204]. However, further uses of DMs have not been well-researched. In particular, the application of nanoparticle DMs for problematic filtrations involving colloidal clays and other fine particles has not be established.

The main benefit of DMs lie in the ability to remove one membrane layer once it has become severely fouled and form a fresh layer to continue filtration operations. However,

DMs have not been applied in large-scale applications due to the difficulty in predicting their physical properties [298].

The objective of this work is to prepare intrinsically porous aggregates of nanosheets. The distribution of aggregates should be optimal to obtain a densely-packed dynamic membrane eliminating interstitial aggregate pores.

In this study, nano-alumina aggregates were hydrothermally synthesized at various ethanol-water concentrations. Then, alumina DMs were formed *in situ* by the deposition of the nano-alumina aggregates on filter support. A mathematical model of the packing density for each alumina aggregate was developed. A colloid clay solution consisting of sonicated bentonite was used to test the filtration properties of the alumina DMs. The flux decline, turbidity reduction, separation factor, and particle retention were studied as a function of the ethanol-water concentration used in the synthesis of the nanosheets.

4.2 Experimental

4.2.1 Materials

Cetyl trimethylammonium bromide (CTAB), sodium hydroxide pellets, anhydrous ethanol, isopropanol (99%), and bentonite (montmorillonite) were purchased from Sigma-Aldrich (Canada). Aluminum chloride hexahydrate (99%, nitrogen flushed) was purchased from Acros Organics. Cellulose filter paper (Whatman #4) was purchased from Fisher Scientific (Canada). All materials were used as purchased.

4.2.2 Methods

4.2.2.1 Alumina Synthesis

Boehmite nanosheets were synthesized by metal salt hydrolysis. A known mass of aluminum chloride hexahydrate was dissolved in distilled, deionized water under vigorous

stirring. The pH of the solution was raised to 14 using sodium hydroxide pellets. CTAB was dissolved in anhydrous ethanol or distilled, deionized water. The surfactant solution was added to the precursor solution and left to stir at room temperature for 24 h. After stirring, the solution was poured into a Teflon-lined stainless steel autoclave (Parr Instrument Company, Illinois), sealed, and heated to 165°C for 12 h under autogenous pressure. The precipitate formed during crystallization accumulated at the bottom of the autoclave in the form of a disk. The disk of particles was placed in a fume hood to dry. Structures synthesized in 0 vol%, 25 vol%, and 50 vol% ethanol-water were calcined at 600°C for 4 h to produce alumina particles (referred to as Al-0, Al-25, and Al-50).

4.2.2.2 Alumina Dynamic Membrane Filtration

A typical filtration experiment was as follows: a clean 5.5 cm filter paper was placed in a flow cell. Initially, 500 g of distilled water was passed through the filter paper to determine its hydraulic permeability. 250 mg of alumina particles were suspended in 2500 g of distilled water and deposited as a DM at an applied pressure of 6.89 kPa. 500 g of distilled water was passed through the DM at 6.89 kPa. 125 mg of bentonite was ultrasonicated using a Fisher Scientific Sonic Dismembranator 550 in 80 g of distilled water for 60 s at 50% power and added to 4020 g of distilled water. The turbidity of this mixture was measured three times using an HF Scientific Inc. Micro 100 Turbidimeter (Fort Myers, Florida); it was then filtered through the alumina DM at 34.47 kPa. The mass of filtrate leaving the flow cell was continuously monitored by a balance using LabVIEW software (National Instruments, Québec). The turbidity was measured manually at 250 g intervals. A control run was performed without the deposition of a dynamic membrane on the filter paper.

4.2.2.3 Particle Characterization

Size distributions for the bentonite samples before and after DM filtration were determined with dynamic light scattering using a Zetasizer ZS90 (Malvern Instruments, Worcestershire, UK). For samples obtained during filtration, the filtration procedure above was followed. In addition, five 50 g samples of permeate were collected at 250 g intervals. The turbidity of all samples were measured manually.

Size distributions of the alumina nanosheets (Figure 4-1a) were obtained by SEM. Alumina samples were mounted on aluminum stubs (Ted Pella, Redding, California). SEM imaging was performed using a Phenom Pro Desktop SEM (Nanoscience Instruments, Virginia) at an accelerating voltage of 10 kV. Sizes were estimated by measuring the length, width, and thickness of 20 nanosheets at each synthesis condition using ImageJ software.

During synthesis, the alumina nanosheets twinned to form alumina particles (Figure 4-1b). These particles then agglomerated to form aggregates (Figure 4-1c). The size distributions of the alumina aggregates were obtained by dynamic particle size analysis. A typical procedure was as follows: a flow cell capillary was cleaned using isopropanol and DI water. A 1-mL aliquot from a 0.01 M alumina stock solution was diluted to 100 mL with DI water. The solution was pumped through the flow cell at 0.1 mL/min using a peristaltic pump and analyzed using a DPA-4100 dynamic particle analyzer at high magnification (Brightwell Technologies Inc., Ottawa).

The bulk density of the alumina aggregates was estimated by measuring the volume of known masses of the samples after settling in water. The porosity of the alumina aggregates was estimated using the water evaporation method [244,299].

The macroscopic surface area of the alumina nanosheets was determined based on the surface area and volume of a single nanosheet as determined by SEM (m^2) [300–302] and the density of alumina (3975 kg/m^3) [303].

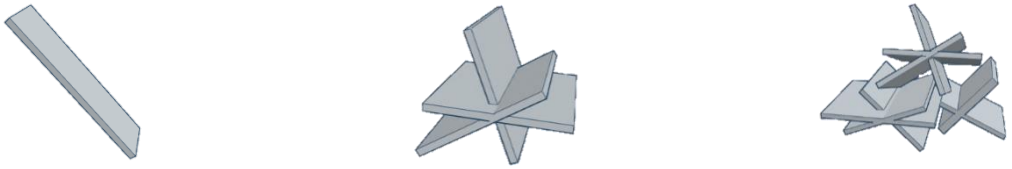

(a) (b) (c)

Figure 4-1: Graphical Representations of (a) Nanosheets; (b) Particles; and (c) Aggregates

4.2.2.4 Dynamic Membrane Characterization

The hydraulic permeabilities of the alumina DMs were measured during filtration by the application of Darcy's law:

$$\lambda = \frac{\Delta P}{\mu}\left(\frac{1}{J_{total}} - \frac{1}{J_0}\right) \tag{4-1}$$

where λ is the resistance of the DM (m^{-1}), ΔP is the pressure difference across the DM and filter paper (Pa), μ is the viscosity of the fluid (Pa·s), J_0 is the average flux across the filter paper (m/s), and J_{total} is the average flux across the DM and filter paper, as determined in separate experiments [304].

The hydraulic permeability of the DM is then

$$\kappa = \frac{x}{\lambda} \tag{4-2}$$

where κ is the hydraulic permeability (m^2), and x is the thickness of the DM (m) [304]. The value of κ is converted to millidarcies with the following conversion factor: 1 mDa = 9.869233×10^{-16} m^2.

Given the bulk density of the aggregates, the thickness of the DM was estimated by

$$x = \frac{m}{\rho_b A} \tag{4-3}$$

where m is the mass of the sample (kg), ρ_b is the bulk density of the sample (kg/m^3), and A is the area of the filter paper available for filtration (m^2). The thickness of the DM was also measured manually using a Mitutoyo digital caliper.

A bentonite turbidity calibration curve was prepared in the range of 0 to 10 NTU. A plot of concentration versus turbidity was constructed to determine an equation relating the two quantities. The separation factor achieved during DM filtration is given by

$$SF = \frac{C_0 - C}{C_0} \tag{4-4}$$

where C_0 is influent solids concentration (g/L) and C is permeate solids concentration (g/L).

The composition of the fouled DMs was characterized using the JEOL 8230 SuperProbe and Energy Dispersive Spectrometry (EDS) at 20 kV under low vacuum.

4.2.2.5 Sphere-Packing Models

A three-sphere packing model was developed to estimate the packing density of the alumina aggregates produced in this work. The aggregates are modelled as perfect spheres. The model is based on the idea that the packing of spheres in a closed container is affected by the distance of the spheres from the boundaries of the container [305]. The packing density for spheres located far from the container boundaries is assumed to be independent of the container shape. This density is referred to as the center part density. Spheres located near the surface of the container are affected by the boundaries of the container, which can be accounted for by a boundary evacuation coefficient.

The model of Yamada [305] was extended from a two-sphere model to a three-sphere model to accommodate the size distributions obtained in this work. The total packing densities for containers packed with one, two, and three sets of mono-sized spheres are given below:

One-Sphere Packing

$$D_1 = \left(1 - \varepsilon r_1 \frac{S}{V}\right) D_c \tag{4-5}$$

where D_1 is the packing density (expressed as a fraction) of mono-sized spheres in a container of surface area S and volume V, $\varepsilon = 0.387 \pm 0.01$ [305] is the boundary evacuation coefficient, and $D_c = 0.543 \pm 0.002$ [305] is the center part density.

Two-Sphere Packing

$$D_{1,2} = D_c \left\{2 - D_c - 3\varepsilon D_c \frac{r_1}{r_2} + \varepsilon \frac{S}{V}[r_2(D_c - 1) - r_1(1 - 3\varepsilon D_c)]\right\} \tag{4-6}$$

where $D_{1,2}$ is the packing density of two sets of mono-sized spheres for $r_1 < r_2$.

Three-Sphere Packing

In this section, we develop a model for packing a container of known volume V and surface area S with three sets of mono-sized spheres with $r_1 < r_2 < r_3$.

As described in [305], we first pack the container with the larger spheres of radius r_3. The volume of the spheres of radius r_3 is approximately

$$V_3 = (V - \varepsilon r_3 S) D_c \tag{4-7}$$

The surface area of the spheres with radius r_3 is

$$S_3 = \frac{3}{r_3} V_3 \tag{4-8}$$

We then fill the remaining volume around the spheres of radius r_3 with spheres of radius r_2. The volume of the spheres with radius r_2 is approximately

$$V_2 = [(V - V_3) - \varepsilon r_2 (S + S_3)] D_c \tag{4-9}$$

The surface area of the spheres with radius r_2 is

$$S_2 = \frac{3}{r_2} V_2 \tag{4-10}$$

This approach was extended to the three-sphere packing model by filling the remaining volume around the spheres of radii r_3 and r_2 with spheres of radius r_1. The volume of the spheres with radius r_1 is approximately

$$V_1 = [(V - V_2 - V_3) - \varepsilon r_1 (S + S_2 + S_3)] D_c \tag{4-11}$$

The surface area of the spheres with radius r_1 is

$$S_1 = \frac{3}{r_1} V_1 \tag{4-12}$$

The total packing density is then determined by

$$D_{1,2,3} = \frac{V_1 + V_2 + V_3}{V} \tag{4-13}$$

After simplification, it can be shown

$$D_{1,2,3} = \frac{D_c}{V} \left\{ V + (K_1 + K_3)(1 - D_c) - \varepsilon r_1 \left[S + 3 D_c \left(\frac{K_1}{r_3} + \frac{K_3}{r_2} \right) \right] \right\} \tag{4-14}$$

$$K_1 = V - \varepsilon r_3 S \tag{4-15}$$

$$K_2 = S + \frac{3}{r_3} D_c K_1 \tag{4-16}$$

$$K_3 = V - D_c K_1 - \varepsilon r_2 K_2 \tag{4-17}$$

where $D_{1,2,3}$ is the packing density of two sets of mono-sized spheres for $r_1 < r_2 < r_3$.

4.2.2.6 Filtration Models

In the linearized form of Hermia's filtration models [306], the value of the slope indicates the primary mode of filtration. The slope values of 0, -1, -2, and -0.5 indicate complete blocking, intermediate blocking, pore constriction, and cake filtration, respectively.

4.3 Results

4.3.1 Particle Characterization

The particle size distribution of the bentonite sample prior to filtration is shown in Figure 4-2. As can be seen from the figure below, the bentonite clay was monodisperse with low variability in particle diameter.

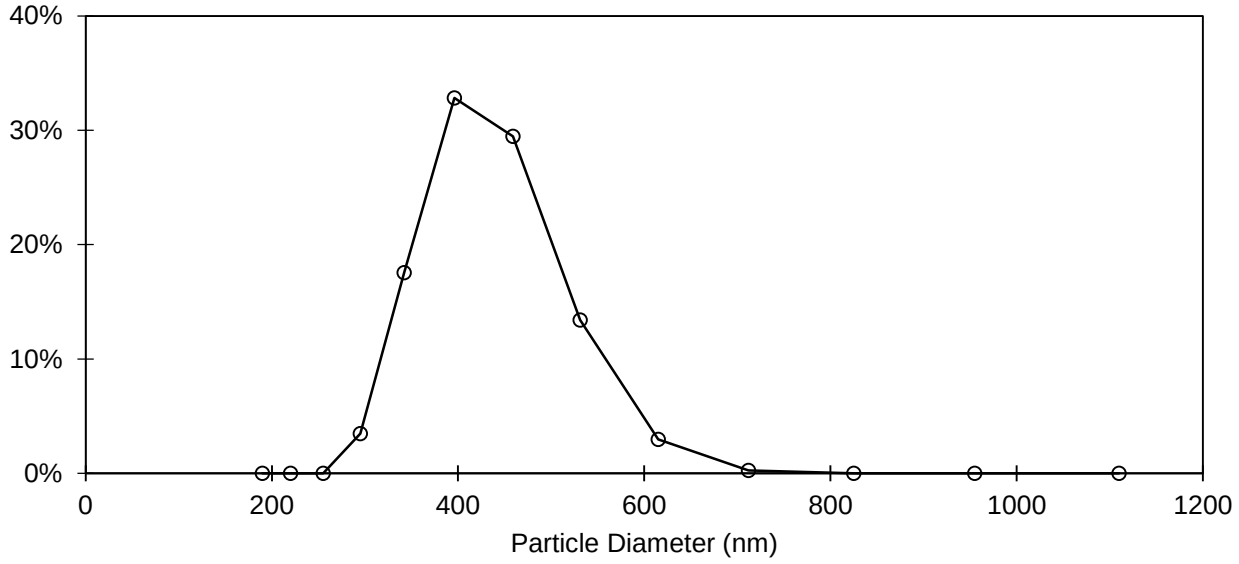

Figure 4-2: Particle Size Distribution of Bentonite Prior to Dynamic Membrane Filtration Determined by Dynamic Light Scattering

The size characteristics of the alumina nanosheets, as measured during SEM analysis, are summarized in Table 4-1 as a function of ethanol-water concentration in the synthesis mixture. As can be seen in Figure 4-3, the alumina nanosheets were monodisperse with low

variability in all size characteristics at each synthesis condition. The length of the nanosheets was not affected by the ethanol-water concentration in the synthesis mixture, and remained constant at an average of 3.7 – 3.9 μm. The average width was 2.5 – 2.6 μm in pure water and 25 vol% ethanol-water. Synthesis in 50 vol% ethanol-water reduced nanosheet width by 35% and increased the aspect ratio from 1.5 to 4.3. Addition of ethanol to the synthesis mixture reduced the nanosheet thickness by a factor of 2.0 and the volume by a factor of 1.9 to 4.8.

Table 4-1: Size Characteristics of Alumina Nanosheets

Ethanol Content by Volume	**Length (μm)**	**Width (μm)**	**Thickness (nm)**	**Volume[1] (μm^3)**
0%	3.8 ± 0.6	2.5 ± 0.6	200 ± 17[2]	1.9 ± 0.7
25%	3.7 ± 0.8	2.6 ± 0.7	100 ± 17[2]	1.0 ± 0.5
50%	3.9 ± 0.6	0.9 ± 0.2	100 ± 17[2]	0.4 ± 0.1

[1]Volume = Length x Width x Thickness

Average ± Standard Deviation ([2]resolution of SEM)

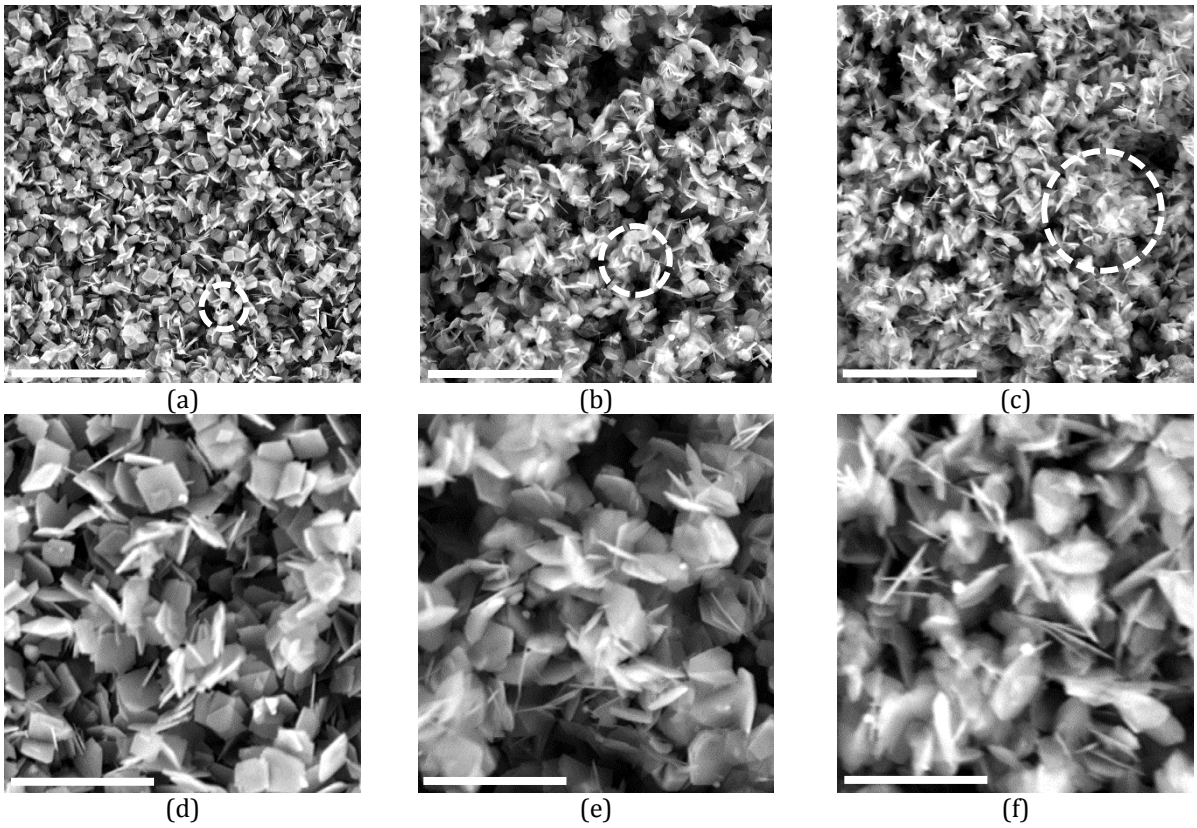

Figure 4-3: SEM Micrographs of Alumina Aggregates Prior to Dynamic Membrane Formation
(a,d) Al-0; (b,e) Al-25; (c,f) Al-50
Scale Bars: 30 μm (a,b,c) and 10 μm (d,e,f)
Dashed Circles Indicate Largest Aggregate, as Described in Figure 4-4

The particle size distributions of the alumina aggregates characterized by dynamic particle size analysis are shown in Figure 4-4. When ethanol was added to the synthesis mixture, the average aggregate size increased by a factor of 2 to 5 and the distribution became trimodal.

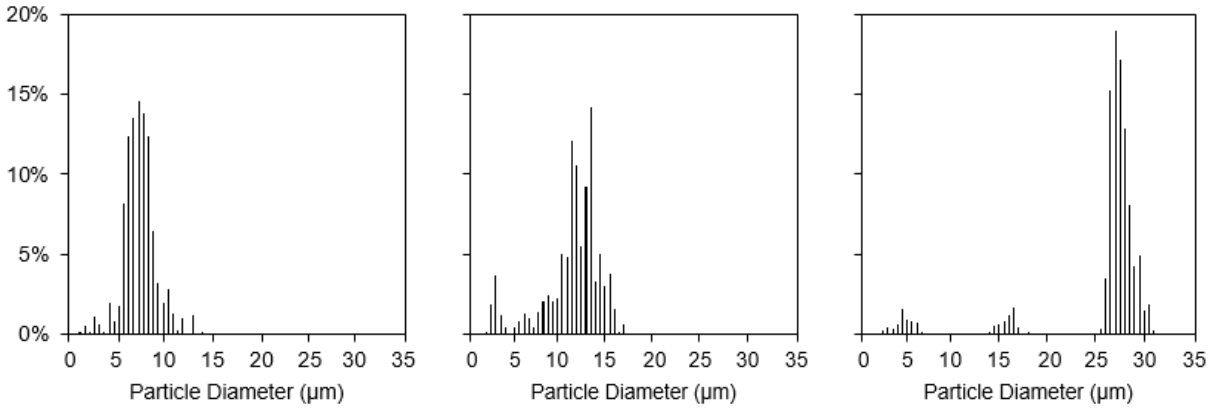

Figure 4-4: Particle Size Distributions of Alumina Aggregates as Measured by Dynamic Particle Size Analysis
(a) Al-0; (b) Al-25; (c) Al-50

The bulk density, porosity, and specific surface area of the alumina aggregates settled in water are listed in Table 4-2 as a function of ethanol-water concentration in the synthesis mixture. The addition of ethanol during the synthesis process reduced the bulk density by 28%, increased the porosity by 11%, and increased the specific surface area by a factor of 2.

Table 4-2: Density and Porosity of Alumina Aggregates Settled in Water

Ethanol Content by Volume	**Bulk Density (kg/m^3)**	**Porosity (%)**	**Macroscopic Surface Area (m^2/g)**
0%	123	79	2.89
25%	91	85	5.31
50%	89	88	5.70

4.3.2 Characteristics of the Dynamic Membranes

The thickness and hydraulic permeability of the alumina DMs are listed in Table 4-3 as a function of ethanol-water concentration in the synthesis mixture. The predicted and measured DM thicknesses coincide well, indicating no significant compaction of the DM during deposition. Although the same mass of alumina was used to form the DMs, the addition of ethanol during synthesis of the aggregates increased the thickness of the DMs by a factor of 1.4 and hydraulic permeability by a factor of 10.9. This pattern coincides with the reduction in bulk density and increase in porosity with the increase in ethanol content in the alumina samples seen in Table 4-2.

Table 4-3: Thickness and Hydraulic Permeability of Alumina Dynamic Membranes

Ethanol Content by Volume	**Predicted Thickness (μm)**	**Measured Thickness (μm)**	**Hydraulic Permeability (mD)**
0%	852	820	65.7
25%	1159	1140	174
50%	1179	1230	714

The dynamic membranes were characterized under pure water filtration at 6.89 kPa, as shown below in Figure 4-5. The pure water flux through the DMs increased as a function of ethanol content in the synthesis mixture, from an average of 765 LMH for Al-0 to 2495 LMH for Al-50.

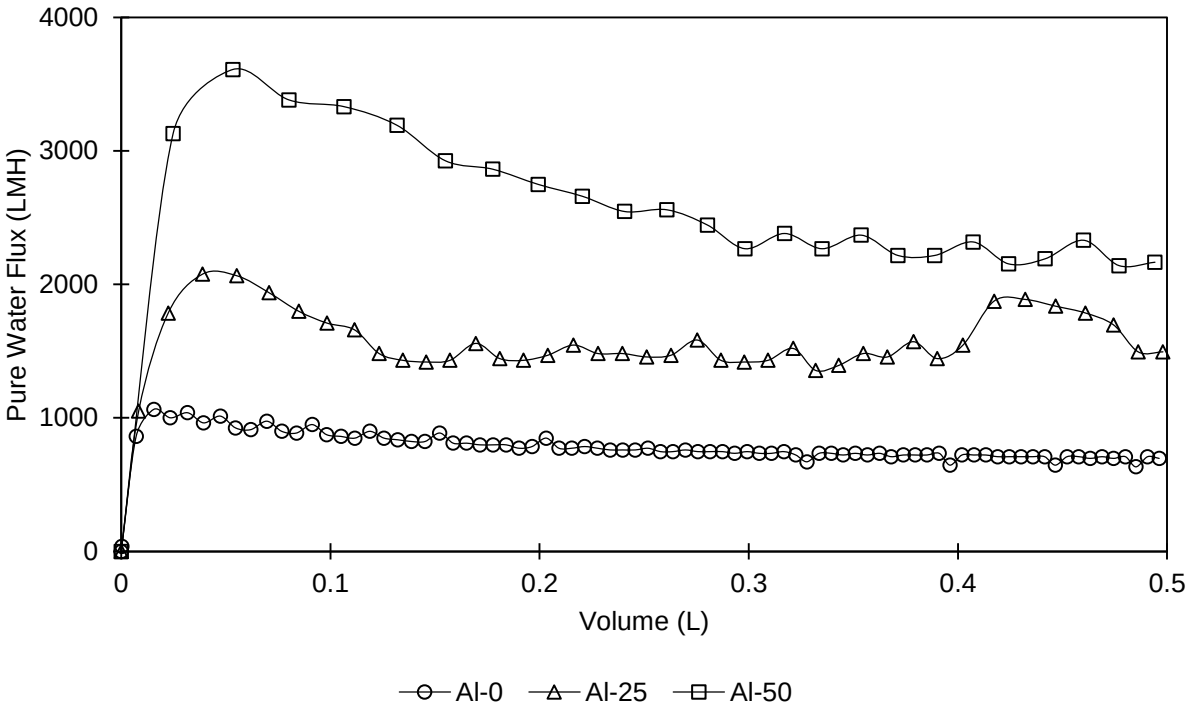

Figure 4-5: Pure Water Fluxes Through Alumina Dynamic Membranes as a Function of Volume at 6.89 kPa

4.3.3 Modelling the Dynamic Membranes Based on Sphere Packing Models

The sphere packing models in Equations (4-5) to (4-17) were used to estimate the packing densities for spheres contained in the DMs. The DMs were modelled as cylindrical disks. The dimensions of the DMs were used to estimate the surface area and volume of the cylindrical disks for the purposes of the model estimates, as specified in Table 4-4. Using the data from the particle size distributions in Figure 4-4a, b, and c for particle diameter, the packing densities of the alumina samples were estimated. These results can be observed in Figure 4-6 to Figure 4-8.

Table 4-4: Size Characteristics of Alumina DMs

Ethanol Content by Volume	Surface Area (m^2)	Volume (m^3)	Surface-to-Volume Ratio
0%	4.89 x 10^{-3}	1.95 x 10^{-6}	2510
25%	4.95 x 10^{-3}	2.71 x 10^{-6}	1830
50%	4.96 x 10^{-3}	2.92 x 10^{-6}	1700

For single sphere packing, the packing density decreases linearly as a function of sphere radius from the maximum value of 54.3% as shown in Figure 4-6. In the limiting value of $r_1 \rightarrow 0$ in Equation (4-5) the packing density of the spheres becomes the center part density, D_c. As r_1 increases, the packing density decreases linearly with slope $-\frac{\varepsilon S}{V}$. The decreased packing density reflects the effects of the container edges on the spheres' ability to pack efficiently. The packing density for Al-0 was estimated to be 54.0 – 54.2% as shown in the shaded region in Figure 4-6.

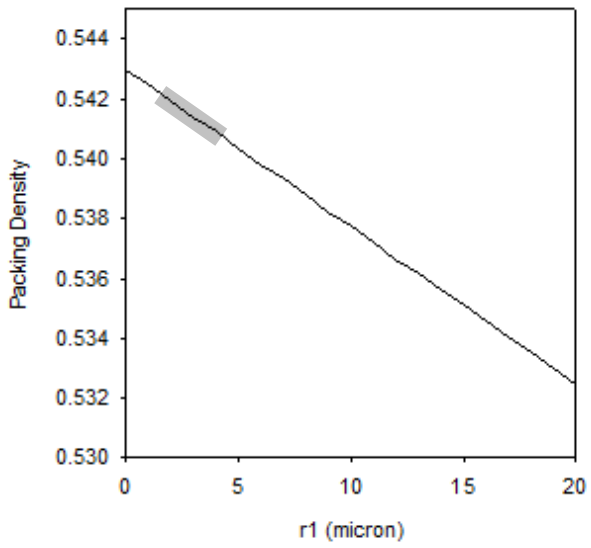

Figure 4-6: Single Sphere Packing Densities in a Cylindrical Container with Dimensions As Specified in Table 4-4
(shaded region designates sample packing density for Al-0)

In two-sphere packing, the packing density increases rapidly as a function of r_2/r_1 for low values of this ratio and decreases steadily for larger values of r_2/r_1, as shown in Figure 4-7a. The maximum value 76.3% occurs in a lobe-shaped region for low values of r_1 and values of $r_2/r_1 > 16$. This value coincides well with the other theoretical maximum packing densities found in the literature for binary sphere packing, 73.9% [307] and 74.8% [308]. The region of rapid increase for low values of r_1 is expanded in Figure 4-7b. The packing density for Al-25 occurs inside the region of rapid increase. It was estimated to be 65.3 – 74.4% as shown in the shaded region in Figure 4-7b.

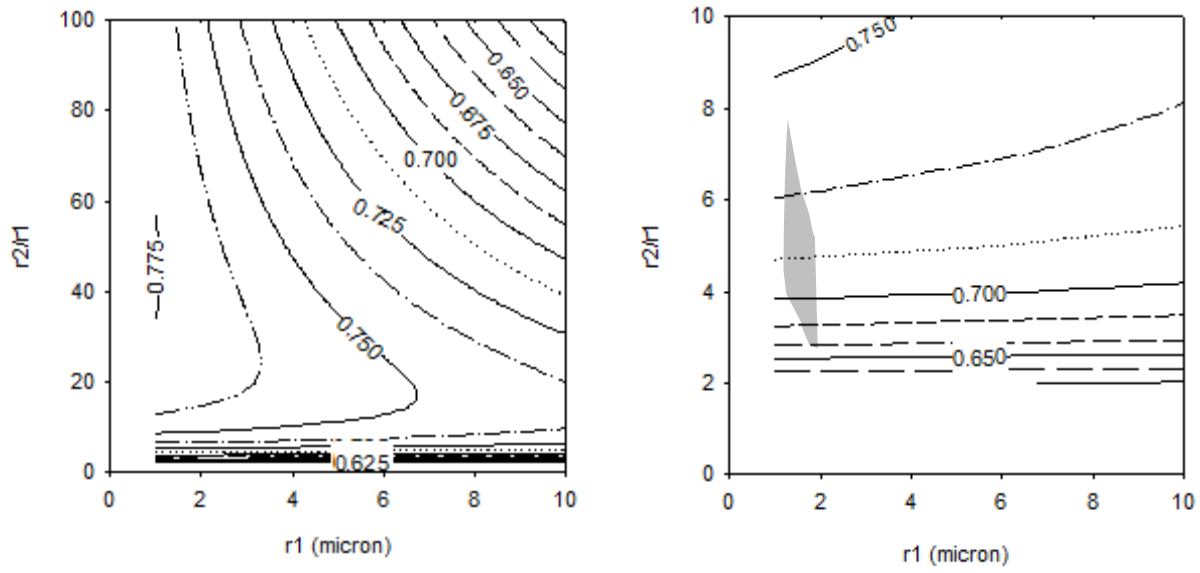

Figure 4-7: Two-Sphere Packing Densities in a Cylindrical Container with Dimensions As Specified in Table 4-4
(a) Full View (b) Restricted View
(shaded region designates sample packing density for Al-25)

In three-sphere packing, the packing density increases rapidly at constant r_2/r_1 for increasing values of r_3/r_1, as shown in Figure 4-8a. The maximum packing density of 85.0% occurs for optimal values of r_2/r_1 and r_3/r_1 inside an elliptical region. The region of rapid increase for low values of r_3/r_1 is expanded in Figure 4-8b. The packing density for Al-50 occurs inside the region of rapid increase. It was estimated to be 74.7 – 78.5% as shown in the shaded region in Figure 4-8b.

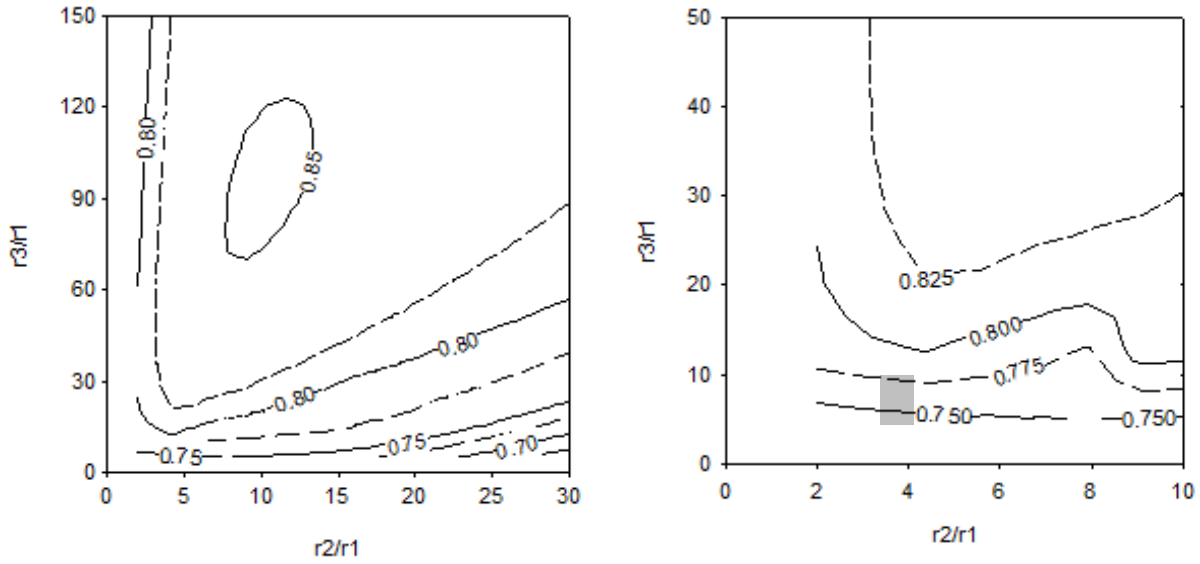

(a) (b)

Figure 4-8: Three-Sphere Packing Densities in a Cylindrical Container with Dimensions As Specified in Table 4-4
(a) Full View (b) Restricted View
(Shaded Region Designates Sample Packing Density for Al-50)

4.3.4 Filtration Results

The flux decline profiles for each DM as a function of permeate volume are shown below in Figure 4-9. All DMs began at fluxes in the range of 7000 – 11000 LMH and declined over the course of the 3 L filtration run to final fluxes in the range of 400 – 1000 LMH. Three individual samples of Al-50 were synthesized as described in Section 2.2.1. They were deposited onto the filter substrates to form three individual Al-50 DMs. Three separate filtration runs were performed on these Al-50 DMs. The average and deviation of the flux values are presented in Figure 4-9.

Each alumina DM had its own unique flux decline profile, indicating that the distinct structural properties of the alumina nanosheets and aggregates had a defining role in how each DM performed during the filter run. The final flux of each alumina DM after

permeating 3 L of bentonite solution increased as a function of ethanol content in the synthesis mixture: 405, 506, and 980 ± 30 LMH, for Al-0, Al-25, and Al-50, respectively. The filtration run without a dynamic membrane did not exhibit the characteristic flux decline profile found in membrane filtration. This indicates that the bentonite particles were not retained on the filter paper during this filtration run. Thus, the dynamic membranes are necessary to retain the bentonite particles.

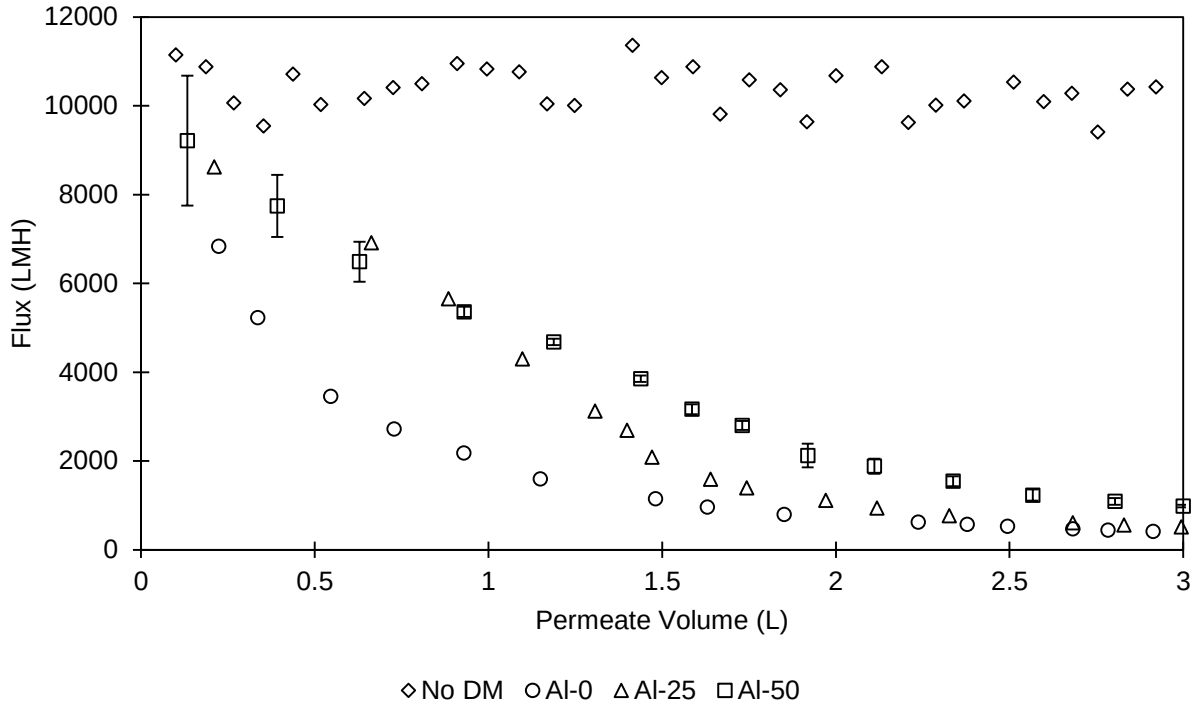

Figure 4-9: Flux Decline During Filtration of Bentonite With and Without Alumina Dynamic Membranes as a Function of Permeate Volume at 34.47 kPa (error bars for Al-50 were determined based on 3 runs at the same experimental conditions)

The filtration mechanisms for each DM can be elucidated from a log-log plot of flux versus time, as shown in Figure 4-10. The slopes of the linearized data for each DM were determined and matched to the corresponding values for Hermia's models. These values are summarized in Table 4-5 below.

It was found that Al-0, Al-25, and Al-50 had slopes of approximately -1 in their first linear region, indicating that each DM initially underwent intermediate blocking. Al-0 transitioned to a slope of
-0.81 at 7.5 min, indicating a shift towards cake filtration. The slope of Al-25 changed to -2.06 at 8 min, indicating a complete transition to pore constriction. After an additional 3 min, the slope changed to -0.81, indicating a shift towards cake filtration. The slope of Al-50 transitioned to
-1.74 after 10 minutes, indicating a shift towards pore constriction. After an additional 4.5 minutes, the slope changed to -0.88, indicating a shift towards cake filtration. The volumes permeated through the DMs for these transition times are listed in Table 4-5.

Overall, no evidence of bentonite cake was found on the surface of the Al-0, Al-25, or Al-50 DMs. In the side-view of the Al-0 and Al-25 DMs in Figure 4-11d and e, agglomerates are visible on the surfaces of the alumina particles. In Figure 4-11f, the agglomerates were distributed evenly across the surface of the Al-50 DM. Thus, the transition to cake filtration was not complete by the end of the filtration runs. This is supported by the values of the slopes in Table 4-5, which are between the values for intermediate blocking and cake filtration.

The amount of ethanol used in the synthesis mixture had an effect on the ability of the alumina DMs to resist fouling by the bentonite particles. With the Al-0 DM (no ethanol), only two distinct fouling regions were observed as shown in Table 4-5. Additionally, the Al-0 had the fastest transition time from intermediate blocking to pore constriction, indicating a low resistance to internal fouling. With the addition of ethanol, a third distinct fouling

region was observed, and the transition time between fouling regions increased. This indicates that the addition of ethanol increased the fouling resistance of the alumina DMs.

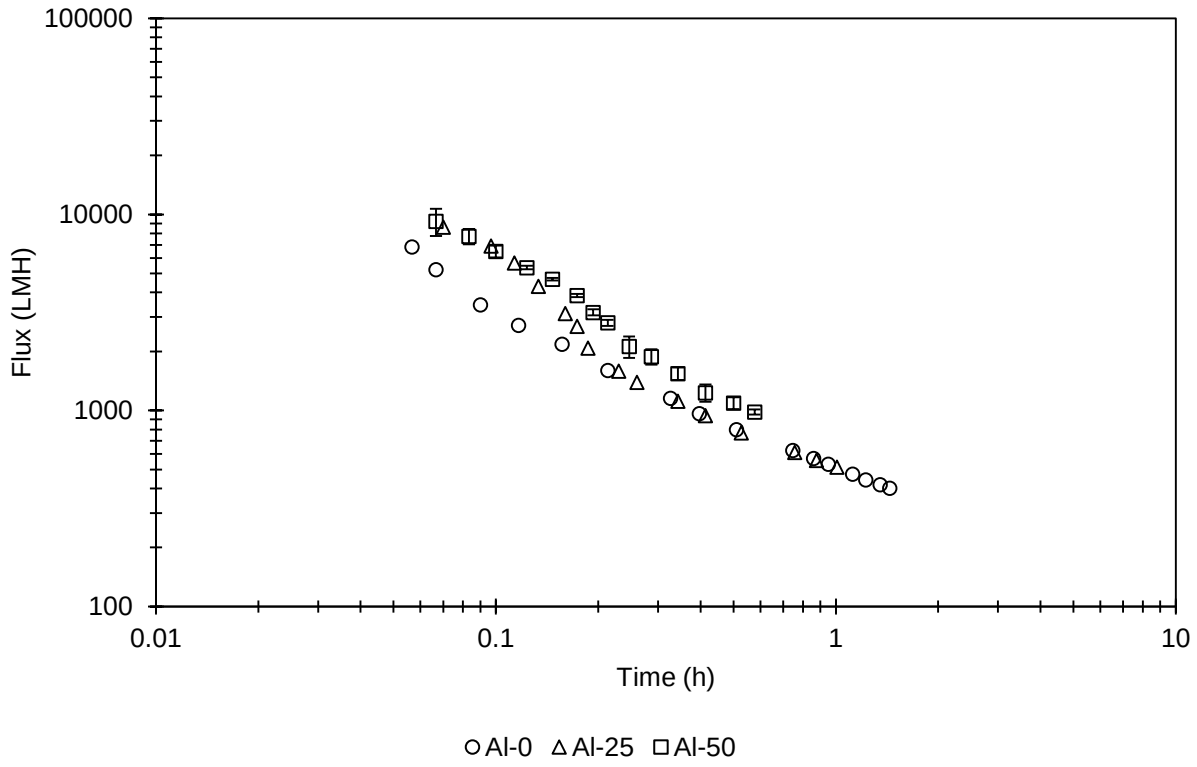

Figure 4-10: Log-Log Plot of Flux Versus Time For Filtration Runs for Alumina Dynamic Membranes at 34.47 kPa (error bars for Al-50 were determined based on 3 runs at the same experimental conditions)

Table 4-5: Filtration Mechanisms and Transition Times for Alumina Dynamic Membranes

	Al-0			**Al-25**			**Al-50**		
Region	*Slope*	*Time (min)*	*Volume (mL)*	*Slope*	*Time (min)*	*Volume (mL)*	*Slope*	*Time (min)*	*Volume (mL)*
1	-1.04	0	0	-0.99	0	0	-0.94	0	0
2	-0.81	7.5	970	-2.06	8	1487	-1.74	10	1778
3	-0.81	-	-	-0.81	11	1676	-0.88	14.5	2158

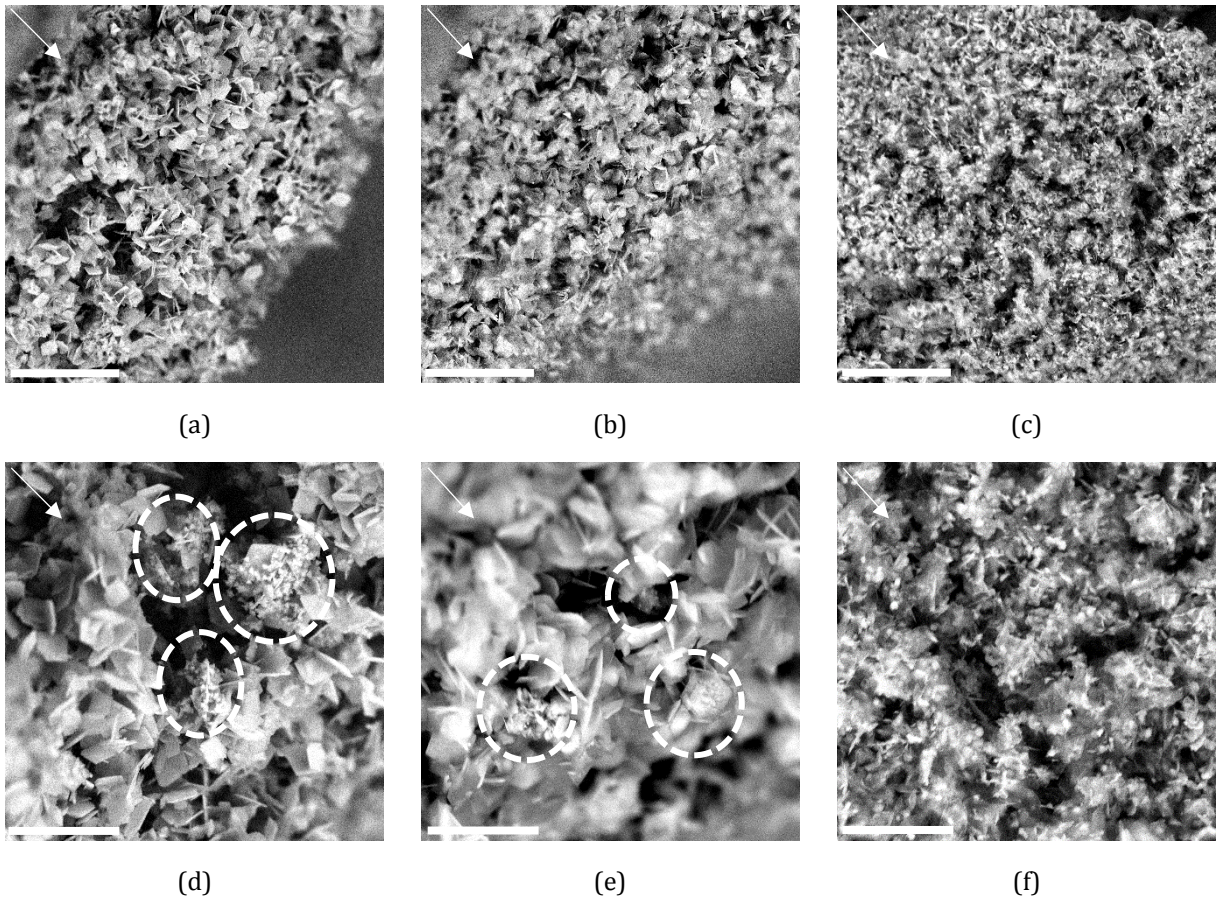

Figure 4-11: SEM Micrographs of Side-View of Fouled Alumina Dynamic Membranes (a, d) Al-0; (b, e) Al-25; (c, f) Al-50
(Scale Bars: 30 μm (a,b,c) and 10 μm (d,e,f); Arrow Indicates Direction of Flow; (d, e) Dashed Circles Indicate Presence of Bentonite Foulant)

The elemental composition of several sites on each fouled dynamic membrane was probed using EDS, as shown in Figure 4-12. In particular, the total calcium content was used to determine whether bentonite was present at the site, as this element was only found in bentonite and not in any other compound used in this work. As shown in Table 4-6, bentonite deposited preferentially at specific sites on the surfaces of certain Al-0 and Al-25 particles, but uniformly across the entire surface of all Al-50 particles.

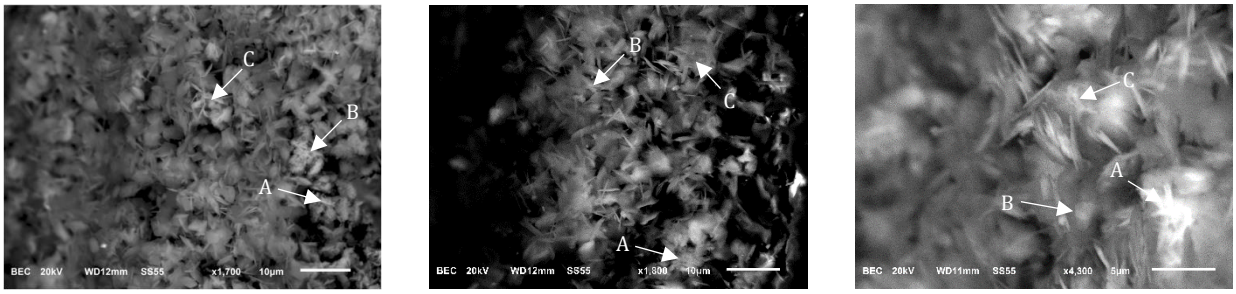

(a) (b) (c)

Figure 4-12: SEM Micrographs of Side-View of Fouled Alumina Dynamic Membranes for Electron Dispersive Microscopy (a) Al-0; (b) Al-25; (c) Al-50

Table 4-6: Calcium Content in Fouled Alumina Dynamic Membranes as Measured by Electron Dispersive Spectrometry

Sample	**Calcium Weight %**	**Observation**	**Identified As**
Al-0-A	6.48	Deposit	Bentonite
Al-0-B	18.75	Deposit	Bentonite
Al-0-C	0	No deposit	Alumina
Al-25-A	3.55	Deposit	Bentonite
Al-25-B	0	No deposit	Alumina
Al-25-C	0	No deposit	Alumina
Al-50-A	5.99	Deposit	Bentonite
Al-50-B	5.24	Deposit	Bentonite
Al-50-C	4.78	Deposit	Bentonite

The separation of foulant achieved during filtration is shown in Figure 4-13 and Figure 4-14. The target level was set to the requirements for drinking water (<0.10 NTU) [309]. A combination of a high flux, low bentonite breakthrough, and high separation factor was the desired outcome. No reduction in turbidity was observed during the control run (without the DM). For runs with DMs, an increase in flux and separation factor was observed as the proportion of ethanol in the synthesis mixture increased. The target level was reached within the first 660 mL of permeate volume at a flux of 7000 LMH for the Al-50 DM, as compared to 710 mL at 6300 LMH for the Al-25 DM and 850 mL at 2400 LMH for the Al-0 DM as shown in Figure 4-13 and Figure 4-14.

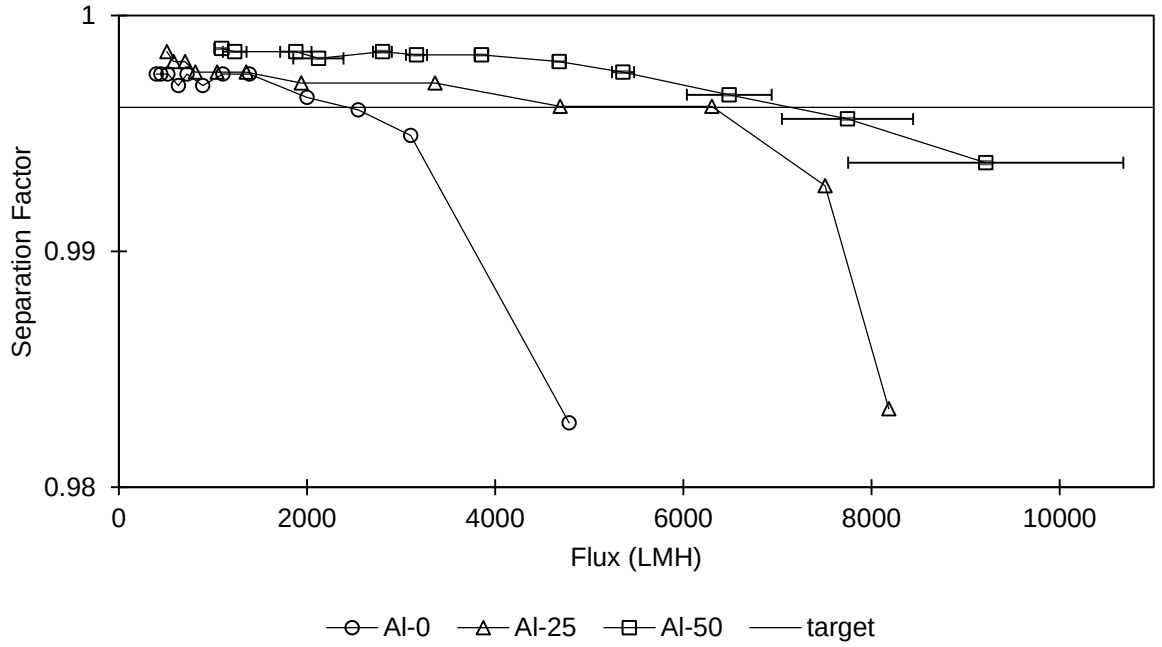

Figure 4-13: Separation of Bentonite During Dynamic Membrane Filtration Run as a Function of Flux at 34.47 kPa (error bars for Al-50 were determined based on 3 runs at the same experimental conditions)

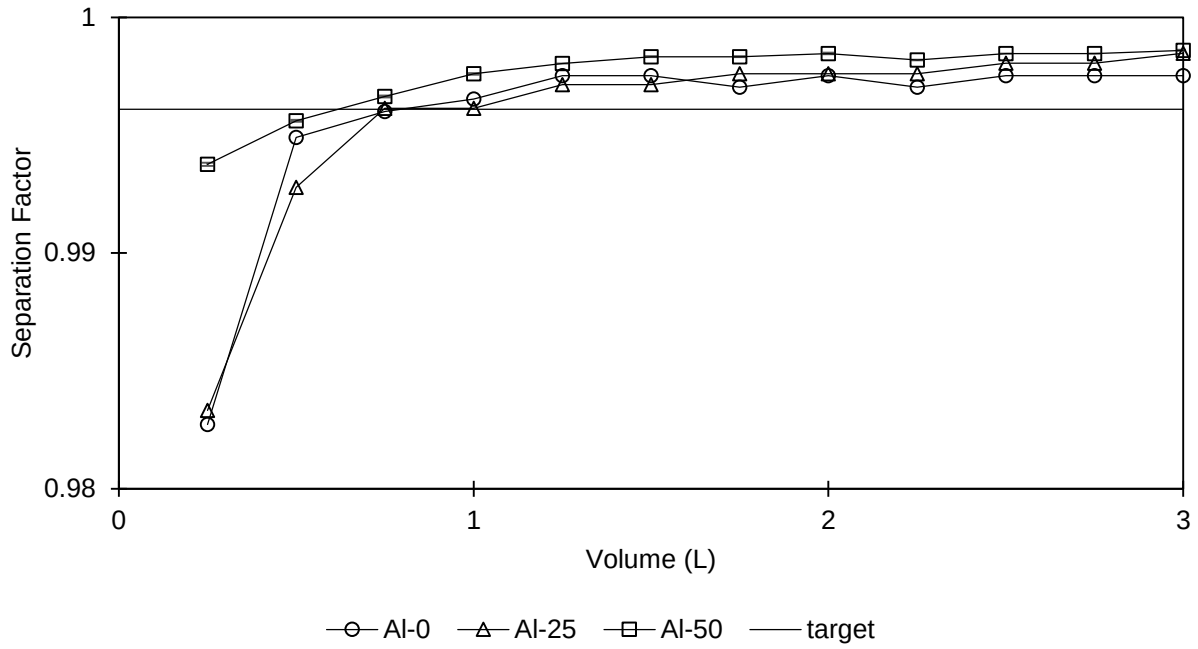

Figure 4-14: Separation of Bentonite During Dynamic Membrane Filtration as a Function of Permeate Volume at 34.47 kPa (error bars for Al-50 were determined based on 3 runs at the same experimental conditions)

The turbidity and particle size distributions of the permeate were monitored as a function of permeate volume during the first 1.25 L of bentonite filtration using no DM and the Al-50 DM. As shown in Figure 4-15, no reduction in turbidity or particle size is observed, indicating that the bentonite particles pass through the filter paper. As shown in Figure 4-16, the reduction in turbidity coincides with a reduction in permeate particle size. Compared to the feed turbidity and average particle size (6.54 NTU and 0.43 μm), the sudden reduction in particle size after the first reading is indicative of the ability of the Al-50 DM to retain the bentonite particles with little breakthrough. Furthermore, the particle size distributions gradually shifted towards lower particle sizes, showing a further reduction in average particle diameter over time.

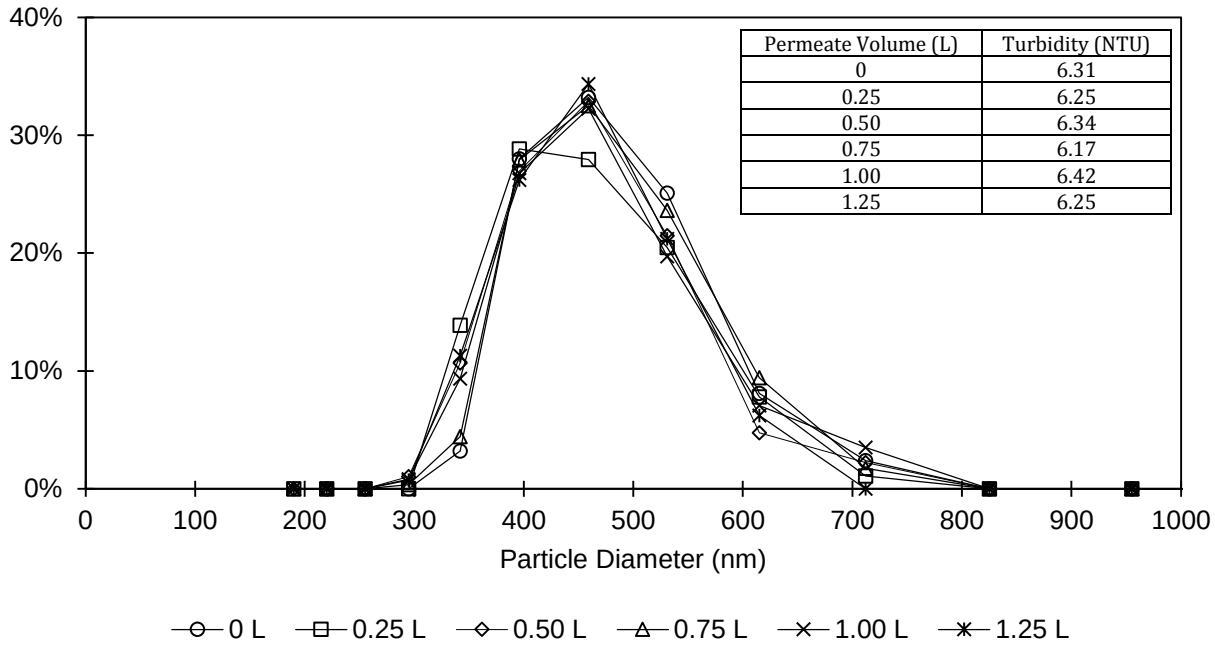

Figure 4-15: Bentonite Particle Size Distributions and Turbidity During Membrane Filtration Using No DM

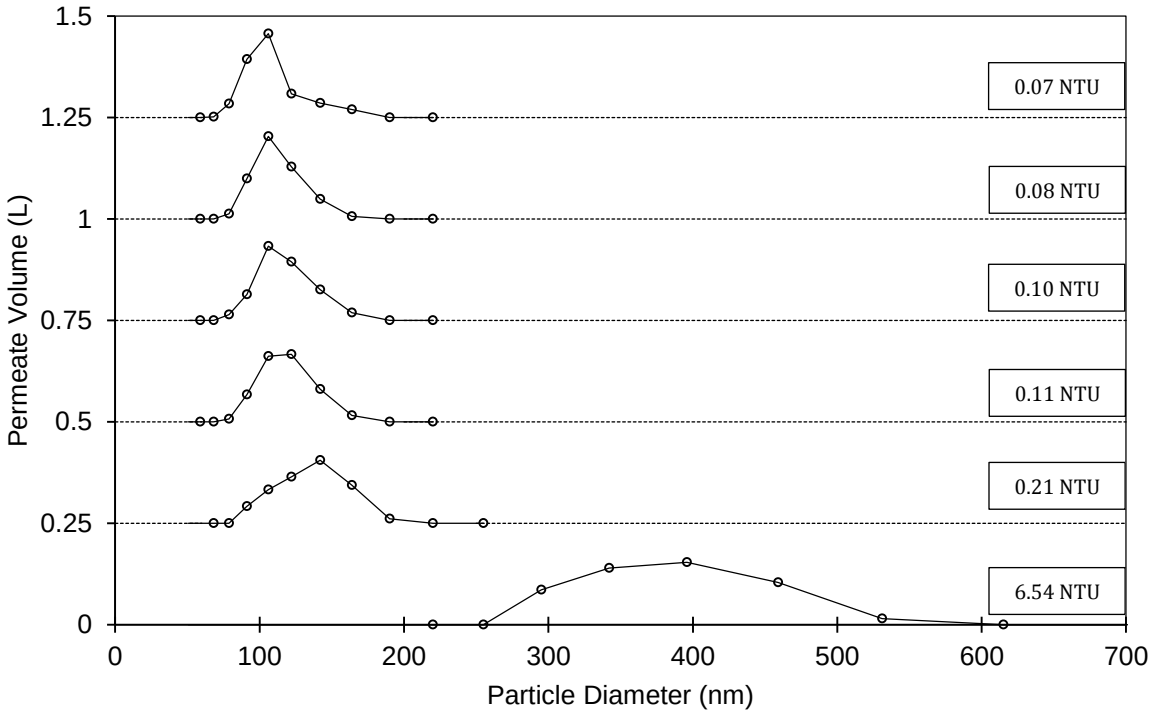

Figure 4-16: Bentonite Particle Size Distributions and Turbidity During Membrane Filtration Using Al-50 DM

4.4 Discussion

Monodisperse alumina nanosheets were successfully synthesized in various ethanol-water mixtures. The size characteristics of the nanosheets were dependent on the ethanol content in the synthesis mixture. An increase in ethanol decreased the width and thickness of the nanosheets, while the length remained the same. Overall, an increase in ethanol content in the synthesis mixture reduced the volume of the nanosheets by a factor of 2.0 to 4.8. During synthesis without ethanol, the alumina nanosheets twinned to form particles as shown in Figure 4-4a. As the ethanol content in the synthesis mixture was increased, the particles aggregated into 3D superstructures with unique particle size distributions, as shown in Figure 4-4b and c.

A mathematical model was developed to represent the packing density of the clusters, by extending a binary sphere packing model in confined geometries [305] to a three-sphere packing model. The three alumina samples were modeled using one-, two-, and three-sphere packing models. Al-0, Al-25, and Al-50 had packing densities 54.0 – 54.2%, 67.3 – 72.7%, and 74.6 – 75.5%, respectively. These values show that the reduction in volume of the Al-50 particles allows for a higher packing density of these particles in a given container size.

Dynamic membranes were formed by the deposition of the alumina particles on filter support. In It was determined that the Al-50 DM had the highest porosity and hydraulic permeability of the three samples, at 88% and 714 mD, respectively. This unique combination of high packing density, porosity and hydraulic permeability is an indication that Al-50 is a highly monodisperse material with little to no defects.

In Table 4-7, the performance of the DMs produced in this work are compared to those obtained in the literature. Based on turbidity removal, the alumina DMs perform better than the majority of the DMs listed. Furthermore, the flux during filtration operation achieved in this work is higher than almost all of the fluxes of the DMs in Table 4-7. Therefore, the alumina DMs achieve both metrics for good membrane performance: a high filtration flux and high turbidity removal.

Table 4-7: Dynamic Membranes for Turbidity Reduction

Dynamic Membrane Material(s)	Material(s) Filtered	Flux (LMH)	Turbidity Reduction	Reference
Alumina	Colloidal clay (bentonite)	405, 506, 982	>99%	This work
Diatomite	Raw water	92.5	>99%	[203]
Diatomite	Polluted surface water	30, 50, 80	85 – 96%	[310]
Heavy kaolin, light kaolin, diatomite, Fuller's earth	Secondary effluent from wastewater treatment plant	50	68 – 96%	[202]
$FeCl_3$	Raw water	-	60 – 90%	[200]
MnO_2	Secondary effluent from wastewater treatment plant	58	>99%	[192]
MnO_2	Mineral processing water and oil refinery wastewater	990	85 – 98%	[311]
PAC	Formazin solution	150	97 – 99%	[297]
PAC	Raw water	100	97%	[201]
Sludge	Raw wastewater	6, 19, 91, 99	95 – 98%	[199]
Sludge	Raw wastewater	12.6	75 – 81%	[205]
Sludge	Synthetic wastewater	2.6	97 – 99%	[312]
TiO_2	4-chlorophenol	100	98 – >99%	[313]

Bentonite (montmorillonite) was used as a representative particle to characterize the filtration abilities of the alumina DMs. The bentonite used in this work was sonicated for 60 s at 50% power to break up aggregates. The particle size distribution of bentonite was shown in Figure 4-2. Bentonite is a hydrated smectite mineral composed of two silica tetrahedral layers with a central octahedral layer. Water and cations occupy the space in

between the layers [314]. The bentonite used in this study had a mixture of sodium and calcium cations.

Colloidal clays are known membrane foulants [315–317]. Bentonite, in particular, was specifically chosen as a model clay due to its unique ability to swell in aqueous solution and form an impenetrable cake [314].

The alumina nanosheets are highly homogeneous at all synthesis conditions with low variability in size parameters. Twinning of the nanosheets during crystal growth produced an open, highly porous 3D network of monodisperse particles that resisted compaction during dynamic membrane formation. In particular, the Al-50 DM reached the highest final flux (980 $\pm$ 30 LMH), indicating that its twinned nanosheet structure is particularly ideal for this type of filtration.

The differences in aggregate structure and their effect on filtration become apparent when the SEM images were analyzed. As evidenced by the distribution of bentonite particles on the surface of the Al-0 DM in Figure 4-11d, filtration occurred through preferential channeling. The Al-0 DM also had the lowest packing density of the three DMs (54.0 – 54.2%), and therefore the largest pore channels available for flow. From the log-log plot in Figure 4-10, it was determined that the Al-0 DM transitioned directly from intermediate blocking to early cake filtration, without a third fouling regime (pore constriction) like the other two DMs. Due to the large internal channels of the Al-0 DM, any bentonite particles that entered the pores passed directly through the channels. Thus, the Al-0 DM was slower at reaching the target turbidity of 0.10 NTU and did so at a lower flux than the other two DMs.

Conversely, as shown in Figure 4-11f, foulant particles were distributed evenly across the surface of the Al-50 DM. The Al-50 DM had the highest packing density (74.6 – 75.5%) and porosity (88%) of the three DMs. These values indicate that the Al-50 particles packed most efficiently together when forming aggregates with high interparticle porosity due to their low nanosheet volume. This combination of high packing density and high porosity also indicates that the alumina aggregates were intrinsically porous with three-dimensional connectivity. Overall, the high degree of packing allowed for an even distribution of flow throughout the internal aggregate pores of the Al-50 DM. Turbidity reduction occurred much more rapidly as compared to the mechanism exhibited by the Al-0 DM.

The ability of the Al-50 DM to retain bentonite particles is illustrated in Figure 4-16. During the first 0.25 L of filtration, Al-50 reduces the feed turbidity by 97%, from 6.54 NTU to 0.21 NTU. The feed solution contains bentonite particles with an average particle size of 0.43 μm $\pm$ 0.05 μm. The alumina DMs are composed of aggregates with an average particle size up to 9x larger than the bentonite particles. During the first 0.25 L, the particle size is reduced by 65% to <0.15 μm. Separation is very high from the beginning, indicating that the pore size distribution of the Al-50 DM is narrow. If it were not, there would be breakthrough.

The particle size distributions remain constant during the filtration run in Figure 4-16, further supporting the idea that a bentonite cake does not build up on the surface of the DM. Instead, the bentonite is retained inside the body of the DM.

Based on the initial particle size distribution obtained by DLS shown in Figure 4-2, no bentonite particles are in the range of <0.295 μm. DLS relies on cumulative light scattering to determine the size of particles in a sample. It is best suited to monodisperse particles in

low-viscosity solvents. In the case of polydisperse samples, DLS will favour the larger particles due to their proportionally higher light scattering effect [318]. The small particles that passed through the Al-50 DM were present in the original sample, but not in a significant enough quantity to be picked up by DLS.

4.5 Conclusions

Alumina aggregates were manufactured in 0, 25, and 50 vol% ethanol-water solutions by the calcination of boehmite powders synthesized under the same conditions.

Using dynamic image analysis, it was determined that the alumina nanosheets linked together to form aggregates of similar sizes under each synthesis condition. In particular, Al-0 formed one set of monodisperse aggregates; Al-25 formed two sets of monodisperse aggregates; and Al-50 formed three sets of monodisperse aggregates. A sphere-packing model was developed to model the packing densities of the alumina aggregates. Al-0, Al-25, and Al-50 had packing densities of 54.0 – 54.2%, 67.3 – 72.7%, and 74.6 – 75.5%, respectively.

The operating flux of the Al-50 DM was the highest of all the DMs during bentonite filtration. The initial flux was 9200 $\pm$ 1500 LMH (35% higher), and the final flux after 3 L of bentonite solution was 980 $\pm$ 30 LMH (145% higher). Furthermore, the Al-50 DM reduced the turbidity of the permeate from the initial value of 6.54 NTU to the target of <0.10 NTU within the first 580 mL of filtration, 32% faster than the other DMs.

The Al-50 DM had the highest packing density and porosity of the three DMs tested in this work. The aggregates were intrinsically porous with three-dimensional connectivity. The high degree of packing allowed for an even distribution of flow throughout the internal aggregate pores of the Al-50 DM.

5 Highly Permeable Twinned Alumina Nanoparticles for the Precoat Filtration of Fine Colloids

K. Roebuck and A. Y. Tremblay. Separation and Purification Technology 182 (2017): 197-206.

Pretreatment is key to the success of any fine filtration process. Precoat filtration is a common method to reduce fine particulate matter in feed streams. In this study, precoat filters were formed by the deposition of the diatomaceous earth (DE) or twinned alumina nanosheets (TAN) particles on a substrate. The TAN particles were produced via metal salt hydrolysis. The performance of the precoat filters was investigated during the constant-pressure filtration of a bentonite solution. The results showed that the TAN precoat exhibited enhanced flow properties and reduced the turbidity of the filtrate more rapidly than either of the DE precoats. The TAN precoat reached the required turbidity level of ≤0.10 NTU at a flux that was up to 28 times higher than the fluxes obtained by the DE precoats. The superior performance of the TAN precoat was explained by (1) the ability of the TAN precoat to resist compaction during filtration due to the unique twinning of the alumina nanosheets forming the TAN particles, (2) the strong attractive forces between the bentonite and TAN particles based on their opposite surface charges, and (3) the isotropic permeability of the TAN aggregates.

5.1 Introduction

Membrane fouling due to finely suspended solids and colloids continue to be problematic in the long term operation of nanofiltration (NF), reverse osmosis (RO) and electrodialysis (ED) water treatment systems. Excessive particulates can also block spacers in NF/RO and

ED membrane modules. These fine suspended solids are increasingly being removed by precoat filtration [319,320].

The operating lifetime of membranes can be increased by adopting methods that reduce fouling [284,285]. In addition, these methods have the potential to decrease maintenance time [286,287], plant operating costs [285–287], and overall energy consumption [284–287]. They also play a pivotal role in the operation of desalination plants. In 2007, the largest desalination plant in North America, located in Tampa, Florida, could be reopened by the addition of a diatomaceous earth (DE) precoat filtration system [321].

Precoat filtration is a common method to reduce fouling and flux decline during treatment, whereby large particles and debris are removed by a thin, dense, and highly permeable layer of particles. Foulants are separated during prefiltration primarily by sieving. Common filter aids include diatomaceous earth (DE), perlite, cellulose and activated carbon [322–324].

Prefilters and filter aids have been studied extensively in the literature. Lihong et al. compared the compressibility of DE and cellulose filter aids during the filtration of highly viscous gels [323]; Michen et al. fabricated a depth filter from DE and investigated its ability to remove colloidal latex particles from solution [325]; Valderamma-Bravo et al. explored the effect of DE precoat thickness on filtration rate during constant pressure filtration of corn liquor [326]; Farag and El-Anany explored the effect of different filter aids (Magnesol XL, DE, and kaolin) on the removal of secondary oxidation products from used fryer oils [327].

Filter aids find great applicability in drinking water filtration [328], as they can be used to reduce parameters like turbidity to acceptable levels. High turbidity can be an indication of

contaminated water [309], therefore it is desirable to minimize turbidity values. Turbidity targets for drinking water are shown below in Table 5-1.

Table 5-1: Turbidity Regulations for Drinking Water

Regulatory Agency	Turbidity Target	References
World Health Organization	Median turbidity ≤0.1 NTU	[329]
Health Canada	Conventional and direct filtration: ≤ 0.3 NTU Slow sand and diatomaceous earth filtration: ≤ 1.0 NTU Membrane filtration: ≤ 0.1 NTU	[309]
United States Environmental Protection Agency	≤0.3 NTU in 95% of tests	[330]

With common filter aids like diatomaceous earth and perlite, there is a tradeoff between permeability and achievable turbidity reduction during filtration. In the studies on precoat filtration cited above, it was found that the effectiveness of the filter aids was reduced due to either the low porosity, low hydraulic permeability or compaction of the precoat. There is a need for filter aids with enhanced flow properties, whereby a rapid decrease in turbidity can be achieved at high filtrate throughput. The fabrication of such a filter aid is therefore of great interest.

In a previous work, low density, high porosity alumina filter aids were manufactured under hydrothermal conditions at three ethanol-water concentrations (0 vol%, 25 vol%, and 50 vol%) [331]. The filter aid synthesized at 50 vol% ethanol-water had the highest hydraulic permeability, and was therefore selected for use in this study. However, the performance of the alumina filter aids in comparison to widely-used industrial filter aids is unknown.

In this study, twinned alumina nanosheets were hydrothermally synthesized in a 50 vol% ethanol-water mixture. Then, the TAN and diatomaceous earth precoats were formed *in situ* by the deposition of the materials on a substrate. The precoats were challenged with sonicated bentonite to compare the filtration performances of the TAN and diatomaceous earth filter aids.

5.2 Experimental

5.2.1 Materials

Cetyl trimethylammonium bromide (CTAB), sodium hydroxide pellets, anhydrous ethanol, isopropanol, diatomaceous earth (medium grade DE-512 and fine-grade DE-577), and bentonite (montmorillonite) were purchased from Sigma-Aldrich (Canada). Aluminum chloride hexahydrate (99%, nitrogen flushed) was purchased from Acros Organics. Cellulose filter paper (Whatman #4) was purchased from Fisher Scientific (Canada). All materials were used as purchased.

5.2.2 Methods

5.2.2.1 Alumina Synthesis

Boehmite nanosheets were synthesized by metal salt hydrolysis. A precursor solution was formed by the dissolution of a known quantity of aluminum chloride hexahydrate in distilled, deionized water under vigorous stirring. The pH of the solution was raised to 14 using sodium hydroxide pellets. A surfactant solution was formed by the dissolution of CTAB in anhydrous ethanol. The surfactant solution was added to the precursor solution to form a 50 vol% ethanol-water mixture. The final mixture was left to stir at room temperature in a fume hood. After 24 h of stirring, the solution was poured into a Teflon-lined stainless steel autoclave (Parr Instrument Company, Illinois), sealed, and placed in a

165°C oven for 12 h under autogenous pressure. The precipitate formed under crystallization accumulated at the bottom of the autoclave in the form of a disk. The disk of particles was placed in a fume hood to dry. The particles were calcined at 600°C for 4 h in a muffle furnace to produce twinned alumina nanosheets (TAN).

5.2.2.2 Precoat Filtration

A typical filtration experiment was as follows: a clean 5.5 cm diameter filter paper was placed in a filtration cell. Initially, 500 g of distilled water was passed through the filter paper to determine its hydraulic permeability. Two hundred and fifty milligrams of alumina or diatomaceous earth particles were suspended in 2500 g of distilled water and deposited as a filter cake at an applied pressure of 6.89 kPa. Five hundred grams of distilled water was passed through the filter cake at 6.89 kPa to determine the hydraulic permeability of the cake. One hundred and twenty-five milligrams of bentonite was ultrasonicated using a Fisher Scientific Sonic Dismembranator 550 in 80 g of distilled water for 60 s at 50% power and added to 4020 g of distilled water. The turbidity of this mixture was measured three times using an HF Scientific Inc. Micro 100 Turbidimeter (Fort Myers, Florida); it was then filtered through the cake at 34.47 kPa. The mass of filtrate leaving the flow cell was continuously monitored by a balance using LabVIEW software (National Instruments, Québec). The permeate flow was redirected manually into a sample vial at 250 g intervals to allow for the immediate measurement of the turbidity. A 30 mL vial was used to collect these samples.

5.2.2.3 Particle Characterization

SEM imaging was performed using a Phenom Pro Desktop SEM (Nanoscience Instruments, Virginia) at an accelerating voltage of 10 kV.

The particle size distribution of the bentonite particles was determined with dynamic light scattering using a Zetasizer ZS90 (Malvern Instruments, Worcestershire, UK).

The particle size distributions of the DE and TAN particles were determined by dynamic particle size analysis. A typical procedure was as follows: a capillary flow cell was cleaned using isopropanol and deionized (DI) water. A 1-mL aliquot from a 0.01 M of DE or TAN stock solution was diluted to 100 mL with DI water. The solution was pumped through the flow cell at 0.1 mL/min using a peristaltic pump and analyzed using a DPA-4100 dynamic particle analyzer at high magnification (Brightwell Technologies Inc., Ottawa).

The bulk density of the DE and TAN samples were determined by measuring the volume of known masses of these samples after settling in water. The porosities of the samples were determined using the water evaporation method [244,299].

The hydraulic permeabilities of the filter aids were measured during filtration by the application of Darcy's law:

$$\lambda = \frac{\Delta P}{\mu}\left(\frac{1}{J_{total}} - \frac{1}{J_0}\right) \tag{5-1}$$

where λ is the resistance of the precoat (m^{-1}), ΔP is the pressure difference across the precoat and filter paper (Pa), μ is the viscosity of the fluid (Pa·s), J_0 is the average flux across the filter paper (m/s), and J_{total} is the average flux across the precoat and filter paper, as determined in separate experiments [304].

The hydraulic permeability of the precoat is then

$$\kappa = \frac{x}{\lambda} \tag{5-2}$$

where κ is the hydraulic permeability (m^2), and x is the thickness of the precoat (m) [304]. The value of κ is converted to millidarcies with the following conversion factor: 1 mDa = 9.869×10^{-16} m^2.

Given the bulk density of the particles, the thickness of the precoat was estimated by

$$x = \frac{m}{\rho_b A} \tag{5-3}$$

where m is the mass of the sample (kg), ρ_b is the bulk density of the sample (kg/m^3), and A is the area of the filter paper available for filtration (m^2). The thickness of the precoat was also measured manually using a Mitutoyo digital caliper.

A bentonite turbidity calibration curve was prepared in the range of 0 to 10 NTU. A plot of concentration versus turbidity was constructed to determine an equation relating the two quantities based on non-linear regression ($R^2 = 0.999$).

5.2.2.4 Filtration Models

Filtration occurs by four basic mechanisms: complete blocking, intermediate blocking, pore constriction, and cake filtration. Equations for these fouling mechanisms, as given by Peng and Tremblay [306], are shown below in Table 5-2.

Table 5-2: Primary Filtration Models

Filtration Model		Equation*	
Complete blocking	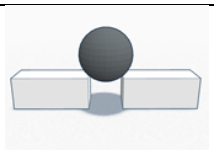	$\frac{J_v}{J_0} = exp(-K_{block}t)$	(5-4)
Intermediate blocking	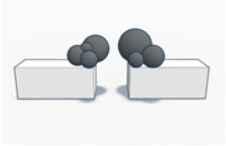	$\frac{J_v}{J_0} = (1 + K_{inter}t)^{-1}$	(5-5)
Pore constriction		$\frac{J_v}{J_0} = (1 + K_{cons}t)^{-2}$	(5-6)
Cake filtration	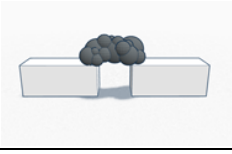	$\frac{J_v}{J_0} = (1 + K_{cake}t)^{-1/2}$	(5-7)

*where J_v is the permeate flux, J_0 is the initial permeate flux through the clean membrane, K_j is the proportionality constant in each model, and t is time.

The following general filtration model, based on Equations (5-4) to (5-7), was created to fit the normalized flux data:

$$\frac{J_v}{J_0} = (1 + Kt)^n \tag{5-8}$$

Equation (5-4) can be represented as the first two terms of a truncated MacLaurin series where K < 0 and n = 1. This permits us to use Equation (5-8) to fit all of the fouling models. Normalized flux data was fitted to Equation (5-8) using Excel Solver by minimizing the sum of the squared residuals. The parameter *n* was restricted between -2 and 1 to correspond to the values in Table 5-2. The data was split into several regions, and a fouling model was found for each region. The residuals plots were analyzed to assure that the error stayed randomly distributed about the x-axis. The times at which the residuals ceased being

randomly distributed about the x-axis were designated as division points between different fouling regimes.

5.3 Results

5.3.1 Particle Characterization

The particle size distribution of the bentonite sample prior to filtration is shown in Figure 5-1. The data was fit with a log-normal distribution (μ = 425 nm, σ = 73 nm). The residual sum of squared errors was 0.0138% with the log-normal distribution versus 0.223% when fitted with a Gaussian distribution. As can be seen from the figure below, the bentonite clay was monodisperse with low variability in particle diameter.

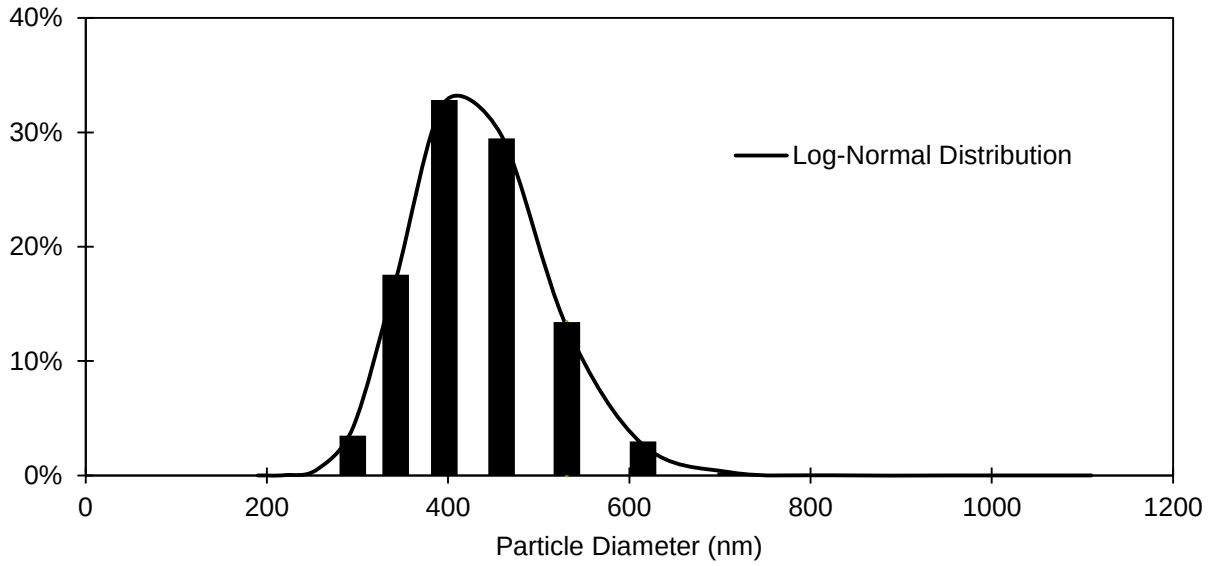

Figure 5-1: Particle Size Distribution of Bentonite Prior to Precoat Filtration Determined by Dynamic Light Scattering (data was fit with a log-normal distribution)

The particle size distributions of the DE and TAN particles as measured by dynamic particle size analysis are shown below in Figure 5-2. The two DE samples are polydisperse, while for the TAN, three distinct normally-distributed particle sizes could be identified (μ_1 = 3.7

μm, σ_1 = 0.9 μm, a_1 = 0.05; μ_2 = 14.6 μm, σ_2 = 0.6 μm, a_2 = 0.05; μ_3 = 25.7 μm, σ_3 = 0.9 μm, a_3 = 0.8; a is a scaling factor. DE-512 is composed of very large irregularly-shaped particles with smaller broken fragments dispersed throughout and a few large particles of diameter 33 μm as seen in Figure 5-3a and d. DE-577 is composed of fragments between 1 and 5 μm. It is also composed of a majority of disks having diameters of 6 and 10 μm, and a few larger disks having diameters 14, 15, 16, and 17 μm, as shown in Figure 5-3b and e.). The alumina sample is composed of aggregates of twinned nanosheets of various sizes, as shown in Figure 5-3c and f.

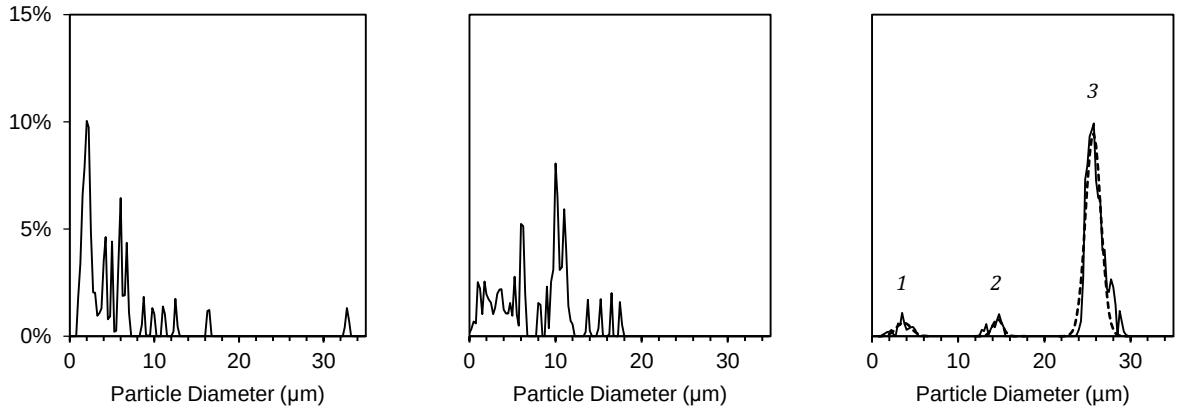

(a) (b) (c)

Figure 5-2: Particle Size Distributions of Diatomaceous Earth and Twinned Alumina Nanosheet Particles as Measured by Dynamic Particle Size Analysis
(a) DE-512; (b) DE-577; (c) TAN

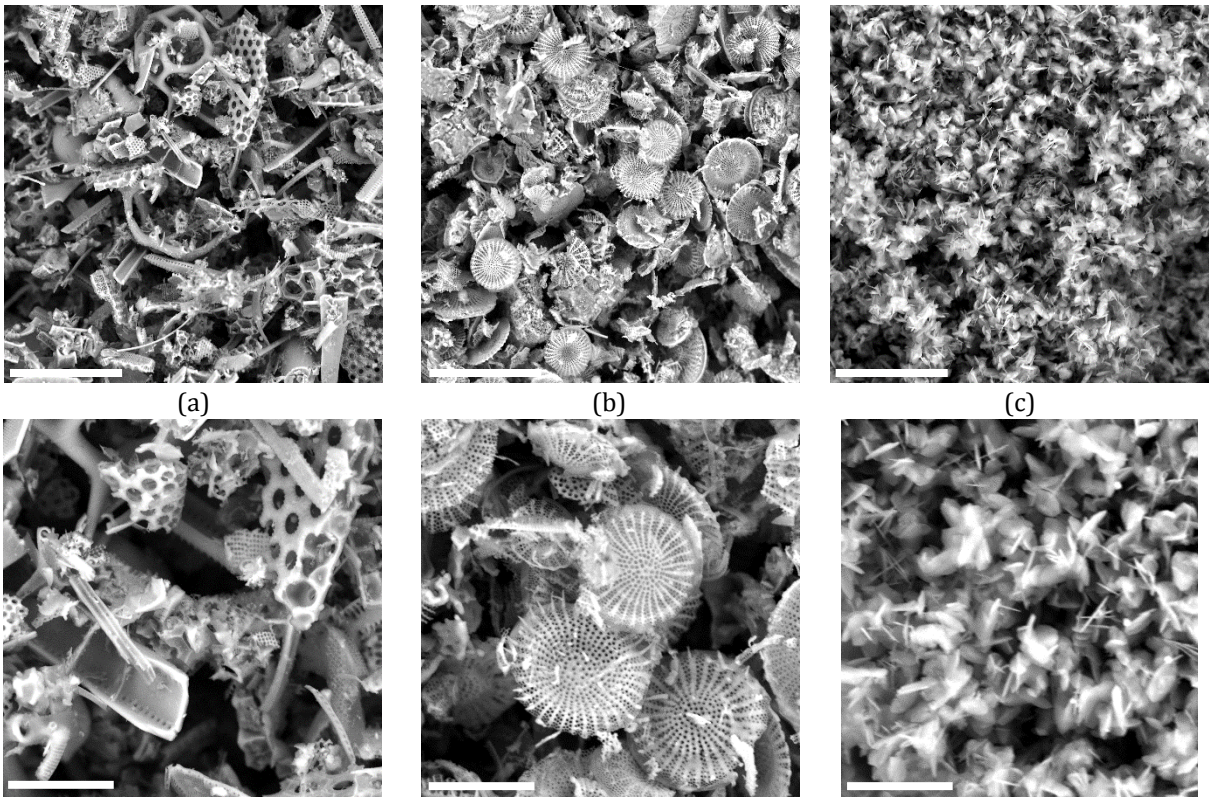

Figure 5-3: SEM Micrographs of Diatomaceous Earth and Twinned Alumina Nanosheet Particles Prior to Precoat Filtration
(a,d) DE-512; (b,e) DE-577; (c,f) TAN
(scale bars: 30 μm (a,b,c) and 10 μm (d,e,f))

The bulk density, porosity, and specific surface area of the DE and TAN particles settled in water are listed in Table 5-3. There is no significant difference in porosity between the two DE samples. The porosity determined in this work corresponds well with the porosity of a sample of diatomaceous earth from the literature: 64 $\pm$ 6% [325]. The bulk density of the fine-grade DE measured in this work was 19% lower than that of the medium-grade DE. The TAN have a 66% lower density and are 1.5 times greater porosity than the DE particles.

Table 5-3: Density and Porosity of the Diatomaceous Earth and Twinned Alumina Nanosheet Particles Settled in Water

Sample	Bulk Density (kg/m^3)	Porosity (%)
DE-512	259	59
DE-577	211	60
TAN	89	88

5.3.2 Characteristics of the Precoats

The thickness and hydraulic permeability of the DE and TAN precoats are listed in Table 5-4. These parameters were determined as discussed in Section 5.2.2. For equal masses of DE and TAN particles, the TAN precoat was 3.1 to 4.4 times thicker and 14 to 29 times more hydraulically permeable than the two DE precoats.

Table 5-4: Thickness and Hydraulic Permeability of the Diatomaceous Earth and Twinned Alumina Nanosheet Precoats

Sample	Predicted Thickness of Precoat (μm)	Measured Thickness of Precoat (μm)	Hydraulic Permeability (mD)
DE-512	408	277	25
DE-577	500	400	52
TAN	1179	1230	714
TAN-HV	1177	1260	561

5.3.3 Filtration Results

The flux decline profiles for each filter aid as a function of permeate volume are shown below in Figure 5-4. The DE-512, DE-577, and TAN runs were repeated in triplicate for a total of 9 runs. An additional run was performed to determine the volume of bentonite

solution required to reduce the flux through the TAN precoat from the initial value to the lowest value attained by the DE precoats. This run was designated TAN-HV (high-volume). A total of 10 runs were conducted.

All filter aid filtration runs began at fluxes in the range of 5900 – 11000 LMH. During the control run, no flux decline was observed, indicating that the bentonite particles passed through the substrate without any retention. The two DE filter aids followed similar flux decline profiles, ending at fluxes of 187 $\pm$ 7 LMH and 176 $\pm$ 8 LMH for DE-512 and DE-577, respectively. The flux through the TAN precoat at the end of the 3 L filtration run was 980 $\pm$ 28 LMH, which was 5.2 to 5.7 times higher than the final fluxes through the DE precoats.

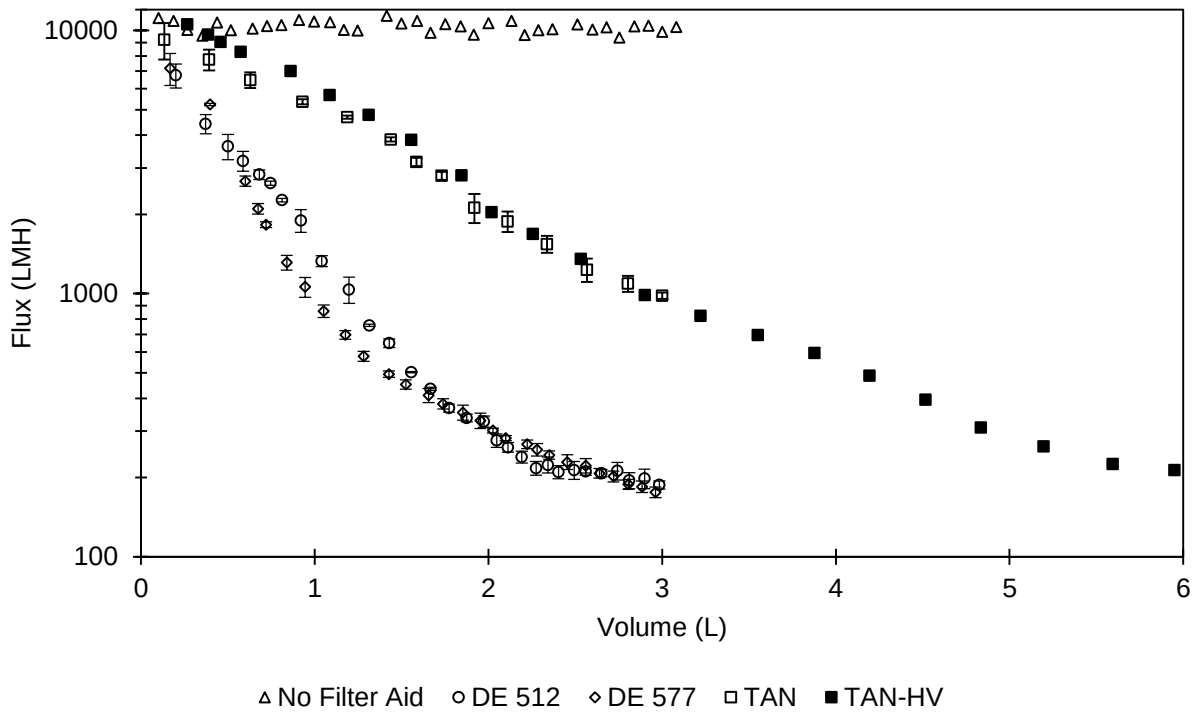

Figure 5-4: Semilog Plot of Flux Decline During Filtration of Bentonite Through Diatomaceous Earth and Twinned Alumina Nanosheet Precoats as a Function of Permeate Volume (error bars were determined based on 3 repeat experiments)

For the same mass of filter aid, it was found that the TAN precoat could treat twice the volume of bentonite solution before it reached the final flux of the DE precoats.

The filtration mechanisms for each filter aid can be determined by fitting the flux versus time data to Equation (5-8) using non-linear regression, as discussed in Section 5.2.2.4. Specifically, the value of the parameter *n* is indicative of the filtration model, as summarized in Table 5-2. These values, along with the sum of the squared residuals (SSR) and the volume at which this filtration model ceases to fit the data, are summarized in Table 5-5 to Table 5-8 below.

The results indicate that bentonite particle penetrated the open DE pores, then began to bridge across the blocked pores, and eventually form a cake. The transition to cake filtration was completed during the 3 L filtration run for the DE filter aids.

From the *n* values in Table 5-7 and Table 5-8, it can be seen that the bentonite particles are initially rejected from the TAN filter aids (intermediate blocking). After 3.6 $\pm$ 1.3 min, bentonite particles penetrate into the body of the deposited filter aid and become trapped inside (pore constriction). After a total of 14.8 $\pm$ 1.6 min, the fouling regime transitions back to intermediate blocking, showing that the TAN filter aid sufficiently rejects the bentonite particles. The TAN-HV (Table 5-8) follows the same trends as the TAN filtration run. After a total of 70.8 min, cake filtration becomes the dominating filtration mechanism.

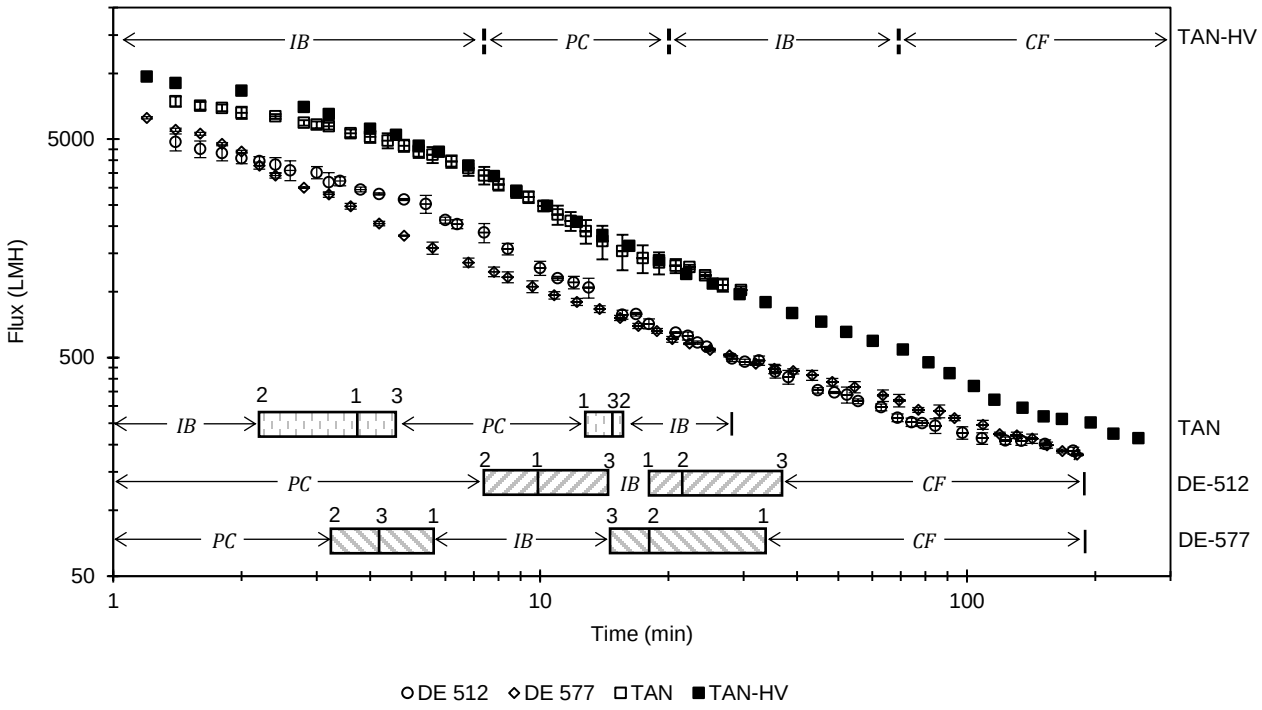

Figure 5-5: Log-Log Plot of Flux Versus Time For Filtration of Bentonite Through Diatomaceous Earth and Twinned Alumina Nanosheet Filter Aids (error bars were determined based on 3 repeat experiments). Transitions between fouling regimes are indicated on figure for each filter aid. Individual runs are numbered 1, 2, 3. Acronyms for fouling regimes: CF (cake filtration), IB (intermediate blocking), PC (pore constriction)

Table 5-5: Filtration Mechanisms for DE-512 Filter Aids. The value of the parameter *n* is indicative of the filtration model, as summarized in Table 5-2.

	Repeat 1				Repeat 2				Repeat 3				Average	
Region	*n*	*K*	*SSR*	*Time (min)*	*n*	*K*	*SSR*	*Time (min)*	*n*	*K*	*SSR*	*Time (min)*	*n*	*K*
1	-2.0000	0.0020	0.3253	10.0	-2.0000	0.0022	0.2118	7.6	-1.6750	0.0023	0.1527	11.6	-1.8915 ± 0.1879	0.0022 ± 0.0002
2	-1.0320	0.0064	0.0014	22.2	-1.0040	0.0070	0.0269	38.4	-0.9778	0.0061	0.0091	18.2	-1.0047 ± 0.0270	0.0065 ± 0.0005
3	-0.5851	0.0438	0.0075	-	-0.4911	0.1372	0.0148	-	-0.5550	0.0486	0.0511	-	-0.5438 ± 0.0480	0.0765 ± 0.0526

Table 5-6: Filtration Mechanisms for DE-577 Filter Aids. The value of the parameter *n* is indicative of the filtration model, as summarized in Table 5-2.

	Repeat 1				Repeat 2				Repeat 3				Average	
Region	*n*	*K*	*SSR*	*Time (min)*	*n*	*K*	*SSR*	*Time (min)*	*n*	*K*	*SSR*	*Time (min)*	*n*	*K*
1	-2.0000	0.0045	0.0156	5.8	-1.8907	0.0057	0.2228	3.2	-1.8777	0.0051	0.1191	4.2	-1.9215 ± 0.0681	0.0051 ± 0.0006
2	-0.6460	0.0064	0.0011	35.0	-0.7429	0.0309	0.0682	18.2	-0.7438	0.0277	0.0004	16.2	-0.7109 ± 0.05617	0.0217 ± 0.0013
3	-0.5705	0.0886	0.0021	-	-0.5275	0.1366	0.0198	-	-0.5592	0.0913	0.0020	-	-0.5524 ± 0.0223	0.1055 ± 0.0270

Table 5-7: Filtration Mechanisms for TAN Filter Aids. The value of the parameter *n* is indicative of the filtration model, as summarized in Table 5-2.

	Repeat 1				Repeat 2				Repeat 3				Average	
Region	*n*	*K*	*SSR*	*Time (min)*	*n*	*K*	*SSR*	*Time (min)*	*n*	*K*	*SSR*	*Time (min)*	*n*	*K*
1	-0.9667	0.0026	0.0125	3.8	-1.0670	0.0032	0.0031	2.2	-1.1549	0.0038	0.0015	4.8	-1.0629 ± 0.0941	0.0062 ± 0.0006
2	-2.0000	0.0012	0.0170	13.0	-2.0000	0.0016	0.0038	16.0	-2.0000	0.0019	0.0045	15.4	-2.0000 ± 0.0000	0.0016 ± 0.0003
3	-1.0060	0.0039	0.0021	-	-1.0226	0.0047	0.0071	-	-0.9679	0.0069	0.0097	-	-0.9987 ± 0.0280	0.0051 ± 0.0015

Table 5-8: Filtration Mechanisms for TAN-HV Filter Aid. The value of the parameter n is indicative of the filtration model, as summarized in Table 5-2.

Region	*n*	*K*	*SSR*	*Time (min)*
1	-1.1250	0.0040	0.0121	7.6
2	-2.0000	0.0118	0.0118	20.2
3	-0.6795	0.0186	0.0014	70.8
4	-0.5867	0.0499	0.0039	-

From an SEM image of the side view of the fouled DE filter aids in Figure 5-6a and b, cake build-up on the top surface of the precoat can be seen. In Figure 5-6c, no evidence of cake build-up on the top surface of the TAN precoat was observed. Therefore, the transition to cake filtration was not complete during the 3 L filtration run. However, for the 6 L TAN-HV run, evidence of cake layer formation on the surface of the precoat was observed, as seen in Figure 5-6d.

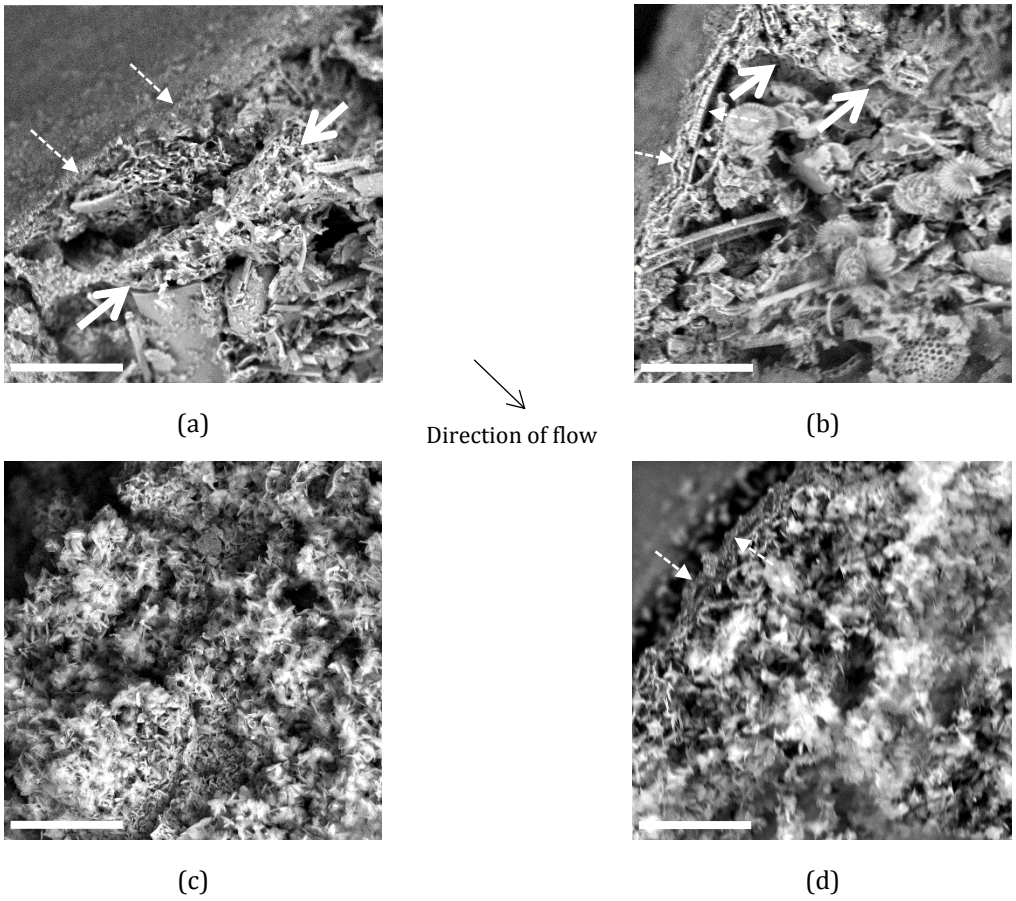

Figure 5-6: SEM Micrographs of Side-View of Precoat Filters After Filtration Run (a) DE-512; (b) DE-577; (c) TAN (no bentonite cake layer was observed); (d) TAN-HV (Scale Bar: 30 µm; direction of flow is perpendicular to bentonite cake layer; dashed white arrows indicates bentonite cake layer; solid, bold lined, arrows in (a) and (b) indicate particle compaction in the DE precoat layer)

Permeate turbidity as a function of flux and permeate volume through the precoats is shown in Figure 5-7 and Figure 5-8. The target level was set to the drinking water recommendations in Canada and internationally ($\leq$0.10 NTU) [309,329]. A combination of a high flux and low bentonite breakthrough was the desired outcome. For the TAN precoat, the target level was reached within the first 610 $\pm$ 130 mL of permeate volume at a flux of 7246 $\pm$ 649 LMH, as compared to 2380 $\pm$ 480 mL at 258 $\pm$ 84 LMH for the DE-512 precoat and 1180 $\pm$ 410 mL at 808 $\pm$ 387 LMH for the DE-577 precoat and as shown in Figure 5-7 and Figure 5-8. In addition to this, when the TAN-HV reached cake filtration, it had a

turbidity of 0.05 NTU versus 0.16 ± 0.03 NTU and 0.11 ± 0.04 NTU for DE-512 and DE-577, respectively. This indicates that the DE precoat had defects that permitted the passage of a considerable amount of bentonite particles via preferential channeling. Conversely, the TAN precoat deposited in a more uniform way, eliminating preferential channeling through the cake layer and the body of the precoat.

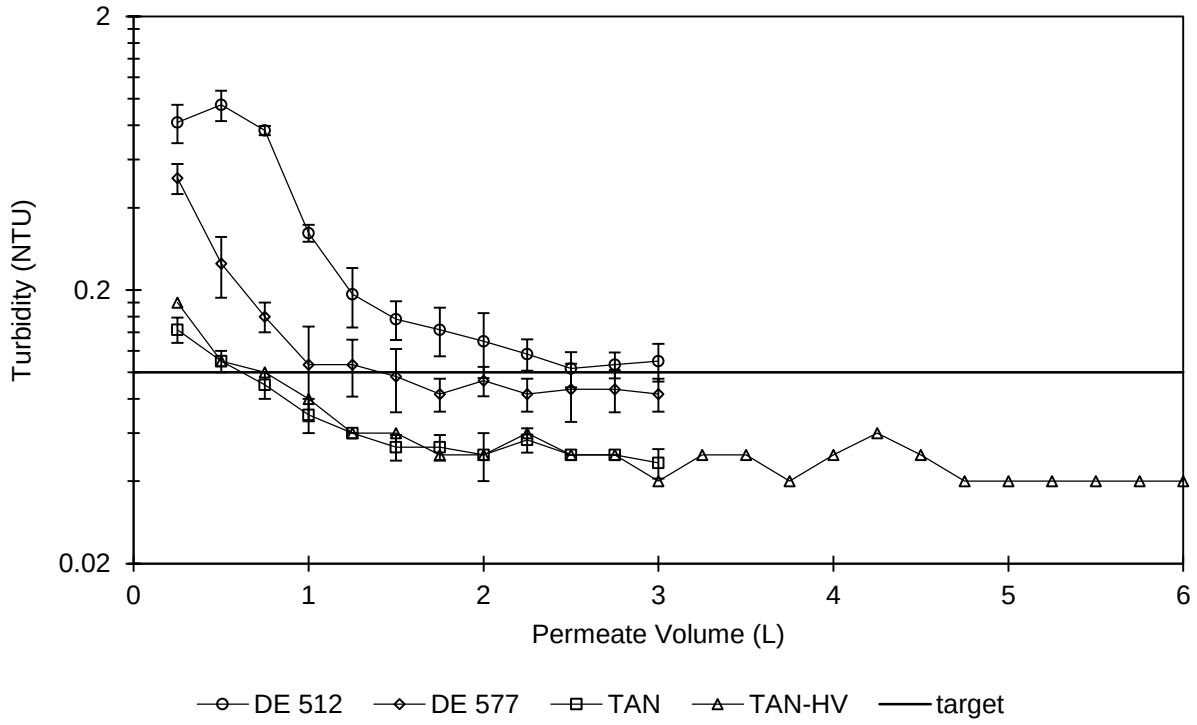

Figure 5-7: Semilog Plot of Permeate Turbidity Versus Flux For Filtration of Bentonite Through Diatomaceous Earth and Twinned Alumina Nanosheet Filter Aids (error bars were determined based on 3 repeat experiments)

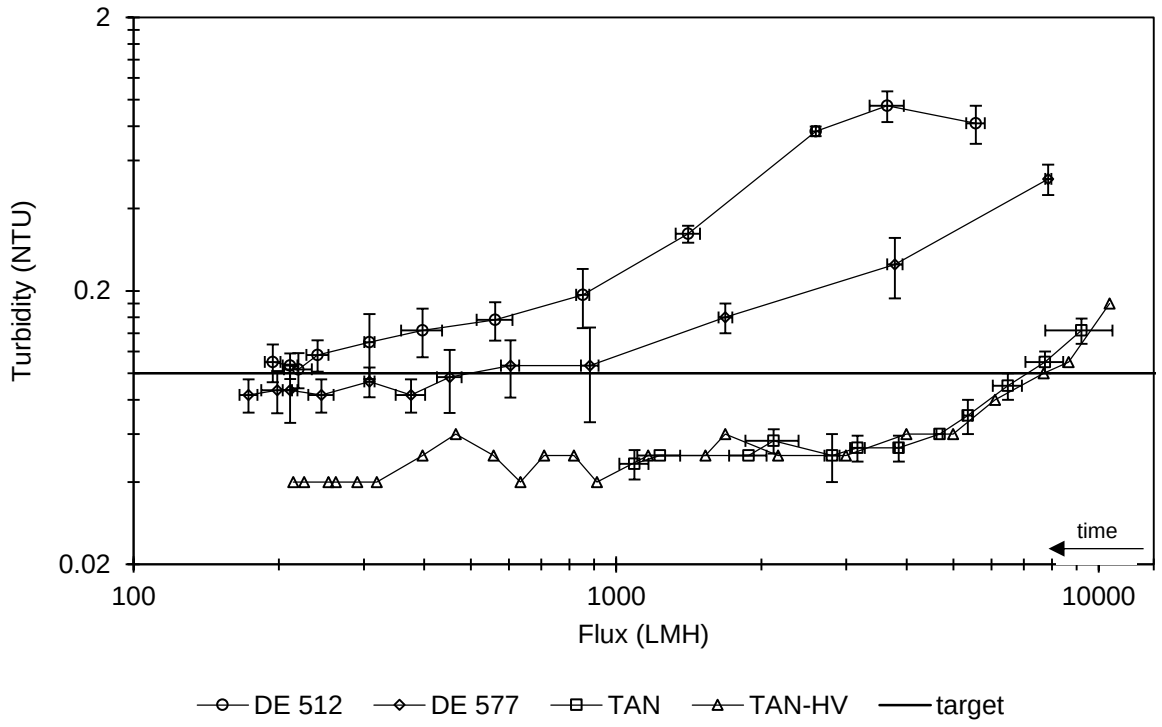

Figure 5-8: Log-Log Plot of Permeate Turbidity Versus Permeate Volume For Filtration of Bentonite Through Diatomaceous Earth and Twinned Alumina Nanosheet Filter Aids (error bars were determined based on 3 repeat experiments)

5.4 Discussion

Three particles (DE-512, DE-577, and TAN) were tested in this work to determine their filtration performance and flow properties during filtration with a bentonite solution. The DE-512 and 577 particles were polydisperse with average diameters of 5.0 and 7.6 μm, as shown in Figure 5-2a and b. The size distribution of the TAN particles could be modeled using three distinct Gaussian distributions, with the majority of particles having an average diameter of 25.7 μm as shown in Figure 5-2c. Based on the flux decline curves in Figure 5-4, the superior performance of the TAN precoat suggests that particles having a tri-modal particle size distribution with a majority of larger particles exhibit enhanced flow properties versus polydisperse particles with a smaller average particle diameter.

The predicted and measured thicknesses of the TAN precoat coincide well, indicating no significant compaction of the filter cake during deposition. The measured precoat thicknesses of the DE filter cakes were 36 to 39% lower than the predicted values, indicating that the filter cakes compacted during deposition. From this result, it is expected that the true porosities of the DE filter cakes are lower than those given for the settled particles in Table 5-3. Similarly, the hydraulic permeabilities of the DE samples, calculated using the bulk density measured from the settled particles, do not coincide with the actual hydraulic permeabilities of the filter cakes. In actuality, due to compaction, the hydraulic permeabilities of the DE filter cakes are expected to be lower than those given in Table 5-4. TANs retain their porosity and hydraulic permeability when subjected to flow. The TAN precoat had a similar measured and calculated precoat thickness, indicating that the particles stack similarly when they are settled under gravity or when they are settled under flow (Figure 5-9a). This explains why the TAN particles do not compact when subject to flow. Conversely, the DE particles stack differently when settled under gravity than when settled under flow, as shown in Figure 5-9b and c. The reduction in thickness of the DE precoats demonstrate the significant compaction of the DE particles during filtration. This is partly due to the weak particle interactions between the disk-like DE particles. This causes them to slip relative to each other, and form a denser, anisotropic filter cake.

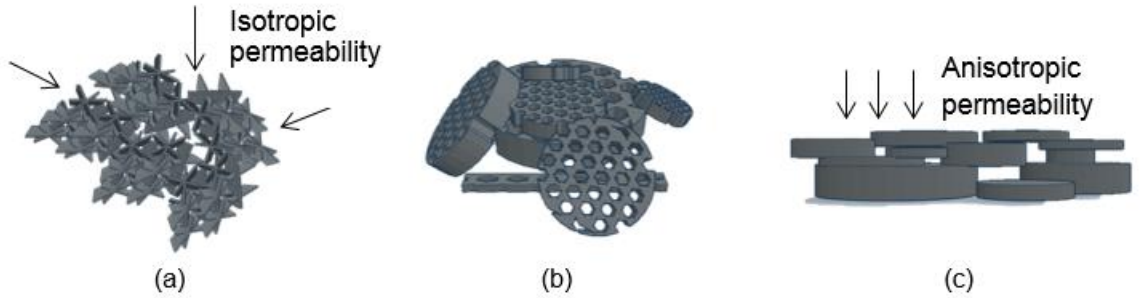

Figure 5-9: Stacking of (a) TAN Particles Settled Under Gravity or Precoat Formed Under Flow; (b) DE Particles Settled Under Gravity; (c) Precoat from DE Particles Formed Under Flow

Evidence of compaction can be seen in the SEM images of the side views of the fouled DE filter cakes in Figure 5-6a and b. Unlike the settled DE in Figure 5-3a and b, interparticle distance in the fouled DE precoat was reduced, indicating significant precoat layer compaction. In comparison, the TAN precoat layer did not exhibit significant compaction. The fouled TAN precoat in Figure 5-6c maintained the structural integrity of the settled TAN in Figure 5-3c. The ability of the TAN precoat to retain its porosity under flow demonstrates the importance of the twinned aggregate structure of the particles.

As shown in Figure 5-9a, the TAN particles are porous aggregates that are permeable to flow in all directions (isotropic permeability). This accounts for the higher hydraulic permeability of the TAN precoat. The DE particles are porous circular disks that are only permeable in one direction (anisotropic permeability) once deposited as a precoat (Figure 5-9c). Hydraulic permeability of the DE precoats is limited when compared to the TAN precoat. It was found that the permeability of the DE precoats were 13 to 29 times lower than that of the TAN precoat as shown in Table 5-4.

The inability of the DE precoats to retain their porosity also accounts for the higher flux decline during the filtration run in comparison to the TAN precoat. Low adhesion forces between the particles made them slip to more stable positions (Figure 5-9c) and produced a less permeable precoat layer [332,333]. Furthermore, a collapse of the porous structure of the DE precoats reduced the ability of the bentonite to pass through the precoat layer. Instead, the bentonite was retained on the top surface of the precoat as a cake layer. The transition towards cake filtration occurred within the first 23.1 $\pm$ 10.3 minutes and 26.3 $\pm$ 10.7 of filtration for DE-512 and DE-577, compared to 70.8 minutes for TAN, as shown in Table 5-5, Table 5-6, and Table 5-8.

In addition, the surface charges of the particles played a role in the filterability of the bentonite solution. The surface charges of the three materials, silica (DE), bentonite, and alumina (TAN), are plotted as a function of pH in Figure 5-10. The pH of the filtration solution was 6. At this pH, particles of bentonite and silica exhibit a repulsive force, further preventing penetration of the bentonite solution into the DE precoat. Therefore, a cake layer was formed. With a strong positive surface charge (0.08 C/m^2), the alumina particles can attract the negative bentonite particles (-0.11 C/m^2) into the TAN precoat layer.

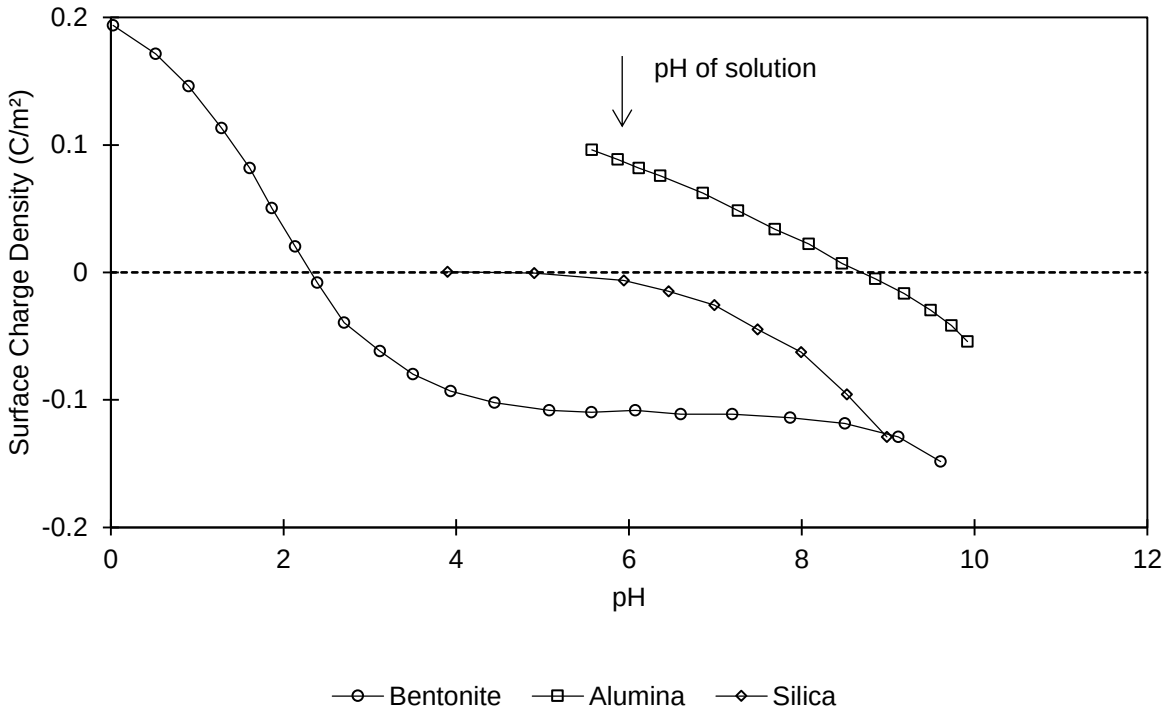

Figure 5-10: Surface Charge Densities of Bentonite [334], Alumina [335], and Silica [335] as a Function of pH

The final flux through the two DE precoats tended towards 180 LMH, indicating that the cake layer on top of the precoats became the determining factor in the flux values. For the TAN precoat, the cake layer did not dominate the filtration run until two times more bentonite solution had been passed through the precoat layer.

The hydraulic permeabilities of the TAN precoats produced in this work were compared, as a function of pore diameter, to common DE filter aids used in industry [336]. The pore diameter of the TAN aggregates was determined to be 0.2 μm [337]. As shown in Figure 5-11, there is a power-law relationship between DE particle pore diameter and the hydraulic permeability of the cake layer. Extrapolation of this relationship to an average pore diameter of 0.2 μm indicates that a precoat produced of TAN aggregates would be 275 to 350 times more hydraulically permeable than one produced of DE particles. This

illustrates the advantages of the thin nanosheet structure, isotropic permeability of the TAN aggregates, and the enhanced flow properties of the TAN particles, in direct contrast to the anisotropic permeability of DE particles.

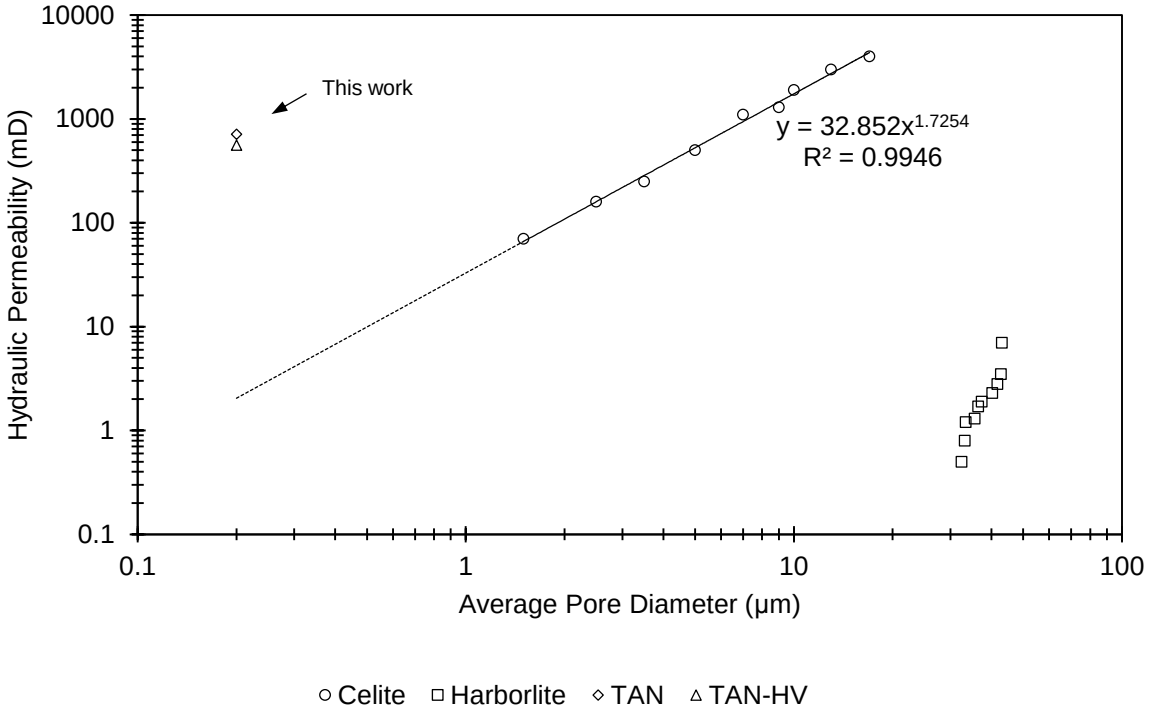

Figure 5-11: Pure Water Hydraulic Permeabilities of TAN, Celite (DE), and Harborlite (Perlite)
Data for Celite and Harborlite are from Hendricks, 2011.

5.5 Conclusions

Twinned alumina nanosheets (TAN) were manufactured by first synthesizing boehmite nanosheets in a 50 vol% ethanol-water solution, followed by calcination.

Using dynamic image analysis, it was determined that the two DE samples were polydisperse, while for the TAN, three distinct normally-distributed particle sizes could be identified.

The operating flux of the TAN precoat was the highest during the 3 L filtration run. The final flux through the TAN precoat was 980 $\pm$ 28 LMH, which was 5.2 to 5.7 times higher than the fluxes through the DE-512 and DE-577 precoats. It was found that the TAN precoat could treat twice the volume of bentonite solution before it reached the final flux of the DE precoats. The TAN precoat reached the required turbidity level of $\leq$0.10 NTU at a flux that was 28 times and 9 times higher than the fluxes obtained by the DE-512 and DE-577 precoats, respectively.

Filtration through the TAN precoat was dominated by intermediate blocking and pore constriction, whereas pore constriction, intermediate blocking and cake filtration were the main modes of filtration for the DE precoats. Based on a power-law relationship, at a pore diameter of 200 nm, precoats produced of TAN aggregates would be 275 to 350 times more hydraulically permeable than one produced of DE particles.

The target turbidity level of $\leq$0.10 NTU is difficult to reach using the conventional DE precoat.

The alumina filter aid reaches the target turbidity level of $\leq$0.10 NTU at high flux values. The enhanced flow properties of twinned alumina nanosheets bridges the gap between membrane ultrafiltration and conventional DE precoat filtration.

6 Lipase Immobilization on Twinned Alumina Nanosheets

K. Roebuck, X. X. Shi, and A.Y. Tremblay

Nanostructured supports offer high porosity and surface area for enzyme immobilization. As highly open and porous supports, they offer increased accessibility to substrates. In this work, two lipases (crude porcine pancreatic lipase and lipase from Candida rugosa) were immobilized on highly open and porous twinned alumina nanosheets. The nanosheets were synthesized in various ethanol-water mixtures, calcined, and functionalized by epoxysilanes having a hydrophobic spacer arm. It was determined that nanosheets produced in 50 vol% ethanol-water followed by a 24 h epoxysilane treatment process produced particles with the highest lipase immobilization and retention (16.7 $\pm$ 0.2 mg/g Al-50-24-cPPL and 39.7 $\pm$ 0.9 mg/g Al-50-24-CRL). Extended silylation of the supports beyond 24 h did not significantly increase enzyme immobilization.

For the most densely-packed supports, the specific activity of immobilized cPPL was 5.5 times higher than that of the free enzyme in solution. This was due to the ability of the lipase to preferentially bond to the hydrophobic functionalized alumina surface. The specific activity of immobilized CRL on these supports was 66% when compared to the free enzyme in solution. The loss of activity after immobilization was attributed to multipoint covalent attachment and attachment to the active site of the enzyme.

6.1 Introduction

In biocatalytic processes, enzymes facilitate reactions between organic compounds. Unlike traditional chemical catalysts, enzymes operate with high substrate specificity and

selectivity at moderate operating conditions [338]. For example, there are growing interests in the use of lipase in transesterification reactions and the production of biodiesel as opposed to methoxide catalysts. However, large-scale production of biocatalysts is cost-prohibitive when compared to traditional methods due to the high costs associated with the synthesis and purification of enzymes [339,340]. Furthermore, biodegradation and limited reusability are continuing problems in the widespread application of biocatalysts. A common solution is immobilization of the enzyme on or in an inert material, using strategies like adsorption, entrapment, or covalent bonding. Immobilized enzymes are more stable over a broader range of operating conditions than their free counterparts in solution [341,342]. Adsorption relies on weak, non-covalent bonds between the enzyme and inert surface. The process is inherently reversible, and consequently, enzymes frequently detach into the solvent medium [341,343,344]. Entrapment involves the formation of a permeable matrix around the protein structure of the enzyme, protecting it from denaturation. However, this strategy can lead to diffusional limitations and kinetic changes between the enzyme and substrate [341,345].

Immobilization via covalent bonding forms permanent, stable linkages between the enzyme molecules and the inert surface. This technique circumvents the main drawbacks of the aforementioned techniques. However, the inert material must be functionalized prior to enzyme attachment. Surface functionalization using silane coupling agents (SCAs) is one such method. Using alkoxysilanes, $RSiX_3$ (where R is a non-hydrolyzable organofunctional group and X is an alkoxy moiety), a durable siloxane network with outward-facing R groups can be formed on an inorganic surface by attachment to hydroxyl groups through

hydrolysis, condensation, and polymerization reactions [346,347]. Careful selection of the R group will impart desirable properties to the functionalized material.

Epoxysilanes are particularly useful in enzyme immobilization. The epoxy groups are highly reactive towards the amine, thiol, and hydroxyl groups on enzyme molecules, and form stable covalent linkages to these functional groups [348]. However, preservation of the epoxy group during silane deposition can be difficult. Premature cleavage of the epoxy ring results in the formation of less reactive functional groups on the outer surface of the interconnected siloxane network.

It is well-established that acid or base catalysts are used to catalyze epoxy ring opening [349]. The use of certain reagents can also lead to epoxy ring opening. Derouet et al. studied the effects of alcohol concentration and temperature on ring opening of epoxidized 1,4-polyisoprene using cerium aluminum nitrate as a catalyst. It was determined that a combination of high alcohol concentration, moderate temperature (>50°C), and the presence of a catalyst was necessary for substantial ring opening [350]. Surface modification of inorganic substrates with epoxysilanes in the presence of high temperature also results in premature cleavage of the epoxy ring. Chehimi et al. treated hydrated α-alumina with aqueous γ-glycidoxypropyltrimethoxysilane (GPS) and dried the samples at temperatures ranging from 25°C to 120°C. Above 80°C, degradation of the epoxy ring and the formation of alcohol moieties was observed [351]. Similarly, Prapainainar et al. treated protonated sodium mordenite with GPS in dichloromethane at room temperature, followed by drying at 100°C for 24 h. Based on their FTIR analysis, the epoxy group was not present on the clay surface after silane treatment [352]. This is due to their extensive oven drying process, which was used to facilitate curing of the siloxane network to form Si-O-Si bonds

[353]. Overall, the avoidance of reaction conditions that lead to premature epoxy ring opening is paramount when working with epoxysilanes.

Immobilized enzymes are of great interest due to their reusability and increased stability. Immobilization also allows for enzyme recovery by filtration. Meng et al. reported on the long-term stability of fatty acid ethyl ester production by immobilized lipase from *Yarrowia lipolytica*. Twenty-five batches of product were generated, with intermittent enzyme filtration and washing, before a rapid decline in esterification degree was noted [354]. A heterogeneous enzyme-support system can also be used in packed bed reactors (PBRs). In a study on the continuous production of ketoprofen catalyzed by immobilized lipase from *Candida rugosa* in a PBR, Xi and Xu reported on the high enantiomeric selectivity (>99%) for the desired *(S)* enantiomer achieved over the 60 h experimental run [355]. Kittikun et al. studied the continuous production of monoacylglycerols (MAGs) from palm olein catalyzed by immobilized lipase from *Pseudomonas sp.* They were able to achieve a yield of 18.6 g MAG/day under optimized conditions [356].

The choice of immobilization support is very important. The use of hydrophilic supports can lead to a decrease in lipase activity relative to the free enzyme, while immobilization on hydrophobic supports often leads to an increase in lipase activity. Paula et al. immobilized PPL on a glutaraldehyde-activated polysiloxane-polyvinyl alcohol (POS-PVA) matrix, a hydrophilic-hydrophilic activator-support combination. This resulted in a 77% reduction in enzyme activity after immobilization [357]. Similarly, Bagi and Simon reported 88% and 98% reductions in lipolytic activities after PPL immobilization onto hydrophilic supports Akrilex C-100 and Silochrome, respectively [358]. In a study exploring the effects of carrier hydrophobicity on lipolytic activity, Kéry et al. concluded that the most hydrophobic

support produced immobilized lipase with the highest relative activity [359]. Bai et al. reported an 18% increase in lipolytic activity relative to the free enzyme after modification of silica nanoparticles using hydrophobic vinyltriethoxysilane (VTES) [360]. Similarly, Lee et al. reported a 55% increase in lipolytic activity after modification of magnetite nanoparticles using sodium dodecyl sulfate (SDS) due to the hydrophobic nature of the modified particles [361].

In this work, twinned alumina nanosheets that aggregate to form a densely-packed, highly porous network with great internal accessibility were surface functionalized with an epoxysilane molecule to facilitate the attachment of lipase to the alumina particles. To our knowledge, this is the first time that an enzyme is immobilized on alumina nanosheets. The silylation was performed in 1-propanol at a moderate temperature in the absence of chemical catalyst to prevent premature epoxy ring opening. The effects of ethanol concentration during the alumina synthesis, as well as silylation time were tested to determine their effects on lipase immobilization and activity. Two lipases were compared in this study: crude porcine pancreatic lipase (cPPL) and lipase from *Candida rugosa* (CRL).

6.2 Experimental

6.2.1 Materials

Cetyl trimethylammonium bromide (CTAB), sodium hydroxide pellets, and anhydrous ethanol, were purchased from Sigma-Aldrich (Canada). Aluminum chloride hexahydrate (99%, nitrogen flushed), extra pure olive oil (74.5% oleic acid based on the certificate of analysis), ethyl oleate (>98% pure, mixture of homologeous fatty acid esters, 86% from oleic acid based on the certificate of analysis), and gum arabic powder were purchased from Acros Organics. Phosphate buffer solution (potassium phosphate monobasic, sodium

hydroxide, 0.05 M, pH 7.00 at 25°C), 1-propanol, Coomassie Brilliant Blue G-250 assay reagent, bovine serum albumin (BSA) standards, and cellulose filter paper (Whatman #1), were purchased from Fisher Scientific (Canada). 2-(3,4-Epoxycyclohexyl)ethyltriethoxysilane) (ETES, Figure 6-1) was purchased from Gelest, Inc. (Pennsylvania). cPPL was purchased from MP Biomedicals (California), and CRL was purchased from Sigma-Aldrich (Canada). All materials were used as purchased.

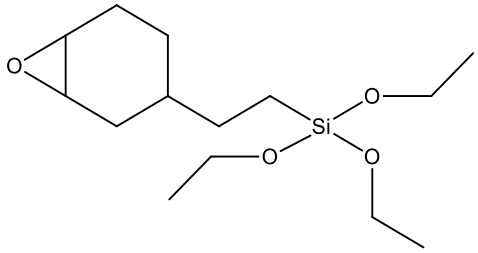

Figure 6-1: Silane coupling agent (ETES) used in this work

6.2.2 Methods

6.2.2.1 Preparation of Immobilization Supports

Boehmite nanosheets were synthesized by metal salt hydrolysis in various ethanol-water solutions as detailed in previous works [331,362]. The boehmite nanosheets were calcined for 4 h at 600°C to produce twinned alumina nanosheets. Three ethanol contents (0, 25, and 50 vol%) were selected to provide a broad range of nanosheet aggregate porosity as detailed in our previous work [362].

A 20:80 v/v% solution of ETES in 1-propanol was formed by the addition of 8 mL of ETES to 32 mL of 1-propanol. 400 mg of twinned alumina nanosheets were added to the solution and stirred briefly to suspend the particles. The nanosheets were silylated in a 60°C water bath for 4, 24, or 96 h to test the effects of different silylation times on the total uptake of lipase during enzyme immobilization. After silylation, the nanosheets were filtered through

a Büchner funnel with Whatman filter paper and washed several times with 1-propanol to remove any unbound ETES molecules.

6.2.2.2 Enzyme Immobilization

Immobilization of cPPL and CRL was performed as follows: 500 mg of lipase was dissolved in 10.00 mL of buffer and homogenized for 1 min using a PowerGen 125 homogenizer at setting #6 (Fisher Scientific, Canada). The solution was filtered through a Büchner funnel with Whatman filter paper. 200 mg of silylated nanosheets were added to the lipase solution. The resulting solution was incubated in an INFORS HT Multitron Pro incubator at 4°C at 150 rpm for 24 h. 100 µL samples were taken in triplicate for protein assay at 0, 1, 2, 4 and 24 h during the lipase immobilization. After immobilization, the resulting particles were filtered through a Whatman #1 filter paper, washed several times with phosphate buffer solution (PBS), and dried. The above procedure was conducted for nanosheets that were not treated with ETES.

Figure 6-2 details the naming convention used in this work for the particles to differentiate between different samples based on distinct preparation methods.

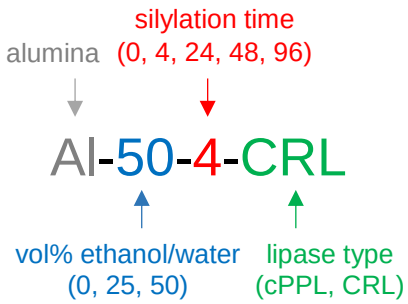

Figure 6-2: Naming convention used for modified twinned alumina nanosheet samples synthesized in this work

6.2.2.3 Characterization of Immobilization Supports

As-synthesized twinned alumina nanosheets were characterized via ATR-FTIR analysis (Cary 630 FTIR Spectrometer, Agilent Technologies, Canada) before and after silylation in the infrared region from 4000 to 650 cm^{-1}. This technique was used to verify the binding of ETES to the surface of the twinned alumina nanosheets.

The twinned alumina nanosheets were also characterized by SEM before and after enzyme immobilization to verify that the integrity of the internal porous network formed by the nanosheets remained intact after the silylation and immobilization procedures. SEM imaging was performed using a Phenom Pro Desktop SEM (Nanoscience Instruments, Virginia) at accelerating voltages of 5 and 10 kV.

6.2.2.4 Protein Assay

Protein concentration in enzyme solutions prior and after attachment was determined using the Bradford method [363] with Coomassie Brilliant Blue G-250 as the dye reagent. Measurements were performed in triplicate using UV-Vis spectroscopy (HACH DR 6000, Canada) at an absorbance of λ = 595 nm. A calibration curve for protein concentration was constructed using BSA as a standard.

6.2.2.5 Determination of Enzyme Activity

Enzyme activity was quantified using a modified IOC standard method [364–366]. An olive oil emulsion was prepared by homogenizing olive oil and a 7 wt/wt% gum arabic/PBS solution to form a solution of 25:75 vol/vol% olive oil:emulsifier.

Free lipase activity was tested using a lipase solution of known protein concentration. The solution was formed using a 5:2:1 mixture of olive oil emulsion:PBS:lipase by volume, and incubated at 37°C in an orbital shaker at 120 rpm for 30 minutes. The reaction was stopped

with a 50:50 vol/vol% mixture of acetone/ethanol. The resulting solution was titrated to the phenolphthalein endpoint with 0.05 M NaOH.

Immobilized lipase activity was tested using the particles synthesized in Section 6.2.2.1. 50 mg of these particles were added to a 5:2 volume ratio reaction mixture of olive oil emulsion:PBS solution. The mixture was incubated at 37°C under stirring at 120 rpm for 30 minutes. The reaction was stopped with a 50:50 vol/vol% mixture of acetone/ethanol. The resulting solution was titrated to the phenolphthalein endpoint with 0.05 M NaOH.

One unit of lipase activity was defined as the amount of enzyme which liberated 1 μmol of fatty acids per minute.

6.2.2.6 Statistical Analyses

Standard statistical procedures were used, including mean averaging and standard deviation for triplicate results. A Student's *t*-test was used to test for significance. A *p*-value < 0.05 was considered statistically significant. The mean and variance of continuous data was estimated from its median, range, and sample size, as detailed by Hozo et al. [367].

6.3 Results

6.3.1 Characterization of Immobilization Supports

The FTIR spectra in Figure 6-3 show the effects of ethanol concentration and silylation time on the amount of SCA deposited on nanosheet surface. In the absence of SCA, the samples exhibit a characteristic broad Al-O peak from 350-1000 cm^{-1} [157,368]. The strong double peaks between 1000-1200 cm^{-1} are indicative of the presence of Si-O-Si and Al-O-Si bonds formed during the deposition of the SCA [369]. The two peaks appear close together due to the similar atomic masses of Al and Si. The lower peak of the pair can be assigned to Si-O-Si, as Si atoms cause higher wavenumber shifts in FTIR spectra than Al atoms [370]. Epoxy groups show characteristic peaks in the region 736-864 and 863-950 cm^{-1} [371].

Specifically, Mayhan et al. assigned FTIR bands at 730, 835, and 880 cm^{-1} to the epoxy groups of 2-(3,4-epoxycyclohexyl)methyltriethoxysilane, a SCA that differs only in its leaving groups from the one used in this work [372]. The leaving groups are not present in the siloxane network that is formed when the SCA bonds to the inert surface. Therefore, the FTIR epoxy peaks assigned by Mayhan et al. can also be assigned to ETES.

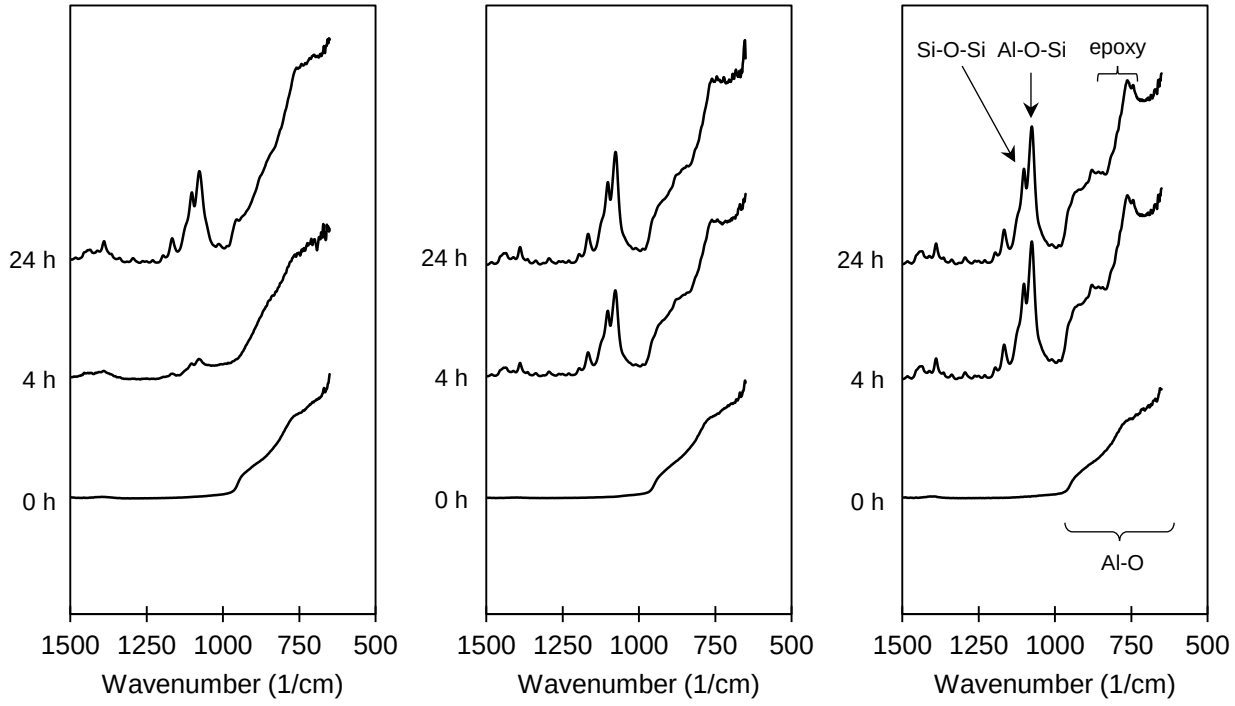

Figure 6-3: FTIR spectra (650-1500 cm^{-1}) of alumina nanosheets (a) Al-0; (b) Al-25; (c) Al-50. Silylation time is indicated on the ordinate axis. Important peaks are labelled on (c) and described in the text.

The SEM images in Figure 6-4 show the effects of silylation and enzyme immobilization on the morphology of the macroporous structure of the Al-50 twinned alumina nanosheets. As seen in Figure 6-4a, the nanosheets form a densely-packed but highly porous network. In

Figure 6-4b, it can be seen that this densely-packed but highly porous network is maintained after silylation and enzyme attachment.

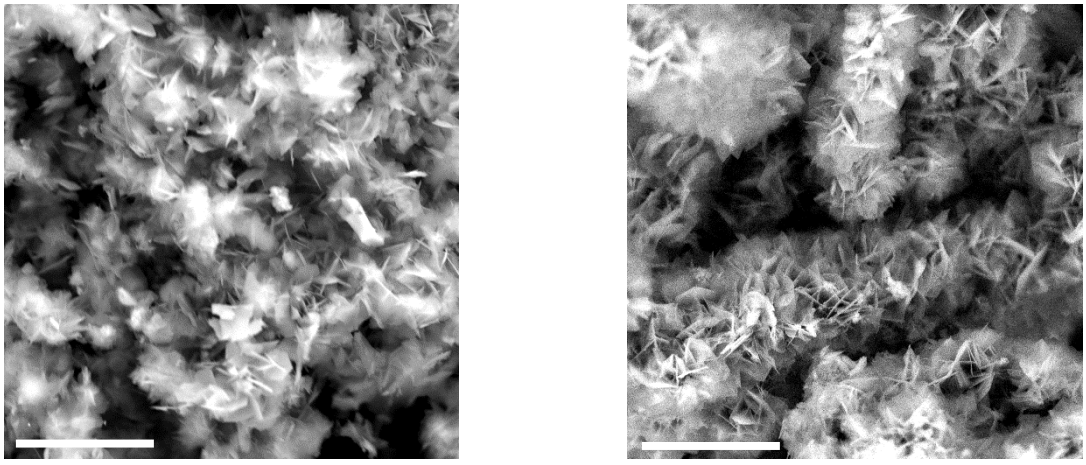

(a) (b)

Figure 6-4: SEM images of Al-50 nanosheets before and after silylation and enzyme immobilization with CRL (a) Al-50 nanosheets; (b) Al-50-24-CRL nanosheets Scale bar: 10 μm.

6.3.2 Lipase Immobilization

Table 6-1 shows the effects of ethanol concentration and silylation time on cPPL immobilization. Silylation time and ethanol concentration both increased total lipase uptake during cPPL immobilization. The relative increases in immobilization were greatest at low silylation times. An increase in ethanol concentration from 0 to 50 vol% in the synthesis mixture with no silylation led to a 179% increase in lipase immobilization, while the same increase in ethanol concentration with 24 h of silylation led to a 14% increase in lipase immobilization. The greatest immobilization was observed in 50 vol% ethanol at 0, 4, and 24 h of silylation time. To test the effects of longer silylation times on enzyme immobilization, lipase was immobilized on twinned alumina nanosheets synthesized in 50

vol% ethanol after a 96 h silylation treatment. However, no significant increase in immobilization was observed between the Al-50-24-cPPL and Al-50-96-cPPL (two-sided *t*-test, *p*-value > 0.50). The maximum uptake was 16.9 ± 0.5 mg/g Al-50-96-cPPL.

Table 6-1: cPPL immobilization on twinned alumina nanosheets as a function of silylation time and ethanol concentration, quantified in milligrams of lipase immobilized per gram of support

Silylation Time (h)	**Ethanol Concentration in Synthesis Mixture (vol%)**	**Immobilized Lipase (mg/g support)***
0	0	2.4 ± 0.7
	25	5.4 ± 0.6
	50	6.7 ± 0.5
4	0	10.1 ± 1.2
	25	11.0 ± 1.8
	50	14.5 ± 0.2
24	0	14.7 ± 0.8
	25	13.8 ± 2.0
	50	16.7 ± 0.2
96	50	16.9 ± 0.5

*Results are from measurements done in triplicate, as described in Methods.

After incubating for 24 h, each sample was filtered and washed with buffer solution. The wash solution was tested for protein concentration to determine the quantity of lipase that remained attached to the supports. The effect of silylation on enzyme attachment is shown in Figure 6-5. It was determined that silylation (4 h or 24 h) was necessary to securely

bond the cPPL to the twinned alumina nanosheets (Figure 6-5). Without silylation, 36 to 80% of the cPPL was washed away with the buffer solution.

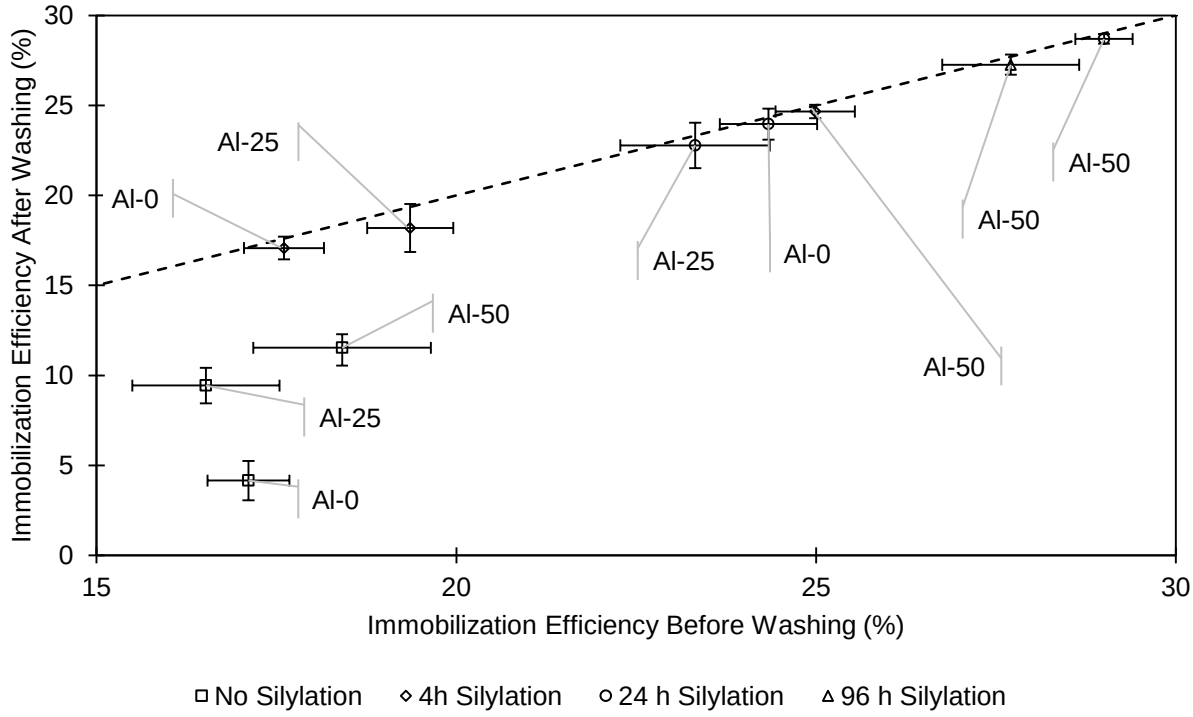

Figure 6-5: cPPL immobilization efficiency on twinned alumina nanosheets as a function of washing. Immobilization efficiency = amount of cPPL loaded / amount of cPPL initially introduced. Error bars are from measurements conducted in triplicate, as described in Methods.

From the studies on cPPL immobilization, it was determined that a 24 h silylation process produced particles with optimal lipase immobilization and retention after washing. Thus, for subsequent CRL immobilization studies, only the Al-(0,25,50)-24-CRL samples were tested.

From Table 6-2, it is evident that CRL binds more effectively to the twinned alumina nanosheets than cPPL under equivalent experimental conditions. The highest immobilization uptake of CRL found in this work was 39.7 $\pm$ 0.9 mg/g Al-50-24-CRL,

compared to the highest immobilization uptake for cPPL of 16.7 mg/g Al-50-24-cPPL. Washing of the silylated CRL samples resulted in a loss of 0.3 to 10.7% of the total immobilized CRL to the wash solution (Figure 6-6).

Table 6-2: CRL immobilization on twinned alumina nanosheets as a function of ethanol concentration, quantified in milligrams of lipase immobilized per gram of support

Silylation Time (h)	**Ethanol Concentration in Synthesis Mixture (%)**	**Immobilized Lipase (mg/g support)***
	0	35.6 ± 2.2
24	25	37.8 ± 0.7
	50	39.7 ± 0.9

*Results are from measurements done in triplicate, as described in Methods.

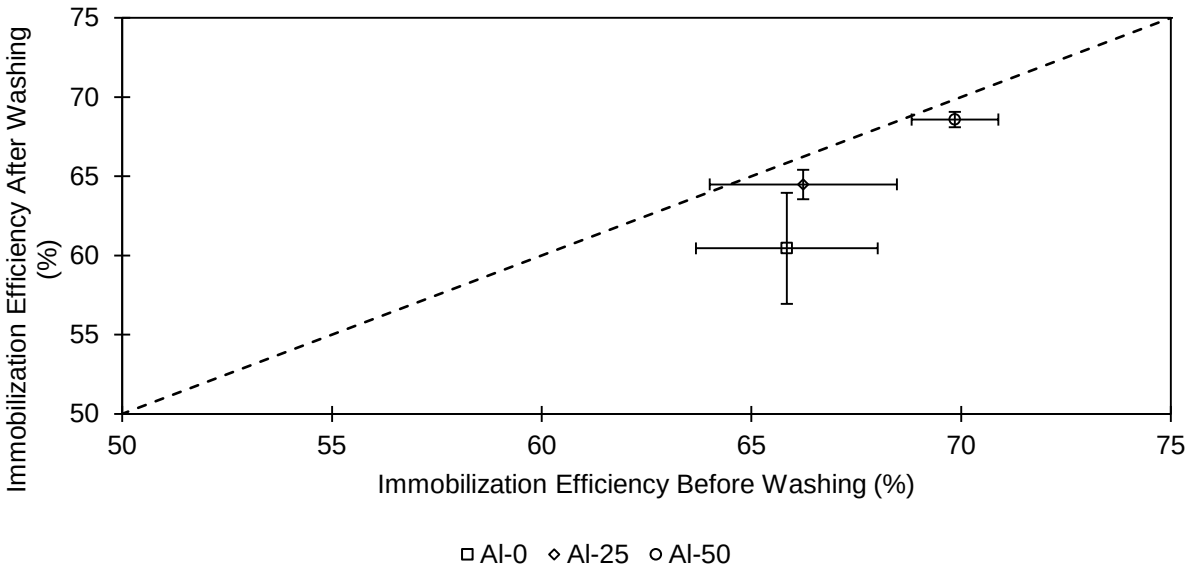

Figure 6-6: Effect of washing on immobilization efficiency during the immobilization of CRL on twinned alumina nanosheets. Immobilization efficiency = amount of CRL loaded / amount of CRL initially introduced. Results are from measurements done in triplicate, as described in Methods.

6.3.3 Activity of Free and Immobilized Lipase

The specific activity of free and immobilized lipase was quantified by olive oil titration. Free cPPL had a specific activity of 16.4 U/mg cPPL. Table 6-3 shows the effects of ethanol concentration and silylation time on immobilized cPPL activity. Immobilization of cPPL increased specific activity relative to the free enzyme in solution. In addition, silylation time and ethanol concentration both caused an increase in specific lipase activity. The maximum specific activity was 93.2 U/mg (sample Al-50-96-cPPL), 5.5 times higher than the specific activity of free cPPL in solution.

Table 6-3: Specific activity of immobilized cPPL on twinned alumina nanosheets as a function of silylation time and ethanol concentration, quantified in units per milligram of protein.

Silylation Time (h)	**Ethanol Concentration in Synthesis Mixture (vol%)**	**Specific Activity (U/mg)**
0	0	20.1
	25	27.3
	50	31.4
4	0	30.4
	25	48.7
	50	81.1
24	0	31.4
	25	81.4
	50	90.7
96	50	93.2

A similar study was carried out on free and immobilized CRL (Table 6-4). Free CRL had a specific activity of 138.7 U/mg CRL, 8.4 times higher than free cPPL. Immobilization of CRL reduced specific activity relative to the free enzyme in solution by up to 47%. However, an increase in ethanol content increased enzyme activity for immobilized CRL. The maximum specific activity for the immobilized samples was 90.9 U/mg CRL (sample Al-50-24-CRL), comparable to the highest specific activity achieved by cPPL immobilization.

Table 6-4: Specific Activity of Free and Immobilized *C. rugosa* Samples

Sample	**Specific Activity (U/mg)**
Free	138.7
Al-0-24-CRL	64.8
Al-25-24-CRL	76.4
Al-50-24-CRL	90.9

6.4 Discussion

Highly porous and densely-packed twinned alumina nanosheets were functionalized with the epoxysilane ETES to promote lipase attachment during the subsequent immobilization procedure. The functionalization and immobilization mechanisms are reported in Figure 6-7. In the literature, it has been demonstrated that lipases bond covalently by surface amino groups to linker molecules during immobilization to functionalized supports [373–375].

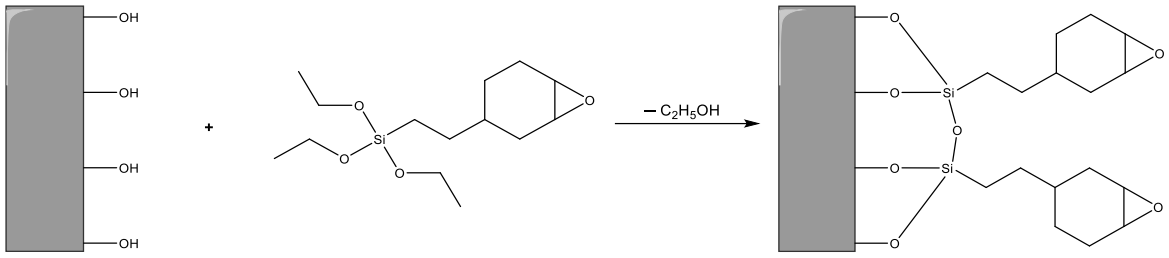

(a)

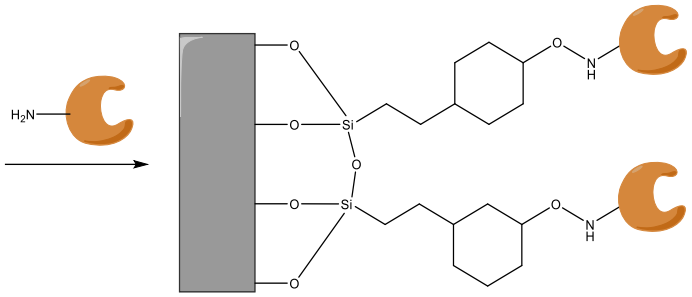

(b)

Figure 6-7: Mechanisms for (a) functionalization of twinned alumina nanosheets with ETES and (b) subsequent lipase immobilization on the functionalized twinned alumina nanosheets

The nanosheets were silylated in 1-propanol in the absence of acid/base catalysts at moderate temperatures to prevent epoxy ring opening during the hydrolysis, condensation, and polymerization reactions of the SCA to the nanosheet surface. The presence of FTIR peaks at 730, 835, and 880 cm^{-1} in Figure 6-3 confirm that the epoxy ring remained intact during silane deposition.

In our work, the alumina nanosheet aggregates were silylated at 60°C for either 4 h, 24 h, or 96 h, and dried under ambient conditions overnight in a fumehood. The presence of the

characteristic Al-O-Si and Si-O-Si peaks in Figure 6-3 show that the silylation treatment and subsequent drying process were adequate for successful silane deposition.

Extending the silylation treatment time from 4 to 24 h increased the total peak heights of the Al-O-Si and Si-O-Si peaks (Figure 6-3), indicating that the 24 h treatment time created robust siloxane networks. The same trend was observed when the amount of ethanol in the nanosheet synthesis mixture was increased from 0 vol% to 50 vol%.

Ratios of the Al-O-Si / Si-O-Si peak heights were calculated (Table 6-5) to assess the effects of silylation time and type of support on the formation of the siloxane network. The increase in this ratio indicates the formation of more direct bonds between the alumina nanosheet surface and silane molecules and less cross-linking in the siloxane network.

Table 6-5: Relative Height of Al-O-Si / Si-O-Si Peaks from FTIR Spectra of Silylated Alumina Nanosheets (Figure 6-3)

Sample	**Silylation Time (h)**	
	4	**24**
Al-0	1.20	1.26
Al-25	1.27	1.34
Al-50	1.38	1.42

During synthesis, the twinned alumina nanosheets agglomerated to form highly porous spherical-like aggregates. In our previous work, we measured the particle size distributions of the twinned alumina nanosheet aggregates at each synthesis condition using dynamic particle size analysis [337]. With no ethanol in the synthesis mixture, the aggregates

exhibited a unimodal size distribution (d_{50} = 7.5 μm). In 25 vol% ethanol-water, the aggregates exhibited a bimodal size distribution ($d_{50,1}$ = 2.5 μm, $d_{50,2}$ = 10.5 μm). In 50 vol% ethanol-water, the aggregates exhibited a trimodal size distribution ($d_{50,1}$ = 4.0 μm, $d_{50,2}$ = 15.0 μm, $d_{50,3}$ = 27.5 μm). We measured the porosities and macroscopic surface areas of the nanosheets and each synthesis condition [337]. We determined that the Al-0, Al-25, and Al-50 had porosities of 79, 85, and 88%, and macroscopic surface areas of 2.89, 5.31, and 5.70 m^2/g, respectively.

An increase in ethanol concentration was found to increase the porosity and surface area of the internal network formed by the twinned alumina nanosheets, providing greater access to the internal porous network of the twinned alumina nanosheet structure. With greater internal accessibility, silane molecules can penetrate deeper into the porous network formed by the nanosheets and bond directly with a greater number of aluminum atoms, resulting in a higher Al-O-Si/Si-O-Si ratio. The higher ratios represent a preference for silane molecules to bond to surface aluminum atoms instead of cross-link to adjacent silane molecules in the siloxane network. This preference is driven by the need to minimize alumina surface energy [376]. In a study on frictional properties of surface coatings, Kośla et al. determined that silylation reduced alumina surface energy by 42 to 71% [376]. In this work, silane cross-linking was not observed as the modified supports were not heat treated [377].

Two different lipases were immobilized on the silylated supports to assess the effect of lipase type on immobilization efficiency and activity. cPPL was successfully immobilized on the silylated nanosheets, with a maximum uptake of 16.9 $\pm$ 0.5 mg cPPL/g Al-50-96-cPPL (Table 6-1). However, immobilization uptake was not significantly higher when compared

to the lipase immobilization achieved using Al-50-24, a support silylated for 72 hours less than Al-50-96. Furthermore, extending the silylation treatment from 24 h to 96 h only led to a 2.8% increase in immobilized enzyme activity. Therefore, the use of extended silylation times beyond 24 h is not justified, as significant increases in immobilization uptake and immobilized enzyme activity were not seen. As such, we recommend limiting the silylation time to 24 h.

In general, an increase in either silylation time (up to a maximum of 24 h) or ethanol concentration increased total cPPL immobilization. The supports were not cured after silylation to avoid premature epoxy ring opening. From Table 6-5, it was shown that an increase in silylation time increases the relative amount of Al-O-Si bonds on the nanosheet surface. With more silane molecules covalently bonded to the nanosheet surface, a greater amount of lipase could be immobilized. Sufficient surface saturation with silane molecules occurs after a 24 h silylation treatment, as suggested by the insignificant increase in enzyme immobilization between Al-50-24-cPPL and Al-50-96-cPPL (Table 6-1). The results show that the Al-50 nanoparticles have a maximum capacity for lipase of 16.9 $\pm$ 0.5 mg cPPL/g support, with a specific activity of 93.2 U/mg.

cPPL immobilization efficiency was compared before and after washing with buffer solution (Figure 6-5). The results confirmed that silylation was necessary to permanently bond the protein molecules to the nanosheet surface. Without silylation, 36 to 80% of the cPPL was washed away with the buffer solution. In the absence of silylation, an adsorption/desorption mechanism is employed by cPPL to temporarily bond to the nanosheet surface. Lipase readily adsorbs to hydrophobic surfaces and remains adsorbed unless exposed to extreme temperatures or pH [361,378]; the protein does not bond

effectively to hydrophilic surfaces [379]. Alumina is hydrophilic at pH 7.0, necessitating the use of alternative immobilization strategies. With 4, 24 or 96 h of silylation, up to 99.8% of the cPPL was retained on the nanosheet surface through covalent bonding.

In the study on cPPL immobilization, it was determined that 96 h of silylation led to the highest uptake of lipase (Table 6-1). However, extending the silylation time beyond 24 h did not increase enzyme immobilization significantly. Therefore, only Al-(0,25,50)-24 nanosheets were used during CRL immobilization, as these silylated nanosheets were found to be the most effective supports for immobilization and had reasonable preparation times. In Figure 6-6a, the effects of ethanol concentration and incubation time on CRL immobilization can be seen. These results are independent of the silylation time, and depend only on the properties of the nanosheets themselves. As with cPPL immobilization, using a higher ethanol concentration in the production of the alumina nanosheets led to a higher lipase uptake during immobilization. Washing after CRL immobilization on Al-(0,25,50)-24 led to a higher reduction in immobilization efficiency (0.3 to 10.7%) when compared to washing after cPPL immobilization on Al-(0,25,50)-24 (0.04 to 3.5%). This indicates that CRL bonded less effectively to the epoxysilane than cPPL. Difficulty in the retention of CRL during immobilization compared to cPPL has been reported in the literature [380].

The specific activities of both lipases were tested using olive oil hydrolysis, where an emulsified olive oil mixture was hydrolyzed by the enzyme to form free fatty acids. The amount of FFAs produced during the reactions were quantified by titration with phenolphthalein. This technique is a well-known and accepted method for the determination of specific lipase activity due to the tendency for lipase-catalyzed reactions

to occur preferentially at lipid-water interfaces [364,381–383]. An olive oil emulsion is specifically used in this method to promote interfacial activation and enhance substrate-enzyme contact during the hydrolysis reaction [384].

As shown in Table 6-6, the specific activity of cPPL increased by a factor of up to 5.5 times (relative activity ratio in Table 6-6) when the enzyme was immobilized on twinned alumina nanosheets compared to the free enzyme in solution. This is due to the ability of lipase to preferentially bond to hydrophobic surfaces [361,378]. The cPPL used in this work is a crude mixture of 10 to 50 enzymes [385], up to 10% of which is actual PPL [386]. Other lipolytic/esterolytic enzymes in the mixture compete with lipase for substrate material. Silylation increased the hydrophobicity of the twinned alumina nanosheets, thereby drawing the more hydrophobic PPL out of the crude enzyme mixture during the immobilization process. Immobilization therefore was selective for pancreatic lipase. This increased the specific activity of the bound lipase relative to the free enzymes in solution. The selective adsorption of lipase onto hydrophobic supports from crude enzyme preparations has been well documented in the literature [387–390]. The increased activity of lipase when immobilized on hydrophobic spacer arms has also been reported [391].

In addition, immobilization induced a conformational change in the lipase molecule. The active site of PPL is isolated from the reaction medium by a hydrophobic polypeptide chain or “lid” region [392]. The active site can only be reached after the enzyme undergoes conformational changes to open the lid. The open conformation is stabilized by bile salts *in vivo* [393]; this environment can be simulated by using a buffer solution containing ions with low polarizability [394]. The buffer solution used in this work contained potassium phosphate monobasic and sodium hydroxide within the recommended levels of ionic

strength for optimal enzyme activation based on the Hofmeister effect as determined by Salis et al. [394]. Once purified from the crude enzyme mixture, the buffer salts had greater access to the lipase molecules and could help stabilize the open conformation, thereby increasing enzyme activity.

The specific activity of the immobilized lipases is also related to the structure of the support material; more specifically, the porosity of the alumina aggregates. Increasing the ethanol concentration in the synthesis mixture of the support increases the overall porosity of the internal network, thereby increasing accessibility to the immobilized enzyme. The specific lipase activity never reached a plateau (Figure 6-8), indicating that the nanosheet aggregate network maintained its internal accessibility in all cases. Furthermore, the most porous alumina aggregates create the most accessible catalyst support material.

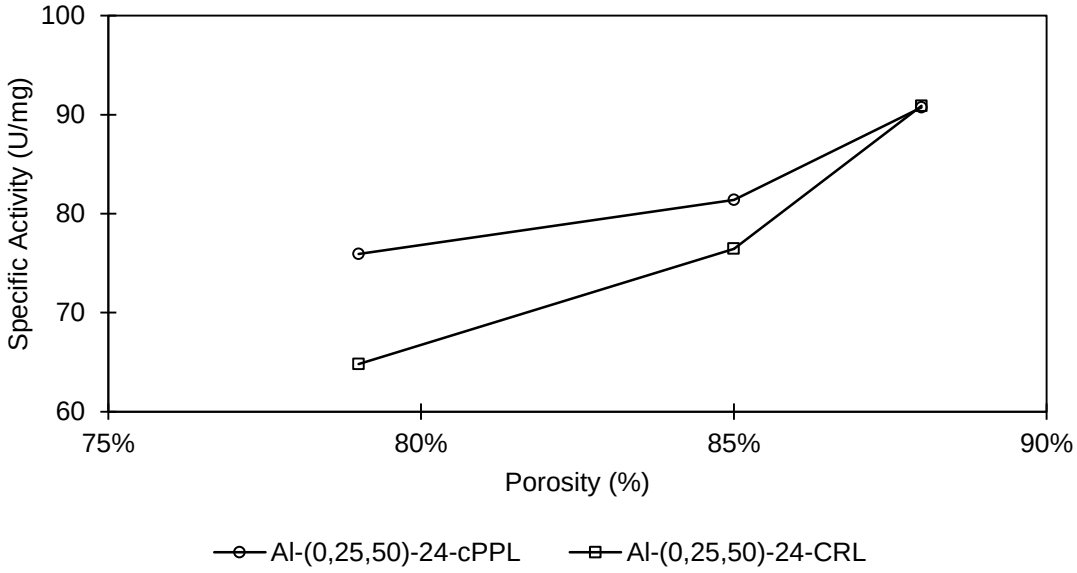

Figure 6-8: Specific activity of the immobilized lipases as a function of the porosity of the support material

In this work, we have shown that up to 66% of specific activity is retained after immobilization of CRL, when compared to the free enzyme in solution. Unlike PPL, the CRL used in this work was a pure enzyme preparation. Although the uptake of CRL on the supports was greater than that of the cPPL, the enzyme was less active once immobilized. Other studies from the literature show that CRL specific activity is lowered after immobilization (Table 6-6). Negishi et al. reported reductions in specific activity after CRL immobilization on various supports, including an 80 – 85% reduction after immobilization on powdered pig bone, and a 99.2 – 99.5% reduction after immobilization on Amberlite IRA-94 [395].

Knezevic et al. studied the effects of various covalent bonding mechanisms on the reduction in specific activity after CRL immobilization on Eupergit C. Immobilization via an epoxy group accounted for 20.7% residual specific activity due to multipoint attachment and attachment to the active site of the enzyme [396]. In their work, a methoxypropane spacer arm was used to attach the enzyme. In our work, an ethylcyclohexyl spacer arm was used (Figure 6-1), accounting for the higher residual activity of our immobilized CRL due to the increased hydrophobicity and chain length of this spacer. The residual activity was 66% versus the 20.7% residual activity reported in Knezevic et al. This phenomenon was also demonstrated in the work of Bayramoğlu et al., who reported that 81% of the specific activity was retained after the immobilization of CRL on magnetic beads activated with epoxy groups and a glutaraldehyde spacer arm [397].

Table 6-6: Specific activities of free and immobilized lipases from the literature

Support	Lipase Source	Test Conditions	Specific Activity of Free Enzyme in Solution (U/mg protein)	Specific Activity of Immobilized Enzyme (U/mg protein)	Relative Activity (ratio)	Source
Al-0-24	Porcine pancreatic	Olive oil emulsion, 37°C, pH 7.0	16.4	75.9	4.63	This work
Al-25-24				81.4	4.96	
Al-50-24				90.7	5.53	
Glutaraldehyde-activated polysiloxane-polyvinyl alcohol particles (POS-PVA)		Olive oil emulsion, 37°C, pH 7.0	2107	485	0.23	[357]
Polyacrylamide (Akrilex C-100)		Olive oil emulsion, 37°C, pH 7.5	2.5	0.3	0.12	[358]
Silica (Silochrome)				0.05	0.02	
VTES-modified nanosized silica		Olive oil emulsion, 37°C, pH 6.9	177.3	209.2	1.18	[360]
SDS-modified nanosized magnetite		Olive oil emulsion, 37°C, pH 7.7	6.37	9.87	1.55	[361]
Al-0-24	*Candida rugosa*	Olive oil emulsion, 37°C, pH 7.0	138.7	64.8	0.47	This work
Al-25-24				76.4	0.55	
Al-50-24				90.9	0.66	
Powdered pig bone		Olive oil, 37°C, pH 7.7	2200	330 – 440	0.15 – 0.20	[395]
Anion exchange resin (Amberlite IRA-94)				11 – 17	0.005 – 0.008	
Epoxy-activated acrylic beads (Eupergit C)		Olive oil emulsion, 37°C, pH 7.7	1.55	0.31	0.207	[396]
Epoxy-activated magnetic poly(GMA-MMA) beads		Olive oil emulsion, 35°C, pH 7.0	935	757	0.81	[397]

6.5 Conclusions

Twinned alumina nanosheets were manufactured by first synthesizing boehmite nanosheets in various ethanol-water mixtures, followed by calcination. The nanosheets were functionalized by treatment with an epoxysilane to promote lipase immobilization. Using FTIR, it was determined that the epoxy group remained intact after the silane molecules were attached to the alumina nanosheet surface.

Two types of lipases were immobilized on the alumina nanosheets: crude porcine pancreatic lipase and lipase from *Candida rugosa*. In both cases, it was determined that nanosheets produced in 50 vol% ethanol-water followed by a 24 h silylation process produced particles with the highest lipase immobilization and retention after washing with buffer solution (16.7 $\pm$ 0.2 mg/g Al-50-24-cPPL and 39.7 $\pm$ 0.9 mg/g Al-50-24-CRL). Extended silylation beyond 24 h did not significantly increase lipase immobilization on the twinned alumina nanosheets.

The specific activity of immobilized lipases was related to the structure of the twinned alumina nanosheet support material. Supports synthesized in 50 vol% ethanol had the highest porosity (89%) thereby increasing accessibility to the immobilized enzyme.

The specific activity of immobilized cPPL was up to 5.5 times higher than that of the free enzyme in solution. This was due to the ability of the lipase to preferentially bond to the hydrophobic functionalized alumina surface. The retained specific activity of immobilized CRL was up to 66% when compared to the free enzyme solution. The loss of activity after immobilization was likely due to multipoint covalent attachment and attachment to the active site of the enzyme. The use of a longer and more hydrophobic spacer arm in this

work led to a greater residual specific activity for immobilized CRL than that obtained with Eupergit C.

7 FFA-Selective Catalyst for the Pretreatment of Acidic Oils

Katrina Roebuck, Jiarong Zhou, A.Y. Tremblay

Oils with high free fatty acid content are a low-cost feedstock for biodiesel synthesis. However, these feedstocks must be pretreated to reduce the FFA content to <0.50 wt% so they can be transesterified at an industrial scale via the conventional alkaline method. Significant FFA reduction can be accomplished via pretreatment with immobilized lipases. In this study, shape-controlled twinned alumina nanosheets (TAN) were functionalized with an epoxysilane to promote the immobilization of lipase from Candida antarctica (CALB). The resulting immobilized enzyme preparation was used to catalyze FFA reduction in a 2.5 wt% FFA in canola oil mixture at loadings of 0.3 wt% CALB on TAN and 0.03 wt% CALB on TAN. We compared our enzyme preparation to a commercially-available enzyme (Novozym 435) at equivalent catalyst loadings. Due to excessive oil hydrolysis, the commercial catalyst was unable to maintain the FFA content below 0.50 wt% for an extended period of time. The immobilized enzyme produced in this work rapidly reduced the FFA content during the initial 2 to 4 h of each run and maintained the FFA content below 0.50 wt% for up to 56 h. CALB immobilized on TAN showed high reusability with no observable reduction in immobilized catalyst activity after 5 uses.

7.1 Introduction

In recent years, biodiesel has emerged as a non-toxic, biodegradable alternative to replace petroleum-based diesel fuel [398]. Renewable fuels are becoming increasingly important as petroleum fuel stocks diminish [398,399] and their continued use impacts the environment [400,401].

Biodiesel is industrially produced by the transesterification of triglycerides (TGs) with excess alcohol in the presence of an alkaline catalyst [402]. The ideal feedstock for this process is vegetable oil that is free from impurities such as water, free fatty acids (FFAs), sterols, or phospholipids, which produce unwanted byproducts during the transesterification reaction that hinder downstream processing [402]. In particular, the presence of excess water or FFAs lead to saponification, resulting in an emulsified product that is difficult to separate [403].

Up to 95% of biodiesel feedstock is currently derived from edible oils [403,404]. Non-edible oils and waste oils are an alternative feedstock for biodiesel that do not directly interfere with the production of food crops [404]. However, these feedstocks contain significantly higher amounts of impurities than their edible counterparts. For biodiesel production by the conventional homogeneous alkaline method, the FFA content must be minimized to prevent saponification (<0.50 wt%) [405,406].

The reduction of FFAs in waste oil can be facilitated through the use of an enzymatic pretreatment process. In the presence of excess alcohol, lipases (EC 3.1.1.3) will esterify FFAs to form fatty acid alkyl esters (FAAE) [407,408]. Immobilized lipases are particularly useful in this processing strategy due to their increased thermal stability and inherent reusability [342]. Lipases also catalyze the transesterification of triglycerides into FAAE [402,408]; however, the process is significantly slower than chemical methods [409,410]. Therefore, once the concentration of FFAs is reduced below the threshold level (<0.50 wt%), the conventional homogeneous alkaline method can be employed to convert the remaining feedstock into biodiesel. However, lipases are lipid-hydrolyzing enzymes. In the presence of free water, lipases catalyze the hydrolysis of triglycerides to form additional

FFAs [411,412]. Therefore, process parameters must be carefully controlled to reduce free water content in the reaction mixture and minimize the hydrolysis reaction.

Methanol is the most commonly used alcohol in the transesterification process due to its low cost [413]. Increasing the proportion of methanol in the reactor can be used to drive the esterification and transesterification reactions forward. Furthermore, methanol is able to compatibilize other aqueous compounds (e.g. glycerol) produced during the series of reactions which would otherwise adsorb onto the immobilization support [414,415]. However, the irreversible loss of lipase activity has been reported when excess methanol is used [416,417]. The tolerability of various lipases to methanol is dependent on the source of lipase. For example, compared to lipases from *Pseudomonas cepacia* and *Thermomyces lanuginosa*, lipase from *Candida antarctica* has been reported as highly methanol-resistant [416].

In this work, we use a mixture of 2.5 wt% FFA in canola oil to determine the FFA reduction capability of lipase from *Candida antarctica* type B (CALB) immobilized on silylated twinned alumina nanosheets (TAN). This was compared to a commercially-available supported enzyme.

TAN was synthesized in our laboratory as previously discussed by Roebuck et al. [331,362,418]. We also describe the immobilization of CALB on functionalized TAN supports and explore the capability of this immobilized enzyme preparation to favour the esterification of FFAs over the hydrolysis of triglycerides.

7.2 Experimental

7.2.1 Materials

Cetyl trimethylammonium bromide (CTAB), sodium hydroxide pellets, potassium hydroxide pellets, anhydrous ethanol, oleic acid (technical grade, 90%), bromophenol blue, phenolphthalein, Novozymes CALB L (aqueous lipase solution from *C. sp.*), and Novozym 435 (*C. antarctica* immobilized on Lewatit VP OC 1600) were purchased from Sigma-Aldrich (Canada). Aluminum chloride hexahydrate (99%, nitrogen flushed) was purchased from Acros Organics. Phosphate buffer solution (PBS) (potassium phosphate monobasic, sodium hydroxide, 0.05 M, pH 7.00 at 25°C), 1-propanol, isopropanol, hydrochloric acid (2N standard solution), Coomassie Brilliant Blue G-250 assay reagent, bovine serum albumin (BSA) standards, and cellulose filter paper (Whatman #1), were purchased from Fisher Scientific (Canada). 2-(3,4-Epoxycyclohexyl)ethyltriethoxysilane) (ETES) was purchased from Gelest, Inc. (Pennsylvania). Refined canola oil (Mazola) was purchased from Loblaw Co. Inc. All materials were used as purchased.

7.2.2 Methods

7.2.2.1 Preparation of Immobilization Supports

Boehmite nanosheets were synthesized by metal salt hydrolysis in a 50% ethanol-water solution as detailed in previous works [331,362,418]. The boehmite nanosheets were calcined for 4 h at 600°C to produce TAN.

To promote enzyme attachment, the TAN were silylated. A 20:80 v/v% solution of ETES in 1-propanol was formed by the addition of 8 mL of ETES to 32 mL of 1-propanol. 400 mg of TAN were added to the solution and stirred briefly to suspend the particles. The nanosheets were silylated for 24 h in a 60°C water bath. After silylation, the nanosheets

were filtered through a Büchner funnel using a Whatman #1 filter paper and rinsed several times with 1-propanol to remove any unbound ETES.

7.2.2.2 Enzyme Immobilization

Immobilization of Novozymes® CALB L onto TAN was carried out as follows: 5 mL of the aqueous lipase formulation was mixed with 5 mL of PBS in a 125 mL Erlenmeyer flask. 200 mg of silylated TAN were added to the lipase solution. The resulting mixture was incubated in an INFORS HT Multitron Pro incubator at 4°C at 150 rpm for 24 h. 100 µL samples were taken in triplicate for protein assay at 0, 1, 2, 4, 8 and 24 h during the lipase immobilization. After immobilization, the resulting particles were filtered through a Whatman #1 filter paper, rinsed several times with PBS, and dried.

Assay samples were tested for protein concentration using the Bradford method [363] using UV-Vis spectroscopy at an absorbance of λ = 595 nm (HACH Spectrophotometer DR 6000, Canada). Measurements were performed in triplicate. A calibration curve was constructed using BSA as a standard.

7.2.2.3 Characterization of Immobilization Supports

The particle size distributions of the unmodified and modified TAN were determined by dynamic particle size analysis. A capillary flow cell was cleaned using isopropanol and deionized (DI) water. A 1-mL aliquot from a 0.01 M stock solution was diluted to 100 mL with DI water. The solution was pumped through the flow cell at 0.1 mL/min using a peristaltic pump and analyzed using a DPA-4100 dynamic particle analyzer at high magnification (Brightwell Technologies Inc., Ottawa).

7.2.2.4 Free Fatty Acid Reduction in a Stirred Tank Batch Reactor

Canola oil was acidified with oleic acid to produce a 2.5 wt% FFA solution. Methanol was added in a 6:1 molar ratio of methanol:FFA. Catalyst loading of 0.3 or 0.03 wt% based on FFA content in the feed mixture were added (Table 7-1) and the mixture was transferred to a 250 mL round-bottom flask. The flask was immersed in a 45°C water bath. Its contents were magnetically stirred at 700 rpm. Samples of 0.4 – 0.6 g were taken at regular intervals and quenched in 10 mL of isopropanol prior to testing for FFA (Section 7.2.2.5) and free water (Section 7.2.2.6). The batch experiment was carried out for 24 or 56 hours. The entire immobilized enzyme content in the reactor was recovered by centrifugation. A new batch experiment was performed using the recovered immobilized lipase to assess its reusability. A single batch experiment was conducted using TAN particles without immobilized lipase to determine whether any reduction in FFA was associated with the enzyme support.

Table 7-1: Catalyst Loadings Used for Free Fatty Acid Reduction in a Stirred Tank Batch Reactor

Support Type	Mass of Immobilized Enzyme (mg)	Mass of Enzyme Preparation (mg)	Experiment Label[c]
Lewatit VP OC 1600 (Novozym 435)	3[a]	100	0.3 wt% CALB on Novozym 435
	0.3[a]	10	0.03 wt% CALB on Novozym 435
TAN	3[b]	1000	0.3 wt% CALB on TAN
	0.3[b]	100	0.03 wt% CALB on TAN

a. Mass of CALB immobilized on Novozym 435 based on Cabrera et al. [37]
b. Mass of CALB immobilized on TAN based on results in this work.
c. Catalyst loading based on 2.5 wt% FFA feed mixture: 1 g oleic acid, 39 g canola oil.

7.2.2.5 Analysis for Free Fatty Acid Content

FFA content in the oil samples was determined based on the modified AOCS method Cc 17-79 by Van Gerpen et al. [419]. Stock solutions of 0.01 N potassium hydroxide (KOH) in isopropanol and 0.01 N hydrochloric acid (HCl) in isopropanol were prepared. Solutions of the required pH indicators (phenolphthalein and bromophenol blue) in isopropanol were prepared.

The FFA/oil sample was shaken in isopropanol until dissolved. The mixture was transferred to a 125 mL Erlenmeyer flask. Approximately 100 µL of phenolphthalein in isopropanol was added to the mixture. The mixture was titrated to the phenolphthalein endpoint using 0.01 N KOH in isopropanol in a 25.00 mL burette. Approximately 100 µL of bromophenol in isopropanol was added to the mixture. The mixture was titrated to the bromophenol blue endpoint using 0.01 N HCl in isopropanol in a 25.00 mL burette. The acid and base titration volumes were recorded in millilitres.

The concentration of FFA was then calculated by the following equation:

$$C_{FFA} = \frac{C_{acid} V_{acid} MW_{FFA}}{m_{sample}} \times 100\% \quad (7\text{-}1)$$

where C_{FFA} is the concentration of FFA (wt%), C_{acid} and V_{acid} are the concentration (mol/L) and volume (L) of hydrochloric acid added during the titration, MW_{FFA} is the molecular weight of oleic acid, and m_{sample} is the mass of the titration sample measured using the analytical balance (g).

The reduction in FFA can then be calculated using the following equation:

$$reduction\ in\ FFA = \left(1 - \frac{C_{FFA}}{C_{FFA,0}}\right) \times 100\% \quad (7\text{-}2)$$

where C_{FFA} is the current concentration of FFA (wt%) and $C_{FFA,0}$ is the initial concentration of FFA (wt%).

7.2.2.6 Analysis for Free Water Content

Samples were prepared for analysis by centrifugation. The non-polar and polar phases were analyzed for free water content using a Karl-Fischer titrator (TitroLine KF *trace* Titrator, Schott Instruments, Germany). Anhydrous isopropanol was used as a standard.

7.2.2.7 Statistical Analyses

Standard statistical procedures were used, including mean averaging and standard deviation for triplicate results. A one-sided *t*-test was used to determine whether any statistically significant difference existed between two independent immobilization experiments. One-way analysis of variance (ANOVA) was used to determine whether any statistically significant differences exist between three or more independent immobilization experiments. A significance level of $\alpha = 0.01$ was used. Reactor data was

analyzed by linear regression. An R^2 value of 0.90 was set as the minimum value required for linearity.

7.3 Results

7.3.1 Characterization of Supports

The particle size distributions of the unmodified and modified TAN are shown below in Figure 7-1. Roebuck and Tremblay [362] showed that TAN synthesized in 50 vol% ethanol-water solutions exhibit a trimodal particle size distribution. The silylation and CALB immobilization procedures do not significantly change the particle size distributions of the TAN, indicating that the particles do not further aggregate during the silane functionalization and enzyme immobilization procedures.

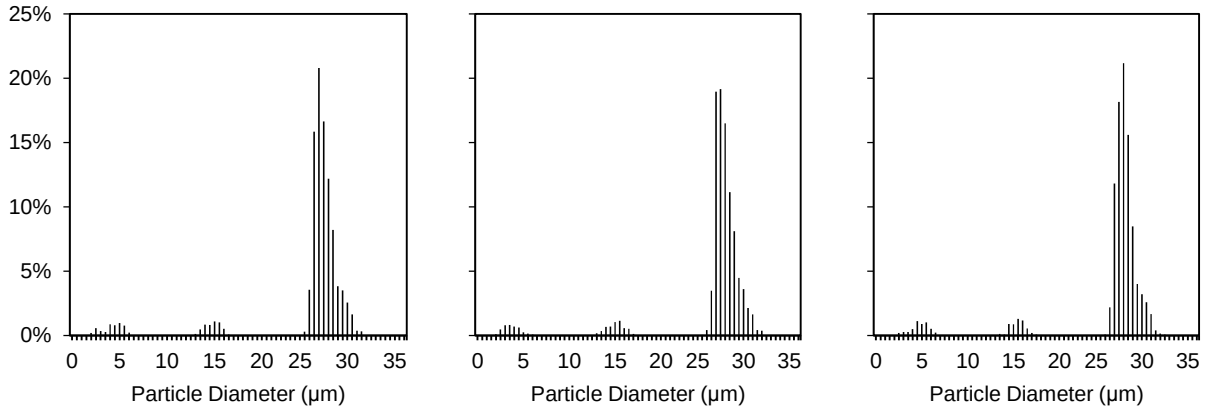

(a) (b) (c)

Figure 7-1: Particle size distributions of unmodified and modified TAN as measured by dynamic particle size analysis (a) unmodified TAN; (b) silylated TAN; (c) silylated TAN with immobilized CALB.

Novozym 435 is prepared by physically immobilizing CALB to the macroporous hydrophilic support Lewatit VP OC 1600, a spherical resin formed from DVB-crosslinking methyl methacrylate [420]. Novozym 435 has a broad particle size distribution (200 to 1000 μm, d_{50} = 472 μm) [421].

7.3.2 Free Fatty Acid Reduction in the Absence of Catalyst

Alumina is a well-known adsorbent [152,184,422,423]. A batch experiment was performed at 45°C for 24 h to determine whether the TAN, used as an enzyme support in these experiments, acted as an adsorbent towards the FFA present 2.5 wt% FFA oil. The oil mixture was prepared as discussed in Section 7.2.2.4. The concentration of FFA was measured at regular intervals during the 24 h experiments. The concentration remained constant at 2.50 $\pm$ 0.02 wt% over the 24 h period. From these results, it is evident that the enzyme support does not act as an adsorbent towards FFA.

7.3.3 Immobilization of CALB on Silylated Twinned Alumina Nanosheets

Three tests were performed to establish the protocol to immobilize CALB on silylated TAN. The reproducibility of CALB retention on silylated TAN was assessed during these tests. The amount of lipase loaded on the TAN supports during the 24 h immobilization procedure is shown in Figure 7-2. The results are reported for 3 immobilization tests (Imm. Tests 1 to 3), with each protein measurement repeated in triplicate. The lipase was loaded on the silylated TAN with high reproducibility. There is no statistically significant difference between the mean average loadings after 24 h (one-way ANOVA, $F = 5.57$, $F_{critical} = 10.92$, p-value = 0.043). The average loading after 24 h was 3.3 $\pm$ 0.1 mg lipase/g support. After rinsing with buffer solution, the average loading was 3.1 $\pm$ 0.2 mg lipase/g support. There was no statistical difference in the loading before or after rinsing (one-sided t-test, p-value = 0.175), indicating that the lipase was successfully immobilized onto the support during the immobilization procedure.

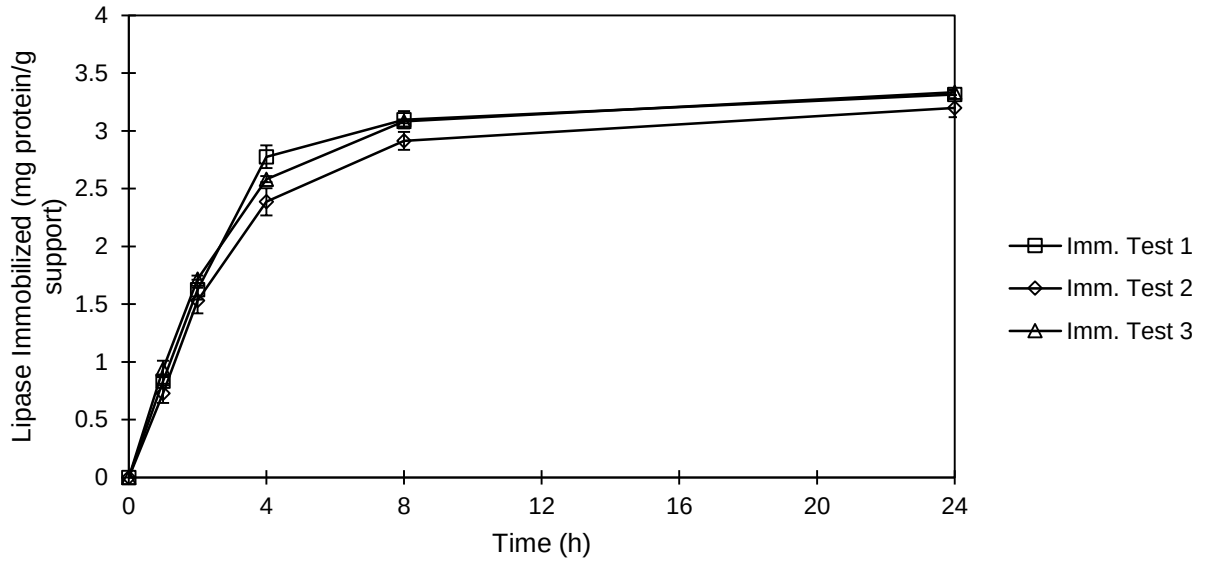

Figure 7-2: Enzyme loading during immobilization of CALB on silylated twinned alumina nanosheets. Results are reported for three separate immobilization tests (Imm. Test 1 to 3) with each protein measurement taken in triplicate.

7.3.4 Free Fatty Acid Reduction using 0.3 wt% CALB on Novozym 435

Figure 7-3, Figure 7-4, and Table 7-2 show the results of the 4 batch experiments carried out using a catalyst loading of 0.3 wt% CALB on Novozym 435. The immobilized enzyme sample was recovered by centrifugation and reused in subsequent runs.

The amount of FFA in the process decreased rapidly during the first 2 hours of each run at a rate of 0.53 to 1.04 wt% per hour (Figure 7-3). The threshold level ($\leq$0.50 wt%) was reached within the first 0.9 to 3.7 h. The minimum level of 0.10 to 0.34 wt% FFA was reached within the first 2 to 4 h in each experimental run. However, the FFA content was not maintained below the threshold level. It rapidly increased to 0.85 to 1.57 wt% after 24 h, representing 39 to 59% of the initial FFA concentration.

The Novozym 435 beads swelled and degraded over the course of the 4 batch runs from solid polymeric beads to a translucent gel. This phenomenon is well-reported in the literature [424–426], and is due to the swelling and dissolution of the Lewatit VP OC 1600

bead's polymeric matrix by the diffusing and reacting species such as FFAs [424] and short-chain alcohols [426].

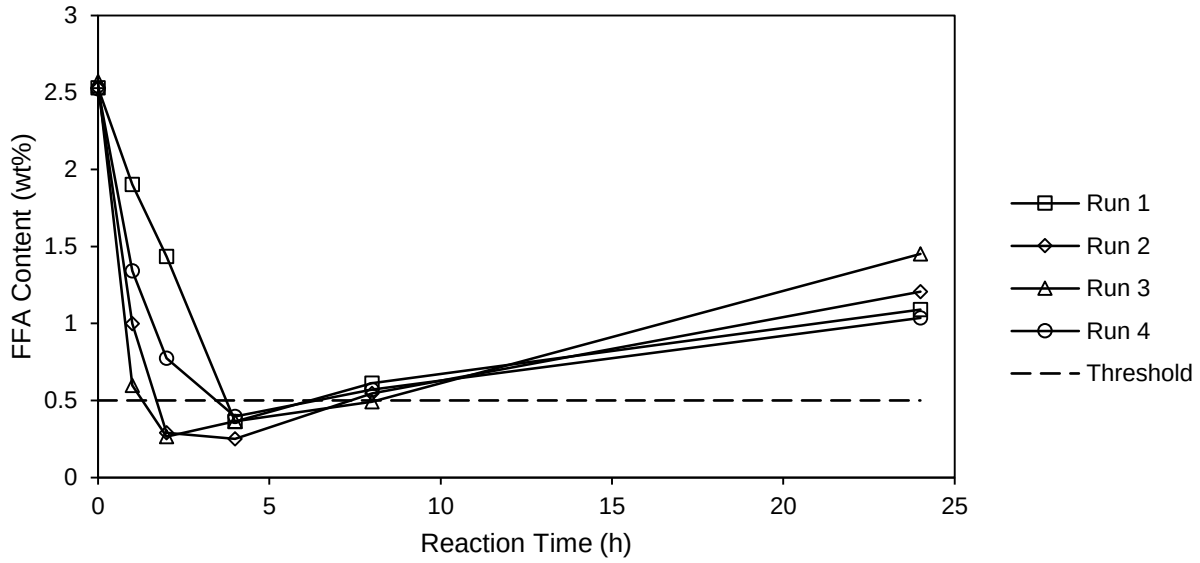

Figure 7-3: Reduction in FFA during batch experiments using 0.3 wt% CALB on Novozym 435. Results are from four experimental runs with the same sample of Novozym 435. The sample was separated by centrifugation and reused in subsequent runs.

The water content in the reaction mixture was monitored by Karl Fischer titration at regular intervals during the course of each 24 h run during the 0.3 wt% CALB on Novozym 435 batch experiments (Figure 7-4). The initial water content in the 40 g of reaction mixture was 564 $\pm$ 151 ppm. The water content in the oil phase of the reaction mixture in runs 1 to 3 rapidly increased during the first 2 to 4 h, coinciding with the rapid decrease in FFA content seen in Figure 7-3. The triglyceride hydrolysis reaction is triggered at high water concentration (1019 to 1247 ppm, according to Figure 7-4), leading to the consumption of water after 2 to 4 h in these runs. In run 4, the water content remained relatively steady for the duration of the reaction time, likely due to the increasing presence of diglycerides, monoglycerides, and glycerol accumulating in the polar phase of the reaction mixture as it was transferred from one 24 h batch experiment to the next.

The water content in fresh Novozym 435 beads and the degraded Novozym 435 gel was measured (Table 7-2). It was determined that the water content in the catalyst sample increased by a factor of 3.47, indicating that water accumulated in the polar phase of the reaction mixture.

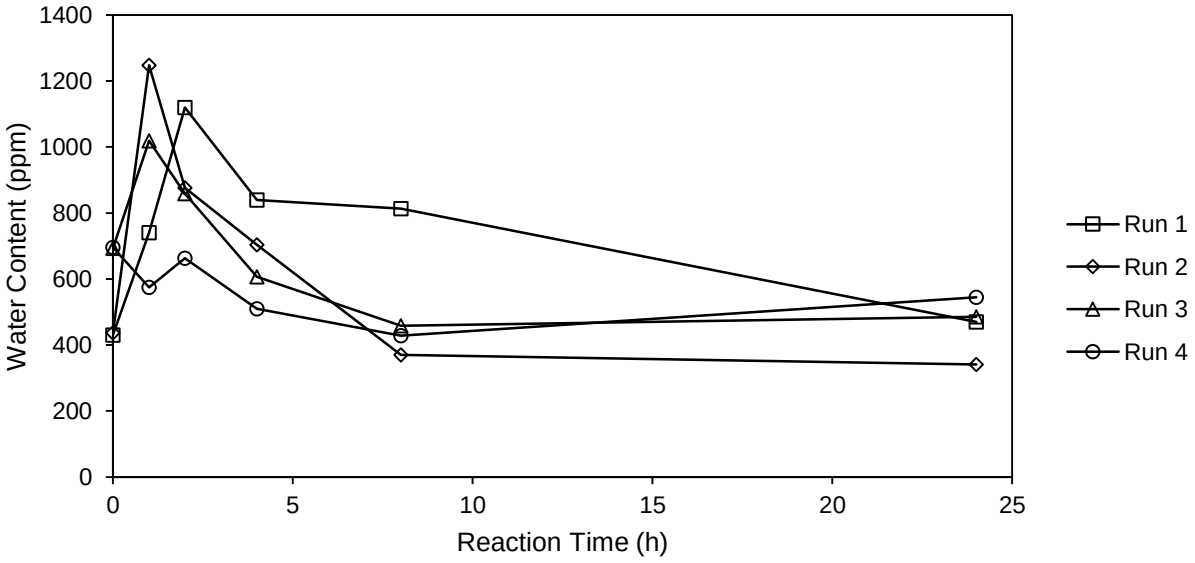

Figure 7-4: Water content in the oil phase of the reaction mixture during batch experiments using 0.3 wt% CALB on Novozym 435. Results are from four experimental runs with the same sample of CALB on Novozym 435. The sample was separated by centrifugation and reused in subsequent runs.

Table 7-2: Water content measured by Karl Fischer titration of enzyme-immobilized Novozym 435 particles before and after use in a stirred tank batch reactor.

Sample	Water Content[1] (wt%)
Fresh Novozym 435	1.06
0.3 wt% CALB on Novozym 435 Saturated with Reaction Mixture After 4 Batch Experiments	3.68

1. Average value of duplicate measurements

7.3.5 Free Fatty Acid Reduction using 0.3 wt% CALB on TAN

Figure 7-5, Figure 7-6, and Table 7-3 show the results of the 4 batch experiments carried out using a catalyst loading of 0.3 wt% CALB on TAN, equivalent to the catalyst loading on Novozym 435 used in Section 7.3.4. This allowed us to compare the two catalyst supports on a lipase-to-lipase basis. The immobilized enzyme sample was recovered by centrifugation and reused in subsequent runs.

The amount of FFA in the process decreased rapidly during the first 2 hours at a rate of 1.04 to 1.10 wt% per hour. The threshold level (<0.50 wt%) was reached within the first 1.4 to 1.9 h. The minimum FFA content of 0.15 to 0.20 wt% FFA was reached between the first 2 to 4 h in each experimental run. In addition, the FFA content was maintained below the threshold level for the remainder of the experiment in each run. The TAN runs showed high reproducibility with no observable reduction in activity over 4 repeated experiments at a catalyst loading of 0.3 wt% CALB on TAN.

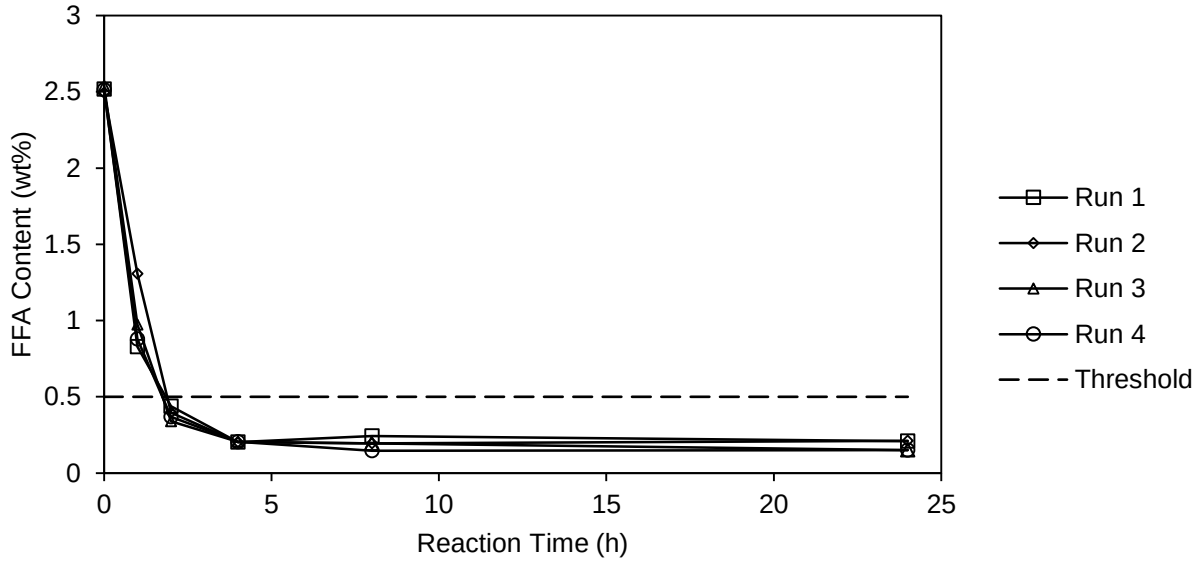

Figure 7-5: Reduction in FFA during batch experiments with 0.3 wt% CALB on TAN. Results are from four experimental runs with the same sample of CALB immobilized on silylated TAN. The sample was separated by centrifugation and reused in subsequent runs.

The water content in the reaction mixture was monitored by Karl Fischer titration at regular intervals during the course of each 24 h run during the 0.3 wt% CALB on TAN batch experiments (Figure 7-6). The initial water content in the 40 g of reaction mixture was 821 ± 140 ppm. The water content in the oil phase of the reaction mixtures in runs 1 and 2 decreased during the first 2 h; in run 3, the water content was relatively stable; and in run 4, the water content rapidly increased during the first 2 h. After 2 h, the water content in each run was relatively constant.

Based on the FFA content in Figure 7-5, it is evident that the triglyceride hydrolysis reaction was not triggered during any of the 4 runs at 0.3 wt% CALB on TAN. The water content in this reaction mixture was measured to be as high as 1326 ppm, 6 to 30% higher than the values determined to trigger the hydrolysis reaction in the 0.3 wt% CALB on Novozym 435 runs.

The water content in fresh CALB on TAN particles and the particles after 4 batch runs was measured (Table 7-3). It was determined that the water content in the catalyst sample increased by a factor of 87.5. This did not affect the ability of the immobilized enzyme to reduce FFAs nor did it cause the immobilized enzyme to catalyze the hydrolysis of TGs to form additional FFAs (Figure 7-5).

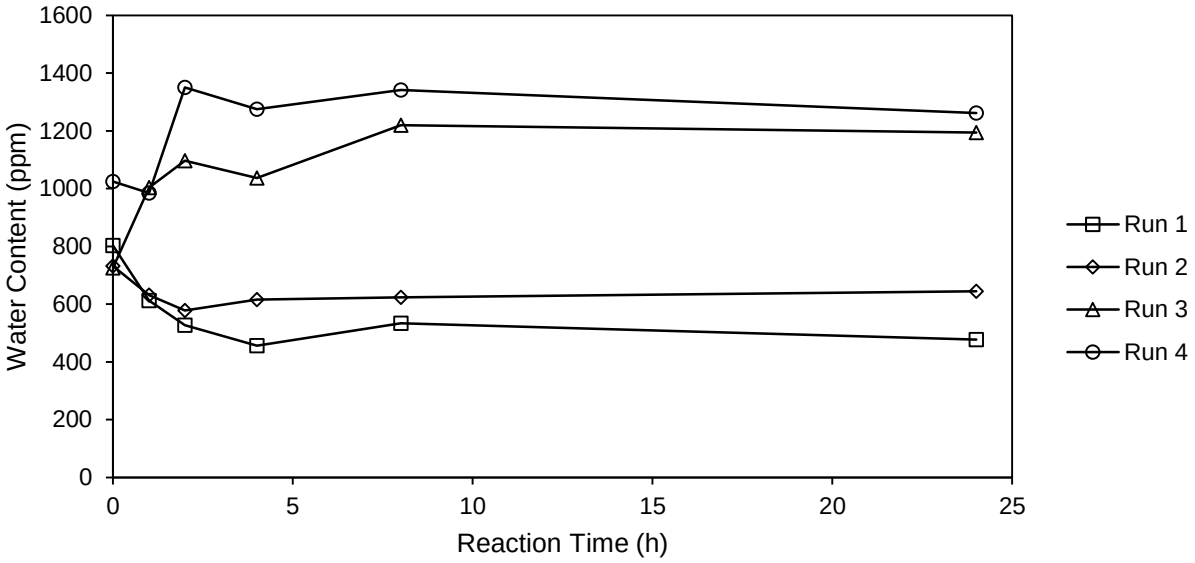

Figure 7-6: Water content in the oil phase of the reaction mixture during batch experiments using 0.3 wt% CALB on TAN. Results are from four experimental runs with the same sample of CALB on TAN. The sample was separated by centrifugation and reused in subsequent runs.

Table 7-3: Water content measured by Karl Fischer titration of enzyme-immobilized TAN particles before and after use in a stirred tank batch reactor.

Sample	Water Content[1] (wt%)
Fresh CALB on TAN	0.12
0.3 wt% CALB on TAN Saturated with Reaction Mixture After 4 Batch Experiments	10.5

1. Average value of duplicate measurements

7.3.6 Free Fatty Acid Reduction using 0.03 wt% CALB on Novozym 435

Figure 7-7 summarizes the results of the 5 batch experiments carried out using a catalyst loading of 0.03 wt% CALB on Novozym 435, 10% of the catalyst loading used in Sections 7.3.4 and 7.3.5. The immobilized enzyme sample was recovered by centrifugation and reused in subsequent runs.

The amount of FFA in the process decreased steadily during the first 2 hours at a rate of 0.25 to 0.54 wt% per hour. The amount of FFA continued to decrease during the first 24 to

56 h to minimum values between 0.33 to 0.48 wt%, lower than the threshold level of 0.50 wt%. The minimum concentration corresponds to a reduction from the initial FFA concentration of between 81 and 87%. The FFA content was maintained below the threshold level of 0.50 wt% FFA for 1.5 to 23.2 h. Subsequently, the amount of FFA increased to values between 0.80 to 1.23 wt%.

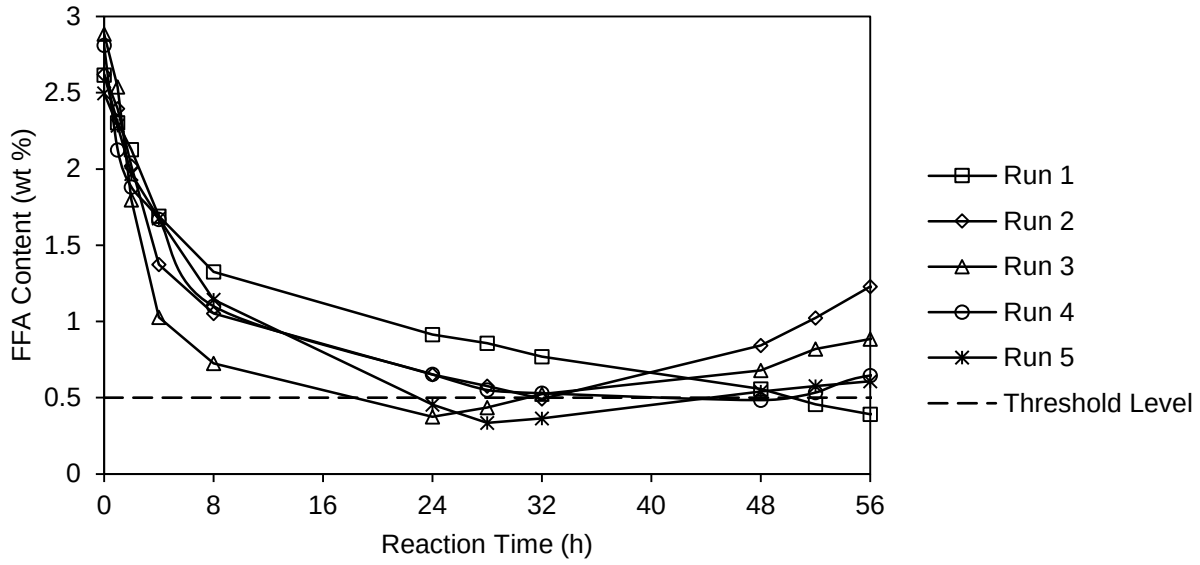

Figure 7-7: Reduction in FFA during batch experiments 0.03 wt% CALB on Novozym 435. Results are from five experimental runs with the same sample of Novozym 435. The sample was separated by centrifugation and reused in subsequent runs.

7.3.7 Free Fatty Acid Reduction using 0.03 wt% CALB on TAN

Figure 7-8 summarizes the results of the 5 batch experiments carried out a catalyst loading of 0.03 wt% CALB on TAN, equivalent to the catalyst loading on Novozym 435 used in Section 7.3.6. This allowed us to compare the two catalyst supports on a lipase-to-lipase basis. The immobilized enzyme sample was recovered by centrifugation and reused in subsequent runs.

The amount of FFA in the process decreased rapidly during the first 2 hours at a rate of 0.50 to 0.62 wt% per hour. The threshold level of <0.50 wt% FFA was reached within 22 to 26 h in each run. The minimum concentration of FFA was reached between 48 and 56 h. This corresponds to a reduction from the initial FFA concentration of between 89 and 96%. The FFA content was maintained below the threshold level of 0.50 wt% for the remainder of the observation time in each experimental run. The TAN runs showed high reproducibility with no observable reduction in activity over 5 repeated experiments at a catalyst loading of 0.03 wt% CALB on TAN.

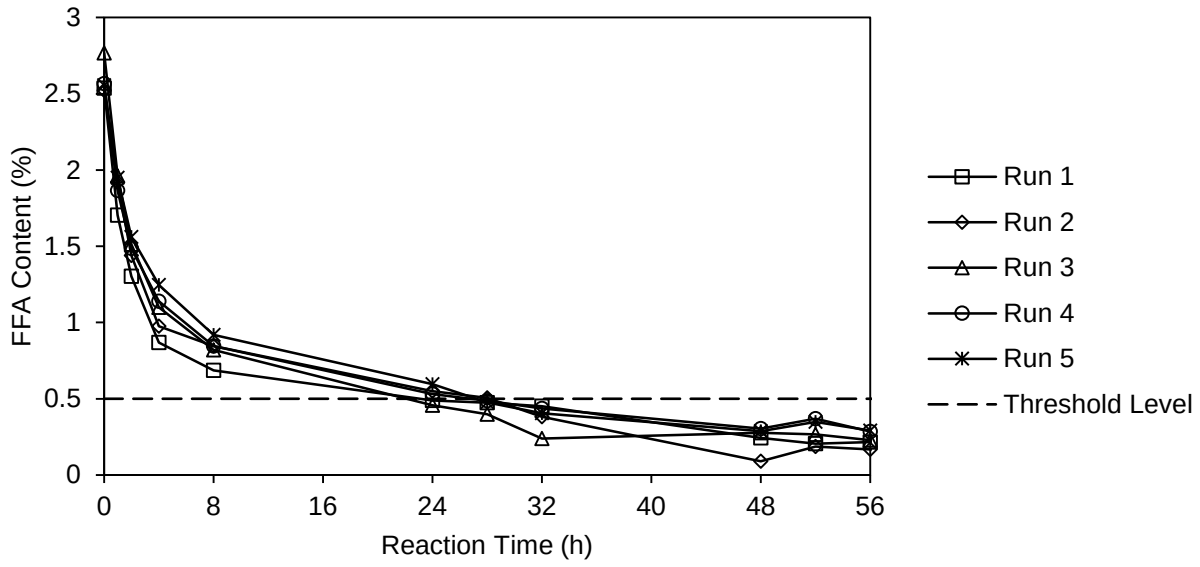

Figure 7-8: Reduction in FFA during batch experiments with 0.03 wt% CALB on TAN. Results are from five experimental runs with the same sample of CALB immobilized on silylated TAN. The sample was separated by centrifugation and reused in subsequent runs.

7.4 Discussion

Lipase from a commercial liquid enzyme solution (Novozymes® CALB L) was successfully immobilized on silylated twinned alumina nanosheets in repeated experiments with high reproducibility. The average loading was 3.1 $\pm$ 0.2 mg lipase/g support.

The high retention of lipase on the TAN demonstrates that the primary mechanism for lipase immobilization was covalent bonding. The epoxysilane ETES was used in this work for the purposes of facilitating the covalent bonding. The epoxy group is reactive even under mild conditions. It reacts with nucleophiles such as thiols, amines, and hydroxyls to form stable covalent bonds in a simple, one-step coupling procedure [348,427,428]. In the literature, it has been demonstrated that lipases bond covalently by their surface amino groups [373,374,429].

Lipases are used to catalyze numerous reactions, including the esterification of free fatty acids, transesterification of triglycerides, and the hydrolysis of triglycerides. The hydrolysis reaction is favoured when lipase has access to free water; the esterification and/or transesterification reaction(s) are favoured in low water environments. In the pretreatment of acidic oils, the hydrolysis reaction must be minimized to prevent the formation of additional FFAs. Therefore, when pretreating acidic oils with lipase, it is imperative to minimize the enzyme's access to free water.

In general, the hydrolysis reaction does not go to completion, resulting in a mixture of triglycerides, diglycerides (DGs), monoglycerides (MGs), free fatty acids, glycerol, and water [430]. This mixture can separate into aqueous and organic layers or microlayers, with more surface active compounds like FFAs, DGs, and MAGs migrating to the interfacial layer and displacing less surface-active compounds like TGs and lipase [430]. Lipase must be present at the interface of these layers/microlayers for optimal conversion. Therefore, phase separation rapidly reduces the overall rate of hydrolysis, a phenomenon that is well reported in the literature [430–433]. In this work, our goal is to minimize and ultimately

prevent the hydrolysis reaction from occurring, as it produces additional FFAs. As such, phase separation can be used to our advantage to reduce/prevent hydrolysis.

In this work, we compared our prepared immobilized lipase (CALB immobilized on silylated TAN) with a commercial product (Novozym 435) to test their respective abilities to reduce FFA content in a mixture of 2.5 wt% FFA in canola oil and reduce/prevent the hydrolysis reaction in a series of experiments in a stirred tank batch reactor. In the two Novozym 435 experiments, the FFA content rapidly decreased to <0.50 wt%, the threshold level of FFA required for the oil to be used as feedstock for transesterification by the conventional alkaline method [405,406]. However, the FFA content could not be maintained below the threshold level. Following the initial period of rapid FFA reduction, a subsequent increase in FFA content was observed in all of the Novozym 435 experiments (Figure 7-3 and Figure 7-7). At the end of the experiments, the overall reduction in FFAs was found to be 44 – 59% and 53 – 85% for the 0.3 and 0.03 wt% CALB on Novozym 435 experiments, respectively (Table 7-4). In the two TAN experiments, the FFA content rapidly decreased to <0.50 wt% and was maintained below the threshold level for the remainder of each experiment. At the end of the experiments, the overall reduction in FFAs was found to be 92 – 94% and 89 – 93% for the 0.3 and 0.03 wt% CALB on TAN experiments, respectively (Table 7-4). These observations suggest that the following was occurring: (1) when the overall concentration of FFAs was decreasing, the esterification reaction was favoured, and (2) when the overall concentration of FFAs was increasing, the hydrolysis reaction was favoured.

The initial reduction and subsequent increase in FFA content using Novozym 435 to reduce FFAs in acidic oils has been reported in the literature. Nordblad et al. showed that the

increase in FFA after the minimum value is reached is due to the hydrolysis reaction being thermodynamically favoured [434]. The rapid FFA reduction and subsequent increase in FFA content was observed in the two Novozym 435 experiments conducted in this work. The transition from FFA reduction to FFA production was more rapid in the experiments with 0.3 wt% CALB on Novozym 435 versus 0.03 wt% CALB on Novozym 435. Using 0.3 wt% CALB on Novozym 435, the FFA content reached the threshold level between 0.9 to 3.7 h and remained below this level for 4.2 to 7.0 h (Figure 7-3). Using 0.03 wt% CALB on Novozym 435, the FFA content reached the threshold level between 18 to 49 h (Figure 7-7), 13 to 54 times slower than the reactions carried out with 0.3 wt% CALB on Novozym 435. Using 0.3 wt% CALB on TAN, the FFA content reached the threshold level between 1.4 to 1.9 h and remained below this level for the remainder of each of the four 24 h runs (Figure 7-5). Using 0.03 wt% CALB on TAN, the FFA content reached the threshold level between 22 and 28 h, 15 to 20 times slower than the reactions carried out with 0.3 wt% CALB on TAN. However, the FFA content still remained below the threshold level for the remainder of each of the five 56 h runs (Figure 7-8). This demonstrates that our prepared catalyst, CALB immobilized on silylated TAN, successfully inhibited the hydrolysis reaction at both catalyst loadings in our mixture of 2.5 wt% FFA in canola oil.

Table 7-4: Overall reduction in FFA content during repeated batch experiments

	Overall reduction in FFA content (%)			
Experimental Run	0.3 wt% CALB on Novozym 435†	0.3 wt% CALB on TAN†	0.03 wt% CALB on Novozym 435‡	0.03 wt% CALB on TAN‡
1	57	92	85	91
2	52	92	53	93
3	44	94	69	92
4	59	94	77	89
5	-	-	76	89

†Reduction in FFA content was calculated using Equation (7-2) for each 24 h.
‡ Reduction in FFA content was calculated using Equation (7-2) for each 56 h.

TAN are nanosized platelets that interconnect to form a highly porous superstructure [362,418]. The morphology of the TAN support provided unique advantages over the spherical Novozym 435 particles. The flat surface of the individual TAN platelets allowed for the buildup of a thin, uniform layer of weakly physisorbed water [435] (Figure 7-9a). Once the platelets were saturated with water, additional water that penetrated to the support surface was rejected back into the reaction mixture and removed from the vicinity of lipase molecules by the hydrophobic cross-linked silane network. By rejecting excess free water, the immobilized lipase particles favoured the reduction of FFAs over the hydrolysis of triglycerides.

The results from Figure 7-6 support this finding. In the first 2 to 4 h of each run, the FFA content decreased rapidly (Figure 7-5), coinciding with a production in water. In runs 1 and 2, the consumption of water was due to adsorption on the catalyst support, since no additional FFAs were produced. In all runs, the water content stabilized in the oil phase

after the initial FFA reduction period. This demonstrates that the hydrolysis reaction was successfully inhibited. The water content in the TAN sample increased by a factor of 87.5 during the 0.3 wt% CALB on TAN batch experiments.

The morphology of Novozym 435 particles have been discussed in the literature. Using synchrotron infrared microspectroscopy, Mei et al. demonstrated that immobilized CALB is localized in the outermost 100 μm of the intact Novozym 435 particle [436] (Figure 7-9b). In our reaction media, FFA and TG compete to react with immobilized lipase molecules. Since FFAs are smaller molecules, they can easily diffuse through the reaction media and reach the outer layer of the Novozym 435 particles more readily. TG molecules, which are bulkier than FFAs, take longer to reach the outer layer of the Novozym 435 particles. Furthermore, the water content required for the hydrolysis reaction is provided by the initial consumption of FFA.

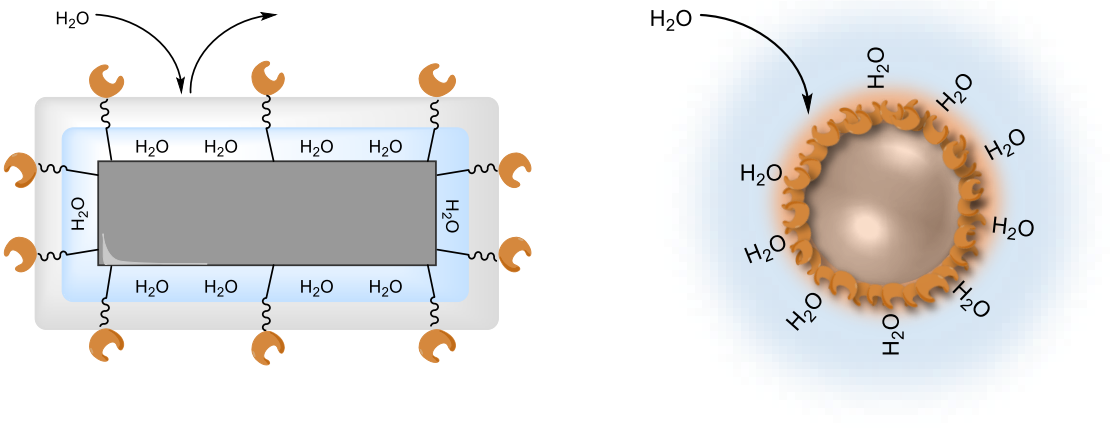

(a) (b)

Figure 7-9: (a) Mechanism for water adsorption during reduction of FFA catalyzed by CALB immobilized on TAN. Water is adsorbed as a thin layer on the surface of the alumina platelet. ETES spacer arm produces a hydrophobic layer that aids in the rejection of water from the vicinity of the immobilized lipase. (b) Mechanism for water absorption during reduction of FFA catalyzed by CALB immobilized on Lewatit VPOC 1600 (Novozym 435). Absorbed water swells the support, and is localized in the vicinity of reactive immobilized CALB.

7.5 Conclusions

Lipase from Novozymes® CALB L was successfully immobilized on silylated twinned alumina nanosheets with high reproducibility. The average loading was 3.1 $\pm$ 0.2 mg lipase/g support after rinsing with buffer solution.

We compared the FFA reduction capabilities of our prepared immobilized enzyme (CALB on TAN) against that of a commercially available enzyme in a set of repeated batch experiments.

Using catalyst loading of 0.3 and 0.03 wt% CALB, we determined that the commercial catalyst was unable to maintain the FFA content below the threshold level of 0.50 wt% FFA for an extended period of time. Instead, the undesired hydrolysis reaction was promoted when water was absorbed by the catalyst support.

Using catalyst loadings of 0.3 and 0.03 wt% CALB on TAN, we demonstrated that our prepared immobilized enzyme rapidly reduced the FFA content during the first 2 to 4 h of each run to below the threshold level of 0.50 wt% FFA. The FFA level was maintained below the threshold level for the remainder of each of the TAN runs. The TAN runs showed high reproducibility with no observable reduction in immobilized catalyst activity. The ability of the TAN support to adsorb excess water and inhibit the undesired hydrolysis reaction demonstrates its superiority as an enzyme support in the reduction of FFAs in acidic oils.

8 General Discussion, Conclusions, and Recommendations

8.1 General Discussion

In this work, we explored the synthesis and applications of hierarchically-structured twinned alumina nanosheets. We first developed a synthesis regime to reproducibly manufacture shape-controlled TAN with a highly porous and open superstructure. The TAN were synthesized by a two-step process: synthesis of boehmite nanosheets via hydrothermal processing in ethanol-water mixtures (0, 25, 50 vol%) with varying concentrations of CTAB (25% below to 25% above the CMC in 5% increments), followed by calcination to produce TAN. We determined that the CMC of CTAB in 0, 25 and 50 vol% ethanol-water mixtures were 0.90 $\pm$ 0.06, 3.90 $\pm$ 0.71, and 19.20 $\pm$ 0.55 mM respectively by conductometry (Table 3-1). The rapid increase in the CMC as a function of ethanol content demonstrated the ethanol's ability to reduce the dielectric constant of the solvent mixture and increase the solubility of the hydrophobic moiety of the surfactant.

Based on the Gibbs free energy of micellization, we showed that CTAB micelles are most favourably formed in pure water (Figure 3-1). This process is entropy-driven, whereas micelle formation in mixed solvents, such as ethanol-water mixtures, is enthalpy-driven. In pure water, the self-assembly of CTAB monomers into micelles causes a breakdown in the structure of the local water network as a result of the hydrophobic effect. The hydrophobic effect is reduced when ethanol is added, as the hydrophobic moiety of CTAB is stabilized by the presence of the cosolvent.

Boehmite nanosheets were successfully produced by metal salt hydrolysis of aluminum chloride hexahydrate in 0, 25, and 50 vol% ethanol-water mixture. The effect of surfactant

concentration and the effect of micelles on the shape and thickness of boehmite nanosheets during the self-assembly of boehmite nanosheets was assessed by FTIR, XRD, SEM and image analysis software (Figure 3-2 and Figure 3-3). The shape of the nanosheets was assessed by SEM. Boehmite naturally self-assembles in a rhombic structure, which was evident in the nanosheets synthesized in pure water (Figure 3-7a). The introduction of ethanol into the synthesis solution decreased the surface tension of the solvent mixture and facilitated the selective adsorption of surfactant molecules on the boehmite surface. This adsorption stabilized the crystal faces, increasing growth in the lateral direction. This effect was more prominent at higher ethanol concentrations (Figure 3-7c).

Image analysis was used to determine the effects of ethanol content and surfactant concentration on nanosheet thickness which indicated that the availability of surfactant monomers controlled particle thickness. In pure water and 25 vol% ethanol in water mixtures, surfactant monomers were readily available for nanosheet templating below the CMC. The thicknesses of nanosheets synthesized in pure water and 25% vol ethanol in water mixtures below the CMC were constant (200 $\pm$ 17 nm and 110 $\pm$ 17 nm, respectively) (Figure 3-4a,b, Figure 3-5, and Figure 3-6). Above the CMC, surfactant monomers aggregated to form micelles, and the thicknesses of nanosheets synthesized in pure water and 25 vol% ethanol in water mixtures increased as a function of surfactant concentration. Particle thickness was constant (103 $\pm$ 15 nm) in 50 vol% ethanol-water mixtures, indicating that free monomers were always available for particle templating (Figure 3-4c, Figure 3-5, and Figure 3-6).

Calcination of the boehmite nanosheets produced TAN. Using image analysis, we determined that the volume of individual TAN nanosheets synthesized in 0, 25, and 50

vol% ethanol-water mixtures were 1.9 $\pm$ 0.7, 1.0 $\pm$ 0.5, and 0.4 $\pm$ 0.1 μm^3, respectively (Table 4-1). Using dynamic particle size analysis, we determined the TAN synthesized in 0, 25, and 50 vol% ethanol-water mixtures exhibit mono-, di-, and tri-modal particle size distributions (Figure 4-4). The aggregates were intrinsically porous with three-dimensional pore connectivity.

We developed mathematical models to estimate the packing density of the alumina aggregates in a closed container (Equations (4-5) to (4-17)). The aggregates were modelled as perfect spheres. We estimated the packing densities of the TAN-0, TAN-25, and TAN-50 to be 54.0 – 54.2%, 65.3 – 74.4%, and 74.7 – 78.5%, respectively (Figure 4-6 to Figure 4-8). The TAN-50 nanosheets allowed for a higher packing density of aggregates in a given container size.

Dynamic membranes were formed by the deposition of the TAN on filter supports. The DMs were first characterized under pure water filtration at 6.89 kPa (Figure 4-5). We determined that the TAN-50 DM had the highest porosity (88%) and hydraulic permeability (714 mD) (Table 4-3).

The filtration properties of the TAN DMs were assessed during the constant-pressure filtration of a colloidal bentonite clay solution (d_{av} = 0.43 + 0.05 μm) (Figure 4-9). Based on filtration models, it was concluded that the DMs initially filtered through intermediate blocking, and had begun to shift to cake filtration towards the end of the filtration run. Using SEM imaging, no evidence of a bentonite cake was found on the surface of the TAN DMs (Figure 4-11). Instead, agglomerates of clay particles were visible on the surfaces of the TAN-0 and TAN-25 DMs (Figure 4-11d,e). The agglomerates were evenly distributed

across the surface of the TAN-50 DM (Figure 4-11f). The transition to cake filtration was not complete by the end of the filtration run with TAN-50.

We analyzed the distribution of the clay agglomerates further by probing their elemental composition using EDS. In particular, the total calcium content was used to determine whether bentonite was present at the site, as this element was only found in bentonite and not in any other compound used in this work. Bentonite deposited preferentially at specific sites on the surfaces of certain TAN-0 and TAN-25 particles, but uniformly across the entire surface of all TAN-50 particles (Figure 4-12, Table 4-6). We determined that the TAN-0 and TAN-25 DMs filtered via preferential channeling. Conversely, the TAN-50 particles were packed the most efficiently together with high porosity due to their low nanosheet volume. This combination of high packing density and high porosity also indicates that the TAN-50 aggregates were intrinsically porous with three-dimensional connectivity. Overall, the high degree of packing allowed for an even distribution of flow throughout the internal aggregate pores of the TAN-50 DM.

Having determined that TAN-50 produced DMs with the best performance during filtration of colloidal bentonite solutions, we compared their performance to common filter aids found in industry (diatomaceous earth). We used two grades of DE in this work: DE-512 (medium-grade) and DE-577 (fine-grade). We assessed the performance of the filter aids during the filtration of colloidal bentonite solutions at 34.47 kPa. We developed a general filtration model to fit the normalized flux data obtained in this work (Equation (5-8)). Based on this model, we determined that the dominating filtration mechanism during the DE runs was cake filtration (Figure 5-5, Table 5-5, and Table 5-6). This was confirmed by SEM imaging (Figure 5-6a,b). The dominating filtration mechanisms during the TAN runs

were pore constriction and intermediate blocking (Figure 5-5). No evidence of cake buildup was seen on the TAN filter aids (Figure 5-6c) during the 3 L run.

We measured the precoat thickness of the TAN precoat before and after filtration and found no evidence of compaction (Table 5-4). Conversely, the DE precoats compacted by up to 39% during deposition and subsequent filtration. From this, we determined that TAN particles stack similarly when they are settled under gravity or under flow, allowing the precoat to retain its open and porous structure when subject to flow. The DE particles slip relative to one another, causing them to form a denser, anisotropic filter cake when subject to flow. As a consequence, the hydraulic permeability of the TAN precoats were 13 to 29 times greater than the DE precoats (Table 5-4).

A solution of 125 mg of ultrasonicated bentonite in 4 L of water was passed through the filter aids. The permeate turbidity was monitored at regular intervals, and the flux and volume at which the target level ($\leq$0.10 NTU) was reached were determined. A combination of a high flux and low bentonite breakthrough was the desired outcome. For the TAN precoat, the target level was reached within the first 610 $\pm$ 130 mL of permeate volume at a flux of 7246 $\pm$ 649 LMH, as compared to 2380 $\pm$ 480 mL at 258 $\pm$ 84 LMH for the DE-512 precoat and 1180 $\pm$ 410 mL at 808 $\pm$ 387 LMH for the DE-577 precoat (Figure 5-7 and Figure 5-8). This indicates that the DE precoat had defects that permitted the passage of a considerable amount of bentonite particles via preferential channeling. It was observed that the TAN precoat deposited in a more uniform way, eliminating preferential channeling through the cake layer and the body of the precoat.

We also explored the potential for TAN to be used as catalyst supports in biocatalytic processes. We first established a synthesis protocol for the immobilization of lipase from

crude porcine pancreas, *Candida rugosa*, and *Candida antarctica* onto epoxysilane-functionalized TAN with high reproducibility. Lipases bond covalently by surface amino groups to linker molecules on functionalized supports. We used a one-step immobilization method whereby the alumina platelet was functionalized with a highly reactive epoxysilane spacer molecule (Figure 6-1). Silane treatment was carried out under moderate conditions (60°C, no acid or base catalyst) to prevent premature epoxy ring opening. We confirmed the presence of the epoxy groups after silane deposition by FTIR (Figure 6-3). Extending the silane treatment time from 4 to 24 h created more robust siloxane networks, which in turn resulted in higher lipase uptake (Table 6-1 and Table 6-5). The greatest lipase uptake was obtained using TAN synthesized in 50 vol% ethanol in water solutions and silane functionalized for 24 h (16.7 $\pm$ 0.2 mg cPPL/g TAN-50-24, 39.7 $\pm$ 0.9 mg CRL/g TAN-50-24, and 3.1 $\pm$ 0.2 mg CALB/g TAN-50-24) (Table 6-1, Table 6-2, and Figure 7-2).

The specific activities of free and immobilized crude porcine pancreas and *Candida rugosa* were assessed by olive oil hydrolysis, where an emulsified olive oil mixture was hydrolyzed to form FFAs. The specific activity of cPPL increased by a factor of up to 5.5 times when the enzyme was immobilized on TAN compared to the free enzyme in solution (Table 6-3). cPPL is a crude mixture of various lipolytic and esterolytic enzymes, of which approximately 10% is lipase. Silylation with ETES increased the hydrophobicity of the enzyme support. During immobilization, lipase, a highly hydrophobic enzyme, was able to preferentially bond to the more hydrophobic surface of the enzyme support. Furthermore, the buffer solution used in this work induced and stabilized the "lid" opening mechanism in the immobilized PPL molecule. It is reported that the open conformation is stabilized by bile salts *in vivo* [393]; this environment can be simulated by using a buffer solution

containing ions with low polarizability, such as PBS [394]. Immobilized CRL retained up to 66% specific activity compared to the free enzyme in solution (Table 6-4). The reduction in activity of CRL after immobilization is well reported in the literature [395–397], and has been attributed to multipoint attachment and attachment to the active site of the enzyme [396].

We explored the use of *Candida antarctica* lipase immobilized on TAN supports in the treatment of acidic oil. High acid oil is a low-cost feedstock for biodiesel synthesis. The oil must be pretreated to reduce the FFA content to <0.50 wt% so that it can be transesterified at an industrial scale via the conventional alkaline method. We compared our enzyme preparation to a commercially-available enzyme at equivalent catalyst loadings to determine their viability in this pretreatment process. Using catalyst loadings of 0.3 and 0.03 wt% CALB, we determined that the commercial catalyst was unable to maintain the FFA content below the threshold level of 0.50 wt% FFA for an extended period of time (Figure 7-3 and Figure 7-7). Instead, triglyceride hydrolysis was promoted when water was absorbed by the catalyst support, resulting in the production of additional FFAs. Using catalyst loadings of 0.3 and 0.03 wt% CALB on TAN, we demonstrated that our prepared immobilized enzyme rapidly reduced the FFA content during the first 2 to 4 h of each run to below the threshold level of 0.50 wt% FFA (Figure 7-4 and Figure 7-8). The FFA level was maintained below the threshold level for the remainder of each of the TAN runs. The TAN runs showed high reproducibility with no observable reduction in immobilized catalyst activity. The determining factor in the usefulness of an enzyme support in acidic oil treatment was its ability to promote the FFA reduction reaction over TG hydrolysis. The ability of the TAN support to adsorb excess water, reduce accessibility of immobilized

enzyme to free water, and favour the FFA reduction over TG hydrolysis demonstrates its superiority as an enzyme support in the reduction of FFAs in acidic oils.

In this work, we have demonstrated the benefits of TAN in filtration and biocatalytic applications. We have shown that TAN are highly porous, isotropically permeable, densely-packed particles that retain their structure during flow, and that silane-functionalized TAN are excellent biocatalytic supports. Continuous flow reactors are difficult to operate using immobilized enzymes due to high pressure drops [437,438]; the supports we synthesized offer great potential in addressing this issue. In this work, we demonstrated the superiority of TAN as an enzyme support in batch reactors. In addition, TAN maintain high flux when filtering colloidal particles, and retain an open structure during flow.

8.2 Conclusions

The main objectives of this thesis were to develop new hierarchically-structured materials, optimize their synthesis technique and explore applications of these newly-developed materials. During our synthesis experiments, we concluded from the FTIR and XRD analyses that the as-prepared nanosheets were boehmite. From our results, we concluded that the availability of surfactant monomers controlled particle thickness. The rapid increase in the CMC as a function of ethanol content demonstrated the ethanol's ability to reduce the dielectric constant of the solvent mixture and increase the solubility of the hydrophobic moiety of the surfactant.

The first application that we explored was the use of our newly-developed material as a filtration aid. We developed mathematical models to estimate the packing density of the TAN. We concluded that the TAN-50 nanosheets allow for a higher packing density of

aggregates in a given container size. From our results, we concluded that the TAN-0 and TAN-25 DMs filtered via preferential channeling. Conversely, the TAN-50 particles were packed the most efficiently together with high porosity due to their low nanosheet volume. We concluded that the dominating filtration mechanisms during the TAN runs were pore constriction and intermediate blocking (Figure 5-5). No evidence of cake buildup was seen on the TAN filter aids (Figure 5-6c) during the 3 L run as compared to the DE filter aids. The TAN particles stacked similarly when they were settled under gravity or under flow. This allowed the precoat to retain its open and porous structure when subject to flow. It was concluded that the TAN precoat deposited in a more uniform way, eliminating preferential channeling through the cake layer and the body of the precoat.

The second application that we explored was the use of our TAN as an enzyme support in heterogeneous catalysis for biodiesel pretreatment. We concluded that extending the silane treatment time from 4 to 24 h created more robust siloxane networks, which in turn resulted in higher lipase uptake. The silylation increased the hydrophobicity of the enzyme support. We concluded that the determining factor in the usefulness of an enzyme support in acidic oil treatment was its ability to promote the FFA reduction reaction over TG hydrolysis.

The following is a summary of the conclusions of this work:

1. A new hierarchically-structured material with high porosity and isoporous permeability was successfully and reproducibly synthesized.
2. The TAN-50 prefilter was 300x more permeable than a “theoretical” DE prefilter of equivalent pore diameter.

3. ETES successfully immobilized *Candida rugosa* and *Candida antarctica* (CALB) on twinned alumina nanosheets.
4. TAN-50-24 had the highest lipase retention and immobilized lipase specific activity of the compositions tested.
5. The new catalyst supports show great potential in pretreating waste oils and algae feedstocks in the production of biodiesel.

8.3 Recommendations

Based on the results of this thesis, the following recommendations for ongoing research are proposed.

1. Different synthesis mechanisms should be explored to reduce the total production costs of TAN.
2. Methods for the large-scale production of TAN should be explored.
3. A synthesis method to bond TAN to a backflushable support should be explored. This would allow the TAN filter aids to be physically cleaned and reused.
4. The continuous production of biodiesel feedstock from acidic oil should be explored using lipase immobilized on TAN in packed bed reactors. We also recommend using real, used waste oils as biodiesel feedstocks.
5. The use of lipase immobilized on TAN for other esterification reactions should be explored. Such applications include the production of flavouring compounds, scents, and food additives.

9 References

[1] M. Hartmann, W. Schwieger, Hierarchically-structured porous materials: from basic understanding to applications, Chem. Soc. Rev. 45 (2016) 3311–2. doi:10.1039/C6CS90043G.

[2] H. Zhang, L.M. Zhang, L. Han, S.S. Shen, W.C. Lu, Synthesis, Characterization and Growth Mechanism of Hierarchical Cantaloupe-Like AlOOH Superstructures by a Simple Hydrothermal Process, Integr. Ferroelectr. 129 (2011) 111–121. doi:10.1080/10584587.2011.576919.

[3] B. Xu, J. Wang, H. Yu, H. Gao, Large-scale synthesis of hierarchical flowerlike boehmite architectures, J. Environ. Sci. 23 (2011) S49–S52. doi:10.1016/S1001-0742(11)61076-0.

[4] Y. Liu, D. Ma, X. Han, X. Bao, W. Frandsen, D. Wang, et al., Hydrothermal synthesis of microscale boehmite and gamma nanoleaves alumina, Mater. Lett. 62 (2008) 1297–1301. doi:10.1016/j.matlet.2007.08.067.

[5] P. V. Krivoshapkin, E.F. Krivoshapkina, B.N. Dudkin, Growth and structure of microscale fibers as precursors of alumina nanofibers, J. Phys. Chem. Solids. 74 (2013) 991–996.

[6] Y. Mathieu, L. Vidal, V. Valtchev, B. Lebeau, Preparation of γ-Al2O3 film by high temperature transformation of nanosized γ-AlOOH precursors, New J. Chem. 33 (2009) 2255. doi:10.1039/b9nj00351g.

[7] Y.K. Park, E.H. Tadd, M. Zubris, R. Tannenbaum, Size-controlled synthesis of alumina nanoparticles from aluminum alkoxides, Mater. Res. Bull. 40 (2005) 1506–1512. doi:10.1016/j.materresbull.2005.04.031.

[8] Y. Mathieu, V. Valtchev, A. Werner, M. Cedex, Control of the Morphology and Particle Size of Boehmite Nanoparticles Synthesized under Hydrothermal Conditions, Langmuir. 23 (2007) 9435–9442.

[9] H.F. Lopez, H. Mendoza, Temperature Effects on the Crystallization and Coarsening of Nano-CeO2 Powders, ISRN Nanomater. (2013) 1–7.

[10] L. Ge, X. Wang, Z. Tu, C. Pan, C. Wang, Z. Gu, Fabrication of Multilayered Hollow Nanofibers and Estimation of Its Young's Modulus, Jpn. J. Appl. Phys. 46 (2007) 6790–6795. doi:10.1143/JJAP.46.6790.

[11] X. Han, Z. Huang, C. He, L. Liu, Preparation and Characterization of Core-Shell Structured Nanofibers by Coaxial Electrospinning, High Perform. Polym. 19 (2007) 147–159. doi:10.1177/0954008306072499.

[12] D. Li, Y. Xia, Direct Fabrication of Composite and Ceramic Hollow Nanofibers by Electrospinning, Nano Lett. 4 (2004) 933–938. doi:10.1021/nl049590f.

[13] M. Pritchard, J.A. Howell, R.W. Field, The ultrafiltration of viscous fluids, J. Memb. Sci. 102 (1995) 223–35. doi:10.1016/0376-7388(94)00309-M.

[14] J. Howell, R. Field, D. Wu, Ultrafiltration of High-Viscosity Solutions: Theoretical Developments and Experimental Findings, Chem. Eng. Sci. 51 (1996) 1405–15. doi:10.1016/0009-2509(95)00315-0.

[15] D. Maxime, M.L. Lameloise, Filterability and Filtration Experiences of Viscous Complex Food Salting Solutions, Chem. Eng. Res. Des. 81 (2003) 1150–7.

[16] R. Fabris, E.K. Lee, C.W.K. Chow, V. Chen, M. Drikas, Pre-treatments to reduce fouling of low pressure micro-filtration (MF) membranes, J. Memb. Sci. 289 (2007) 231–40. doi:10.1016/j.memsci.2006.12.003.

[17] A.R. Costa, M.N. de Pinho, M. Elimelech, Mechanisms of colloidal natural organic matter fouling in ultrafiltration, J. Memb. Sci. 281 (2006) 716–725. doi:10.1016/j.memsci.2006.04.044.

[18] N. Lee, G. Amy, J.P. Croué, Low-pressure membrane (MF/UF) fouling associated with allochthonous versus autochthonous natural organic matter, Water Res. 40 (2006) 2357–2368. doi:10.1016/j.watres.2006.04.023.

[19] E. Hernandez, C.S. Chen, J. Johnson, R.D. Carter, Viscosity changes in orange juice after ultrafiltration and evaporation, J. Food Eng. 25 (1995) 387–96. doi:10.1016/0260-8774(94)00013-Y.

[20] C.I. Nindo, J. Tang, J.R. Powers, P. Singh, Viscosity of blueberry and raspberry juices for processing applications, J. Food Eng. 69 (2005) 343–50. doi:10.1016/j.jfoodeng.2004.08.025.

[21] E.F. Leonard, C. Van Vooren, D. Hauglustaine, S. Haumont, Shear-Induced Formation of Aggregates during Hemodialysis, Biocompat. Hemodial. 36 (1982) 34–45.

[22] J. Lu, W. Lu, An approximate analytical solution to the ultra-filtration profile in a hemodialysis process between parallel porous plates, Sci. Bull. 53 (2008) 3402–8. doi:10.1007/s11434-008-0472-5.

[23] G. Fiore, C. Ronco, Mathematical Model to Characterize Internal Filtration, Cardiovasc. Disord. Hemodial. 149 (2005) 27–34.

[24] C. Wu, Y. Wang, Y. Zhou, C. Zhu, Pretreatment of Petrochemical Secondary Effluent by Micro-flocculation and Dynasand Filtration: Performance and DOM Removal Characteristics, Water, Air, Soil Pollut. 227 (2016) 415. doi:10.1007/s11270-016-3118-2.

[25] S. Karan, S. Samitsu, X. Peng, K. Kurashima, I. Ichinose, Ultrafast Viscous Permeation of Organic Solvents through Diamond-Like Carbon Nanotubes, Science (80-.). 335 (2012) 444–7.

[26] H. Peng, A.Y. Tremblay, Membrane regeneration and filtration modeling in treating oily wastewaters, J. Memb. Sci. 324 (2008) 59–66. doi:10.1016/j.memsci.2008.06.062.

[27] X. Yin, P. Han, X. Lu, Y. Wang, A review on the dewaterability of bio-sludge and

ultrasound pretreatment, Ultrason. Sonochem. 11 (2004) 337–48. doi:10.1016/j.ultsonch.2004.02.005.

[28] S.V. Ranganathan, S.L. Narasimhan, K. Muthukumar, An overview of enzymatic production of biodiesel, Bioresour. Technol. 99 (2008) 3975–81. doi:10.1016/j.biortech.2007.04.060.

[29] N. Dizge, B. Keskinler, Enzymatic production of biodiesel from canola oil using immobilized lipase, Biomass and Bioenergy. 32 (2008) 1274–8. doi:10.1016/j.biombioe.2008.03.005.

[30] D. Fritsch, G. Bengtson, Catalytic Polymer Membranes for high Temperature Hydrogenation of viscous Liquids, Adv. Eng. Mater. 8 (2006) 386–9. doi:10.1002/adem.200600019.

[31] M.W. Balakos, E.E. Hernandez, Catalyst characteristics and performance in edible oil hydrogenation, Catal. Today. 35 (1997) 415–25. doi:http://dx.doi.org/10.1016/S0920-5861(96)00212-X.

[32] M. Gabrovska, J. Krstić, R. Edreva-Kardjieva, M. Stanković, D. Jovanović, The influence of the support on the properties of nickel catalysts for edible oil hydrogenation, Appl. Catal. A Gen. 299 (2006) 73–83. doi:10.1016/j.apcata.2005.10.011.

[33] R. Lakes, Materials with structural hierarchy, Nature. 361 (1993) 511–5. doi:10.1038/361511a0.

[34] K.A. Cychosz, R. Guillet-Nicolas, J. García-Martínez, M. Thommes, Recent advances in the textural characterization of hierarchically structured nanoporous materials, Chem. Soc. Rev. 46 (2017) 389–414. doi:10.1039/C6CS00391E.

[35] W. Stern, On the nature and structure of character, J. Pers. 3 (1935) 270–89. doi:10.1111/j.1467-6494.1935.tb02011.x.

[36] M. Nadler, Error and Reject Rates in a Hierarchical Pattern Recognizer, IEEE Trans. Comput. 100 (1971) 1598–1601.

[37] F.J. Hatfield, S.J. Fenves, The Information Organizer: A System for Symbolic Data Manipulation, Comput. Struct. 1 (1971) 85–102.

[38] A.L. Girard, F. Lowenstein, On the Applicability of Modern Algebra Techniques to Adaptive Pattern Recognition, Pattern Recognit. 2 (1970) 33–8. doi:10.1016/0031-3203(70)90039-7.

[39] S.-K. Chang, Picture Processing Grammar and its Applications, Inf. Sci. (Ny). 3 (1971) 121–48.

[40] A.S. Reznikovskii, Control of the Operating Regimes of Water Resources Systems, Power Technol. Eng. 6 (1971) 56–61.

[41] H. Diekmann-Moeller, Process control system for a continuous slab casting plant, Metall. Plant Technol. 10 (1987) 50–60.

[42] W. Oberreiter, A. Schuler, A. Chowdhury, Improvement of performance and efficiency of industrial process control systems, Euromicro Newsl. 5 (1979) 295–301.

[43] K.C. Holmes, Selbstorganisation biologischer Strukturen, Umschau. 1 (1974) 739–41.

[44] T. Noguti, N. Gō, Structural Basis of Hierachical Multiple Substates of Proteins. I: Introduction, Proteins Struct. Funct. Genet. 5 (1989) 125–131.

[45] T. Noguti, N. Gō, Structural Basis of Hierachical Multiple Substates of Proteins. II: Monte Carlo Simulations of Native Thermal Fluctuations and Energy Minimization, Proteins Struct. Funct. Genet. 5 (1989) 104–12. doi:10.1002/prot.340050203.

[46] T. Noguti, N. Gō, Structural Basis of Hierarchical Multiple Substates of a Protein. III: Side Chain and Main Chain Local Conformations, Proteins Struct. Funct. Genet. 5 (1989) 113–24. doi:10.1002/prot.340050203.

[47] T. Noguti, N. Gō, Structural Basis of Hierachical Multiple Substates of Proteins. IV: Rearrangements in Atom Packing and Local Deformations, Proteins Struct. Funct. Genet. 5 (1989) 125–31. doi:10.1002/prot.340050203.

[48] M.H. Zehfus, Continous Compact Protein Domains, Proteins Struct. Funct. Genet. (1987) 90–110.

[49] G.T. Montelione, H. Scheraga, Formation of local structures in protein folding, Acc. Chem. Res. 22 (1989) 70–6. doi:061/7.

[50] J.L. Katz, H.S. Yoon, The Structure and Anisotropic Mechanical Properties of Bone, IEEE Trans. Biomed. Eng. BME-31 (1984) 878–84. doi:10.1109/TBME.1984.325252.

[51] J. Lawrence Katz, H.S. Yoon, S. Lipson, R. Maharidge, A. Meunier, P. Christel, The effects of remodeling on the elastic properties of bone, Calcif. Tissue Int. 36 (1984) S31–S36. doi:10.1007/BF02406131.

[52] L. Borland, G. Harauz, G. Bahr, M. van Heel, Packing of the 30 nm chromatin fiber in the human metaphase chromosome, Chromosoma. 97 (1988) 159–63.

[53] T. Taniguchi, S. Takayama, High-order structure of metaphase chromosomes: evidence for a multiple coiling model, Chromosoma. 93 (1986) 511–4. doi:10.1007/BF00386792.

[54] G. Harauz, L. Borland, G.F. Bahr, E. Zeitler, M. van Heel, Three-dimensional reconstruction of a human metaphase chromosome from electron micrographs, Chromosoma. 95 (1987) 366–74. doi:10.1007/BF00293184.

[55] C. Mao, H. Li, F. Cui, Q. Feng, H. Wang, Biomimetic synthesis of inorganic materials, Prog. Chem. 10 (1998).

[56] C. Chaput, A. Selmani, C.H. Rivard, Artificial scaffolding materials for tissue extracellular matrix repair, Curr. Opin. Orthop. 7 (1996) 62–8.

[57] J. Hirai, T. Oka, T. Matsuda, Application of hierarchically structured hybrid vascular tissue to a venous system, Japanese J. Artif. Organs. 24 (1995) 156–61.

[58] J. Hirai, T. Matsuda, Self-organized, tubular hybrid vascular tissue composed of vascular cells and collagen for low-pressure-loaded venous system, Cell Transplant. 4 (1995) 597–608.

[59] K. Ishibashi, K. Kawazoe, T. Matsuda, Development of a hybrid vascular graft hierarchically layered three cell types, Japanese J. Artif. Organs. 25 (1996) 733–7.

[60] T. Matsuda, H. Miwa, A hybrid vascular model biomimicking the hierarchic structure of arterial wall: Neointimal stability and neoarterial regeneration process under arterial circulation, J. Thorac. Cardiovasc. Surg. 110 (1995) 988–97. doi:10.1016/S0022-5223(05)80166-7.

[61] S.J. Pan, H.R. Brown, A. Hiltner, E. Baer, Biaxial Orientation of Polypropylene by Hydrostatic Solid State Extrusion. Part I: Orientation Mechanism and Structural Hierarchy, Polym. Eng. 26 (1986) 997–1006.

[62] S.J. Pan, H.I. Tang, A. Hiltner, E. Baer, Biaxial Orientation of Polypropylene by Hydrostatic Solid State Extrusion. Part II: Morphology and Properties, Polym. Eng. 27 (1987) 869–75.

[63] H.I. Tang, A. Hiltner, E. Baer, Biaxial Orientation of Polypropylene by Hydrostatic Solid State Extrusion. Part III: Mechanical Properties and Deformation Mechanisms, Polym. Eng. 27 (1987) 876–86.

[64] V.M. Startsev, N.F. Chugunova, V. V Matveyev, A.Y.E. Chalykh, Changes in supermolecular structure of polyamic acid during thermal cyclization, Polym. Sci. U.S.S.R. 28 (1986) 2642–6.

[65] B.T. Holland, C.F. Blanford, A. Stein, Synthesis of Macroporous Minerals with Highly Ordered Three-Dimensional Arrays of Spheroidal Voids, Science (80-.). 281 (1998) 538–40. doi:10.1126/science.281.5376.538.

[66] B.O.D. Velev, E.W. Kaler, Structured Porous Materials via Colloidal Crystal Templating: From Inorganic Oxides to Metals, Advanced. 12 (2000) 531–4.

[67] M.-O. Coppens, J. Sun, T. Maschmeyer, Synthesis of Hierarchical Porous Silicas with a Controlled Pore Size Distribution at Various Length Scales, Catal. Today. 69 (2001) 331–5. doi:10.1016/S0920-5861(01)00386-8.

[68] C. Danumah, S. Vaudreuil, L. Bonneviot, M. Bousmina, S. Giasson, S. Kaliaguine, Synthesis of macrostructured MCM-48 molecular sieves, Microporous Mesoporous Mater. 44–45 (2001) 241–7. doi:10.1016/S1387-1811(00)00287-0.

[69] O.D. Velev, T. a Jede, R.F. Lobo, a M. Lenhoff, Microstructured Porous Silica Obtained via Colloidal Crystal Templates, Chem. Mater. 10 (1998) 3597–3602. doi:10.1021/cm980444i.

[70] S.A. Davis, S.L. Burkett, N.H. Mendelson, S. Mann, Bacterial templating of ordered macrostructures in silica and silica-surfactant mesophases, Lett. to Nat. 385 (1997) 420–3.

[71] Y. Shin, J. Liu, J.H. Chang, Z. Nie, G.J. Exarhos, Hierarchically ordered ceramics through surfactant-templated sol-gel mineralization of biological cellular structures, Adv. Mater. 13 (2001) 728–32.

[72] B. Gates, Y.D. Yin, Y.N. Xia, Fabrication and characterization of porous membranes with highly ordered three-dimensional periodic structures, Chem. Mater. 11 (1999) 2827–36. doi:10.1021/cm990195d.

[73] B. Lebeau, C.E. Fowler, S. Mann, C. Farcet, B. Charleux, C. Sanchez, Synthesis of hierarchically ordered dye-functionalised mesoporous silica with macroporous architecture by dual templating, J. Mater. Chem. 10 (2000) 2105–8. doi:10.1039/b003796f.

[74] B.T. Holland, L. Abrams, A. Stein, Dual templating of macroporous silicates with zeolitic microporous frameworks, J. Am. Chem. Soc. 121 (1999) 4308–9. doi:10.1021/ja990425p.

[75] A. Xu, J.C. Yu, H. Zhang, L. Zhang, Continuous Formation of Supported Unusual Mesostructured Silica Films by Sol-Gel Dip Coating, Langmuir. 18 (2002) 9570–3.

[76] Z. Dai, L. Dähne, H. Möhwald, B. Tiersch, Novel Capsules with High Stability and Controlled Permeability by Hierarchic Templating, Angew. Chemie Int. Ed. English. 41 (2002) 4019–22.

[77] J. El Haskouri, D.O. de Zárate, C. Guillem, A. Beltrán-Porter, M. Caldés, M.D. Marcos, et al., Hierarchical Porous Nanosized Organosilicas, Chem. Mater. 14 (2002) 4502–4.

[78] B. Zhang, S.A. Davis, S. Mann, Starch gel templating of spongelike macroporous silicalite monoliths and mesoporous films, Chem. Mater. 14 (2002) 1369–75. doi:10.1021/cm011251p.

[79] T. Sen, G.J.T. Tiddy, J.L. Casci, M.W. Anderson, One-pot synthesis of hierarchically ordered porous-silica materials with three orders of length scale, Angew. Chemie - Int. Ed. 42 (2003) 4649–4653. doi:10.1002/anie.200351479.

[80] T. Sen, G.J.T. Tiddy, J.L. Casci, M.W. Anderson, Synthesis and characterization of hierarchically ordered porous silica materials, Chem. Mater. 16 (2004) 2044–2054. doi:10.1021/cm034946u.

[81] J.R. Jones, L.L. Hench, Effect of surfactant concentration and composition on the structure and properties of sol-gel-derived bioactive glass foam scaffolds, J. Mater. Sci. 8 (2003) 3783–3790.

[82] N. Huesing, C. Raab, V. Torma, A. Roig, H. Peterlik, Periodically mesostructured silica monoliths from diol-modified silanes, Chem. Mater. 15 (2003) 2690–2692. doi:10.1021/cm034036c.

[83] K. Suzuki, K. Ikari, H. Imai, Synthesis of mesoporous silica foams with hierarchical trimodal pore structures, J. Mater. Chem. 13 (2003) 1812. doi:10.1039/b302466k.

[84] J.H. Smått, S. Schunk, M. Lindén, Versatile double-templating synthesis route to silica

monoliths exhibiting a multimodal hierarchical porosity, Chem. Mater. 15 (2003) 2354–2361. doi:10.1021/cm0213422.

[85] H. Zhang, G.C. Hardy, Y.Z. Khimyak, M.J. Rosseinsky, A.I. Cooper, Synthesis of hierarchically porous silica and metal oxide beads using emulsion-templated polymer scaffolds, Chem. Mater. 16 (2004) 4245–4256. doi:10.1021/cm0492944.

[86] F. Carn, A. Colin, M.-F. Achard, H. Deleuze, E. Sellier, M. Birot, et al., Inorganic monoliths hierarchically textured via concentrated direct emulsion and micellar templates, J. Mater. Chem. 14 (2004) 1370. doi:10.1039/b400984c.

[87] S. Areva, C. Boissière, D. Grosso, T. Asakawa, C. Sanchez, M. Lindén, One-pot aerosol synthesis of ordered hierarchical mesoporous core-shell silica nanoparticles., Chem. Commun. (Camb). 14 (2004) 1630–1631. doi:10.1039/b405690f.

[88] D. Kuang, T. Brezesinski, B. Smarsly, Hierarchical porous silica materials with a trimodal pore system using surfactant templates, J. Am. Chem. Soc. 126 (2004) 10534–10535. doi:10.1021/ja0470618.

[89] L.A. Villaescusa, A. Mihi, I. Rodríguez, A.E. García-Bennett, H. Míguez, Growth of mesoporous materials within colloidal crystal films by spin-coating, J. Phys. Chem. B. 109 (2005) 19643–9. doi:10.1021/jp053511m.

[90] J. Pang, H. Na, Y. Lu, Effect of ionic polymer on cetyltrimethyl ammonium bromide templated synthesis of mesoporous silica, Microporous Mesoporous Mater. 86 (2005) 89–95. doi:10.1016/j.micromeso.2005.07.015.

[91] Z.-Y. Yuan, W. Zhou, B.-L. Su, Hierarchical interlinked structure of titanium oxide nanofibers, Chem. Commun. 11 (2002) 1202–3. doi:10.1039/b202489f.

[92] S. Nagamine, T. Ueda, I. Masuda, T. Mori, E. Sasaoka, I. Joko, Removal of Phosphorus from Wastewater by Crystallization on the Surface of Macroporous TiO 2 with a Fibrous Microstructure, Ind. Eng. Chem. Res. 42 (2003) 4748–4752. doi:10.1021/ie030189y.

[93] Z.Y. Yuan, T.Z. Ren, B.L. Su, Hierarchically mesostructured titania materials with an unusual interior macroporous structure, Adv. Mater. 15 (2003) 1462–1465. doi:10.1002/adma.200305075.

[94] L. Zhang, J.C. Yu, A sonochemical approach to hierarchical porous titania spheres with enhanced photocatalytic activity, Chem. Commun. 16 (2003) 2078. doi:10.1039/b306013f.

[95] J.L. Blin, A. Léonard, Z.Y. Yuan, L. Gigot, A. Vantomme, A.K. Cheetham, et al., Hierarchically mesoporous/macroporous metal oxides templated from polyethylene oxide surfactant assemblies, Angew. Chemie - Int. Ed. 42 (2003) 2872–2875. doi:10.1002/anie.200250816.

[96] T. Peng, A. Hasegawa, J. Qiu, K. Hirao, Fabrication of titania tubules with high surface area and well-developed mesostructural walls by surfactant-mediated templating method, Chem. Mater. 15 (2003) 2011–2016. doi:10.1021/cm020828f.

[97] X. Wang, J.C. Yu, C. Ho, Y. Hou, X. Fu, Photocatalytic Activity of a Hierarchically Macro/Mesoporous Titania, Langmuir. 21 (2005) 2552–9.

[98] Z.Y. Yuan, A. Vantomme, A. Leonard, B.L. Su, Surfactant-assisted synthesis of unprecedented hierarchical meso-macrostructured zirconia, Chem. Commun. 13 (2003) 1558–1559. doi:10.1039/b303272h.

[99] A. Vantomme, Z.-Y. Yuan, B.-L. Su, One-pot synthesis of a high-surface-area zirconium oxide material with hierarchically three-length-scaled pore structure, New J. Chem. 28 (2004) 1083. doi:10.1039/b402915a.

[100] D. Wang, C. Song, Z. Hu, X. Fu, Fabrication of hollow spheres and thin films of nickel hydroxide and nickel oxide with hierarchical structures, J. Phys. Chem. B. 109 (2005) 1125–9. doi:10.1021/jp046797o.

[101] Z. Liu, T. Fan, W. Zhang, D. Zhang, The synthesis of hierarchical porous iron oxide with wood templates, Microporous Mesoporous Mater. 85 (2005) 82–8. doi:10.1016/j.micromeso.2005.06.021.

[102] K.A. DeFriend, A.R. Barron, A simple approach to hierarchical ceramic ultrafiltration membranes, J. Memb. Sci. 212 (2003) 29–38. doi:10.1016/S0376-7388(02)00450-7.

[103] R.W. Hicks, T.J. Pinnavaia, Nanoparticle assembly of mesoporous AlOOH (boehmite), Chem. Mater. 15 (2003) 78–82. doi:10.1021/cm020753f.

[104] T.Z. Ren, Z.Y. Yuan, B.L. Su, Microwave-Assisted Preparation of Hierarchical Mesoporous-Macroporous Boehmite AlOOH and gamma-Al2O3, Langmuir. 20 (2004) 1531–1534. doi:10.1021/la0361767.

[105] W. Deng, B.H. Shanks, Synthesis of Hierarchically Structured Aluminas under Controlled Hydrodynamic Conditions, Chem. Mater. 17 (2005) 3092–100. doi:10.1021/cm050315j.

[106] K.H. Rhodes, S.A. Davis, F. Caruso, B. Zhang, S. Mann, D.- Potsdam, Hierarchical Assembly of Zeolite Nanoparticles into Ordered Macroporous Monoliths Using Core-Shell Building Blocks, Chem. Mater. 12 (2000) 2832–4.

[107] B. Zhang, S. Davis, S. Mann, N.H. Mendelson, Bacterial templating of zeolite fibres with hierarchical structure, Chem. Commun. 2 (2000) 781–2. doi:10.1039/b001528h.

[108] A. Léonard, J.-L. Blin, B.-L. Su, One-pot surfactant assisted synthesis of aluminosilicate macrochannels with tunable micro- or mesoporous wall structure., Chem. Commun. (Camb). 1 (2003) 2568–2569. doi:10.1039/b307720a.

[109] M. Hartmann, Hierarchical zeolites: A proven strategy to combine shape selectivity with efficient mass transport, Angew. Chemie - Int. Ed. 43 (2004) 5880–5882. doi:10.1002/anie.200460644.

[110] Z. Li, S.W. Chung, J.M. Nam, D.S. Ginger, C.A. Mirkin, Living templates for the hierarchical assembly of gold nanoparticles, Angew. Chemie - Int. Ed. 42 (2003) 2306–2309. doi:10.1002/anie.200351231.

[111] W. Zhang, S.S. Liao, F.Z. Cui, Hierarchical self-assembly of nano-fibrils in mineralized collagen, Chem. Mater. 15 (2003) 3221–3226. doi:10.1021/cm030080g.

[112] C.E. Fowler, M. Li, S. Mann, H.C. Margolis, Influence of surfactant assembly on the formation of calcium phosphate materials—A model for dental enamel formation, J. Mater. Chem. 15 (2005) 3317–25. doi:10.1039/b503312h.

[113] J. Yu, J.C. Yu, L. Zhang, X. Wang, L. Wu, Facile fabrication and characterization of hierarchically porous calcium carbonate microspheres., Chem. Commun. (Camb). 1 (2004) 2414–2415. doi:10.1039/b406839d.

[114] Z. Yuan, T. Ren, B. Su, Facile and Generalized Preparation of Hierarchically Mesoporous - Macroporous Binary Metal Oxide Materials, Chem. Mater. 16 (2004) 5096–5106. doi:10.1021/cm0494812.

[115] J. Andersson, S. Areva, B. Spliethoff, M. Lindén, Sol-gel synthesis of a multifunctional, hierarchically porous silica/apatite composite, Biomaterials. 26 (2005) 6827–35. doi:10.1016/j.biomaterials.2005.05.002.

[116] S.H. Tolbert, P. Sieger, G.D. Stucky, S.M.J. Aubin, C.C. Wu, D.N. Hendrickson, Control of inorganic layer thickness in self-assembled iron oxide/surfactant composites, J. Am. Chem. Soc. 119 (1997) 8652–61. doi:10.1021/ja970695c.

[117] H.-P. Lin, S.-B. Liu, C.-Y. Mou, C.-Y. Tang, Hierarchical organization of mesoporous MCM-41 ropes, Chem. Commun. (1999) 583–4. doi:10.1039/a809767d.

[118] M.T. Anderson, P.S. Sawyer, T. Rieker, Surfactant-templated silica aerogels, Microporous Mesoporous Mater. 20 (1998) 53–65. doi:10.1016/S1387-1811(97)00008-5.

[119] A. Vantomme, Z.-Y. Yuan, B.-L. Su, One-pot synthesis of a high-surface-area zirconium oxide material with hierarchically three-length-scaled pore structure, New J. Chem. 28 (2004) 1083. doi:10.1039/b402915a.

[120] Z.Y. Yuan, A. Vantomme, A. Leonard, B.L. Su, Surfactant-assisted synthesis of unprecedented hierarchical meso-macrostructured zirconia, Chem. Commun. 13 (2003) 1558–1559. doi:10.1039/b303272h.

[121] Z. Yuan, T. Ren, B. Su, Facile and Generalized Preparation of Hierarchically Mesoporous - Macroporous Binary Metal Oxide Materials, Chem. Mater. 16 (2004) 5096–5106. doi:10.1021/cm0494812.

[122] P.T. Tanev, Y. Liang, T.J. Pinnavaia, Assembly of Mesoporous Lamellar Silicas with Hierarchical Particle Architectures, J. Am. Chem. Soc. 119 (1997) 8616–24. doi:10.1021/ja970228v.

[123] J. Wang, Q. Xiao, H. Zhou, P. Sun, Z. Yuan, B. Li, et al., Budded, mesoporous silica hollow spheres: Hierarchical structure controlled by kinetic self-assembly, Adv. Mater. 18 (2006) 3284–8. doi:10.1002/adma.200601321.

[124] P. Schmidt-Winkel, P. Yang, D.I. Margolese, B.F. Chmelka, G.D. Stucky, Fluoride-

induced hierarchical ordering of mesoporous silica in aqueous acid-syntheses, Adv. Mater. 11 (1999) 303–7. doi:10.1002/(SICI)1521-4095(199903)11:4<303::AID-ADMA303>3.0.CO;2-M.

[125] J. Ruokolainen, G. Ten Brinke, O. Ikkala, Supramolecular Polymeric Materials with Hierarchical Structure-Within-Structure Morphologies, Adv. Mater. 11 (1999) 777–80. doi:10.1002/(SICI)1521-4095(199906)11:9<777::AID-ADMA777>3.3.CO;2-D.

[126] L. Zhang, J.C. Yu, A sonochemical approach to hierarchical porous titania spheres with enhanced photocatalytic activity, Chem. Commun. 16 (2003) 2078. doi:10.1039/b306013f.

[127] J. Yu, J.C. Yu, L. Zhang, X. Wang, L. Wu, Facile fabrication and characterization of hierarchically porous calcium carbonate microspheres., Chem. Commun. (Camb). 1 (2004) 2414–2415. doi:10.1039/b406839d.

[128] F. Bosc, P. Lacroix-Desmazes, A. Ayral, TiO2 anatase-based membranes with hierarchical porosity and photocatalytic properties, J. Colloid Interface Sci. 304 (2006) 545–8. doi:10.1016/j.jcis.2006.09.064.

[129] M.M. Pereira, J.R. Jones, L.L. Hench, Bioactive glass and hybrid scaffolds prepared by sol–gel method for bone tissue engineering, Adv. Appl. Ceram. 104 (2005) 35–42. doi:10.1179/174367605225011034.

[130] S. Duan, Y. Yang, C. Zhang, N. Zhao, F.J. Xu, NIR-Responsive Polycationic Gatekeeper-Cloaked Hetero-Nanoparticles for Multimodal Imaging-Guided Triple-Combination Therapy of Cancer, Small. 13 (2017) 1–10. doi:10.1002/smll.201603133.

[131] D. Liu, H. Zhang, E. Mäkilä, J. Fan, B. Herranz-Blanco, C.F. Wang, et al., Microfluidic assisted one-step fabrication of porous silicon@acetalated dextran nanocomposites for precisely controlled combination chemotherapy, Biomaterials. 39 (2015) 249–59. doi:10.1016/j.biomaterials.2014.10.079.

[132] N.G.M. Palmqvist, J.M. Nedelec, G.A. Seisenbaeva, V.G. Kessler, Controlling nucleation and growth of nano-CaCO3 via CO2 sequestration by a calcium alkoxide solution to produce nanocomposites for drug delivery applications, Acta Biomater. 57 (2017) 426–34. doi:10.1016/j.actbio.2017.05.006.

[133] C.W. He, M. Parowatkin, V. Mailänder, M. Flechtner-Mors, U. Ziener, K. Landfester, et al., Sequence-controlled delivery of peptides from hierarchically structured nanomaterials, ACS Appl. Mater. Interfaces. 9 (2017) 3885–94. doi:10.1021/acsami.6b13176.

[134] N. Shrestha, M.A. Shahbazi, F. Araújo, E. Mäkilä, J. Raula, E.I. Kauppinen, et al., Multistage pH-responsive mucoadhesive nanocarriers prepared by aerosol flow reactor technology: A controlled dual protein-drug delivery system, Biomaterials. 68 (2015) 9–20. doi:10.1016/j.biomaterials.2015.07.045.

[135] A. Fujishima, T.N. Rao, D.A. Tryk, Titanium dioxide photocatalysis, J. Photochem. Photobiol. C Photochem. Rev. 1 (2000) 1–21. doi:10.1016/S1389-5567(00)00002-2.

[136] K.J. Bayer, A process for the production of aluminium hydroxide, 382505, 1888.

[137] S.J. Lindsay, Key Physical Properties of Smelter Grade Alumina, Light Met. (2014) 597–601. doi:10.1002/9781118888438.ch101.

[138] P. Héroult, Process for the production of electrolytic aluminium, 175711, 1886.

[139] C.M. Hall, Process of Reducing Aluminium from its Fluoride Salts by Electrolysis, 400664, 1889.

[140] S. Namboothiri, M.P. Taylor, J.J.J. Chen, M.M. Hyland, M. Cooksey, Aluminium production options with a focus on the use of a hydrogen anode: a review, Asia-Pacific J. Chem. Eng. 2 (2007) 442–7.

[141] W. Cai, J. Yu, M. Jaroniec, Q. Liu, W.G. Song, L.J. Wan, et al., Template-free synthesis of hierarchical spindle-like γ-Al2O3 materials and their adsorption affinity towards organic and inorganic pollutants in water, J. Mater. Chem. 20 (2010) 4587–94. doi:10.1039/b924366f.

[142] H. Javadian, M.T. Angaji, M. Naushad, Synthesis and characterization of polyaniline/γ-alumina nanocomposite: A comparative study for the adsorption of three different anionic dyes, J. Ind. Eng. Chem. 20 (2014) 3890–900. doi:10.1016/j.jiec.2013.12.095.

[143] S. Ghosh, K.P. Dey, M.K. Naskar, Synthesis of nanofiber-like mesoporous γ-Al2O3 toward its adsorption efficiency for congo red, J. Am. Ceram. Soc. 96 (2013) 28–31. doi:10.1111/jace.12084.

[144] A. Miyazaki, I. Balint, K. Aika, Y. Nakano, Preparation of Ru Nanoparticles Supported on γ-Al2O3 and Its Novel Catalytic Activity for Ammonia Synthesis, J. Catal. 204 (2001) 364–71. doi:10.1006/jcat.2001.3418.

[145] A.M. Karim, V. Prasad, G. Mpourmpakis, W.W. Lonergan, A.I. Frenkel, J.G. Chen, et al., Correlating Particle Size and Shape of Supported Ru/γ-Al2O3 Catalysts with NH3 Decomposition Activity, J. Am. Chem. Soc. 131 (2009) 12230–9. doi:10.1021/ja902587k.

[146] V. Sundaramurthy, A.K. Dalai, J. Adjaye, Effect of EDTA on hydrotreating activity of CoMo/γ-Al2O3 catalyst, Catal. Letters. 102 (2005) 299–306. doi:10.1007/s10562-005-5872-4.

[147] B. Li, K. Maruyama, M. Nurunnabi, K. Kunimori, K. Tomishige, Effect of Ni Loading on Catalyst Bed Temperature in Oxidative Steam Reforming of Methane over α-Al2O3-Supported Ni Catalysts, Ind. Eng. Chem. Res. 44 (2005) 485–94.

[148] C. Liang, W. Li, Z. Wei, Q. Xin, C. Li, Catalytic Decomposition of Ammonia over Nitrided MoNx/α-Al2O3 and NiMoNy/α-Al2O3 Catalysts, Ind. Eng. Chem. Res. 39 (2000) 3694–7. doi:10.1021/ie990931n.

[149] J. Li, N. Yan, Z. Qu, S. Qiao, S. Yang, Y. Guo, et al., Catalytic Oxidation of Elemental Mercury over the Modified Catalyst Mn /α-Al2O3 at Lower Temperatures, Environ. Sci. Technol. 44 (2010) 426–31.

[150] J. Jia, K. Haraki, J.N. Kondo, K. Domen, K. Tamaru, Selective Hydrogenation of Acetylene over Au/Al2O3 Catalyst, J. Phys. Chem. B. 104 (2000) 11153–6. doi:10.1021/jp001213d.

[151] R.W. Siegel, Nanostructured Materials - Mind Over Matter, Nanostructured Mater. 3 (1993) 1–18.

[152] H. Javadian, M.T. Angaji, M. Naushad, Synthesis and characterization of polyaniline/γ-alumina nanocomposite: A comparative study for the adsorption of three different anionic dyes, J. Ind. Eng. Chem. 20 (2014) 3890–900. doi:10.1016/j.jiec.2013.12.095.

[153] Q. Liu, A. Wang, X. Wang, P. Gao, X. Wang, T. Zhang, Synthesis, characterization and catalytic applications of mesoporous γ-alumina from boehmite sol, Microporous Mesoporous Mater. 111 (2008) 323–33. doi:10.1016/j.micromeso.2007.08.007.

[154] B.E. Yoldas, Hydrolysis of aluminium alkoxides and bayerite conversion, J. Appl. Chem. Biotechnol. 23 (1973) 803–809. doi:10.1002/jctb.5020231103.

[155] W. Wu, Z. Wan, M. Zhu, D. Zhang, A facile route to aqueous phase synthesis of mesoporous alumina with controllable structural properties, Microporous Mesoporous Mater. 223 (2016) 203–12. doi:10.1016/j.micromeso.2015.11.004.

[156] B.E. Yoldas, Alumina gels that form porous transparent Al2O3, J. Mater. Sci. 10 (1975) 1856–1860.

[157] K. Wefers, C. Misra, Oxides and Hydroxides of Aluminum, (1987) 1–100.

[158] P.A. Buining, C. Pathmamanoharan, J.B.H. Jansen, H.N.W. Lekkerkerker, Preparation of Colloidal Boehmite Needles by Hydrothermal Treatment of Aluminum Alkoxide Precursors., J. Am. Ceram. Soc. 74 (1991) 1303–1307.

[159] J.F. Poco, J.H. Satcher, L.W. Hrubesh, Synthesis of high porosity, monolithic alumina aerogels, J. Non. Cryst. Solids. 285 (2001) 57–63. doi:10.1016/S0022-3093(01)00432-X.

[160] S.A. Lermontov, E.A. Straumal, A.A. Mazilkin, I.I. Zverkova, A.E. Baranchikov, B.B. Straumal, et al., How to Tune the Alumina Aerogels Structure by the Variation of a Supercritical Solvent. Evolution of the Structure during Heat Treatment, J. Phys. Chem. C. 120 (2016) 3319–25. doi:10.1021/acs.jpcc.5b10461.

[161] L.L. Hench, J.K. West, The Sol-Gel Process, Chem. Rev. 90 (1990) 33–72. doi:10.1021/cr00099a003.

[162] A.E. Danks, S.R. Hall, Z. Schnepp, The evolution of "sol–gel" chemistry as a technique for materials synthesis, Mater. Horizons. 3 (2016) 91–112. doi:10.1039/C5MH00260E.

[163] Y.H. Chiou, M.T. Tsai, H.C. Shih, The preparation of alumina fibre by sol-gel processing, J. Mater. Sci. 29 (1994) 2378–2388.

[164] N. Nagai, F. Mizukami, Properties of boehmite and Al2O3 thin films prepared from boehmite nanofibres, J. Mater. Chem. 21 (2011) 14884. doi:10.1039/c1jm11571e.

[165] L. Wan, H. Fu, K. Shi, X. Tian, Simple synthesis of mesoporous alumina thin films, Mater. Lett. 62 (2008) 1525–1527. doi:10.1016/j.matlet.2007.09.046.

[166] K.-H. Song, H.-Y. Kim, B.-M. Kim, K.-R. Lee, Boehmite sol-coated membrane preparation for the separation of aqueous alcohol, Desalination. 234 (2008) 244–251. doi:10.1016/j.desal.2007.09.091.

[167] Y. Gu, S. Ted Oyama, Ultrathin, hydrogen-selective silica membranes deposited on alumina-graded structures prepared from size-controlled boehmite sols, J. Memb. Sci. 306 (2007) 216–227. doi:10.1016/j.memsci.2007.08.045.

[168] J. Chandradass, M. Balasubramanian, Sol–gel processing of alumina fibres, J. Mater. Process. Technol. 173 (2006) 275–280. doi:10.1016/j.jmatprotec.2005.11.030.

[169] W.B. Deichmann, H.W. Gerarde, Toxicology of Drugs and Chemicals, Academic Press, New York, 1969.

[170] L. Adelson, Fatal intoxication with isopropyl alcohol (rubbing alcohol), Am. J. Clin. Pathol. 38 (1962) 144–51.

[171] Toxicity of Isopropanol, J. Lab. Clin. Med. 12 (1927) 326.

[172] Toxicity of 2-Butanol, J. Ind. Hyg. Toxicol. 25 (1943) 282.

[173] Nitric Acid, Gekkan Yakuji (Pharmaceuticals Mon. 22 (1980) 651.

[174] A. Henderson, M. Wright, S.M. Pond, Experience with 732 acute overdose patients admitted to an intensive care unit over six years, Med. J. Aust. 158 (1993) 28–30.

[175] O. Schäf, H. Ghobarkar, P. Knauth, Hydrothermal Synthesis of Nanomaterials, in: P. Knauth, J. Schoonman (Eds.), Nanostructured Mater. Sel. Synth. Methods, Prop. Appl., Kluwer Academic Publishers, New York, 2004: pp. 23–42.

[176] H. Hayashi, Y. Hakuta, Hydrothermal Synthesis of Metal Oxide Nanoparticles in Supercritical Water, Materials (Basel). 3 (2010) 3794–817. doi:10.3390/ma3073794.

[177] T. Noguchi, K. Matsui, N.M. Islam, Y. Hakuta, H. Hayashi, Rapid synthesis of γ-Al2O3 nanoparticles in supercritical water by continuous hydrothermal flow reaction system, J. Supercrit. Fluids. 46 (2008) 129–36. doi:10.1016/j.supflu.2008.04.011.

[178] H. Ghobarkar, O. Schäf, Effect of temperature on hydrothermal synthesis of analcime and viséite, Mater. Sci. Eng. B. 60 (1999) 163–7. doi:10.1016/S0921-5107(99)00012-4.

[179] T. Kim, J. Lian, J. Ma, X. Duan, W. Zheng, Morphology controllable synthesis of γ-alumina nanostructures via an ionic liquid-assisted hydrothermal route, Cryst. Growth Des. 10 (2010) 2928–33. doi:10.1021/cg901422v.

[180] F. Mirjalili, H. Mohamad, L. Chuah, Preparation of nano-scale α-Al2O3 powder by the sol-gel method, Ceramics. 55 (2011) 378–383.

[181] H. Schmidt, Nanoparticles by chemical synthesis, processing to materials and

innovative applications, Appl. Organomet. Chem. 15 (2001) 331–43. doi:10.1002/aoc.169.

[182] R. Bleta, P. Alphonse, L. Pin, M. Gressier, M.-J. Menu, An efficient route to aqueous phase synthesis of nanocrystalline γ-Al2O3 with high porosity: From stable boehmite colloids to large pore mesoporous alumina, J. Colloid Interface Sci. 367 (2012) 120–8. doi:10.1016/j.jcis.2011.08.087.

[183] Y. Zhao, R.L. Frost, W.N. Martens, H.Y. Zhu, Growth and Surface Properties of Boehmite Nanofibers and Nanotubes at Low Temperatures Using a Hydrothermal Synthesis Route, Langmuir. 23 (2007) 9850–9.

[184] H.Y. Zhu, J.D. Riches, J.C. Barry, γ-Alumina Nanofibers Prepared from Aluminum Hydrate with Poly (ethylene oxide) Surfactant, Chem. Mater. 14 (2002) 2086–2093.

[185] A.G. Fane, R. Wang, M.X. Hu, Synthetic membranes for water purification: Status and future, Angew. Chemie - Int. Ed. 54 (2015) 3368–86. doi:10.1002/anie.201409783.

[186] S. Judd, The status of membrane bioreactor technology, Trends Biotechnol. 26 (2008) 109–16. doi:10.1016/j.tibtech.2007.11.005.

[187] H. Chang, F. Qu, H. Liang, R. Jia, H. Yu, S. Shao, et al., Correlating ultrafiltration membrane fouling with membrane properties, water quality, and permeate flux, Desalin. Water Treat. 56 (2015) 1746–57. doi:10.1080/19443994.2014.951972.

[188] R. Kumar, A.F. Ismail, Fouling control on microfiltration/ultrafiltration membranes: Effects of morphology, hydrophilicity, and charge, J. Appl. Polym. Sci. 132 (2015) 1–20. doi:10.1002/app.42002.

[189] H. Chang, B. Liu, H. Liang, H. Yu, S. Shao, G. Li, Effect of filtration mode and backwash water on hydraulically irreversible fouling of ultrafiltration membrane, Chemosphere. 179 (2017) 254–64. doi:10.1016/j.chemosphere.2017.03.122.

[190] S.A. Avlonitis, K. Kouroumbas, N. Vlachakis, Energy consumption and membrane replacement cost for seawater RO desalination plants, Desalination. 157 (2003) 151–8. doi:10.1016/S0011-9164(03)00395-3.

[191] M.E. Ersahin, H. Ozgun, R.K. Dereli, I. Ozturk, K. Roest, J.B. van Lier, A review on dynamic membrane filtration: Materials, applications and future perspectives, Bioresour. Technol. 122 (2012) 196–206. doi:10.1016/j.biortech.2012.03.086.

[192] M.H. Al-Malack, G.K. Anderson, Cleaning techniques of dynamic membranes, Sep. Purif. Technol. 12 (1997) 25–33.

[193] M. Ye, H. Zhang, Q. Wei, H. Lei, F. Yang, X. Zhang, Study on the suitable thickness of a PAC-precoated dynamic membrane coupled with a bioreactor for municipal wastewater treatment, Desalination. 194 (2006) 108–20. doi:10.1016/j.desal.2005.11.005.

[194] A.E. Marcinkowsky, K.A. Kraus, H.O. Phillips, J. J.S. Johnson, A.J. Shor, Hyperfiltration Studies. IV. Salt Rejection by Dynamically Formed Hydrous Oxide Membranes1, J. Am.

Chem. Soc. 88 (1966) 5744–6. http://pubs.acs.org/doi/pdf/10.1021/ja00976a013.

[195] D. Jeison, I. Díaz, J.B. van Lier, Anaerobic membrane bioreactors: Are membranes really necessary?, Electron. J. Biotechnol. 11 (2008) 1–7. doi:10.2225/vol11-issue4-fulltext-9.

[196] Y. Kiso, Y.J. Jung, T. Ichinari, M. Park, T. Kitao, K. Nishimura, et al., Wastewater treatment performance of a filtration bio-reactor equipped with a mesh as a filter material, Water Res. 34 (2000) 4143–50. doi:10.1016/S0043-1354(00)00201-3.

[197] X. Zhang, Z. Wang, Z. Wu, F. Lu, J. Tong, L. Zang, Formation of dynamic membrane in an anaerobic membrane bioreactor for municipal wastewater treatment, Chem. Eng. J. 165 (2010) 175–183. doi:10.1016/j.cej.2010.09.013.

[198] Y. Wu, X. Huang, X. Wen, F. Chen, Function of dynamic membrane in self-forming dynamic membrane coupled bioreactor, Water Sci. Technol. 51 (2005) 107–14.

[199] L. Chu, S. Li, Filtration capability and operational characteristics of dynamic membrane bioreactor for municipal wastewater treatment, Sep. Purif. Technol. 51 (2006) 173–9. doi:10.1016/j.seppur.2006.01.009.

[200] M.M. Sharp, I.C. Escobar, Effects of dynamic or secondary-layer coagulation on ultrafiltration, Desalination. 188 (2006) 239–49. doi:10.1016/j.desal.2005.04.122.

[201] C. Xu, X. Wang, X. Dou, B. Gao, Coagulation-dynamic membrane filtration process at constant flow rate for treating polluted river water, Desalin. Water Treat. 52 (2014) 102–10. doi:10.1080/19443994.2013.781965.

[202] M.J.M.M. Noor, F.R. Ahmadun, T.A. Mohamed, S.A. Muyibi, M.B. Pescod, Performance of flexible membrane using kaolin dynamic membrane in treating domestic wastewater, Desalination. 147 (2002) 263–8. doi:10.1016/S0011-9164(02)00548-9.

[203] H. Chu, B. Dong, Y. Zhang, X. Zhou, Z. Yu, Pollutant removal mechanisms in a bio-diatomite dynamic membrane reactor for micro-polluted surface water purification, Desalination. 293 (2012) 38–45. doi:10.1016/j.desal.2012.02.021.

[204] L. Alibardi, N. Bernava, R. Cossu, A. Spagni, Anaerobic dynamic membrane bioreactor for wastewater treatment at ambient temperature, Chem. Eng. J. 284 (2016) 130–8. doi:10.1016/j.cej.2015.08.111.

[205] Y. Zhang, B. Gao, L. Lu, Q. Yue, Q. Wang, Y. Jia, Treatment of produced water from polymer flooding in oil production by the combined method of hydrolysis acidification-dynamic membrane bioreactor-coagulation process, J. Pet. Sci. Eng. 74 (2010) 14–9. doi:10.1016/j.petrol.2010.08.001.

[206] L.J. Gimbert, P.M. Haygarth, R. Beckett, P.J. Worsfold, Comparison of centrifugation and filtration techniques for the size fractionation of colloidal material in soil suspensions using sedimentation field-flow fractionation, Environ. Sci. Technol. 39 (2005) 1731–5. doi:10.1021/es049230u.

[207] B. Jirgensons, M.E. Straumanis, Filtration and ultrafiltration, in: Colloid Chem., 2nd

ed., Pergamon Press, Oxford, 1962: pp. 21–3.

[208] S. Mostafa, F. Behafarid, J.R. Croy, L.K. Ono, L. Li, J.C. Yang, et al., Shape-dependent catalytic properties of Pt nanoparticles., J. Am. Chem. Soc. 132 (2010) 15714–9. doi:10.1021/ja106679z.

[209] G. Guisbiers, G. Abudukelimu, D. Hourlier, Size-dependent catalytic and melting properties of platinum-palladium nanoparticles., Nanoscale Res. Lett. 6 (2011) 396. doi:10.1186/1556-276X-6-396.

[210] K. Chattopadhyay, R. Dey, B.C. Ranu, Shape-dependent catalytic activity of copper oxide-supported Pd(0) nanoparticles for Suzuki and cyanation reactions, Tetrahedron Lett. 50 (2009) 3164–3167. doi:10.1016/j.tetlet.2009.01.027.

[211] C. Hrelescu, T.K. Sau, A.L. Rogach, F. Jäckel, J. Feldmann, Single gold nanostars enhance Raman scattering, Appl. Phys. Lett. 94 (2009) 1–3.

[212] H. Liao, C.L. Nehl, J.H. Hafner, Biomedical applications of plasmon resonant metal nanoparticles, Nanomedicine. 1 (2006) 201–8.

[213] S.E. Skrabalak, L. Au, X. Lu, X. Li, Y. Xia, Gold nanocages for cancer detection and treatment, Nanomedicine. 2 (2007) 657–68.

[214] X. Huang, I.H. El-Sayed, W. Qian, M.A. El-Sayed, Cancer cell imaging and photothermal therapy in the near-infrared region by using gold nanorods, J. Am. Chem. Soc. 128 (2006) 2115–20.

[215] H. Liao, J.H. Hafner, Gold Nanorod Bioconjugates, Chem. Mater. 17 (2005) 4636–41.

[216] L. Au, D. Zheng, F. Zhou, Z.-Y. Li, X. Li, Y. Xia, A Quantitative Study on the Photothermal Effect of Immuno Gold Nanocages Targeted to Breast Cancer Cells, ACS Nano. 2 (2009) 1645–1652. doi:10.1021/nn800370j.A.

[217] M. Mulvihill, A. Tao, K. Benjauthrit, J. Arnold, P. Yang, Surface-enhanced Raman spectroscopy for trace arsenic detection in contaminated water, Angew. Chemie Int. Ed. English. 47 (2008) 6456–60.

[218] X. Zou, S. Dong, Surface-enhanced Raman scattering studies on aggregated silver nanoplates in aqueous solution, J. Phys. Chem. B. 110 (2006) 21545–50.

[219] Y. Wang, X. Zou, W. Ren, W. Wang, E. Wang, Effect of Silver Nanoplates on Raman Spectra of p-Aminothiophenol Assembled on Smooth Macroscopic Gold and Silver Surface, J. Phys. Chem. C. 111 (2007) 3259–3265.

[220] J. Xie, Q. Zhang, J.Y. Lee, D.I.C. Wang, The Synthesis of SERS-Active Gold Nanoflower Tags for In Vivo Applications, ACS Nano. 2 (2008) 2473–80.

[221] X. Ju, W. Feng, K. Varutt, T. Hori, A. Fujii, M. Ozaki, Fabrication of oriented ZnO nanopillar self-assemblies and their application for photovoltaic devices, Nanotechnology. 19 (2008) 1–6.

[222] Q. Wei, K. Hirota, K. Tajima, K. Hashimoto, Design and Synthesis of TiO2 Nanorod

Assemblies and Their Application for Photovoltaic Devices, Chem. Mater. 18 (2006) 5080–7.

[223] K. Holmberg, Surfactant-templated nanomaterials synthesis, J. Colloid Interface Sci. 274 (2004) 355–64. doi:10.1016/j.jcis.2004.04.006.

[224] Y. Lu, Surfactant-templated mesoporous materials: from inorganic to hybrid to organic., Angew. Chemie Int. Ed. English. 45 (2006) 7664–7. doi:10.1002/anie.200602489.

[225] C.-H. Tsai, J.L. Vivero-Escoto, I.I. Slowing, I.-J. Fang, B.G. Trewyn, V.S.-Y. Lin, Surfactant-assisted controlled release of hydrophobic drugs using anionic surfactant templated mesoporous silica nanoparticles., Biomaterials. 32 (2011) 6234–44. doi:10.1016/j.biomaterials.2011.04.077.

[226] M.P. Pileni, Reverse micelles as microreactors, J. Phys. Chem. 97 (1993) 6961–73.

[227] J. Sjöblom, R. Lindberg, S.E. Friberg, Microemulsions - phase equilibria characterization, structures, applications and chemical reactions, Adv. Colloid Interface Sci. 95 (1996) 125–287.

[228] M. Antonietti, Surfactants for novel templating applications, Curr. Opin. Colloid Interface Sci. 6 (2001) 244–248. doi:10.1016/S1359-0294(01)00089-9.

[229] M.A. López-Quintela, Synthesis of nanomaterials in microemulsions: formation mechanisms and growth control, Curr. Opin. Colloid Interface Sci. 8 (2003) 137–144. doi:10.1016/S1359-0294.

[230] A.R. Auxilio, P.C. Andrews, P.C. Junk, L. Spiccia, D. Neumann, W. Raverty, et al., Functionalised pseudo-boehmite nanoparticles as an excellent adsorbent material for anionic dyes, J. Mater. Chem. 18 (2008) 2466–74.

[231] M. Zhang, B. Gao, Removal of arsenic, methylene blue, and phosphate by biochar/AlOOH nanocomposite, Chem. Eng. J. 226 (2013) 286–92.

[232] M. Xuan, W. Huixin, S. Li, Reactive Adsorption of Thiophene on ZnNi/Diatomite-Pseudo-Boehmite Adsorbents, China Pet. Process. Petrochemical Technol. 14 (2012) 33–8.

[233] G.M.S. El Shafei, C.A. Philip, Interactions at an Alumina-Aqueous Glycine Interface: Characterization of Glycine-Modified Boehmite, J. Colloid Interface Sci. 176 (1995) 55–62.

[234] D. Palit, S.P. Moulik, Adsorption Behaviors of L-Histidine and DL-Tryptophan on Cholesterol, Silica, Alumina, and Graphite, J. Colloid Interface Sci. 239 (2001) 20–6.

[235] W.P. Tang, O. Shima, A. Ookubo, K. Ooi, A kinetic study of phosphate adsorbtion by boehmite, J. Pharm. Sci. 86 (1997) 230–5.

[236] I.S. Park, M.S. Kwon, N. Kim, J.S. Lee, K.Y. Kang, J. Park, Rhodium nanoparticles entrapped in boehmite nanofibers: recyclable catalyst for arene hydrogenation under mild conditions, Chem. Commun. (2005) 5667–9.

[237] Z. Wu, Y. Mao, M. Song, X. Yin, M. Zhang, Cu/boehmite: A highly active catalyst for hydrogenolysis of glycerol to 1,2-propanediol, Catal. Commun. 32 (2013) 52–7.

[238] G. Huang, T.-M. Li, S.-Y. Liu, M.-G. Fan, Y.-X. Jiang, Y.-A. Guo, A robust boehmite-supported cobalt tetraphenylporphyrin catalyst for aerobic oxidation of cyclohexane, Appl. Catal. A Gen. 371 (2009) 161–5.

[239] K. Nitta, T.M. Shau, J. Sugahara, Flaky aluminum oxide and pearlescent pigment, and production thereof, EP 0 763 573 B1, 2001.

[240] F.J. Maile, G. Pfaff, P. Reynders, Effect pigments - Past, present and future, Prog. Org. Coatings. 54 (2005) 150–163. doi:10.1016/j.porgcoat.2005.07.003.

[241] D. Kuang, Y. Fang, H. Liu, C. Frommen, D. Fenske, Fabrication of boehmite AlOOH and γ-Al2O3 nanotubes via a soft solution route, J. Mater. Chem. 13 (2003) 660–2. doi:10.1039/b212885c.

[242] H. Shao, J. Sönnke, J. Morel, S. Krug, In situ determination of anisotropic permeability of clay, Phys. Chem. Earth. 36 (2011) 1688–92. doi:10.1016/j.pce.2011.07.028.

[243] I. Gruber, I. Zinovik, L. Holzer, a. Flisch, L.D. Poulikakos, A computational study of the effect of structural anisotropy of porous asphalt on hydraulic conductivity, Constr. Build. Mater. 36 (2012) 66–77. doi:10.1016/j.conbuildmat.2012.04.094.

[244] J.E. Unosson, C. Persson, H. Engqvist, An evaluation of methods to determine the porosity of calcium phosphate cements, J. Biomed. Mater. Res. Part B Appl. Biomater. 103 (2015) 62–71.

[245] J. Zhang, S. Liu, J. Lin, H. Song, J. Luo, E.M. Elssfah, et al., Self-Assembly of Flowerlike AlOOH (Boehmite) 3D Nanoarchitectures, J. Phys. Chem. B. 110 (2006) 14249–52. doi:10.1021/jp062105f.

[246] R. Patakfalvi, S. Papp, I. Dékány, Silver and Palladium Nanoparticles Incorporated in Layer Structured Materials, in: Adsorpt. Aggreg. Surfactants Solut., Marcel Dekker, Inc., New York, 2003: pp. 247–70.

[247] D.-W. Kim, S.-I. Shin, S.-G. Oh, Preparation of and Stabilization Silver Colloids in Aqueous Surfactant Solutions, in: Adsorpt. Aggreg. Surfactants Solut., Marcel Dekker, Inc., New York, 2003: pp. 234–46.

[248] M.J. Rosen, J.T. Kunjappu, Micelle Formation by Surfactants, in: Surfactants Interfacial Phenom., 4th ed., Wiley, Hoboken, New Jersey, 2012: pp. 123–201.

[249] S. Yiv, R. Zana, Chemical Relaxation and Equilibrium Studies of Association in Aqueous Solutions of Bolaform Detergents, J. Colloid Interface Sci. 77 (1980) 449–55.

[250] M.K. Baloch, G. Hameed, A. Bano, Effect of Electrolyte Concentration and Temperature on CMC of Surfactants, J. Chem. Soc. Pakistan. 24 (2002) 77–86. http://jcsp.org.pk/ArticleUpload/1505-7185-1-RV.pdf.

[251] A. Bhattarai, S.K. Shah, A.K. Yadav, Effect of Solvent Composition on the Critical Micelle Concentration of Cetylpyridinium Chloride in Ethanol-Water Mixed Solvent

Media, Nepal J. Sci. Technol. 13 (2012) 89–93.

[252] S. Paria, K.C. Khilar, A review on experimental studies of surfactant adsorption at the hydrophilic solid-water interface., Adv. Colloid Interface Sci. 110 (2004) 75–95. doi:10.1016/j.cis.2004.03.001.

[253] C. Wohlfarth, Dielectric constant of the mixture (1) water; (2) ethanol, Landolt-Börnstein - Gr. IV Phys. Chem. 17 (2008) 520–3.

[254] N. de Nevers, Liquid-Liquid, Liquid-Solid, and Gas-Solid Equilibrium, in: Phys. Chem. Equilib. Chem. Eng., 2nd ed., Wiley, Hoboken, New Jersey, 2012: pp. 181–216.

[255] H. Akbaş, Ç. Kartal, Conductometric studies of hexadecyltrimethylammonium bromide in aqueous solutions of ethanol and ethylene glycol, Colloid J. 68 (2006) 125–130. doi:10.1134/S1061933X06020013.

[256] O. Owoyomi, O. Alo, O. Soriyan, G. Ogunlusi, Micellisation thermodynamics of sodium lauroylsarcosinate in water–alcohol binary mixtures, Phys. Chem. Liq. 52 (2013) 305–319. doi:10.1080/00319104.2013.832249.

[257] B. Kronberg, M. Costas, R. Silveston, Thermodynamics of the hydrophobic effect in surfactant solutions: micellization and adsorption, Pure Appl. Chem. 67 (1995) 897–902. doi:10.1351/pac199567060897.

[258] J. Yan, D. Wang, F. Bu, F.F. Yang, Investigation of the thermodynamic properties of the cationic surfactant CTAC in EG + water binary mixtures, J. Solution Chem. 39 (2010) 1501–1508. doi:10.1007/s10953-010-9551-8.

[259] P.K. Misra, B.K. Mishra, G.B. Behera, Micellization of ionic surfactants in tetrahydrofuran-water and acetonitrile-water mixed-solvent systems, Colloids and Surfaces. 57 (1991) 1–10. doi:10.1016/0166-6622(91)80175-N.

[260] C.C. Ruiz, Thermodynamics of micellization of tetradecyltrimethylammonium bromide in ethylene glycol-water binary mixtures, Colloid Polym. Sci. 277 (1999) 701–707. doi:10.1007/s003960050443.

[261] L.D. Frederickson, Characterization of Hydrated Aluminas by Infrared Spectroscopy, Application to Study of Bauxite Ores, Anal. Chem. (1954) 1883–1885.

[262] J.J. Fripiat, H.J. Bosmans, P.G. Rouxhet, Proton mobility in solids. I. Hydrogenic vibration modes and proton delocalization in boehmite, J. Phys. Chem. 71 (1967) 1097–1111.

[263] G. García, M. Falco, P. Crespo, S. Cabrera, U. Sedran, Characterization and catalytic evaluation of aluminum oxides obtained by the atrane route, Catal. Today. 166 (2011) 60–66. doi:10.1016/j.cattod.2010.08.003.

[264] J.T. Kloprogge, H.D. Ruan, R.L. Frost, Thermal decomposition of bauxite minerals: infrared emission spectroscopy of gibbsite, boehmite and diaspore, J. Mater. Sci. 37 (2002) 1121–1129.

[265] Y.I. Ryskin, V.C. Farmer, The infrared spectra of minerals, (1974) 137–181.

[266] H.W. van der Marel, H. Beutelspacher, Atlas of infrared spectroscopy of clay minerals and their admixtures, (1976) 194.

[267] Y. Li, J. Liu, Z. Jia, Fabrication of boehmite AlOOH nanofibers by a simple hydrothermal process, Mater. Lett. 60 (2006) 3586–90. doi:10.1016/j.matlet.2006.03.083.

[268] R. Tettenhorst, D.A. Hofmann, Crystal Chemistry of Boehmite, Clays Clay Miner. 28 (1980) 373–380.

[269] P.D.S. Santos, A.C.V. Coelho, H.D.S. Santos, P.K. Kiyohara, Hydrothermal synthesis of well-crystallised boehmite crystals of various shapes, Mater. Res. 12 (2009) 437–45. doi:10.1590/S1516-14392009000400012.

[270] G. Murugadoss, V. Ramasamy, Synthesis, effect of capping agents and optical properties of manganese-doped zinc sulphide nanoparticles, Luminescence. 28 (2013) 69–75. doi:10.1002/bio.2346.

[271] P.K. Sharma, R.K. Dutta, C.H. Liu, R. Pandey, A.C. Pandey, Surfactant mediated optical properties of cytosine capped CdSe quantum dots, Mater. Lett. 64 (2010) 1183–6. doi:10.1016/j.matlet.2010.02.045.

[272] B.C. Lippens, Structure and Texture of Aluminas, Delft University of Technology, 1961.

[273] X. Wu, B. Zhang, Z. Hu, Morphology-controlled hydrothermal synthesis of boehmite via an anions competition method, Powder Technol. 239 (2013) 272–6. doi:10.1016/j.powtec.2013.02.023.

[274] T. He, L. Xiang, S. Zhu, Different nanostructures of boehmite fabricated by hydrothermal process: effects of pH and anions, CrystEngComm. 11 (2009) 1338–42. doi:10.1039/b900447p.

[275] I. Sunagawa, Regular intergrowth of particles, in: Cryst. Growth, Morphol. Perfect., Cambridge University Press, Cambridge, United Kingdom, 2005: pp. 127–49.

[276] H. Liang, W. Chen, R. Wang, Z. Qi, J. Mi, Z. Wang, X-shaped hollow α-FeOOH penetration twins and their conversion to α-Fe2O3 nanocrystals bound by high-index facets with enhanced photocatalytic activity, Chem. Eng. J. 274 (2015) 224–230. doi:10.1016/j.cej.2015.03.125.

[277] M. Rubbo, M. Bruno, F.R. Massaro, D. Aquilano, The Five Twin Laws of Gypsum (CaSO4·2H2O): A Theoretical Comparison of the Interfaces of the Contact Twins, Cryst. Growth Des. 12 (2011) 3018–24. doi:10.1021/cg201031s.

[278] Z.-F. Dou, C.-Y. Cao, Q. Wang, J. Qu, Y. Yu, W.-G. Song, Synthesis, self-assembly, and high performance in gas sensing of X-shaped iron oxide crystals, ACS Appl. Mater. Interfaces. 4 (2012) 5698–703. doi:10.1021/am3016944.

[279] M. Nespolo, G. Ferraris, The oriented attachment mechanism in the formation of twins - a survey, Eur. J. Mineral. 16 (2004) 401–46.

[280] B. Velde, A. Meunier, Fundamentals of Clay Mineral Crystal Structure and Physicochemical Properties, in: Orig. Clay Miner. Soils Weather. Rocks, 1st ed., Springer, Berlin, 2008: pp. 3–74.

[281] J.J. Beresford, P.M. Cashman, R.G. Hollamby, The merits of polymeric fluids as support slurries, in: J. Burland, J. Mitchell (Eds.), Piling Deep Found., 1st ed., A.A. Balkerma, Rotterdam, The Netherlands, 1989: p. 4.

[282] R. Bai, H.F. Leow, Microfiltration of activated sludge wastewater - the effect of system operation parameters, Sep. Purif. Technol. 29 (2002) 189–198.

[283] K. Scott, Introduction to Membrane Separations, in: Handb. Ind. Membr., 2nd ed., Elsevier, Amsterdam, The Netherlands, 1998: pp. 3–185.

[284] A.G. Fane, W. Xi, W. Rong, Membrane filtration processes and fouling, in: Interface Sci. Drink. Water Treat., Elsevier, 2006: pp. 109–132.

[285] S. Hasan, Design and Performance of a Pilot Submerged Membrane Electro-Bioreactor (SMEBR) for Wastewater Treatment, Concordia University, 2012.

[286] J.T. Kraemer, A.L. Menniti, Z.K. Erdal, T.A. Constantine, B.R. Johnson, G.T. Daigger, et al., A practitioner's perspective on the application and research needs of membrane bioreactors for municipal wastewater treatment, Bioresour. Technol. 122 (2012) 2–10.

[287] R. Field, Fundamentals of Fouling, in: Membr. Water Treat., Wiley, Weinheim, 2010: pp. 1–23.

[288] J. Lu, G. Lipscomb, Cleaning membranes with focused ultrasound beams for drinking water treatment, 2009 IEEE Int. Ultrason. Symp. (2009) 1195–8. doi:10.1109/ULTSYM.2009.5441719.

[289] W.S. Ang, S. Lee, M. Elimelech, Chemical and physical aspects of cleaning of organic-fouled reverse osmosis membranes, J. Memb. Sci. 272 (2006) 198–210. doi:10.1016/j.memsci.2005.07.035.

[290] J.P. Chen, S.L. Kim, Y.P. Ting, Optimization of membrane physical and chemical cleaning by a statistically designed approach, J. Memb. Sci. 219 (2003) 27–45. doi:10.1016/S0376-7388(03)00174-1.

[291] X. Chai, T. Kobayashi, N. Fujii, Ultrasound-associated cleaning of polymeric membranes for water treatment, Sep. Purif. Technol. 15 (1999) 139–146. doi:10.1016/S1383-5866(98)00091-4.

[292] H. Zhu, M. Nyström, Cleaning results characterized by flux, streaming potential and FTIR measurements, Colloids Surfaces A Physicochem. Eng. Asp. 138 (1998) 309–21. doi:10.1016/S0927-7757(97)00072-1.

[293] A.-A. A., P. Williams, S. Mandale, R.W. Lovitt, Cleaning results of new and fouled nanofiltration membrane characterized by zeta potential and permeability, Sep. Purif. Technol. 54 (2007) 234–40. doi:10.1016/j.apsusc.2007.12.052.

[294] A. Al-Amoudi, R.W. Lovitt, Fouling strategies and the cleaning system of NF membranes and factors affecting cleaning efficiency, J. Memb. Sci. 303 (2007) 4–28. doi:10.1016/j.memsci.2007.06.002.

[295] E. Zondervan, B. Roffel, Evaluation of different cleaning agents used for cleaning ultra filtration membranes fouled by surface water, J. Memb. Sci. 304 (2007) 40–9. doi:10.1016/j.memsci.2007.06.041.

[296] T. Yang, Z.-F. Ma, Q.-Y. Yang, Formation and performance of Kaolin/MnO2 bi-layer composite dynamic membrane for oily wastewater treatment: Effect of solution conditions, Desalination. 270 (2011) 50–6. doi:10.1016/j.desal.2010.11.019.

[297] A.A. Poostchi, M. Bayat, M. Rezaei, E. Amini, M.R. Mehrnia, Formation of pre-coating dynamic membrane on mesh filter by cross-flow filtration of PAC–water suspension in a bioreactor: experimental and modeling, Desalin. Water Treat. 55 (2015) 17–27. doi:10.1080/19443994.2014.911118.

[298] M. Altman, R. Semiat, D. Hasson, Removal of organic foulants from feed waters by dynamic membranes, Desalination. 125 (1999) 65–75. doi:10.1016/S0011-9164(99)00124-1.

[299] R.L. Day, B.K. Marsh, Measurement of porosity in blended cement pastes, Cem. Concr. Res. 18 (1988) 63–73.

[300] O. Ersoy, Surface area and volume measurements of volcanic ash particles by SEM stereoscopic imaging, J. Volcanol. Geotherm. Res. 190 (2010) 290–6. doi:10.1016/j.jvolgeores.2009.12.006.

[301] Z. Huang, D. a. Dikin, W. Ding, Y. Qiao, X. Chen, Y. Fridman, et al., Three-dimensional representation of curved nanowires, J. Microsc. 216 (2004) 206–14. doi:10.1111/j.0022-2720.2004.01418.x.

[302] B. Minnich, H. Leeb, E.W.N. Bernroider, A. Lametschwandtner, Three-dimensional morphometry in scanning electron microscopy: A technique for accurate dimensional and angular measurements of microstructures using stereopaired digitized images and digital image analysis, J. Microsc. 195 (1999) 23–33. http://www.ncbi.nlm.nih.gov/pubmed/10444299.

[303] R.H. Perry, D.W. Green, Physical and Chemical Data, in: Perry's Chem. Eng. Handb., 7th ed., McGraw-Hill, New York, 1999: p. 337.

[304] J.C. Crittenden, R.R. Trussell, D.W. Hand, K.J. Howe, G. Tchobanoglous, Membrane Filtration, in: MWH's Water Treat. Princ. Des., 3rd ed., John Wiley & Sons, Hoboken, New Jersey, 2012: pp. 819–902.

[305] S. Yamada, J. Kanno, M. Miyauchi, Multi-sized Sphere Packing in Containers : Optimization Formula for Obtaining the Highest Density with Two Different Sized Spheres, Inf. Media Technol. 6 (2011) 493–500. doi:10.2197/ipsjtrans.4.126.

[306] J. Hermia, Constant pressure blocking filtration laws: applications to power-law non-Newtonian fluids, Trans. Inst. Chem. Eng. 60 (1982) 183–7.

[307] E. Santiso, E. Müller, Dense packing of binary and polydisperse hard spheres, Mol. Phys. 100 (2002) 2461–9. doi:10.1080/00268970210125313.

[308] P.I. O'Toole, T.S. Hudson, New High-Density Packings of Similarly Sized Binary Spheres, J. Phys. Chem. C. 115 (2011) 19037–40. doi:10.1021/jp206115p.

[309] Health Canada, Turbidity in Drinking Water, Ottawa, 2012. http://www.hc-sc.gc.ca/ewh-semt/alt_formats/hecs-sesc/pdf/pubs/water-eau/turbidity/turbidity-eng.pdf.

[310] Z. Yu, H. Chu, D. Cao, Y. Ma, B. Dong, Y. Wei, Pilot-scale hybrid bio-diatomite/dynamic membrane reactor for slightly polluted raw water purification, Desalination. 285 (2012) 73–82. doi:10.1016/j.desal.2011.09.036.

[311] B. Cai, H. Ye, L. Yu, Preparation and separation performance of a dynamically formed MnO2 membrane, Desalination. 128 (2000) 247–56. doi:10.1016/S0011-9164(00)00039-4.

[312] M.E. Ersahin, H. Ozgun, Y. Tao, J.B. van Lier, Applicability of dynamic membrane technology in anaerobic membrane bioreactors, Water Res. 48 (2014) 420–9. doi:10.1016/j.watres.2013.09.054.

[313] R.-Y. Horng, C. Huang, M.-C. Chang, H. Shao, B.-L. Shiau, Y.-J. Hu, Application of TiO2 photocatalytic oxidation and non-woven membrane filtration hybrid system for degradation of 4-chlorophenol, Desalination. 245 (2009) 169–82. doi:10.1016/j.desal.2008.06.018.

[314] H.H. Murray, Structure and Composition of the Clay Minerals and their Physical and Chemical Properties, in: Appl. Clay Mineral. Occur. Process. Appl. Kaolins, Bentonites, Palygorskite-Sepiolite, Common Clays, Elsevier, Amsterdam, The Netherlands, 2006: pp. 7–31.

[315] S.R. Santiwong, J. Guan, T.D. Waite, Effect of ionic strength and pH on hydraulic properties and structure of accumulating solid assemblages during microfiltration of montmorillonite suspensions., J. Colloid Interface Sci. 317 (2008) 214–27. doi:10.1016/j.jcis.2007.09.052.

[316] C. Gourgues, P. Aimar, V. Sanchez, Ultrafiltration of bentonite suspensions with hollow fiber membranes, J. Memb. Sci. 74 (1992) 51–69. doi:10.1016/0376-7388(92)87072-6.

[317] U. Farooq, S. Sheikh, Restoration of "dead" clay fouled membranes, Desalin. Water Treat. 51 (2013) 976–82. doi:10.1080/19443994.2012.714653.

[318] J. Ranville, M.D. Montano, Size Distributions, in: M. Baalousha, J.R. Lead (Eds.), Front. Nanosci. Charact. Nanomater. Complex Environ. Biol. Media, 1st ed., Elsevier, Amsterdam, The Netherlands, 2015: pp. 91–121.

[319] B. Van der Bruggen, M. Mänttäri, M. Nyström, Drawbacks of applying nanofiltration and how to avoid them: A review, Sep. Purif. Technol. 63 (2008) 251–263. doi:10.1016/j.seppur.2008.05.010.

[320] I. Sutzkover-Gutman, D. Hasson, Feed water pretreatment for desalination plants, Desalination. 264 (2010) 289–96. doi:10.1016/j.desal.2010.07.014.

[321] Flexicon, Precoat filtration: Diatomaceous earth improves filtration at desalination plant, Filtr. Sep. 47 (2010) 40–1. doi:10.1016/S0015-1882(10)70130-0.

[322] G.S. Logsdon, Precoat Filtration, in: Water Filtr. Pract. Incl. Slow Sand Filters Precoat Filtr., American Water Works Association, Denver, 2008: pp. 229–54.

[323] D. Lihong, C. Xu, L. Wenping, Z. Qixin, A Study on Enhancement of Filtration Process with Filter Aids Diatomaceous Earth and Wood Pulp Cellulose, Chinese J. Chem. Eng. 19 (2011) 792–8.

[324] M.F. Islam, M.H. Rizvi, T.A. Khan, M. Hasanuzzaman, Development of Ceramic Candle Filters by Slip Casting Process, Key Eng. Mater. 608 (2014) 85–90.

[325] B. Michen, A. Diatta, J. Fritsch, C. Aneziris, T. Graule, Removal of colloidal particles in ceramic depth filters based on diatomaceous earth, Sep. Purif. Technol. 81 (2011) 77–87.

[326] C. Valderrama-Bravo, E. Gutiérrez-Cortez, M. Contreras-Padilla, I. Rojas-Molina, J.C. Mosquera, A. Rojas-Molina, et al., Constant pressure filtration of lime water (nejayote) used to cook kernels in maize processing, J. Food Eng. 110 (2012) 478–86. doi:10.1016/j.jfoodeng.2011.12.018.

[327] R.S. Farag, A.M. El-Anany, Improving the quality of fried oils by using different filter aids, J. Sci. Food Agric. 86 (2006) 2228–40. doi:10.1002/jsfa.

[328] G.P. Fulton, Introduction, in: Diatomaceous Earth Filtr. Safe Drink. Water, American Society of Civil Engineers, Reston, Virginia, 2000: pp. 1–27.

[329] World Health Organization, Guidelines for Drinking-Water Quality (4th edition), Geneva, 2011.

[330] Safe Drinking Water Act, United States, 1974.

[331] K. Roebuck, A.Y. Tremblay, The self-assembly of twinned boehmite nanosheets into porous 3D structures in ethanol–water mixtures, Colloids Surfaces A Physicochem. Eng. Asp. (2016).

[332] S. Ripperger, W. Gösele, C. Alt, T. Loewe, Filtration Fundamentals, in: Ullmann's Encylopedia Ind. Chem., Wiley, Weinheim, Germany, 2012: pp. 1–38.

[333] W. Höflinger, C. Stöcklmayer, Investigations about the layered structure of dust filter cakes with a computer-simulation, Staub, Reinhaltung Der L. 55 (1995) 423–8.

[334] I.C. Bourg, G. Sposito, A.C.M. Bourg, Modeling the acid-base surface chemistry of montmorillonite, J. Colloid Interface Sci. 312 (2007) 297–310. doi:10.1016/j.jcis.2007.03.062.

[335] M. Kosmulski, Electric Charge Density of Silica, Alumina, and Related Surfaces, in: P. Somasundaran (Ed.), Encycl. Surf. Colloid Sci., 2nd ed., Taylor & Francis, New York,

2006: pp. 1857–67.

[336] D. Hendricks, Cake Filtration, in: Fundam. Water Treat. Unit Process. - Phys. Chem. Biol., CRC Press, Boca Raton, Florida, 2011: pp. 423–56.

[337] K. Roebuck, A.Y. Tremblay, Optimal aggregate size distribution for the formation of highly efficient nanosheet dynamic membranes, J. Memb. Sci. (2016).

[338] K.M. Koeller, C.H. Wong, Enzymes for chemical synthesis, Nature. 409 (2001) 232–40. doi:10.1038/35051706.

[339] D. Klein-Marcuschamer, P. Oleskowicz-Popiel, B.A. Simmons, H.W. Blanch, The challenge of enzyme cost in the production of lignocellulosic biofuels, Biotechnol. Bioeng. 109 (2012) 1083–7. doi:10.1002/bit.24370.

[340] P.S. Bisen, B.S. Sanodiya, G.S. Thakur, R.K. Baghel, G.B.K.S. Prasad, Biodiesel production with special emphasis on lipase-catalyzed transesterification, Biotechnol. Lett. 32 (2010) 1019–30. doi:10.1007/s10529-010-0275-z.

[341] A.A. Homaei, R. Sariri, F. Vianello, R. Stevanato, Enzyme immobilization: An update, J. Chem. Biol. 6 (2013) 185–205. doi:10.1007/s12154-013-0102-9.

[342] C. Mateo, J.M. Palomo, G. Fernandez-Lorente, J.M. Guisan, R. Fernandez-Lafuente, Improvement of enzyme activity, stability and selectivity via immobilization techniques, Enzyme Microb. Technol. 40 (2007) 1451–63. doi:10.1016/j.enzmictec.2007.01.018.

[343] G. Bayramoglu, B. Altintas, M.Y. Arica, Immobilization of glucoamylase onto polyaniline-grafted magnetic hydrogel via adsorption and adsorption/cross-linking, Appl. Microbiol. Biotechnol. 97 (2013) 1149–59. doi:10.1007/s00253-012-3999-y.

[344] M.S. Carrasco, J.C. Rad, S. González-Carcedo, Immobilization of alkaline phosphatase by sorption on Na-sepiolite, Bioresour. Technol. 51 (1995) 175–81.

[345] Y. Kawachi, S.I. Kugimiya, H. Nakamura, K. Kato, Enzyme encapsulation in silica gel prepared by polylysine and its catalytic activity, Appl. Surf. Sci. 314 (2014) 64–70. doi:10.1016/j.apsusc.2014.06.150.

[346] G.L. Witucki, A Silane Primer: Chemistry and Applications of Alkoxy Silanes, J. Coatings Technol. 65 (1993) 57–60. doi:10.1124/dmd.109.028449.

[347] S. Joughehdoust, A. Behnamghader, M. Imani, M. Daliri, E. Jabbari, Surface modification of high porosity alumina scaffold by silane coupling agent, AIP Conf. Proc. 1400 (2011) 480–5. doi:10.1063/1.3663167.

[348] Q. Zhang, R.F. Huang, L.H. Guo, One-step and high-density protein immobilization on epoxysilane-modified silica nanoparticles, Chinese Sci. Bull. 54 (2009) 2620–2626. doi:10.1007/s11434-009-0210-7.

[349] T.W.G. Solomons, C. Fryhle, Reactions of Epoxides, in: Org. Chem., 8th ed., John Wiley & Sons, New Jersey, 2004: pp. 519–22.

[350] D. Derouet, J.C. Brosse, A. Challioui, Alcoholysis of epoxidized polyisoprenes by direct opening of oxirane rings with alcohol derivatives 2. Study on epoxidized 1,4-polyisoprene, Eur. Polym. J. 37 (2001) 1327–37.

[351] M.M. Chehimi, M.L. Abel, J.F. Watts, R.P. Digby, Surface chemical and thermodynamic properties of γ-glycidoxy-propyltrimethoxysilane-treated alumina: an XPS and IGC study, J. Mater. Chem. 11 (2001) 533–543. doi:10.1039/b005227m.

[352] C. Prapainainar, S. Kanjanapaisit, P. Kongkachuichay, S.M. Holmes, P. Prapainainar, Surface modification of mordenite in Nafion composite membrane for direct ethanol fuel cell and its characterizations: Effect of types of silane coupling agent, J. Environ. Chem. Eng. 4 (2016) 2637–46. doi:10.1016/j.jece.2016.05.005.

[353] N. Ikuta, T. Hori, H. Naitoh, Y. Kera, E. Nishio, I. Abe, Fixation of silane coupling agents to glass fiber in silane treatment process, Compos. Interfaces. 1 (1993) 455–62.

[354] Y. Meng, G. Wang, N. Yang, Z. Zhou, Y. Li, X. Liang, et al., Two-step synthesis of fatty acid ethyl ester from soybean oil catalyzed by Yarrowia lipolytica lipase, Biotechnol. Biofuels. 4 (2011) 1–9. doi:10.1186/1754-6834-4-6.

[355] W.W. Xi, J.H. Xu, Preparation of enantiopure (S)-ketoprofen by immobilized Candida rugosa lipase in packed bed reactor, Process Biochem. 40 (2005) 2161–6. doi:10.1016/j.procbio.2004.08.003.

[356] A. H-Kittikun, W. Kaewthong, B. Cheirsilp, Continuous production of monoacylglycerols from palm olein in packed-bed reactor with immobilized lipase PS, Biochem. Eng. J. 40 (2008) 116–120. doi:10.1016/j.bej.2007.11.023.

[357] A. V. Paula, D. Urioste, J.C. Santos, H.F. de Castro, Porcine pancreatic lipase immobilized on polysiloxane–polyvinyl alcohol hybrid matrix: catalytic properties and feasibility to mediate synthesis of surfactants and biodiesel, J. Chem. Technol. Biotechnol. (82AD) 281–8.

[358] K. Bagi, L.M. Simon, Comparison of esterificafion and transesterification of fructose by porcine pancreas lipase immobilized on different supports, Biotechnol. Tech. 13 (1999) 309–12. doi:10.1023/A:1008980809993.

[359] V. Kéry, J. Haplová, K. Tihlárik, S. Schmidt, Factors Influencing the Activity and Thermostability of Immobilized Porcine Pancreatic Lipase, J. Chem. Technol. Biotechnol. 48 (1990) 201–7.

[360] Y.X. Bai, Y.F. Li, Y. Yang, L.X. Yi, Covalent immobilization of triacylglycerol lipase onto functionalized nanoscale SiO2 spheres, Process Biochem. 41 (2006) 770–7. doi:10.1016/j.procbio.2005.09.012.

[361] D.G. Lee, K.M. Ponvel, M. Kim, S. Hwang, I.S. Ahn, C.H. Lee, Immobilization of lipase on hydrophobic nano-sized magnetite particles, J. Mol. Catal. B Enzym. 57 (2009) 62–6. doi:10.1016/j.molcatb.2008.06.017.

[362] K. Roebuck, A.Y. Tremblay, Optimal aggregate size distribution for the formation of highly efficient nanosheet dynamic membranes, J. Memb. Sci. (2016).

doi:10.1016/j.memsci.2016.04.047.

[363] M.M. Bradford, A Rapid and Sensitive Method for the Quantitation of Microgram Quantities of Protein Utilizing the Principle of Protein-Dye Binding, Anal. Chem. 72 (1976) 248–54.

[364] D.B. Lopes, L.P. Fraga, L.F. Fleuri, G.A. Macedo, Lipase and esterase: to what extent can this classification be applied accurately?, Ciência E Tecnol. Aliment. 31 (2011) 603–613. doi:10.1590/S0101-20612011000300009.

[365] R. Katoch, Determination of Lipase and Lipoxygenase Activity, in: Anal. Tech. Biochem. Mol. Biol., Springer, New York, 2011: pp. 270–1. doi:10.1007/978-1-4419-9785-2.

[366] International Olive Council, Determination of Free Fatty Acids, Cold Method, (2015).

[367] S.P. Hozo, B. Djulbegovic, I. Hozo, Estimating the mean and variance from the median, range, and the size of a sample, BMC Med. Res. Methodol. 5 (2005) 13–22. doi:10.1186/1471-2288-5-13.

[368] J.M. Saniger, Al-O infrared vibrational frequencies of γ-alumina, Mater. Lett. 22 (1995) 109–13. doi:10.1016/0167-577X(94)00234-7.

[369] L.A.S.A. Prado, M. Sriyai, M. Ghislandi, A. Barros-timmons, K. Schulte, Surface Modification of Alumina Nanoparticles with Silane Coupling Agents, J. Braz. Chem. Soc. 21 (2010) 2238–45.

[370] K.M.K. Yu, D. Thompsett, S.C. Tsang, Ultra-thin porous silica coated silver-platinum alloy nano-particle as a new catalyst precursor, Society. (2003) 1522–3. doi:Doi 10.1039/B303989g.

[371] J. Comyn, D.P. Oxley, R.G. Pritchard, C.R. Werrett, A.J. Kinloch, Examination of the interaction of 3-glycidoxypropyltrimethoxysilane with aluminium oxide by inelastic electron tunnelling spectroscopy, Int. J. Adhes. Adhes. 9 (1989) 201–204. doi:10.1016/0143-7496(89)90062-6.

[372] K.G. Mayhan, L.F. Thompson, C.F. Magdalin, Identification of organosilicon liquids by infrared spectroscopy, J. Paint Technol. 44 (1972) 85–93.

[373] X. Liu, Y. Guan, R. Shen, H. Liu, Immobilization of lipase onto micron-size magnetic beads, 822 (2005) 91–97. doi:10.1016/j.jchromb.2005.06.001.

[374] S.H. Chiou, W.T. Wu, Immobilization of Candida rugosa lipase on chitosan with activation of the hydroxyl groups, Biomaterials. 25 (2004) 197–204. doi:10.1016/S0142-9612(03)00482-4.

[375] S.L. Gilani, G.D. Najafpour, A. Moghadamnia, A.H. Kamaruddin, Stability of immobilized porcine pancreas lipase on mesoporous chitosan beads: A comparative study, J. Mol. Catal. B Enzym. 133 (2016) 144–53. doi:10.1016/j.molcatb.2016.08.005.

[376] K. Kośla, J. Grobelny, M. Cichomski, Preparation and frictional investigation of the

two-components silanes deposited on alumina surface, Appl. Surf. Sci. 314 (2014) 500–4. doi:10.1016/j.apsusc.2014.07.043.

[377] S.J. Park, K.S. Cho, Filler-elastomer interactions: Influence of silane coupling agent on crosslink density and thermal stability of silica/rubber composites, J. Colloid Interface Sci. 267 (2003) 86–91. doi:10.1016/S0021-9797(03)00132-2.

[378] J.D. Bianchetta, J. Bidaud, A.A. Guidoni, J.J. Bonicel, M. Rovery, Porcine Pancreatic Lipase - Sequence of the First 234 Amino Acids of the Peptide Chain, Eur. J. Biochem. 97 (1979) 395–405. doi:10.1111/j.1432-1033.1979.tb13126.x.

[379] C. Chapus, H. Sari, M. Sémériva, P. Desnuelle, Role of Colipase in the Interfacial Adsorption of Pancreatic Lipase at Hydrophilic Interfaces, FEBS Lett. 58 (1975) 155–8.

[380] G. Ozyilmaz, E. Gezer, Production of aroma esters by immobilized Candida rugosa and porcine pancreatic lipase into calcium alginate gel, J. Mol. Catal. B Enzym. 64 (2010) 140–5. doi:10.1016/j.molcatb.2009.04.013.

[381] S. Fadıloğlu, Z. Söylemez, Olive Oil Hydrolysis by Celite-Immobilized Candida rugosa Lipase, J. Agric. Food Chem. 46 (1998) 3411–4. doi:10.1021/jf9709865.

[382] S. Fadiloğlu, Z. Söylemez, Kinetics of lipase-catalyzed hydrolysis of olive oil, Food Res. Int. 30 (1997) 171–5. doi:10.1016/S0963-9969(97)00022-7.

[383] S. Gupta, Comparative study on hydrolysis of oils by lipase immobilized biocatalytic PS membranes using biphasic enzyme membrane reactor, J. Environ. Chem. Eng. 4 (2016) 1797–1809. doi:10.1016/j.jece.2016.03.007.

[384] K.-E. Jaeger, M.T. Reetz, Microbial lipases form versatile tools for biotechnology, Trends Biotechnol. 16 (1998) 396–403. doi:10.1016/S0167-7799(98)01195-0.

[385] T. Vorderwülbecke, K. Kieslich, H. Erdmann, Comparison of lipases by different assays, Enzyme Microb. Technol. 14 (1992) 631–9. doi:10.1016/0141-0229(92)90038-P.

[386] R. Birner-Grünberger, H. Scholze, K. Faber, A. Hermetter, Identification of Various Lipolytic Enzymes in Crude Porcine Pancreatic Lipase Preparations Using Covalent Fluorescent Inhibitors, Biotechnol. Bioeng. 85 (2004) 147–54. doi:10.1002/bit.10894.

[387] G. Fernández-Lorente, C. Ortiz, R.L. Segura, R. Fernández-Lafuente, J.M. Guisán, J.M. Palomo, Purification of different lipases from Aspergillus niger by using a highly selective adsorption on hydrophobic supports, Biotechnol. Bioeng. 92 (2005) 773–9. doi:10.1002/bit.20656.

[388] A. Bastida, P. Sabuquillo, P. Armisen, J. Huguet, M. Guisa, A Single Step Purification, Immobilization, and Hyperactivation of Lipases via Interfacial Adsorption on Strongly Hydrophobic Supports, Biotechnol. Bioeng. 58 (1998) 486–93.

[389] P. Sabuquillo, J. Reina, G. Fernandez-Lorente, J.M. Guisan, R. Fernandez-Lafuente,

"Interfacial affinity chromatography" of lipases: Separation of different fractions by selective adsorption on supports activated with hydrophobic groups, Biochim. Biophys. Acta - Protein Struct. Mol. Enzymol. 1388 (1998) 337–48. doi:10.1016/S0167-4838(98)00183-6.

[390] J.M. Palomo, R.L. Segura, G. Fernández-Lorente, M. Pernas, M.L. Rua, J.M. Guisán, et al., Purification, immobilization, and stabilization of a lipase from Bacillus thermocatenulatus by interfacial adsorption on hydrophobic supports, Biotechnol. Prog. 20 (2004) 630–5. doi:10.1021/bp0342957.

[391] G. Ozyilmaz, The effect of spacer arm on hydrolytic and synthetic activity of Candida rugosa lipase immobilized on silica gel, J. Mol. Catal. B Enzym. 56 (2009) 231–6. doi:10.1016/j.molcatb.2008.05.008.

[392] Y. Li, G. Zhou, W. Qiao, Y. Wang, Immobilization of Porcine pancreas lipase on fiber-like SBA-15 mesoporous material, Mater. Sci. Eng. B Solid-State Mater. Adv. Technol. 162 (2009) 120–6. doi:10.1016/j.mseb.2009.03.016.

[393] N. Haque, N.P. Prabhu, Lid Closure Dynamics of Porcine Pancreatic Lipase in Aqueous Solution, Biochim. Biophys. Acta - Gen. Subj. 1860 (2016) 2313–25.

[394] A. Salis, D. Bilaničová, B.W. Ninham, M. Monduzzi, Hofmeister effects in enzymatic activity: Weak and strong electrolyte influences on the activity of Candida rugosa lipase, J. Phys. Chem. B. 111 (2007) 1149–56. doi:10.1021/jp066346z.

[395] S. Negishi, S. Sato, S. Mukataka, J. Takahashi, Utilization of powdered pig bone as a support for immobilization of lipase, J. Ferment. Bioeng. 67 (1989) 350–355. doi:10.1016/0922-338X(89)90254-7.

[396] Z. Knezevic, N. Milosavic, D. Bezbradica, Z. Jakovljevic, R. Prodanovic, Immobilization of lipase from Candida rugosa on Eupergit C supports by covalent attachment, Biochem. Eng. J. 30 (2006) 269–78. doi:10.1016/j.bej.2006.05.009.

[397] G. Bayramoğlu, M.Y. Arica, Preparation of poly(glycidylmethacrylate-methylmethacrylate) magnetic beads: Application in lipase immobilization, J. Mol. Catal. B Enzym. 55 (2008) 76–83. doi:10.1016/j.molcatb.2008.01.012.

[398] S. Chu, A. Majumdar, Opportunities and challenges for a sustainable energy future, Nature. 488 (2012) 294–303. doi:10.1038/nature11475.

[399] A. Demirbas, Importance of biodiesel as transportation fuel, Energy Policy. 35 (2007) 4661–70. doi:10.1016/j.enpol.2007.04.003.

[400] M. Höök, X. Tang, Depletion of fossil fuels and anthropogenic climate change-A review, Energy Policy. 52 (2013) 797–809. doi:10.1016/j.enpol.2012.10.046.

[401] United Nations Development Programme, Energy, The Environment, and Health, in: Communications Development Inc. (Ed.), World Energy Assess. - Energy Chall. Sustain., 2000: pp. 61–110. http://medcontent.metapress.com/index/A65RM03P4874243N.pdf.

[402] M. Fangrui, M. Hanna, Biodiesel production : a review, Bioresour. Technol. 70 (1999) 1–15.

[403] D.Y.C. Leung, X. Wu, M.K.H. Leung, A review on biodiesel production using catalyzed transesterification, Appl. Energy. 87 (2010) 1083–95. doi:10.1016/j.apenergy.2009.10.006.

[404] M.M. Gui, K.T. Lee, S. Bhatia, Feasibility of edible oil vs. non-edible oil vs. waste edible oil as biodiesel feedstock, Energy. 33 (2008) 1646–53. doi:10.1016/j.energy.2008.06.002.

[405] M.K. Lam, K.T. Lee, A.R. Mohamed, Homogeneous, heterogeneous and enzymatic catalysis for transesterification of high free fatty acid oil (waste cooking oil) to biodiesel: A review, Biotechnol. Adv. 28 (2010) 500–18. doi:10.1016/j.biotechadv.2010.03.002.

[406] C.C. Lai, S. Zullaikah, S.R. Vali, Y.H. Ju, Lipase-catalyzed production of biodiesel from rice bran oil, J. Chem. Technol. Biotechnol. 80 (2005) 331–7. doi:10.1002/jctb.1208.

[407] M. Berrios, J. Siles, M.A. Martín, A. Martín, A kinetic study of the esterification of free fatty acids (FFA) in sunflower oil, Fuel. 86 (2007) 2383–8.

[408] X.Y. Wu, S. Jääskeläinen, Y.-Y. Linko, An investigation of crude lipases for hydrolysis, esterification, and transesterification, Enzyme Microb. Technol. 19 (1996) 226–31.

[409] B. Freedman, E.H. Pryde, T.L. Mounts, Variables Affecting the Yields of Fatty Esters from Transesterified Vegetable Oils, J. Am. Oil Chem. Soc. 61 (1984) 1638–43.

[410] J.M. Marchetti, V.U. Miguel, A.F. Errazu, Possible methods for biodiesel production, Renew. Sustain. Energy Rev. 11 (2007) 1300–11. doi:10.1016/j.rser.2005.08.006.

[411] Bryan R. Moser, Biodiesel production, properties and feedstocks, Vitr. Cell. Dev. Biol. - Plant. (2011) 229–66. doi:10.1007/s11627-009-9204-z.

[412] F. Hasan, A.A. Shah, A. Hameed, Industrial applications of microbial lipases, Enzyme Microb. Technol. 39 (2006) 235–51. doi:10.1016/j.enzmictec.2005.10.016.

[413] L. Fjerbaek, K. V. Christensen, B. Norddahl, A review of the current state of biodiesel production using enzymatic transesterification, Biotechnol. Bioeng. 102 (2009) 1298–1315. doi:10.1002/bit.22256.

[414] A.M. V. Dossat, D. Combes, Continuous enzymatic transesterification of high oleic sunflower oil in a packed bed reactor: Influence of the glycerol production, Enzym. Microb. Technol. 25 (1999) 194–200.

[415] S.F.A. Halim, A. Harun Kamaruddin, Catalytic studies of lipase on FAME production from waste cooking palm oil in a tert-butanol system, Process Biochem. 43 (2008) 1436–9. doi:10.1016/j.procbio.2008.08.010.

[416] L. Deng, X. Xu, G.G. Haraldsson, T. Tan, F. Wang, Enzymatic production of alkyl esters through alcoholysis: A critical evaluation of lipases and alcohols, J. Am. Oil Chem. Soc. 82 (2005) 341–7. doi:10.1007/s11746-005-1076-3.

[417] Y. Shimada, Y. Watanabe, T. Samukawa, A. Sugihara, H. Noda, H. Fukuda, et al., Conversion of vegetable oil to biodiesel using immobilized Candida antarctica lipase, J. Am. Oil Chem. Soc. 76 (1999) 789–793. doi:10.1007/s11746-999-0067-6.

[418] K. Roebuck, A.Y. Tremblay, Highly permeable twinned alumina nanoparticles for the precoat filtration of fine colloids, Sep. Purif. Technol. 182 (2017) 197–206.

[419] J. Van Gerpen, B. Shanks, R. Pruszko, D. Clements, G. Knothe, Biodiesel Analytical Methods, Golden, Colorado, 2004. http://www.nrel.gov/docs/fy04osti/36240.pdf.

[420] B. Chen, J. Hu, E.M. Miller, W. Xie, M. Cai, R.A. Gross, Candida antarctica Lipase B chemically immobilized on epoxy-activated micro- and nanobeads: Catalysts for polyester synthesis, Biomacromolecules. 9 (2008) 463–71. doi:10.1021/bm700949x.

[421] K.F. Haigh, S.Z. Abidin, G.T. Vladisavljević, B. Saha, Comparison of Novozyme 435 and Purolite D5081 as heterogeneous catalysts for the pretreatment of used cooking oil for biodiesel production, Fuel. 111 (2013) 186–193.

[422] Z. Zhu, H. Liu, H. Sun, D. Yang, PEG-directed hydrothermal synthesis of multilayered alumina microfibers with mesoporous structures, Microporous Mesoporous Mater. 123 (2009) 39–44. doi:10.1016/j.micromeso.2009.03.028.

[423] Y. Zhao, W.N. Martens, T.E. Bostrom, H.Y. Zhu, R.L. Frost, Synthesis, Characterization, and Surface Properties of Iron-Doped Boehmite Nanofibers, Langmuir. 23 (2007) 2110–2116.

[424] N.W.J.T. Heinsman, C.G.P.H. Schroën, A. Van Der Padt, M.C.R. Franssen, R.M. Boom, K. Van'T Riet, Substrate sorption into the polymer matrix of Novozym 435® and its effect on the enantiomeric ratio determination, Tetrahedron Asymmetry. 14 (2003) 2699–704. doi:10.1016/S0957-4166(03)00577-9.

[425] C. José, G.B. Austic, R.D. Bonetto, R.M. Burton, L.E. Briand, Investigation of the stability of Novozym® 435 in the production of biodiesel, Catal. Today. 213 (2013) 73–80. doi:10.1016/j.cattod.2013.02.013.

[426] C. José, R.D. Bonetto, L.A. Gambaro, M.D.P.G. Torres, M.L. Foresti, M.L. Ferreira, et al., Investigation of the causes of deactivation-degradation of the commercial biocatalyst Novozym® 435 in ethanol and ethanol-aqueous media, J. Mol. Catal. B Enzym. 71 (2011) 95–107. doi:10.1016/j.molcatb.2011.04.004.

[427] H.H. Weetall, Preparation of Immobilized Proteins Covalently Coupled Through Silane Coupling Agents to Inorganic Supports, Appl. Biochem. Biotechnol. 41 (1993) 157–88.

[428] C. Tarducci, E.J. Kinmond, J.P.S. Badyal, S.A. Brewer, C. Willis, Epoxide-Functionalized Solid Surfaces, (2000) 1884–1889.

[429] S.L. Gilani, G.D. Najafpour, A. Moghadamnia, A.H. Kamaruddin, Stability of immobilized porcine pancreas lipase on mesoporous chitosan beads: A comparative study, J. Mol. Catal. B Enzym. 133 (2016) 144–53. doi:10.1016/j.molcatb.2016.08.005.

[430] E. Jurado, F. Camacho, G. Luzón, M. Fernández-Serrano, M. García-Román, Kinetics of the enzymatic hydrolysis of triglycerides in o/w emulsions: Study of the initial rates and the reaction time course, Biochem. Eng. J. 40 (2008) 473–84. doi:10.1016/j.bej.2008.02.002.

[431] D. Goswami, J.K. Basu, S. De, Lipase applications in oil hydrolysis with a case study on castor oil: a review, Crit. Rev. Biotechnol. 33 (2013) 81–96. doi:10.3109/07388551.2012.672319.

[432] M.S. Puthli, V.K. Rathod, A.B. Pandit, Enzymatic hydrolysis of castor oil: Process intensification studies, Biochem. Eng. J. 31 (2006) 31–41. doi:10.1016/j.bej.2006.05.017.

[433] P. Reis, K. Holmberg, R. Miller, M.E. Leser, T. Raab, H.J. Watzke, Lipase reaction at interfaces as self-limiting processes, Comptes Rendus Chim. 12 (2009) 163–70. doi:10.1016/j.crci.2008.04.018.

[434] M. Nordblad, A.K. Pedersen, A. Rancke-Madsen, J.M. Woodley, Enzymatic pretreatment of low-grade oils for biodiesel production, Biotechnol. Bioeng. 113 (2016) 754–60. doi:10.1002/bit.25846.

[435] A. Ionescu, A. Allouche, J.P. Aycard, M. Rajzmann, F. Hutschka, Study of γ-alumina surface reactivity: Adsorption of water and hydrogen sulfide on octahedral aluminum sites, J. Phys. Chem. B. 106 (2002) 9359–66. doi:10.1021/jp020145n.

[436] Y. Mei, L. Miller, W. Gao, R. Gross, Imaging the distribution and secondary structure of immobilized enzymes using infrared microspectroscopy, Biomacromolecules. 4 (2003) 70–4.

[437] Y. Xu, M. Nordblad, J.M. Woodley, A two-stage enzymatic ethanol-based biodiesel production in a packed bed reactor, J. Biotechnol. 162 (2012) 407–14. doi:10.1016/j.jbiotec.2012.05.017.

[438] V.M. Balcão, A.L. Paiva, F.X. Malcata, Bioreactors with immobilized lipases: State of the art, Enzyme Microb. Technol. 18 (1996) 392–416. doi:10.1016/0141-0229(95)00125-5.